Multiscale Modelling of Cancer Cell Motility

Melda Tozluoğlu

January 2013

Biomolecular Modelling Laboratory,
Cancer Research UK London Research Institute
and
Department of Biochemistry and Molecular Biology,
University College London

A thesis submitted in partial fulfilment of the requirements
for the degree of Doctor of Philosophy in Biochemistry
at the University College London.

I, Melda Tozluoğlu, confirm that the work presented in this thesis is my own. Where information has been derived from other sources, I confirm that this has been indicated in the thesis.

Abstract

Cell motility is required for many biological processes, including cancer metastasis. The molecular requirements for migration and, the morphology of migrating cells, can vary considerably depending on matrix geometry. Therefore, predicting the optimal migration strategy or the effect of experimental perturbation is difficult. This thesis presents a computational model of single cell motility that encompasses flexible cell morphology, actin polymerisation based protrusions, cell cortex asymmetry, plasma membrane blebbing, local cortex heterogeneity at the protein level, cell–extracellular matrix adhesion, and varying extracellular matrix geometries. This computational model is used to explore the theoretical requirements for rapid migration in different matrix geometries. The analysis reveals that confinement of the cell within the extracellular matrix brings profound changes in the relationship between cortical contractility and cell velocity. In confined environments with discontinuity, the relationship between adhesion and cell velocity is fundamentally altered: adhesion becomes dispensable for a large range of gap sizes in between the extracellular matrix filaments. The utility of the model is shown by predicting cancer cell behaviour *in vivo*, in terms of both cell velocity and the morphology of the motile cell. Furthermore, the model is challenged to predict the effects of selected biochemical perturbations that alter i) cortical contractility, ii) cell-ECM adhesion, and iii) signalling between the cell-ECM adhesion sites and intracellular regulators of cell motility machinery. Multiphoton intravital imaging is used to verify bleb-driven migration of melanoma, breast cancer cells, and, surprisingly, endothelial cells at tumour margins. Intravital imaging of melanoma verified model predictions on cell velocity, cell morphology, nucleus behaviour, and effects of anti-invasive interventions. The model succesfully predicted melanoma velocities *in vitro* and *in vivo*. Moreover, it successfully predicted the effects of anti-invasive interventions, showing all perturbations will result in significant reduction in cell velocity *in vitro*, whereas only perturbation of cortical contractility will affect cell velocity *in vivo*. The model also successfully predicted the interactions of the cell nucleus with the cell cortex and the cell morphology upon intervensions. Overall, from measure-

ment of rather simple variables *in vitro*, the model has been able to predict the *in vivo* response of three very different putative anti-invasive interventions.

Acknowledgements

This research has been possible with the endless support from my supervisors, colleagues, friends and family. I would like to thank everyone who has shared their knowledge and wisdom with me through the last four years.

Firstly, I would like to thank my examiners Prof. Philip Maini and Dr. Ewa Paluch for agreeing to review this thesis, and allowing me to defend it.

Funding for this work has been provided by Cancer Research UK, and University College London. I would like to thank these institutions, not only to the Charity, but also my thousands of nameless supporters, who ran in the rain, who cycled miles, who gave generously, and made Cancer Research UK the glorious funder of science that it is today. Together, we will beat cancer.

I would like to thank my thesis committee, Dr. Caroline Hill, and Dr. Martin Singleton. They have inspired me and stimulated improvements in my research, in our every encounter.

I shall express my gratitude to my supervisor, Dr. Paul Bates, who accepted me in his group, and gave me the opportunity to undertake this Ph.D. I am forever indebted to him for his support, our long discussions, and his openness in letting me pursue my mind. From the first months, Dr. Erik Sahai, has been a fundamental part of my Ph.D. I would like to thank him for choosing me as the computational minion for his ideas, for his endless patience, for sharing the clarity of his mind with me, for always finding the answer provided that there is one, and for knowing when there is none.

All the members of Biomolecular Modelling Laboratory have been fond friends,

and never spared their wisdom. Some have been bright as the day light at times of trouble – ”Yes, but that is not a theoretical problem, it is a problem of computer resources, therefore it can be solved with proper coding”, some more harsh – ”Then you would have a perpetual motion machine there”, and some more peculiar than the others – ”Yes, that is how U.F.O.s move, Germans discovered it during the WWII”, but all have been equally enthusiastic. I would like to thank all of them, for without them, it would have been a dull, if at all possible, four years. Dr. Raphaël Chaleil for keeping up the computing equipment up and running despite my continuous attempts to crash everything, making even the most hard to compile resources available when needed, and teaching me my way out of the memory leaks. Dr. Xiaofan Li, for showing me how to think about coding, and for always having time to help when I needed. Dr. Iain Moal for being an endless source of topics for discussion, in the lab and in the pub. Dr. Alexander Tournier, for swiftly appearing by my side during every struggle, with code or with theory; and letting me be myself once I stood up again. Dr. Özge Kürkçüoğlu, for being a true companion in the many long years we have known each other, and a solid source of discussions on how to model things in the broad context. Dr. Yanlan Mao, and Dr. Tammy Cheng for their valuable discussions, and feedbacks on manuscripts. Dr. Mieczysław Torchała, Rudi Agius, Sakshi Gulati, and Dr. Robert Jenkins for constructive discussions, and simply for their company. The people who made this Ph.D. possible are not limited to the people in laboratories, I would also like to thank to the support staff at the London Research Institute, including but not limited to Sally Leevers, Sabina Ebbols, Sophie Lutter, Emma Rainbow, Erin Fortin and Mark Henshall.

I would like to extend my gratefulness to my supervisors during my Bachelor and Masters degrees, Dr. Türkan Haliloğlu in Boğaziçi University and Dr. Ruth Nusinov in National Cancer Institute Frederick. Without their knowledge and wisdom that I hope I could inherit a fraction, I would not be able to deliver the work in this thesis.

Finally I would like to thank my family, who always believed in me and supported me. To my brother Alper Yavuztürk, who made me grow up with the knowledge that I will always be safe, embedded the courage and curiousity in me to never hesitate trying. I cannot express enough thankfulness to my other

wing, my husband Çağrı. He has been with me each and every moment through the period of my Ph.D. In his intellectual support, he has enlightened me with his discussions on the physics of materials, and helped me bring together the conclusions I can draw from my observations. In every other moment of our lives, he shared my happiness, endured unthinkable hardships to support me, never left my side, his love ever present. Without him, non of my work, nor my self, would be.

As Douglas Addams put it beautifully, ”Farewell, and thanks for all the fish”.

To Çağrı,
The beauty of his mind, and the strength of his will,
ever inspire me, ever give me a purpose.

Contents

Abstract **3**

Acknowledgements **5**

Contents **9**

List of Figures **15**

List of Tables **20**

List of Abbreviations **21**

1 Introduction **24**

1.1 A Thesis Justified 24

1.1.1 Hallmarks of Cancer and Plasticity of Cell Motility 24

1.1.2 Dissecting Cell Motility Mechanisms 25

1.2 Thesis Summary 26

1.3 Cell Structures Involved in Cell Motility 27

1.3.1 Cytoskeleton, Actomyosin Cortex, Membrane, and the Nucleus 27

1.3.1.1 Cytoskeleton and the Cytoplasm 27

1.3.1.2 The F-Actin Cortex 29

1.3.1.3 Myosin II Driven Contractility 31

1.3.1.4 The Plasma Membrane 33

1.3.1.5 The Cell Nucleus 35

1.3.2 At the Protein Level 37

1.3.2.1 The Many Faces of F-Actin: Lammelipodia and Filopodia 37

1.3.2.2 The F-Actin Cortex – Plasma Membrane Linkers: ERM Proteins 41
1.3.2.3 Cell-Extracellular Matrix Adhesion: Integrins . . 42
1.4 Plasma Membrane Blebbing 44
1.4.1 Definition and Phases of a Membrane Bleb 44
1.4.1.1 Bleb Initiation 46
1.4.1.2 Bleb Expansion 47
1.4.1.3 Bleb Stabilisation and Retraction 48
1.4.1.4 Blebbing in a non-Motilility Context: Apoptosis, Spreading, and Cytokinesis 49
1.4.2 The Dynamics of Membrane Blebbing in Numbers 50
1.5 Cell Motility Mechanisms 51
1.5.1 Mesenchymal and Amoeboid Spreading Cell Motilities . . . 53
1.5.2 Amoeboid Blebbing Cell Motility 56
1.5.2.1 Systems Demonstrating Amoeboid Blebbing Motility 56
1.5.2.2 Translating Membrane Blebbing to Cell Translocation 59
1.5.2.3 Controversy Around Membrane Blebbing in Motility 61
1.5.2.4 An Evolutionary Perspective 62
1.6 Computational Models of Cell Motility 63
1.6.1 Continuum Models of the Tumour Environment 64
1.6.2 Cell Centred Models: From Centre of Mass to Flexible Morphology 64
1.6.2.1 Cell Centred Models: Centre of Mass and Simple Morphology 65
1.6.2.2 Cell Centred Models: Advanced Flexible Morphology 66
1.6.2.3 Cell Centred Models: Bits and Pieces of the Cell . 74
1.6.3 A Hybrid Agent Based/Viscoelastic Network Approach . . . 77

2 Model Construction **80**
2.1 Introduction 80
2.2 Actomyosin Cortex and the Membrane 82
2.2.1 Viscoelasticity of the Actin Cortex 82

2.2.1.1 Maxwell Material 83
2.2.1.2 Kelvin-Voigt Material 86
2.2.1.3 Model Implementation 88
2.2.2 Myosin II Driven Contractility 90
2.2.3 The Plasma Membrane 91
2.2.4 Bending Resistance 93
2.3 The Cell Interior 94
2.3.1 The Cytoskeleton and the Cytoplasm 94
2.3.2 The Nucleus 96
2.4 Mathematical representation 98
2.5 F-actin Cortex–Plasma Membrane Linkers 99
2.5.0.1 Random Walk 99
2.5.0.2 Inverse Transform Sampling Method 100
2.5.0.3 Model Implementation 101
2.5.0.4 Special Cases 103
2.6 Interactions with the Environment 103
2.6.1 The Bell Model of Cell-Cell and Cell-Substrate Adhesion . 104
2.6.2 Cell–ECM Association and Dissosiation, a Monte Carlo approach 105
2.6.3 Elimination of Cell–ECM Penetration 107
2.6.4 Flexible ECM Filaments 107
2.7 Membrane Blebs 109
2.7.1 Bleb Formation 109
2.7.2 Bleb Tearing 111
2.7.3 Bleb Retraction 113
2.7.4 Bleb Necks 114
2.7.4.1 Simple Definition 114
2.7.4.2 Improved Definition 115
2.8 Actin Polymerisation Based Protrusions 117
2.8.1 Protrusion Formation and Elongation 117
2.8.2 Protrusion Spreading 121
2.8.3 Protrusion Retraction 121
2.9 Conservation of Momentum, a Minimisation Approach 122
2.9.1 The Nelder and Mead Simplex Method 124
2.9.2 Model Parameters and Effects of Minimiser 126

2.10 Investigated Scenarios 129
2.10.1 The Modelled Motility Types 129
2.10.2 Definition of Polarity 129
2.10.3 Extracellular Matrix Geometries 130
2.11 The Front End of the Simulation Platform 132

3 Model Parameterisation 134
3.1 Introduction 134
3.2 Cell and Nucleus Size 137
3.3 The F-Actin Cortex 137
3.3.1 Actin Reaccumulation at Bleb Rims 139
3.4 The Cytoskeleton and the Cytoplasm 140
3.5 The Myosin II Driven Contractility 142
3.6 The Plasma Membrane 142
3.7 The F-Actin Cortex–Plasma Membrane Linkers 143
3.8 The Nucleus 146
3.9 Plasma Membrane Bleb Dynamics 148
3.9.1 Parameter Fitting Procedure 149
3.10 The Actin Polymerisation Based Protrusion Dynamics 156
3.11 Cell–Extracellular Matrix Adhesion Levels 156
3.12 Extracellular Matrix Geometry 162
3.12.1 *in vivo* Mimetic ECM Generation 162
3.12.2 Flexible ECM Characterisation 163

4 Optimum Motility Mechanism and the Extracellular Matrix Geometry 165
4.1 Introduction 165
4.2 The Emergent Behaviour of the Model Cell 166
4.3 Extracellular Matrix Geometry and the Optimum Cell Motility Mode 169
4.3.1 Unconfined Surfaces: Benefits of Mesenchymal Motility and the Bell-shaped Curve Reflecting the Relationship Between Cell Adhesion and Velocity 171
4.3.2 Confined Surfaces: Confinement Determines the Contractility-Velocity Relationship 174
4.3.3 Discontinuous Matrices: Benefits of Amoeboid Blebbing Motility and Fundamental Changes in the Adhesion-Velocity Relationship 177

4.3.4 The Plastic Cell 180
4.4 Cross–Talk between Myosin II and ERM proteins 182
4.4.1 Continuous Surfaces: Overcoming the Adhesion Limitation with Blebbing at the Cell Rear 182
4.4.2 Confined Continuous Environments: The Balance Between Actin Protrusions Towards the Cell Front and Detachment of the Cell Rear 185
4.4.3 Discontinuous Environments: Blebbing at the Cell Front Prevails 186

5 Predicting Cell Behaviour and Response to Biochemical Perturbations 187
5.1 Introduction 187
5.2 Model Predicts *in vivo* Behaviour of Invasive Melanoma Cells . . . 189
5.2.1 Model Predictions for Melanoma Motility *in vitro* 192
5.2.2 Model Predictions for Melanoma Motility *in vivo* 195
5.2.3 Influence of the Improved Bleb Neck Cortex Definition and the Nucleus 199
5.2.4 Melanoma Motility: Experimental Observations and Validation of Model Predictions 206
5.3 Model Predicts the Effects of Experimental Interventions for Different Matrix Geometries 213
5.3.1 Characterisation of the Biochemical Perturbation Set 213
5.3.2 The Effects of Biochemical Perturbations: Model Predictions and Experimental Validation 215
5.3.3 Modifications to the ECM Filaments 220

6 Discussions, Conclusions and Future Prospects 225
6.1 Discussion and Conclusions 225
6.2 Future Prospects 234

A Experimental Methods 237
A.1 Cell Culture 237
A.2 Immunofluorescence 238
A.3 Western Blotting 238

B Velocity Profiles for High Polarities, and Simplified Cell Motility Modes 239

C Velocity Profiles for Drug Treatments in the Abscence of a Cell Nucleus 254

Bibliography 259

List of Figures

1.1 Actin Polymerisation Mechanism 30
1.2 Myosin II Force Generation 32
1.3 The Structure of the Plasma Membrane 33
1.4 Membrane Bending 35
1.5 Actin Polymerisation Based Protrusions 37
1.6 The Brownian Ratchet Model 39
1.7 Regulatory Mechanisms of Cytoskeleton 41
1.8 Dynamics of a Plasma Membrane Bleb 45
1.9 Amoeboid Blebbing Motiltiy *in vivo* 58
1.10 Models of Simple Cell Morphology 65
1.11 Models of Grid Based Morphology Modelling 68
1.12 Simple Cell Morphology Outside the Grid 69
1.13 Immersed Boundary Approach 70
1.14 Cell Morphology with Elastic/Viscoelastic Networks 71
1.15 Cell Morphology Modelling with FEM 73
1.16 Models of Plasma Membrane Blebbing 76
1.17 Snapshots from the Multiscale Model of Cancer Cell Motility 79

2.1 Schematic Description of the Multiscale Model of Cancer Cell Motility 81
2.2 Spring 83
2.3 Dashpot 83
2.4 Maxwell Material 84
2.5 Time Responses of a Maxwell Material 85
2.6 Kelvin-Voigt Material 86
2.7 Time Responses of a Kelvin-Voigt Material 87
2.8 Stress Response of Kelvin-Voigt Bodies in the Multiscale Model of Cancer Cell Motility 89

2.9 Membrane Tension as a Function of Total Cell Surface 92
2.10 Bending Resistance Calculation 93
2.11 Internal Pressure Calculation 95
2.12 Nucleus–Cortex Packing Calculation 98
2.13 Random Walk in 1D 100
2.14 Stochastic Update of ERM Concentrations 102
2.15 Binding Energy Landscape 104
2.16 Hard Wall Forces Against Cell Body Penetration into ECM Fibres . 108
2.17 Spring Network Defining an Elastic ECM Filament 108
2.18 Bleb Initiation 111
2.19 Schematic of Bleb Tearing and Forces at Play on the Bleb Neck . . 112
2.20 Model Snapsots for Bleb Tearing 112
2.21 Improved Definition of Bleb Necks 116
2.22 Actin Polymerisation Based Protrusions 118
2.23 Nelder-Mead Simplex Minimiser 127
2.24 The Role of Minimiser in Simulations 128
2.25 Definition of Polarity 130
2.26 Simple ECM Environments 131
2.27 *in vivo* Mimetic ECM Environments 132
2.28 Visualisation Interface of the Multiscale Model of Cancer Cell Motility 133

3.1 Cell and Nuclei Sizes 137
3.2 Discrete Representation of F-actin Cortex 138
3.3 Actin Accumulation at Bleb Rims 140
3.4 Computational Experiment for Internal Cell Body Viscous Damping Coefficient for Macrophages 141
3.5 Measurements of Excess Membrane Pool 143
3.6 Measurements of PIP_2 Distribution 145
3.7 Experimental Measurements and Computational Experiments for Nucleus Size During Spreading. 147
3.8 Plasma Membrane Blebbing Initiation by Serum Stimulation 148
3.9 Small Blebs Demonstrated by SEM Imaging 150
3.10 Model Parameter Fitting to Experimental Data 151
3.11 Bleb Dynamics from Experiments and the Computational Model . . 157
3.12 Crosstalk Between Protrusion Initiation and Contractility 158

3.13 Mapping Model Adhesion Units to Detachment Forces 161
3.14 Quantification of Collagen Fibres Surrounding Melanoma 162
3.15 *In vivo* Mimetic Extracellular Matrix Generation 164
3.16 Elastic ECM Filament Bulk Modulus 164

4.1 Emergent Model Cell Bahaviour: Spreading on Surfaces, and Contractility–Bleb Formation Relationship 167
4.2 Plasma Membrane Bleb Kymographs: Experimentation and Simulation 168
4.3 Cell Velocity on an Unconfined Surface and the Rac-RhoA Crosstalk 170
4.4 Velocity Heatmaps for Unconfined Continuous Surfaces 172
4.5 Cell Detachment from Unconfined Continuous Surfaces 173
4.6 Velocity Heatmaps for Confined Continuous Surfaces 175
4.7 The Change of Contractility-Velocity Relationship with Increasing Confinement 176
4.8 Velocity Heatmaps for Confined Discontinuous Environments . . . 178
4.9 Cell Velocity at Zero Adhesion 181
4.10 Velocity Heatmaps for Spatial Modifications of PIP_2 and Myosin Polarities 183
4.11 Protrusion Spreading with Spatial Modifications of PIP_2 and Myosin Polarities 184

5.1 Experimental Characterisation of A375P and A375M2 Cells 191
5.2 Realignment of Cell Polarity as a Chemotactic Response within *in vivo* Mimetic Environments 193
5.3 Velocities of A375P and A375M2 Cells on Unconfined Surfaces - Model Predictions 194
5.4 Percentage of Simulation Times with Spreading Protrusion for A375M2 and A375P Cells 195
5.5 Velocities of A375P and A375M2 Cells in Confined Continuous Environments - Model Predictions 196
5.6 Velocities of A375P and A375M2 Cells within *in vivo* Mimetic Environments - Model Predictions 197
5.7 Model Snapshots for an A375M2 Cell within an *in vivo* Mimetic Environment 198

5.8 Model Trajectories for A375M2 and A375P Cells within *in vivo* Mimetic Environments 200
5.9 Model Snapshots for an A375M2 Cell within an *in vivo* Mimetic Environment - Nucleus Packing Demonstration 202
5.10 Effects of the Flexible Bleb Neck Cortex and Nucleus Implementation 204
5.15 *In vivo* Time Lapse Images of Endothelial Cells Demonstrating Amoeboid Blebbing Mode of Motility 212
5.16 Characterisation of the Biochemical Perturbations 214
5.17 Model Predictions and Experimental Measurements on Melanoma Cell Motility Profiles upon Biochemical Perturbation 217
5.18 Co-variation of Model Predictions on Cell Velocity and Percentage of Simulation Time Above the Threshold Instantaneous Velocity . . 218
5.19 Model Predictions on Melanoma Velocities upon Biochemical Perturbation - Individual Polarities 219
5.20 Model Predictions and Experimental Observations on the Morphology of the Motile Cell upon Biochemical Perturbations 221
5.21 Model Predictions on Melanoma Velocities upon Biochemical Perturbation – Random Matrices without Embedded Surface Segments 222
5.22 Model Predictions on Melanoma Velocity and Filament Deformation within a Flexible ECM 224

B.1 Velocity Heatmaps for Unconfined Continuous Surfaces - High Polarities, and Additional Motility Modes 240
B.2 Velocity Heatmaps for Confined Continuous Surfaces, Frontal Gap $12\mu m$ - High Polarities, and Additional Motility Modes 242
B.3 Velocity Heatmaps for Confined Continuous Surfaces, Frontal Gap $10\mu m$ - High Polarities, and Additional Motility Modes 244
B.4 Velocity Heatmaps for Confined Discontinuous Environments, Frontal Gap $12\mu m$ Lateral Gap $10\mu m$ - High Polarities, and Additional Motility Modes 246
B.5 Velocity Heatmaps for Confined Discontinuous Environments, Frontal Gap $12\mu m$ Lateral Gap $5\mu m$ - High Polarities, and Additional Motility Modes 248
B.6 Velocity Heatmaps for Confined Discontinuous Environments, Frontal Gap $10\mu m$ Lateral Gap $8\mu m$ - High Polarities, and Additional Motility Modes 250

B.7 Velocity Heatmaps for Confined Discontinuous Environments, Frontal Gap 10μm Lateral Gap 4.3μm - High Polarities, and Additional Motility Modes 252

C.1 Model Predictions on Melanoma Velocities upon Biochemical Perturbation - Simple Model Setups 256
C.2 Model Predictions on Melanoma Velocities - Individual Polarities for Simple Model Setup(a) 257
C.3 Model Predictions on Melanoma Velocities - Individual Polarities for Simple Model Setup(b) 258

List of Tables

1.1 Experimental Measurements on Dynamics of Plasma Membrane Blebbing 51

2.1 Minimiser Parameters Utilised in the Model 127

3.1 Model Parameters 135
3.2 Contractility of A375M2 cells Under Biochemical Perturbation . . . 147
3.3 Parameterisation of the Model with Bleb Dynamics Data 152

5.1 Parameters Defining Metastatic Melanoma Cell Line A375M2 . . . 190
5.2 Parameters Defining the Effects of Biochemical Perturbations . . . 214

List of Abbreviations

A	Area
AFM	Atomic Force Microscopy
B	Bending modulus
CAF	Cancer Related Fibroblasts
CDF	Cumulative Distribution Function
D_{eff}	Effective myosin diffusion constant
d_{ECM}^{on}	Threshold distance below which cell–ECM adhesion is possible.
E_c	Young's modulus of the F-actin cortex
ECM	Extracellular Matrix
ERM	Ezrin-Radixin-Moesin
F	Force
$F_{unnitattach}$	Cortex-membrane adhesion strength per unit adhesion protein of the model
f_{cor}	fraction of cortex at a given cell surface region, normalised to resting state.
FEM	Finite Element Method
FERM	F for 4.1 protein, E for ezrin, R for radixin and M for moesin
GFP	Green Flourescent Protein
h	Thickness of the F-actin cortex
I	Intensity of protein labelling
L_i	Length of the linker between an agent and its neighbour i
k_b	Boltzmann constant
k_m	Spring constant
k_f	Protrusion formation rate per agent under normal myosin concentration
k_{off}	Unstressed dissociation rate constant
k_{on}	Association rate constant
k_{tear}	The upper limit for the value of the membrane spring constant, k_{mem}.
$L_{BN,i}$	In simple bleb neck definition: unit vector from a bleb border to the other border of the bleb, in the direction of neighbour i.

	In improved bleb neck definition: unit vector from a bleb border to the bleb neck agent in the direction of its neighbour i.
$\hat{l}_i$	Unit vector from an agent towards its neighbour i
$\hat{l}_{BN,i}$	In simple bleb neck definition: unit vector from a bleb border to the other border of the bleb, in the direction of neighbour i.
	In improved bleb neck definition: unit vector from a bleb border to the bleb neck agent in the direction of its neighbour i.
P_{CELL}	Hydrostatic pressure of the cell.
P_{nuc}	Hydrostatic pressure difference between the cell and the nucleus.
PDF	Probability Density Function
PGC	Primodial Germ Cells
PIP_2	Phosphatidylinositol 4,5-biphosphate
r_0	The range of the minimum in binding energy well.
R_{CELL}	Cell Radius
S_{mem}^{pool}	Total membrane pool available to the cell.
SEM	Scanning Electron Microscope
T	Temperature
w_{model}	Model cell width

$\Delta t_{cor}, \Delta t_{myo}$	The time delay between bleb initiation and the arrival into a bleb.
$\delta_{stretch}$	The percentage stretch limit after plasma membrane depletion, to reach form zero membrane tension to the maximum value of k_{tear}.
η	The damping coefficient.
τ_a	Actin renewal time.
ζ	Step size for random sampling the CDF of ERM concentration.

Superscripts

0	The value at resting state
bg	Image background
bleb	Plasma membrane bleb

Subscripts

ben	Bending
bleb	Plasma Membrane bleb
BN	Bleb Neck

CELL	Cell
cor	F-actin cortex
cyt	Cytoplasm and cytoskeleton (all inner cell body excluding the nucleus)
ERM	Ezrin-Moesin-Radixin
fil	Extracellular Matrix filament
LNK	Actin polymerisation based protrusion internal linker
mem	Plasma membrane
myo	Myosin II
nuc	Nucleus
prot	Actin polymerisation based protrusion

Chapter 1

Introduction

1.1 A Thesis Justified

1.1.1 Hallmarks of Cancer and Plasticity of Cell Motility

Cell motility is essential in many biological processes, including immune surveillance, development, and cancer metastasis. During cancer development, cancer cells from the primary tumour can invade the surrounding tissue, move to distant parts of the body, and form secondary tumours – metastases (1). This invasion and spread is the cause of ninety per cent of cancer related deaths (2). Hence, being able to block the invasion of cancer, through understanding and blocking cancer cell motility, is a vital approach in reducing cancer metastasis (3).

During invasion and metastasis, cancer cells are required to adapt to a wide range of environments. Therefore, it is beneficial for metastatic cancer cell to have the ability to undergo a range of changes, both in its morphology, and motility. (3–5). The cancer cells can adapt an elongated, rigid morphology, and move in a mesenchymal fashion, with the main driving force behind motility being actin polymerisation based protrusion formation. Alternatively, cancer cells can utilise the amoeboid spreading motility mode, with a round shape, but still relying on actin polymerisation based protrusions (6). As recently established, cancer cells can also move in the amoeboid blebbing mode, where cell morphology is round and flexible. Cells utilising amoeboid blebbing motility depend on cortical contractility, and plasma membrane blebbing: pressure driven balloon-like protrusions of the plasma membrane (7). It has also been demonstrated that these different motility

modes form a continuous spectrum, rather than being completely distinct motility strategies (8, 9). Multiple cell types, including cancer cells, can shift their motility modes through this spectrum (6, 9–11): The combination of intracellular and extracellular factors; such as cortical contractility, cell-extracellular matrix (ECM) adhesion, and the geometry of the ECM; determine the morphology and the effective motility mechanisms of the cell for a given environment (5, 8).

This demonstrated plasticity of cell motility is immediately relevant to development of cancer therapeutics. Effective inhibition of metastasis will require targeting not only one motility mode, but all possible driving mechanisms of cancer cell motility: a combination of ECM adhesion, ECM remodelling and cellular contractility (12). To fully understand the balance between the intracellular and extracellular properties that regulate cell motility modes, it is necessary to understand and probe the whole spectrum of motility.

1.1.2 Dissecting Cell Motility Mechanisms

For a complete understanding of the above motility mechanisms, under differing intra- and extracellular conditions, they must be dissected. Experimental manipulations can be made to observe the effects of perturbations to a particular motility mechanism, by monitoring the cell's motility profile. However, the close coupling of the biochemical pathways makes it impossible to investigate manipulation of one mechanism without changing another. Similarly, utility of experiments in explaining the causes of the efficiency of a particular mechanism is limited. Here, computational modelling can provide some of the answers. By modelling the cell morphology and the basic mechanisms of motility successfully, it is possible to decouple each motility mode, investigate the inputs from each mechanism, and explain why a specific mechanism is successful under specific conditions.

A number of models have been constructed for polymerisation based cell motility (13–15). On the other hand, a model that investigates plasma membrane blebbing in a cell motility context is urgently required in order to reveal the function of these protrusions in cell motility. Meanwhile, keeping in mind the plasticity of cell motility, a framework that incorporates multiple forms of cell motility is also required, to identify which motility mode is more effective under which conditions.

Multiple experimental studies have revealed the properties of the extracellular matrix to influence the motility mode of the cell. Therefore, a model to investigate multiple modes of cell motility should include the geometry of the extracellular matrix, with an explicit distinction between the ”gaps” and ”obstacles” of the environment.

This thesis presents a modelling framework and simulation platform to fill the gap revealed by these problems. The model cell presented here includes flexible cell morphology, plasma membrane blebbing and actin polymerisation based protrusions. The local heterogeneity of the cell is incorporated, and a range of intracellular states, as well as a range of polarities, are investigated. The extracellular matrix is explicitly defined, and a variety of extracellular matrix geometries, from unconfined surfaces, and environments confining the cell between two surfaces, to ECM topologies mimicking *in vivo* interstitial collagen matrices, are investigated.

1.2 Thesis Summary

The thesis begins with the introduction of the cellular structures involved in cell motility, and the range of motility modes available to a cancer cell. Then an overview of modelling methodologies, that have been utilised in theoretical analysis of cell motility, is provided; thereby placing the preferred methodology of the presented computational model in context. After introducing the biological phenomena to be studied, and outlining previous modelling methodologies used to investigate them, details of the modelling methodology used in this thesis is described in Chapter 2. Parametrisation of the model, together with the experimental data generated by Tumour Cell Biology (TCB) Laboratory for the parameterisation, is detailed in Chapter 3. Following model construction and parameterisation, Chapter 4 presents the dependencies of effective cancer cell motility on systematic changes in the ECM geometry, from unconfined 2D planar surfaces to confined discontinuous ECMs. The roles of plasma membrane blebbing in guiding the cell movement are also investigated in this chapter. Once these dependencies are established, in the first part of Chaper 5, the model is challenged to predict the cancer cell motility profile and the morphology of the motile cell, both on unconfined surfaces, and within complex *in vivo* mimetic ECMs. Upon demonstrating that the

model can successfully predict both the motility mode and the cell velocity *in vivo*, the second part of Chapter 5 focuses on predictions of biochemical perturbations. The experimental data generated by the TCB Laboratory for validation of model predictions, on cancer cell motility, morphology, and response to drug treatments, are included in Chapter 5 alongside the model predictions. The final chapter presents the discussions, conclusions, and possible future development of the presented modelling framework and simulation platform.

1.3 Cell Structures Involved in Cell Motility

1.3.1 Cytoskeleton, Actomyosin Cortex, Membrane, and the Nucleus

1.3.1.1 Cytoskeleton and the Cytoplasm

Cell shape and form are maintained by an internal network of filaments, called the cell cytoskeleton, composed of a range of filamentous proteins and helper proteins (16, 17). The cell cytoskeleton governs mechanical responses and a multitude of the chemical processes of the cell, such as phagocytosis, cell adhesion, and cell motility (18, 19). Cell deformation plays a central role in many of these processes, particularly in cell motility. Irrespective of the deformations, and their extent, the cell must also maintain an intact cell body (19). This duality of the requirements on physical responses of the cell; ability of the cell cytoskeleton to respond to elastic deformation to keep an intact cell shape, while allowing morphology changes in the longer time scale; have been attracting attention for more than a century (20). The source of this ability is the viscoelastic nature of the cell cytoskeleton (18): similar to other biopolymer networks, the cytoskeleton demonstrates mechanical behaviour that is in between pure viscous liquids and pure elastic solids, termed viscoelastic (21).

Among the filamentous proteins of the cytoskeletal network, namely microtubules, actin filaments and intermediate filaments; actin filaments (filamentous actin, or shortly F-actin) are the most relevant in terms of facilitating the desired mechanical responses of the cell (19). F-actin is formed by polymerisation of G-actin subunits (monomeric actin or globular actin, for details see Section 1.3.1.2)

(22). The emerging physical properties of the cytoskeleton (and the cortex as will be discussed in Section 1.3.1.2), depend on the physical properties of the single filaments, and the topology of their interactions. The total length of a filament from one end to the other as measured along its contour, is termed the filament's "contour length". At thermal equilibrium, fluctuations of the flexible actin filament result in changes in its overall curvature. The persistence length of an actin filament is the length above which the tangent vectors to the contour of the filament become uncorrelated (22). With these definitions, if the contour length of an actin filament is in the scale of its persistence length, than it will go through significant fluctuations in shape. These fluctuations will in turn affect the polymerisation dynamics of the whole actin network. Moreover, the shapes of individual filaments, and the interactions between them, define the mesh size of the overall network.

The elastic response of F-actin networks is dependent on all the physical attributes described above, contour length of the filaments, persistence length of the filaments, and the network mesh size. The spontaneous assembly of G-actin into F-actin is rapid, and polymerisation and de-polymerisation events are at a dynamic equilibrium (19). The cellular fraction of the actin in F-actin form is regulated by actin filament nucleators and monomer sequestering proteins, the details of actin polymerisation are discussed in detail in the following sections. The speed and extent of monomer sequestering affects filament contour length, which is also more directly regulated by capping proteins (18). Entanglement and cross linking of the filaments defines the network mesh size, linking to the viscous response of the network.

The viscoelastic properties of the cytoskeleton are mainly attributable to the binding fluctuations of cross-liking proteins (19). When the binding and unbinding rates of cross linker proteins are externally modified, the timescale of the viscous response can be modified accordingly. As the binding affinity of cross linkers are reduced, viscous responses are also reduced, but not eliminated (21). The source behind this residual viscous response of non-cross linked actin networks is that the entanglement of, and the friction between, the filaments (17). When F-actin is permanently cross-linked, most of the viscous response is lost, and the network behaves as an elastic solid. Most cross linkers, under physiological conditions, are dynamic with finite binding affinities, thereby providing the required viscoelastic

response (21). Apparently, to fit experimentally observed viscoelastic responses, cross linkers with a range of affinities are necessary (20) As further discussed in the introduction of the cell cortex, (Section 1.3.1.2), cells actively regulate the properties of their F-actin networks, an a computational model aiming to capture the roles of F-actin networks in cell morphology and motility, should account for the dynamic nature of these networks.

The cell cytoplasm comprises of the fluid cytosol and all the organelles embedded within, except the cell nucleus. The cytosol and a sub-population of the organelles are where protein synthesis happens (16). Some of these proteins eventually locate to the plasma membrane of the cell, with their numbers being closely linked to their cytosolic concentrations (23, 24). In addition to the cytoplasm being the transfer and reaction medium for protein activities, its hydraulics are important in cell morphology and motility (25). For example, cytoplasmic flow aids G-actin delivery to polymerisation sites (26), and the cytosol facilitates pressure transfer from one region of the cell to another, as well as the regulation of the overall pressure levels (25). It has been demonstrated that cells can have internal pressure gradients, since the movement of the cytoplasm can be hindered by the cytoskeleton and embedded organelles (25). However, the general consensus is that, local elevations of pressure are equilibrated throughout the cell interior on the time scales relevant to pressure driven cellular protrusions. Indeed, a recent study on the forced initiation of membrane blebs (spherical pressure driven cellular protrusions, see Section 1.4 for full definition) showed that the relative size of the firstly and secondly initiated bleb did not change with the distance between two initiation sites (27). This suggests the internal pressure release upon the initiation of the first bleb is uniformly effecting the whole cell body on a time scale relevant to membrane bleb dynamics.

1.3.1.2 The F-Actin Cortex

There is a dense cross-linked and entangled F-actin network below the cell membrane: the cell cortex (18, 28). Although non-linear elastic and viscoplastic responses are seen under high stress or strain; under low to medium strain, the cell cortex demonstrates a linear viscoelastic response as noted for the cytoskeleton. The physical properties of the cortex need to be rapidly and tightly regulated, and

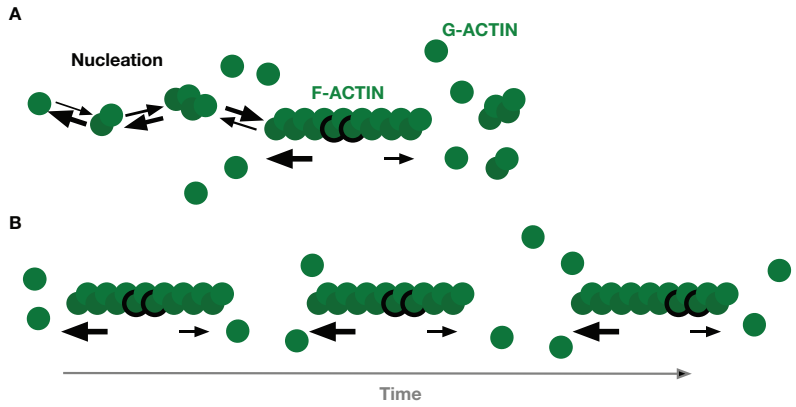

Figure 1.1: A) Nucleation and elongation of an actin filament. Actin dimers and trimers are unstable, while the polymerised form favours continuation of polymerisation. The thickness of the arrows in the above schematic represent the relative rates of each reaction: nucleation events and relative rates of polymerisation at barbed and pointed ends. Polymerisation at the barbed end is higher than the pointed end. Shapes are not to scale. B) Schematic of treadmilling, the individual actin subunits (marked by the black circles) of the filament move from barbed end towards the pointed end, as the filament polymerises at the barbed end, and disassembles at the pointed end.

so called cortex helper proteins are responsible for this regulation (21), by changing filament lengths, density, and cross-linking.

F-actin is formed by helical arrangement of G-actin subunits, with filament lengths being in dynamic equilibrium with the concentration of G-actin monomers (29). In the polymerisation process, the nucleation of the polymer is the slowest, hence the rate determining step. This is a consequence of actin dimers and trimers being less stable than the polymerised form (30). The two ends of F-actin have different dynamic properties, i.e. polymerisation is faster at the barbed end of the filament, and slower at the pointed end. Once the concentration of the free actin monomers reaches the steady state concentration, where the monomer assembly rate at the barbed end is equal to the disassembly rate at the pointed end, the filaments maintain a constant length, with a net flux of monomers from the barbed to pointed end - this process is called treadmilling (16, 29) (Figure 1.1).

This dynamic equilibrium of G-actin and F-actin dictates that the filaments

themselves are continuously renewed. The dynamics of filament assembly and disassembly is strictly regulated depending on local conditions, for example, the cortex is disassembled when the links with the plasma membrane are lost (31). Moreover, the F-Actin cortex is rapidly and continually reorganised (32). It is also thought that rearrangement of cross linkers between unbinding and rebinding events could facilitate stress relaxation in cytoskeletal networks, including the cell cortex (19). The cross linker proteins that influence the viscoelastic properties of the cortex include motor proteins, which can generate force and do mechanical work (19), and F-actin cortex also utilises contractility driven by myosin II (21). With its continuous renewal, and the continuous action of motor proteins, the structure and tension of the cortex is maintained at its dynamic equilibrium.

1.3.1.3 Myosin II Driven Contractility

Myosin II functions as a homodimer, each monomer having an actin binding head, and a flexible tail (22). Myosin II heads generate force by ATP hydrolysis, in a proposed five step mechanism (Figure 1.2). (i) At the beginning of the cycle, the myosin head is tightly attached to the actin filament. (ii) Upon capturing an ATP molecule, the affinity of myosin for actin is reduced by a conformation change, and myosin is released form the filament. (iii) During the hydrolysis of the ATP molecule to ADP, a large conformational change is induced, shifting the myosin head to a cocked position, causing the myosin to move along the filament. (iv) Weak binding of the myosin head to the filament releases the inorganic phosphate group. (v) The release of ADP is accompanied by another large conformational change, the power stroke. Finally the myosin head once again tightly binds to the actin filament, returning the process to the initial step of the cycle (16, 22).

When the two heads of the myosin II dimer are attached to different actin filaments, they can slide the filamets with respect to each other, generate a contractile force in the network, and establish a resting tension in the cortex. Photo bleaching studies have shown that myosin II does not diffuse laterally on a short time scale, and regulation is therefore *via* the delivery of myosin II to the cortex from the cytoplasm (23), and the half-time of recovery to normal myosin levels after bleaching has been measured as 7.01 ± 2.62 s (23).

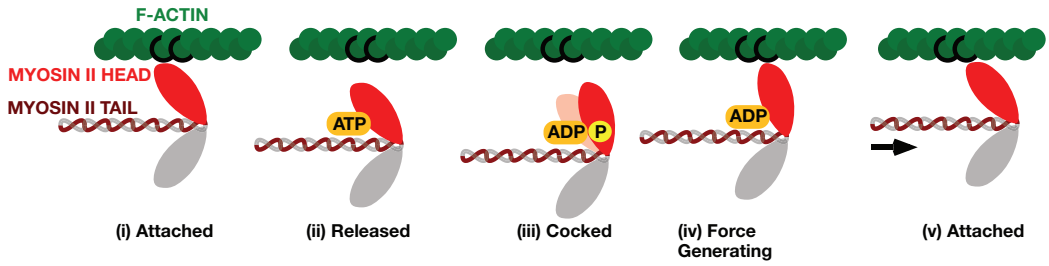

Figure 1.2: Proposed five step mechanism of force generation by myosin II, by hydrolysis of ATP.

The forces generated by the myosin motors, described above, are key to driving cell motility, through intracellular pressure generation, extracellular matrix remodelling, polarised force generation, polarised protrusion formation, and cell–ECM adhesion regulation.

The tension within the cortex that myosin II generated forces produce maintains intracellular pressure. This internal hydrostatic pressure is subsequently drawn upon to control cell morphology (33), and can drive motility, *via* plasma membrane blebbing (31, 34). The internal pressure for HeLa cells have been characterised in the range 17-110 Pa (35), and assuming a spherical cell shape, internal pressure (P_{CELL}) can be evaluated for any cell type from known cortex tension (T) and cell radius (R_{CELL}) by Laplace's Law (27):

$$P_{CELL} = \frac{2 \times T}{R_{CELL}}. \tag{1.1}$$

Depending on the cell type, the overall tension at the cortex have been reported in the range 130 – 4100 $pN\mu m^{-1}$ (27, 35–37). In addition to the maintenance of internal cell pressure, polarised myosin driven contractility has a variety of roles in cell motility. The forces generated by myosin motors can be used to deform the extracellular matrix (ECM) to allow penetration of cells (38). Polarised contractility of the cell rear is sufficient to generate directional motility (39). Increased cell rear contractility can also act coupled with actin polymerisation based cell protrusions, such as lammelipodia and filopodia, through the antagonistic relationship between myosin activity and protrusion formation (9). Finally, increased rear contractility facilitates detachment of the cell rear (40). Myosin has roles in not only formation

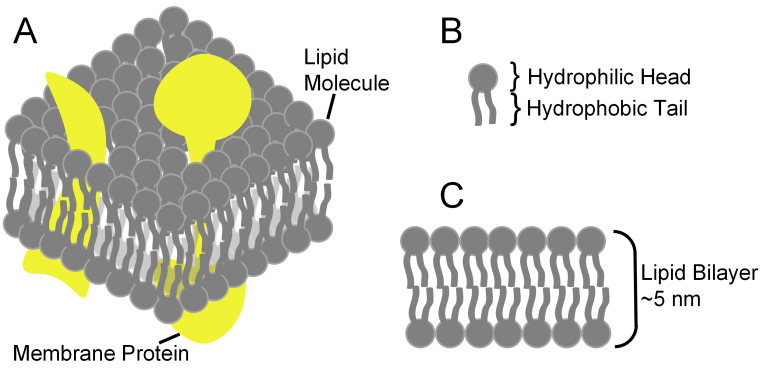

Figure 1.3: A) The structure of the plasma membrane B) A lipid molecule. C) The crossection of the self-assembling lipid bilayer.

but also growth and retraction of both membrane blebs and actin polymerisation based protrusions, details of which are included in Sections 1.3.2.1/1.4. Moreover, cell contractility is central in cell–ECM adhesion independent motility (41). The details of different motility mechanisms are given in Section 1.5.

1.3.1.4 The Plasma Membrane

The plasma membrane encloses the cell, maintaining its boundaries and the chemical differences between the cell and its surroundings (16). It consists of a thin double layer of lipid molecules, held together with non-covalent interactions. This lipid bilayer forms a fluid, dynamic structure, where most of the lipids and embedded proteins can move on the plane of the membrane. The plasma membrane serves as a barrier between the cell interior and the extracellular medium. Other roles of the membrane, such as catalysing membrane associated reactions or selective transportation of specific molecules through the boundaries of the cell, are carried out by the embedded membrane proteins (Figure 1.3A) (16).

The lipid molecules forming the lipid bilayer have a hydrophobic and a hydrophilic end. In aqueous environments, the hydrophobic ends are clustered together, exposing hydrophilic ends to water, and as a result, spontaneously assembling into bilayers (Figure 1.3B-C) (16).

Cells have a pool of excess plasma membrane, which can permit to sudden changes

in morphology (42). As demonstrated in experiments where tethers are pulled from the plasma membrane at different regions of the cell surface, the membrane pool is a shared resource of the whole cell surface. As a result, the functional consequences of membrane depletion emerge depending on the total cell surface area, rather then occuring locally (42). For cellular process on a relatively long time scale, the membrane reservoir is regulated *via* endocytosis, but this has not been observed during membrane blebbing (35, 42). Although the availability of the membrane pool has been demonstrated for many cell types, the size of the membrane pool is strictly cell type dependent, macrophages having the ability to extend their surface areas five fold (37), while the limit is lower for fibroblasts (42). Increases in the cell surface area within the limits of the membrane pool are tolerated without significant increase in the membrane tension (42). On the other hand, when the membrane pool is depleted, the elastic properties of the membrane itself respond to further increases in the cell surface area, i.e. lipid bilayer starts stretching. When the plasma membrane is stretched, it becomes thinner, exposing the hydrophobic core of the lipid bilayer to water, resulting in rupture. The rupture limit for a lipid bilayer, although time dependent, is rather low, in the range 2-5 percent (22). The rupture tension at which the membrane starts to fail is reported in the order 0.01 J m^{-2} (22).

As with resistance to membrane stretching, bending the membrane also moves the lipid molecules away from their equilibrium positions, stretching the top and compressing the bottom layer, and hence, requires energy (Figure 1.4). The bending resistance of plasma membrane is well documented, and is in the range $0.3 - 2 \times 10^{-19}$ Nm (22). It is important to note that the plasma membrane is not the only source of resistance to bending of cell surface, and when the plasma membrane is coupled to the cortex, the cortex density also contributes to the observed bending resistance. Here, the studies on blebbing and non-blebbing regions of the cell surface demonstrate the effect of the underlying cortex, with bending rigidity reported as $0.047 pN\mu m$ for an expanding bleb devoid of a dense cortex, and $0.215 pN\mu m$ for a retracting bleb with an established cortex underlying the bleb rim (35).

The bending and stretching resistance of the plasma membrane are significant in bleb dynamics. Depletion of the membrane and the following increase in cell

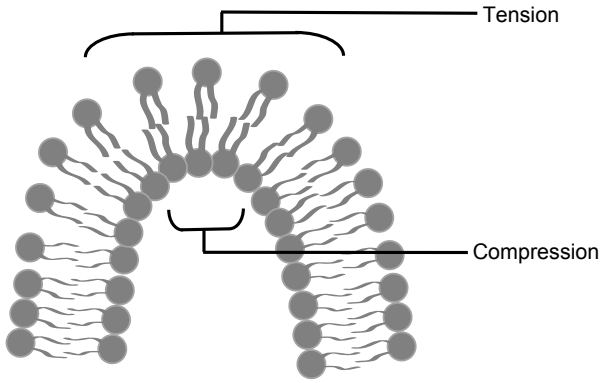

Figure 1.4: Tension and compression on the lipid bilayer under bending.

surface tension is equally important for spread and elongated cells undergoing motion using actin polymerisation-based protrusions, as this tension increase is influential on both protrusion dynamics and cell rear detachment.

1.3.1.5 The Cell Nucleus

The nucleus is where the DNA of the cell is stored. It is enclosed by the nuclear lamina, and the nuclear lipid membrane, which is similar to the plasma membrane, but consists of a double layered lipid bilayer. Structural support for the nucleus is provided by the nucleoskeleton, a meshwork of intermediate filaments (16). The structural properties of both the nucleus and the nucleoskeleton are different than that of the bulk cell body and the F-actin cortex: the nucleus is stiffer and more viscous than the cytoskeleton and the F-actin cortex (43). The stiffness of the nuclear envelope has been reported as 2500 $pN\mu m^{-1}$ for xenopus oocyte, which is orders of magnitudes higher than that of the red blood cell cortex, 1 $pN\mu m^{-1}$ (44). The bulk behaviour of the nucleus is viscoelastic, similar to the rest of the cell, but it is three to ten times stiffer than, and approximately twice as viscous as, the whole cell (45, 46).

Due to the stiff skeleton architecture and higher viscosity of the nucleus, it is considered rigid in most cases. However, the nucleus is deformable, and cells can actively control the morphology of their nucleus. A good example for this regulation is the recent demonstration of a contractile actin cap flattening the nucleus

in spreading cells, and preventing its bulging towards the plasma membrane (47). Moreover, the deformation of the nucleus is highly relevant to cell motility. In 3D collagen matrices and multiple *in vivo* studies, it has been shown that cells deform their nuclei to squeeze through the gaps of the ECM, or to fit into capillaries, and this deformation is dependent on myosin II activity (48–53). Once myosin II is blocked, the cells are able to invade through matrices with gap sizes in the range of the axes of their nuclei, but in any environment with a smaller gap size than the un-deformed nuclei, cells get stuck in the gaps, and are unable to invade (53). Additional to the forces transmitted from the contractility of the F-actin cortex, myosin II has direct effects on the nucleus morphology, as demonstrated from the shrinkage of nuclei upon expression of an active form of Rho-kinase, an activator of myosin II (50). During invasion of the 3D collagen matrices, remodelling of the ECM is also linked with the morphological changes of the nucleus; local degradation of the collagen fibres coincides with points where the nucleus is constricted, and deformed (43). During migration on 2D surfaces, the changes in the morphology of the nucleus is less dramatic, but its position relative to cell direction may become significant (50).

Indeed, cells can actively control not only the morphology, but also the position of their nuclei within the cell. All constituents of the cytoskeleton, microtubules, actin filaments and intermediate filaments, are responsible for the translocation of the nucleus within the cell, however the predominant structure responsible for control changes with cell type (54). The ability of the cells to regulate nuclear positioning is clearly demonstrated in development, where nuclear position determines cell divisions, cell fate, and influences tissue integrity (55–57). For cell motility, the position of the nucleus is important as it can affect cell polarity for specific cell types and environments. Here, it is again the microtubules that play a significant role in positioning (58). In T-cell motility, the nucleus is located at the uropod of the cell, while in *Dictyostelium discoideum* it is dynamically translocated immediately behind the leading pseudopod (59). In fibroblasts, the nucleus is positioned, *via* the microtubules, at the cell rear during motility on 2D surfaces, whereas the orientation of the nucleus is not correlated with cell direction in 3D collagen matrices (60, 61). Hence it seems the ability to change the morphology of the nucleus is influential on motility in 3D environments, while the ability to position the nucleus in the correct sub-compartment of the cell may be important

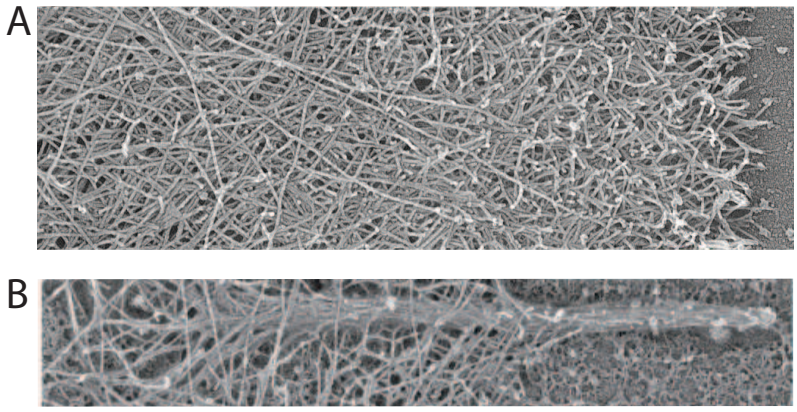

Figure 1.5: Scanning electron microscope (SEM) images of A) Section of fish keratocyte lamellipodia, image reproduced from (65). B) A filopod emerging from the lammelipodia, image reproduced from (66)

for motility on 2D surfaces.

1.3.2 At the Protein Level

1.3.2.1 The Many Faces of F-Actin: Lammelipodia and Filopodia

F-actin forms the major constituent of the cytoskeletal network and forms the F-actin cortex below the plasma membrane, regulating cell shape. F-actin can also modify the morphology of the cell by assembling into actin polymerisation driven protrusions: Lamellipodia and filopodia. Lamellipodia are thin, sheet like structures, with a thickness of 0.1–0.2 μm, and they are formed as a dense network of branched actin filaments (29) (Figure 1.5A). Filopodia are thin, finger like protrusions. Their sizes are in the range 0.1–0.3 μm, and they are formed from parallel bundles of F-actin (62, 63) (Figure 1.5B). These thin bundles of un-branched F-actin can grow on top of lamellipodia (64). In both filopodia and lamellipodia, the fast growing barbed ends of F-actin is oriented towards the membrane (62).

Filopodia can be thought of as the antennas of the cell, used for sensing their environment (62). They are functional in cell migration, cell–ECM adhesion formation, chemotactic response, path finding of neural growth cones, wound

healing, and cell-cell signalling (62, 67). It has been shown that during cell spreading, a process utilising actin polymerisation in a similar way to motility, elimination of filopodia leads to inhibition of spreading (68).

The growth rate of a filopodia is reported to be in the range 0.05–5 $\mu m\ s^{-1}$. The elongation rates of actin polymerisation based protrusions are not limited by the adhesions to extracellular surfaces. Where there is no anchoring to the environment, the actin polymerisation rate and the retrograde flow rate, sliding of the filament backward with respect to the substrate (62), increase in parallel. This results in the same net protrusion elongation velocity as compared to protrusions with anchoring to ECM, with faster polymerisation and retrograde flow (69). This is in line with the theory that protrusion elongation rates are limited by tension from the membrane (70). On the other hand, the maximum length filopodia can reach is linked with adhesion to the underlying substrate, and the thermodynamic limit for un-supported filopodia growth is 1–2 μm (63).

The retraction dynamics of filopodia are linked with myosin activity (64), and the forces filopodia can apply during elongation and retraction are well documented. The peak of retraction force measurements is observed at 3 pN; however, some filopodia can keep retracting under even heavier loads, up to 18 pN (71). During elongation, the forces produced by single actin filaments have been measured to be 1.3 pN, and filopodia pushing forces have been reported to be up to 3 pN (72, 73).

As the measurements demonstrate, the polymerisation of actin can actively be translated into forces pushing the cell membrane outward. The model proposed to describe the underlying mechanism is termed the Elastic Brownian Ratchet model (74). The model proposes that both the filament and the membrane at the protrusion tip constantly undergo thermal fluctuations. At any instance where the gap between the barbed end of the filament and the membrane is large enough to accommodate a polymerisation ready G-actin molecule, the subunit is added to the filament. For the gaps formed by membrane fluctuating away from the filament, this binding event prevents the membrane from translocating back to its original position. Similarly, for the gaps formed by filament fluctuation away form the membrane, the membrane is pushed out when the filament fluctuates back to its original length after a binding event (74). These fluctuations of the membrane

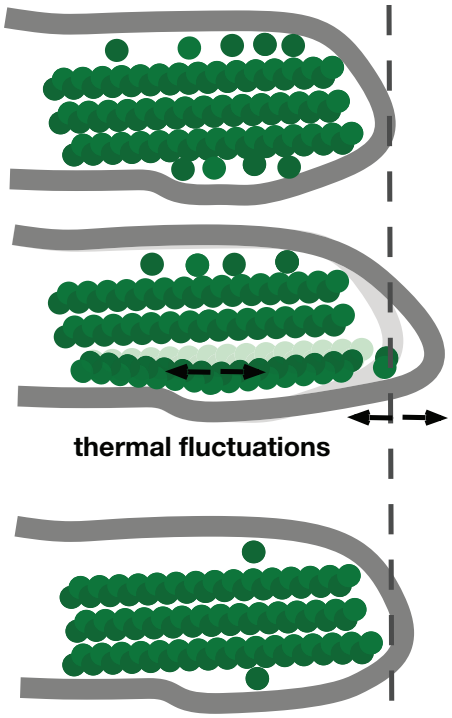

Figure 1.6: Brownian ratchet model. Polymerising actin pushes the membrane. With thermal fluctuations of the membrane and the elastic F-actin, a gap forms between the membrane and the tip of the filament. With the available space, fibres elongate with monomer addition. The membrane can not come back to its original position, and the tip is propelled forward.

and the filements are not mutually exclusive, and are taking place simultaneously during protrusion elongation (Figure 1.6).

Lamellipodia are more stable structures of branched F-actin networks. The thicknesses of lamellipodia are in the range 0.1–0.2 μm and actin polymerisation takes places at the tips of the lamellipodia. In moving cells, the filaments themselves are stationary, with polymerisation at the lamellipodia tips and disassembly at the rear (62, 65). In the context of the Elastic Brownian Ratchet model, the distance from the last cross-linking point to the tip of a polymerising filament is required to be in the range 30–150 *nm*, or filament buckling will prevent effective pushing of the membrane (74). In line with theory, the structure of the lamellipodia is not homogenous, the tips have short, branched filaments; any polymerising

filament is capped before it exceeds 0.5 μm (29, 75). With each filament able to generate picoNewton level forces, lamellipodia can generate forces up to 20 pN (73), and elongate with velocities up to 1 $\mu m\ s^{-1}$ (29). With polymerisation, capping, branching and disassembly, the structure of the lamellipodia is dynamic. The treadmilling does not occur in the sense of a single filament polymerising at the barbed end and depolymerising at the pointed end; rather, the whole F-actin network treadmills, generating a newly formed network at the tips, and dismantling the established network at a distance from tip (65). Myosin motors increase in density towards the lamellipodia–cell body boundary, implying motor activity is also significant in the balance of protrusion, retrograde flow, and motility (75).

For both filopodia and lamellipodia, polymerisation and remodelling drives the movement of the cell. For pure actin *in vitro*, under physiological ion concentrations, but without the guidance of any regulatory proteins, the rate of treadmilling at steady state is approximately 0.04 $\mu m\ min^{-1}$ (65), significantly slower than the velocities reported above for filopodia elongation. Given that the rate–limiting step at steady state is dissociation of actin subunits from filament pointed ends, then the question of how the protrusions maintain high velocities translates into how the polymerisation ready G-actin pool is maintained in the cell. Helper proteins of the cytoskeleton regulate the balance of polymerisation by capping the barbed ends and reducing the rate of polymerisation at these ends, while increasing the rate of depolymerisation at the pointed ends. Therefore, given the strict physical requirements for efficient protrusion dynamics such as the requirement for short filaments at the protrusion tips, it is evident that polymerisation, retrograde flow, cross-linking, and disassembly events are strictly regulated by cells. The ability to regulate these mechanisms also enables the cells to rapidly respond to extracellular signals (65).

Finally, the mechanisms of actin polymerisation are closely linked with that of myosin II driven contractility. Rac1 proteins drive lamellipodia formation (76), and RhoA proteins increase myosin II driven contractility *via* kinases ROCK I and II (77, 78). There is a well established inhibitory cross–talk between Rac1 and RhoA. Activation of RhoA results in increased contractility, which in turn activates a Rac inhibitor, ARFGAP22 (79). Similarly, activation of Rac1 stimulates inhibition of myosin II, *via* WAVE2 (Figure 1.7). This cross–talk induces polarisation

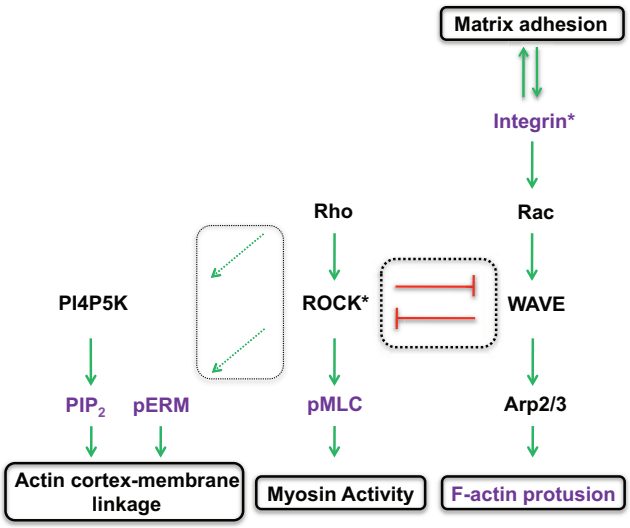

Figure 1.7: A diagram of key regulatory networks of the cytoskeleton. The major molecular players and connections involved in regulation of cortex-membrane linkage, F-actin protrusion, myosin activity and ECM adhesion are shown. Figure is the courtesy of Tumour Cell Biology Laboratory.

in cells, with contractility and F-actin based protrusions segregating to spatially different regions of the cell body. Further, the feedback between contractile and F-actin protrusion pathways induces switches in cell motility mechanisms, which will be investigated in Section 1.5.

1.3.2.2 The F-Actin Cortex – Plasma Membrane Linkers: ERM Proteins

In response to state changes within the cell, and environmental stimulation, the cell body can undergo major changes in volume and morphology, facilitated by the highly dynamic cytoskeleton. As a necessary response, plasma membrane–F–actin cortex adhesion is equally dynamic, adapting to the changes driven by the cortex. As a means to keep the membrane–cortex coupling intact, the components of the protein complexes adhering the membrane to the cortex are constantly redistributed (80). In parallel with this dynamic nature, the majority of the cortex-membrane bonding events are weak, and highly reversible (80).

Ezrin, radixin, moesin proteins, the ERM protein family, are important mediators of dynamic membrane-cytoskeleton adhesion (81). ERM proteins have a conserved FERM domain (F for 4.1 protein, E for ezrin, R for radixin and M for moesin) at their N-terminus, and an actin binding domain at their C-terminus. They bind *trans*–membrane proteins such as integrins and CD44, through the FERM domain, linking the actin cortex to the plasma membrane (82). Regulation of ERM family proteins involves phosphorylation of the C-terminus domain (83), which leads to a conformational change, exposing FERM and actin-binding domains for binding, facilitating the link between cortex and transmembrane proteins. The phosphorylation of ERM is facilitated by Phosphatidylinositol 4,5-bisphosphate (PIP_2) (84), suggesting PIP_2 to be a master regulator of the adhesion between cell cortex and membrane (85). The aforementioned dynamic nature of the adhesion between the plasma membrane and the cortex is exemplified by studies of ezrin networks distributed on the plasma membrane of B cells (86), ERM proteins are continuously changing their location, supporting rapid redistribution and regulation of cortex membrane adhesion.

Upon failure of cortrex–membrane coupling, membrane blebs are initiated (35). During the reassembly of cortex and cortex related proteins at the blebbing membrane, ezrin arrives to the detached membrane patch before actin. The newly formed F-actin cortex is thus coupled to the plasma membrane, stabilising the recovery of the detached region (31). It is of importance to note that actin reassembly is not potentiated by arrival of ezrin (31), and the actin renewal rate is not necessarily linked to ezrin levels.

1.3.2.3 Cell-Extracellular Matrix Adhesion: Integrins

The cell's ability to adhere to its environment is crucial for its survival, differentiation, and in certain cases, migration (87). Adhesion sites function as sites of physical tethering to the matrix and can be considered to be signalling hubs; they are also linked to remodelling of the extracellular matrix (3, 88).

Cell adhesion to the ECM is mainly mediated *via* integrins (87). All integrins function as non-covalently bound heterodimers, composed of an α and a β subunit. Integrins display a significant compositional diversity within mammalian

genomes, with eighteen α subunits, eight β subunits; and twenty-four identified α–β combinations. While some of the subunits appear in only one of these combinations, twelve of the identified combinations include the integrin β1 subunit (89). The extracellular domain of integrin binds to specific sequence motifs of extracellular matrix proteins, such as fibronectin, and collagen (5). The binding of the extracellular domain of integrin to the ECM induces a conformational change on the heterodimer. This conformation change results in exposing the short integrin intracellular tail for binding to the cytoskeleton, *via* a multi-protein complex (5, 87). The multi-protein complex is diverse, and includes proteins that directly bind to actin (5). Some of the most studied of these are talin and vinculin. With its head domain interacting with integrins, and tail domain interacting with actin, talin bears the mechanical load between the inside and outside of the cell, transmitting force from the adhesion point at the ECM, to the cell cytoskeleton (5, 87).

In relation to cancer metastasis, integrins are also involved in remodelling the extracellular matrix. For a tumour to metastasize, cells must penetrate the basement membrane of the tumour, basement membrane of the vasculature, and finally the basement membrane of the target tissue. For example, integrinαvβ3 takes part in regulating the proteolitic enzymes responsible for degradation of these basement membranes, allowing tumour cells to penetrate through tissue barriers (3). Invasion is also linked to the behaviour of the non-cancerous cell types in the tumour, for example cancer related fibroblasts (CAF) can aid invasion by remodelling the matrix, generating paths that cancer cells can follow. It has been reported that with accumulation of integrinα5 at cell–ECM contact sites, CAFs can remodel the ECM in a force dependent mechanism, trans-locating the fibres (88).

The strength of a single integrin to ECM link has been measured by atomic force microscopy (AFM) experiments to be in the order of 47 ± 13 *pN* (90). However, in the context of cell–ECM adhesion, the single bond is rarely the scale of interest as integrins cluster, and the avidity of the contact site as a whole should be of interest. The initial adhesions formed between integrins and the ECM upon contact are small, short-lived contacts that either disassemble or mature within ~60 *s*. These adhesions are termed ”nascent contacts”. Nascent contacts can mature into dot like ”focal complexes”, which are larger in size, approximately 1 μm, and have a life time in the range of minutes. The focal complexes themselves can mature

into "focal adhesions". Focal adhesions can be 3–10 μm long, 2 μm wide, and are usually located at the ends of stress fibres (5). The maturation of focal complexes into focal adhesions takes place within 1 hr, while cell motility events take place in the range of minutes. Therefore, focal complexes, rather than focal adhesions, are functionally more relevant for rapid cell migration. As might be expected from the above discussion, focal complexes can bear forces in the range 1–3 $nN\ \mu m^{-2}$, while focal adhesions can bear larger forces, in the range 4–5.5 $nN\ \mu m^{-2}$ (91, 92).

There are two proposed models for initiation of adhesions: i) Initiation of adhesion with integrin binding to ECM, integrin clustering mediated by the ligation, followed by positive feedback for the formation of new adhesions through clustering of the cytoplasmic domains of adhesion complexes. ii) Initiation of adhesion *via* actin polymerisation, using dendritic actin as the template for adhesion complex formation. The two models are most likely to be working side by side, with both mechanisms contributing to formation of nascent contacts (5). The maturation of the adhesions sites is tension dependent. The effect of the generated tension on maturation and strengthening has been investigated by force application in a two-stage experiment. Beads were attached to cells and initial adhesion strength measured. Then beads attached to cells were restrained with an initial force, released, and pulled again to measure the increase in adhesion strength. The experiment demonstrated the adhesion strength increased 2.9 fold relative to the initial restraining force, and the increase took place within 5–10 s (93). The maturation process of adhesion sites into focal complexes has also been linked to myosin II activity, *via* both the tension generation and crosslinking functions of myosin II (5).

1.4 Plasma Membrane Blebbing

1.4.1 Definition and Phases of a Membrane Bleb

Membrane blebs are balloon like protrusions of the plasma membrane, which form when the membrane loses support of the underlying F-actin cortex (35). Plasma membrane blebs were observed as early as 1920s, in chick tissues (94), but their rigorous investigation in terms of cell motility has been in 1980s (95), mostly due

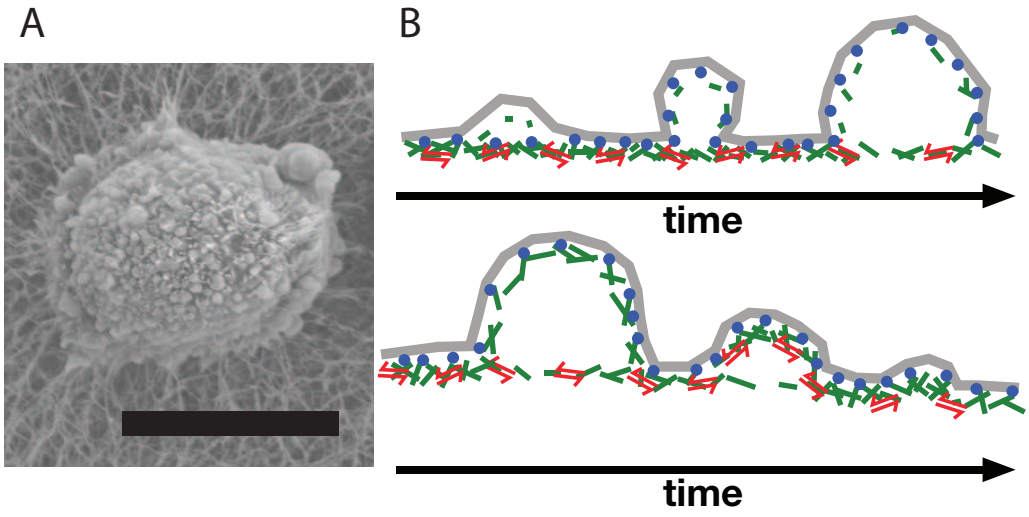

Figure 1.8: A) Scanning Electron Microscopy image of a blebbing melanoma cell. The scale bar is 10 μm B) Schematic representing the dynamics of a plasma membrane bleb initiated by loss of adhesion between the F-actin cortex and the plasma membrane. Plasma membrane in grey, F-actin in green, myosin activity in red, cortex-membrane linkers in blue. Top row: Bleb expansion. Intracellular pressure detaches a membrane patch from the underlying cortex. Flow of fluid expands the bleb, accompanied by tearing and opening of the bleb neck. Bottom row: Bleb retraction. Reformation of the F-actin cortex below the membrane halts the growth of the bleb. With the arrival of myosin II, the bleb is retracted into the cell body. cortex-membrane proteins arrive at the bleb rim before the cortex starts reforming. While the cortex reforms under the bleb rim, the cortex at the bleb neck decays.

to practical limitations, namely their transient nature.

The basis of membrane blebbing is the interplay between the levels of key membrane cortex associated proteins and the physics of the cell. Formation of membrane blebs is linked with the loss of the F-actin cortex or loss of adhesion between the plasma membrane and the underlying F-actin cortex (35, 96, 97). Once the plasma membrane is free of the F-actin cortex, intracellular pressure drives the inflation of the bleb. Cytoplasm flows into the detached membrane patch, resulting in a rapid expansion phase. With re-accumulation of F-actin at the rim of the detached membrane, the rapid expansion comes to a halt, and the bleb, with the help of myosin motor activity, retracts back into the cell body (Figure 1.8)(31).

1.4.1.1 Bleb Initiation

Among the two possible mechanisms of bleb initiation, loss of F-actin cortex and the loss of adhesion between the plasma membrane and F-actin cortex; initiation of a membrane bleb due to loss of the underlying F-actin cortex is obvious under experimental conditions where the cortex is depleted artificially with laser ablation (27). But the occurrence of this type of bleb initiation in spontaneous blebbing in motile cells is rare (98), and biological relevance of the phenomena to cell motility is less obvious. Oscillatory bleb like bulge formation in human lymphoblastic T cells upon myosin overexpression have been suggested to occur due to F-actin cortex rupture, as a result of the elevated levels of stress on the shell. The phenomenon is suggested to be pressure independent. Even though the process is myosin II dependent, the bulge formation was persistent with modification of the osmolarity of the medium (97). It is suggested that upon retraction of the bulge, although myosin II re-distributed in the cell body, there was an elevated level of myosin II at the position of the bulge, which can lead to rupture from the same point. Further studies of actin shells accumulated around beads eventually demonstrated that spontaneous rupture can occur above a certain stress (99). On the other hand, the existence of a residual layer of actin at the bleb neck have been demonstrated in a multitude of studies, including this thesis (31, 35, 98, 100), and there have been suggested roles for the bleb neck actin in cell motility (101). In studies where myosin activity has been kept intact, but where pressure accumulation has been eliminated with electroporation, spontaneous membrane blebbing could not be initiated (100). Moreover, in spontaneous blebbing of HeLa cells, bleb initiation probability was shown to be independent of the positions and timings of previous blebs, thereby contradicting with the suggestion that cortex tearing is more likely to occur at the site of a previous bleb (35). Thus, cortex rupture, although able to produce membrane blebs under a set of conditions, seems to be a less frequent phenomenon in cell motility; therefore, a model based upon plasma membrane detachment from F-actin appears to be the relevant model to construct for a study of membrane blebbing in a cell motility context.

In the model of membrane bleb formation due to detachment of membrane from the underlying cortex, the initiation is pressure driven. With local fluctuations in the F-actin cortex plasma membrane linker proteins, the membrane is detached at the weakest points of the cell surface (35, 100). Since elevated cortical contractility

drives the intracellular pressure increase, bleb initiation in this model is still closely linked with myosin II activity (27, 34, 100, 102). On top of local fluctuations in F-actin cortex plasma membrane linker concentrations, the pressure gradients inside cells have been suggested to determine the position of bleb formation. Indeed, experiments on melanoma cells have shown them to be capable of having pressure gradients: when pressure is artificially reduced on one side of the cell, the cell continues to bleb on the remaining surface (34). The time scale of pressure equilibration is shown to be approximately 10 s within 10 μm of distance upon release of enforced pressure gradient. This heterogeneity of intracellular pressure is dependent on the poroelastic structure of the cell interior. Pressure equilibration is limited by the porous structure the cytoskeleton and organelles, the structures that limit the fluid flow, form (34, 103). While the above study clearly demonstrates cells are able to have pressure gradients, whether such gradients have major roles in determining position of bleb initiation is not clear. Further studies showed, by sequential bleb initiation with laser ablation of the cortex, the size of the second bleb is always smaller than the first, as the pressure is released. However, there is no correlation between the size and position of the second bleb relative to the first. In other words, pressure equilibration appears to be fast enough such that a second bleb initiated immediately after and next to the first bleb, or initiated on the opposite side of the cell, are likely to be of a similar size (27). Additionally, studies in *Entamoeba histolytica* showed no correlation between the positions of local F-cortex contraction sites and bleb initiation points (100). Considering all of these experimental observations, although it is evident pressure equilibration can not be instantaneous, and cells are capable of holding internal pressure gradients, from the perspective of the roles for membrane blebbing in cell motility, the pressure field inside the cell can be assumed homogenous.

1.4.1.2 Bleb Expansion

Expansion of a bleb is not linked with actin polymerisation, and is facilitated by the flow of cytoplasm into the cortex free membrane patch (104, 105). The volume change of cells during blebbing cycles is low – less than 5 per cent – and the fluid entry into the detached membrane patch is indeed from the cell interior, rather than fluid from the extracellular environment flowing into the cell (34, 106, 107). Expansion is rapid, and continues until a new layer of F-actin

network is established at the bleb rim (31, 35). The membrane required to accommodate the size increase of the blebbing surface enters the bleb in two ways. Firstly, due to the fluid like structure of the plasma membrane, lipids flow into the blebbing patch through the borders of the bleb neck. Secondly, blebbing membrane is torn off the underlying F-actin cortex at the borders of the bleb neck, increasing both the bleb neck size, and the available blebbing membrane (34, 35). Although cells are documented to modulate their available plasma membrane *via* exocytosis upon membrane tension increase when all the available membrane is used up (70), exocytosis is not a mechanisms used to regulate plasma membrane during blebbing (107). During the expansion phase, the bleb rim is devoid of a structured F-actin cortex (35, 104), nevertheless the tension of the blebbing membrane is higher than that expected from a pure lipid bilayer (27). There appears to be some form of a residual cytoskeleton at the bleb rim (31). During the expansion phase, large organelles cannot enter into the bleb, as the F-actin cortex of the bleb neck forms a barrier between the fluid bleb interior and the main cell body. Thereby, bleb interior is less viscous compared to the rest of the cell body.

1.4.1.3 Bleb Stabilisation and Retraction

Bleb expansion stops when accumulating actin starts forming a new layer of F-actin cortex under the expanding bleb rim, and as the release of pressure is balanced by the tension from the curvature of the blebbing region (31, 35). Upon slowing down of the expanding membrane, the F-actin cortex plasma membrane linker protein ezrin arrives to the bleb rim prior to actin (31). As actin assembles into a structured cortex, the linkage with the plasma membrane is established, and bleb expansion stops. Upon inhibition of ezrin accumulation into blebs, by the broad specificity kinase inhibitor staurosporine, expanding blebs could not establish a bleb rim, and did not retract. The inhibition of bleb retraction was not related to nucleation of actin filaments, but formation of stable links between the assembling cortex and the plasma membrane (31). More than one study has now established that each cell type has a linear relationship between the maximum size its blebs can reach, and the blebs' expansion rates, with re-assembly of the F-actin cortex taking place at an almost constant time period after initiation, i.e. the time period necessary for actin polymerisation to catch up with the expanding bleb neck is independent of the bleb size, but dependent on the type of the cell (27, 104). Contrary to bleb neck

expansion by tearing of the membrane on the bleb borders during the expansion phase, during stabilisation and retraction, bleb neck size does not change (35).

After a stationary phase, unless the newly assembled F-actin cortex of the blebbing membrane formed adhesions with the ECM, the bleb is retracted back into the cell body (98, 108). The retraction is facilitated by myosin II recruitment to the bleb rim (34, 105), which has a delay after the arrival of actin (31). The rate of bleb retraction is slow compared to the expansion rate (10, 34, 35, 104, 107, 109).

During the life cycle of a bleb, the F-actin cortex left behind at the bleb neck decays and disassembles at a rate similar to actin re-accumulation at the bleb rim (35, 100). While the bleb expands, this remaining cortex of the bleb neck flows rearwards (100). It has been suggested that anchoring of this F-actin network to the ECM or neighbouring cells can assist cell motility, helping the cell to propel itself forwards with blebbing (101).

1.4.1.4 Blebbing in a non-Motilility Context: Apoptosis, Spreading, and Cytokinesis

Many functional roles have been attributed to plasma membrane blebbing in apoptosis, cell spreading, cytokinesis and cell motility (108). During apoptosis, membrane blebbing can occur as a physical side effect of F-actin cortex disassembly, but it also has a role in redistribution of fragmented DNA from the nuclear region of the cell into blebs and apoptotic bodies (110). Apoptotic blebbing occurs transiently, cells stop forming blebs as they proceed into the later stages of apoptosis (111). Membrane blebbing is also observed during initial spreading periods (112–114), and detailed investigation has identified blebs as forming the initial adhesion patches with the ECM surface (115). Here, blebs are linked with the initial slow spreading period, but not the later rapid spreading, where lammelipodia form, from the initial adhesion patches, and dominate the spreading profile (115).

When cells are rapidly detached from their spread states, with biochemical perturbations excessive blebbing is observed. This suggests a possible role to blebbing in regulating the plasma membrane tension the cell feels at any time point.

With rapid detachment, and rapid change of the cell morphology, the tension felt by the cell would go through a rapid change, which blebbing can damp, and ensure homeostasis is maintained (114). This proposal is similar to the roles attributed to blebbing in cytokinesis–separation of a cell into two daughter cells.

During cytokinesis, a cortical ring with high myosin activity forms at the division axis. Although tension is lower at the poles of the cell, there is still a contractile cortex, which is not necessarily homogenous and at equal strength for the two poles. This unbalanced myosin activity brings an inherent instability to cytokinesis, which results in oscillations in cell shape, oscillations in the cleavage furrow position, unequal sizes of daughter cells, and aneuploidy (108, 116). Blebbing at the poles during cytokinesis is proposed to serve as a pressure sink, balancing excess pressure accumulation. This regulation ensures there is no predominant fluid flow from one pole to the other. Further evidence in support of this hypothesis comes from a study where inhibition of blebbing increased the rate of shape instabilities in dividing cells (116).

The roles of plasma membrane blebbing in cell motility will be covered in detail under Section 1.5.2.

1.4.2 The Dynamics of Membrane Blebbing in Numbers

Membrane blebbing has a rapid and dynamic life cycle, initiation, rapid expansion, stabilisation and slow retraction occurring within approximately one to two minutes (105). Depending on the system under investigation, blebs may take 2–30 s to expand, go through a 10–20 s stabilisation period, and retract within 19–120 s (104, 106, 107, 109).

The minimum size of the membrane patch initially detached from the cortex, such that expansion of the bleb is energetically favourable, is calculated as 34 nm (35). Blebs can have a variety of sizes, from 1–2 μm for spontaneously blebbing melanoma cells, to bulges for human lymphoblastic T cells that grow as big as the cell itself (see Table 1.1). Bleb sizes are directly correlated with bleb neck sizes and the rate of bleb expansion (27, 96, 104). Bleb expansion rates are always significantly faster than bleb retraction rates. Expansion is reported in the range 0.3 $\mu m\ s^{-1}$ – 20 $\mu m\ s^{-1}$, while retraction velocities are approximately 0.1

$\mu m\ s^{-1}$. During the expansion phase, bleb necks grow 2.04 ± 0.69–fold while bleb perimeters increase approximately 5.36 ± 1.61-fold. The velocity of growth of the bleb necks is ~$0.1 \mu m\ s^{-1}$ (35). Membrane flow velocity into blebs is approximately $2\ \mu m\ s^{-1}$, which has contributions from both neck enlargement and lipid flow into the blebbing patch from the borders. Accumulation of F-actin in the bleb rim during stabilisation and retraction can be identified from the difference in bending rigidity of an expanding and retracting bleb, $4.7 \times 10^{-20} Nm$ and $2.15 \times 10^{-20} Nm$, respectively (35). Accumulation of actin in the bleb rim stops bleb expansion, and with the arrival of myosin with a delay of $7.3 \pm 2.4\ s$ after actin, the bleb is retracted.

Table 1.1: The Dynamics of plasma membrane blebbing from different model systems

Cell Type	Expansion Times and Maximum Rates	Retraction Times and Maximum Rates	Bleb Size	
HeLa	30 s $\mu m\ s^{-1}$ $0.2 \pm 0.1\ \mu m\ s^{-1}$	120 s $0.047 \pm 0.023\ \mu m\ s^{-1}$	2 μm	(35)
CHO and HeLa	6 s $0.332\ \mu m\ s^{-1}$	26 s $0.012\ \mu m\ s^{-1}$	1.7 μm	(109)
Dictyostelium	2 s	19 s	–	(107)
Human Melanoma	4-7 s	40-60 s	40-90 μm^3	(104)
Entamoeba histolytica	10-20 $\mu m\ s^{-1}$	–	–	(100)
Satellite Cell	15 s	30-45 s	~7 percent of cell length	(10)
Mouse Melanoma	$0.77 \pm 0.19\ \mu m\ s^{-1}$	$0.14 \pm 0.05\ \mu m\ s^{-1}$	$1.03 \pm 0.40\ \mu m$	this study

1.5 Cell Motility Mechanisms

During their movement in the body, cancer cells need to traffic through a wide range of environments, from the basement membrane of the tumour or the vasculature, to interstitial collagen matrices (3, 4). The ability to stay motile requires cancer

cells to adapt their mechanisms of motility to changes within their environment. Indeed, the morphological features of motile cancer cells and the dominant cellular mechanisms utilised for motility, display a wide variation, equal to that of the variability of the environments the cells must penetrate (5). Both highly elongated mesenchymal motility and spreading amoeboid motility modes depend on actin polymerisation mechanisms, while a rounded amoeboid motility mode depends on contractility and membrane blebbing (7). The final morphology and motility mode of a cell is determined by the balance of intracellular and extracellular factors, such as myosin II driven contractility, adhesion to ECM, and the geometry and rigidity of the ECM (5, 8). In that sense, different modes of cell motility, from elongated mesenchymal to round amoeboid, are a continuum of motility modes that cells can adapt, defined by variations in the balance of the above factors, rather than being strictly distinct migratory modes (8, 9). Highly actin polymerisation dependent motility mechanisms of spread cells, and the dynamic, contractility and membrane blebbing dependent motility mechanisms of round cells, are the extremes of the same spectrum (7).

The ability of cells to shift within this spectrum of motility modes has been demonstrated in a multitude of systems, including cancer cells. During gastrularisation of zebrafish embryos, mesodermal cells need to move in an amoeboid fashion, then switch to and elongated mesenchymal form, and at times, form lammelipodia and membrane blebbing simultaneously (11). Human adult skeletal muscle stem cells display an elongated morphology with lammelipodia like protrusions whilst moving on basal lamina. During their emergence from basal lamina, and throughout their motility within myofibrils, they display an amoeboid morphology with polarised membrane blebbing (10). Human fibrocarcinoma and breast cancer cells have been shown to go through a mesenchymal to amoeboid transition upon inhibition of ECM degradation enzymes (6), and manipulation of myosin II driven contractility has been shown to shift the dominant motility mode of human melanoma cells between elongated mesenchymal to amoeboid blebbing (9). During the shift between motility modes, additional to biochemical pathways linking actin polymerisation based protrusions and membrane blebbing, there is also crosstalk between these mechanisms on a purely physical basis. Increasing blebbing frequency *via* cell medium osmolarity results in loss of lammelipodia formation with the available cell surface being occupied by blebs, leaving no space

for lammelipodia formation. Similarly, spreading lammelipodia flattens membrane blebs due to limitations on the available membrane pool of the cell (70, 117).

The necessity of cell–ECM adhesion is also dependent on the geometry and physical properties of the ECM. While adhesion to the ECM is essential on 2D surfaces (118), it has repeatedly been shown that in many 3D environments, adhesion can be expandable to a large extent (41, 118, 119). For instance, inhibition of ECM degradation was shown to be ineffective in clinical trials (6). In an adhesion free environment, cells can utilise both membrane blebbing or actin polymerisation to propel the cell body forward, details of which are poorly understood (7, 120).

1.5.1 Mesenchymal and Amoeboid Spreading Cell Motilities

The point of convergence between mesenchymal and amoeboid spreading motilities is their strong dependency on actin polymerisation. These motility modes differ in the morphology the cell displays; while both motility modes involve spreading cells, mesenchymal cells are characterised by an elongated and rigid morphology (e.g. fibroblasts) (5), while amoeboid spreading cells are characterised by a rounder, and more dynamic morphology (e.g. leukocytes –namely T-cells and dendritic cells– in 2D environments) (7). Mesenchymal cells form strong adhesions to the environment, and their velocity is limited to their adhesion – de-adhesion rates (118, 120). Moreover, degradation of the ECM *via* proteases is also linked with elongated morphology (4).

Protrusion driven motility on 2D surfaces involves four steps, i) protrusions of the leading edge forward, ii) adhesion to the matrix, iii) retraction of the cell rear, and iv) detachment of the cell rear (5). Polymerising actin pushing on the cell membrane facilitates protrusion of the leading edge (120); indeed, even cell fragments from lammelipodia alone can crawl on surfaces (121). Retraction of the cell rear can involve several mechanisms (40). At the molecular level, myosin II driven contractility of the cell rear can pull the cell rear *via* cytoplasmic forward streaming, and help detach the cell rear from the substrate by pulling on molecular bonds at points of adhesion (41, 122). Modulation of integrin binding affinities can also preferentially disassemble adhesions at the cell rear (40). Lastly, plasma

membrane tension can assist detachment at the cell rear. Upon depletion of the membrane pool of the cell, increased membrane tension will pull the cell rear, as membrane behaves similar to a sliding bag over the cell body, which can be pushed forward by actin polymerisation at the cell front (120). The necessity for contractility is cell type dependent. Inhibition of myosin II can cause impairment of cell velocity and elongation in dendritic cells (41), while melanoma cells have been reported to maintain their velocity upon ROCK inhibition (9). Another important aspect of the behaviour of dendritic cells on highly adherent surfaces is that the cells could polarise their front and move towards the chemo–attractant source, while their rear stayed attached to the substrate, causing cell elongation. This demonstrates that the cell polarity, *via* actin polymerisation based protrusion, and myosin II driven contractility, can occur spatially and temporally independent of each other. On 2D surfaces, cell motility is strictly cell–ECM adhesion dependent, with maximal velocities obtained at medium adhesion levels (41, 119). If adhesion levels are too low, the cell cannot generate enough traction for motility; if the adhesion levels are too high, the cell cannot detach its rear, and consequently, the adhesion vs. cell velocity curve takes a bell shaped form.

In 3D environments, the dependencies of cells change significantly with the physical properties of the ECM. In densely packed environments, elongated mesenchymal motility is the dominant mode, where cells have strong adhesions, they remodel the ECM through degradation, and generate migration tracks (4, 6, 120). In this motility mode, integrins and matrix degradation enzymes co-cluster on the sites of contact with ECM fibres (6). Similarly, while penetrating through base membranes, proteases are necessary to initiate and enlarge holes for the cell to migrate, through which actin polymerisation based protrusions can extend, and the cell body pulled (4).

When the 3D environment has gaps that are large enough for cells to squeeze through, and cell–ECM adhesion is low, amoeboid motility dominates, being either actin polymerisation or plasma membrane blebbing dependent. The lower limit of gap size that cells are able to squeeze through has been shown as 4 μm (6). In these environments, cells form less completely assembled focal interactions with the ECM (118); and more importantly, cells can still migrate upon inhibition of integrins or ECM proteases. There is also no permanent remodelling of the

ECM (6, 41, 119). For adhesion independent actin polymerisation based motility, entangling and jamming of the F-actin protrusions with the fibres of the ECM generates sufficient traction for the cells to hold on to the ECM, and generate movement with rear retraction upon increased myosin II driven contractility (120). In environments where the entangling is limited, "chimneying" is suggested as an alternate methodology to generate motility. Here, the cell body pushes on the surrounding walls of ECM, and generates traction *via* friction forces, while actin polymerisation, or membrane blebbing, propels the cell body forward (7). A theoretical study of chimneying with actin polymerisation based protrusion at the cell front demonstrated the plausibility of this model (123).

On top of the changes for the dependence on cell–ECM adhesion, dependence on contractility increases significantly in environments where the cell is required to squeeze its body through narrow gaps. As well as being a driving force to propel the cell body forward, contractility is necessary for a new, adhesion independent type of tail retraction barrier: the stiffer nucleus needs to be deformed and pushed through gaps that are smaller than the size of the nucleus, *via* myosin II driven contractility (7). Upon inhibition of myosin II, cancer cells and dendritic cells have been shown to invade through matrices with gap sizes larger than the nucleus, but are unable to penetrate through matrices with gap sizes smaller than the nuclei diameter (41, 53). Close imaging of dendritic cells confirmed that the nuclei were stuck in the mesh, unable to squeeze through the gaps, while cell front continues to migrate, resulting in excessive cell elongation (41).

Another level of plasticity is the fact that the induced switches in motility modes are reversible, when cells moving in a mesenchymal mode of motility are induced to switch to an amoeboid mode by transient inhibition of proteases, they switch back to the mesenchymal mode within approximately 10 hr (6). In line with the strong dependency of motility mode on the ECM conditions, switches between motility modes are rapid. It has been experimentally demonstrated that adhesion dependent, and independent motility can occur simulataneously in the same cell, on substrates with both adhesive and non-adhesive regions within the size scale of a single cell. The understanding is that actin polymerisation and retrograde flow rates increase in the non-adhesive regions of the substrate, and the retrograde flow drops to the normal values at the boundary of the adhesive region of the

substrate, with a parallel reduction in polymerisation rate. Hence, the cell has a continuous protrusion elongation rate throughout the adhesive and non-adhesive surface. This indicates that the ability to switch motility modes is a property of the cytoskeleton, rather than a change in the proteome of the cell (69). The parallel increase of retrograde flow with polymerisation also indicates the rate limiting step determining the elongation rate of the protrusions is the physical resistance from the membrane, rather than a biochemical limit of the polymerisation event. Plasticity of cell motility in adhesion dependent and independent modes is an emergent physical response to the changing conditions of the extracellular environment.

1.5.2 Amoeboid Blebbing Cell Motility

At the other end of the cell motility spectrum, amoeboid blebbing motility differs from the previously described modes in that it is not dependent on actin polymerisation to push the leading edge of the cell forward. This form of motility depends on hydrostatic pressure driven membrane bleb formation (120). Although leading edge protrusion is not dependent on actin polymerisation, blebbing motility is highly dependent on actomyosin dynamics (105). Amoeboid blebbing motility was observed as early as the late 80s (95), but was not the focus of attention until recently. As with the membrane blebbing phenomena itself; one of the reasons is technical, that amoeboid blebbing motility occurs in complex 3D *in vitro* experimental systems, or in living tissues, making it harder to investigate (10).

The amoeboid blebbing cell has a round and highly flexible morphology, even more so than the amoeboid spreading variant (7, 9). This motility mode is protease independent; requires low adhesion levels, if any; and myosin II driven contractility is at its core (9, 105, 117).

1.5.2.1 Systems Demonstrating Amoeboid Blebbing Motility

Amoeboid blebbing motility has been observed in many systems including cancer cells (7). Motility with polarised blebbing is seen in killifish *Fundulus heteroclitus* deep cells, *Dictyostelium*, zebrafish Primodial Germ Cells (PGC), *Xenopus* PGCs, adult skeletal muscle stem cells, and human melanoma cells

(8, 10, 95, 106, 107, 117, 124). During killifish embryogenesis, deep cells demonstrate random blebbing migration. Upon wounding the yolk sack epithelium, cells start moving towards the wound closure, with the range of the response being as high as 800 μm. The cells have the inherent ability to move with blebbing, and they can be reoriented to have directional motility in response to extracellular signals (95). During the slug stage of *Dictyostelium*, cells have been reported to move with formation of large membrane blebs at the cell front, upon stimulation with cAMP (107, 117). In zebrafish PGCs, the chemokine SDF-1 stimulates polarised amoeboid blebbing motility. In the absence of polarised blebbing, the cells tumble, while SDF-1 polarises blebs to one side of the cell, allowing the cells to move with velocities close to 2 $\mu m\ min^{-1}$ (106). Similar to zebrafish, blebbing migration of PGCs in *Xenopus* is also stimulated by SDF-1 (124). Adult skeletal muscle cells-satellite cells- display mesenchymal motility as they migrate on, and emerge from, the basal lamina. When the cells start migrating along the myofibres, they adapt a round flexible morphology and membrane blebbing based motility. Blebbing occurs over the entire cell surface, with more predominant blebbing on one side, and with an accompanying cell velocity in the order of 0.8 $\mu m\ min^{-1}$ (10). Detailed identification of satellite cell movement has direct clinical implications, as these cells are responsible for tissue repair. So far, clinical trials for tissue repair by cell injection had limitations due to cells not moving further than 200 μm from the injection site. In A375 melanoma cells, polarization of ezrin and myosin at the cell rear drives cell motility with increased blebbing at the cell front. Similar to satellite cells, blebbing is seen over the whole cell body, with reduced blebbing at the cell rear. It is important to note, although accumulation of ezrin on a particular patch of the cell is inherent in all blebbing cells, only a small sub-population of five per cent demonstrated stabilized polarity and directional migration (8). This reflects that formation of polarised blebbing is inherent in melanoma cells; however, mechanisms stabilising this polarity are not fully understood. Movement of endothelial cells, and invasion of melanoma *in vivo* have been demonstrated to utilise polarised membrane blebbing, under control conditions, and a variety of biochemical perturbation conditions, including cell–ECM adhesion reduction *via* integrin β1 inhibition (Figure 1.9). These mechanisms are discussed further in Chapter 4 of this thesis.

In addition to the observed polarised membrane blebbing, cancer cells can display

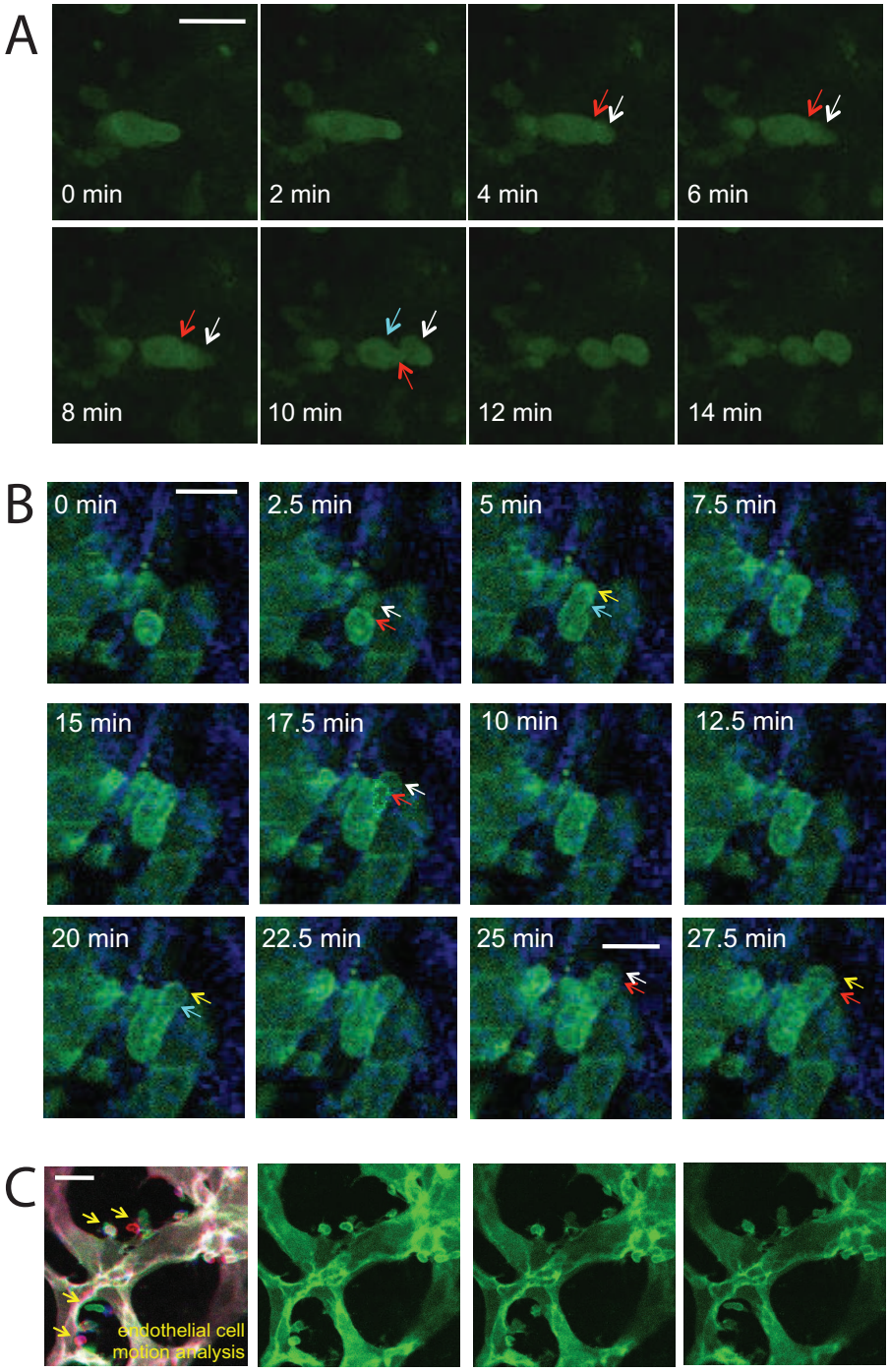

Figure 1.9: A) Intravial image of LifeACT-GFP expressing A375M2 melanoma. Actin in green, collagen in blue. White arrows indicate actin poor bleb initiation, yellow arrow indicates new actin polymerisation in the bleb, red arrows show bleb neck and cyan arrow shows bleb neck dissapperance. B) Amoeboid blebbing motility of A375M2 cell, with integrin β1 depletion. Colour coding same as A. C) Intravial imaging of endothelial cell blebbing at tumour margin.

amoeboid motility modes with non-polarised blebbing, and this blebbing, with no evident polarity, appears to enhance invasion rates (9, 12, 105, 109). For human lymphoblastic T cells, a non-characteristic form of blebbing, oscillatory bulge formation, also correlates with the ability of cells to migrate (97). In melanoma, at cortical regions of the tumour, rapid amoeboid movement have been observed while the cells possess a mesenchymal shape in the inner regions of the tumour. Moreover, a reduction in amoeboid motility, with an induced shift of cancer cells to an elongated morphology, reduces the ability of cancer cells to invade the lung (9). These observations emphasise the link between amoeboid blebbing cell motility and cancer cell invasion.

1.5.2.2 Translating Membrane Blebbing to Cell Translocation

Although the benefits of amoeboid blebbing motility are evident, the underlying mechanisms are not obvious. When a blebbing cell expands a membrane bleb, and the bleb collides with an element on its path, such as an extracellular matrix filament, then the cell body should be pushed backwards by the expansion of the bleb, rather than moving forward (120). There are proposed models for both 2D surfaces and 3D matrices, on how blebbing can be translated into translocation. The first possibility is that blebs can adhere to the environment prior to retraction. Although the blebbing membrane is devoid of actin to serve as a basis in binding the environment during expansion, formation of the F-actin cortex at the bleb rim stabilises the bleb before retraction. Hence, blebs that adhere to the ECM, before the physical retraction of the bleb, can pull the cell body forwards, rather than retracting the bleb into the cell body with no net cell movement (106, 117, 120). The fast propulsion of a bleb from the cell body would also cause a rapid pressure release within the cell, facilitating rapid forward streaming of the cell rear aiding to forward movement. This is indeed observed in *Dictyostelium* motility, where area expansion at the front occurs simultaneously with area reduction at the rear (117). This forward propelling–adhesion model is functional on 2D surfaces, where adhesion is a necessity (7). Actin brush formation, is another possible mechanism for amoeboid blebbing motility (101). In this model, the actin network around the bleb neck adheres to the environment, and the rearward flow of this region with respect to the cell body generates the traction forces that can move the cell forward. Here, membrane blebbing at the cell front is needed to rapidly propel the region of

the cell body that will facilitate movement – bleb necks – forward (101).

The adhesion independent model for amoeboid blebbing motility is where membrane blebs anchor the cell body to the environment. A membrane bleb can expand into a gap of the ECM, filling the gap, and therefore entangling the cell body to the environment (120). This entanglement will serve in place of integrin-mediated adhesion, and while mesenchymal cells use their energy in adhesion formation and de-adhesion, amoeboid blebbing cells will be able to move with low to no adhesion, flexible morphology and rapid protrusion in complex environments. The benefits of amoeboid blebbing motility are emphasised in complex 3D environments, where the cells do not have a risk of loss of contact with the ECM, and where no regular surfaces are available for lammelipodia spreading (108, 120). The dynamic nature of amoeboid blebbing motility is also significant in complex environments; cell membrane can bleb in all directions, and the cell can simply adapt to the topology of the local extracellular matrix in an efficient, rapid manner (10).

Amoeboid motility, encapsulating both actin polymerisation based protrusion and membrane blebbing modes, is not coupled with ECM proteolysis (108, 118). Still, cells can remodel the matrix transiently in a force dependent manner, by pushing and deforming the fibres to generate paths (39).

In amoeboid blebbing motility, there is a strong dependence on myosin II driven contractility. Membrane bleb formation itself is strongly dependent on cortical contractility (see Section 1.4), and polarised contractility of the cell rear is an important characteristic of amoeboid blebbing motility (8, 125). Moreover, similar to amoeboid motility utilising actin polymerisation for protrusion of the cell front, the dependence on contractility for deformation of the cell body and rigid nucleus, enabiling squeezing of the cell through narrow gaps of the ECM, is essential for amoeboid blebbing motility (7).

In PGC of zebrafish, inhibition of myosin II results in cells being able to form filopodia, but eliminates blebbing and cell motility (106). Again in zebrafish development, mesodermal cells moving in an amoeboid blebbing motility mode have reduced velocity upon reduction of myosin II activity (11). In *Dictyostelium*,

myosin II null cells move with velocities less than half of control velocities (117). In cancer cells, reduction of myosin II activity results in cells switching from an amoeboid blebbing motility to a mesenchymal motility mode (12).

1.5.2.3 Controversy Around Membrane Blebbing in Motility

Amoeboid blebbing motility has been observed in a variety of systems, but there is still much controversy around the roles attributed to membrane blebs in cell motility. Additional to polarised membrane blebbing at the cell front, blebs have been observed at the sides and rear of motile cells (39, 109, 126). For invasion of breast tumour cells into matrigel, it has been suggested that polarised contractility alone is sufficient to drive cell motility, with rear membrane blebbing being a side effect of high contractility (39).

The blebbing phenomena displays a threshold-like nature in response to myosin activity with the cells having a tight range of myosin activity defining the extent of membrane blebbing; their frequency and sizes (See Chapter 3), and contractility is an essential part of motility. On the other hand, increased myosin II activity and excessive blebbing can lead to cell detachment from surfaces and impaired tissue cohesion (11, 122). Excess membrane blebbing also interferes with the directionality of the cells, thus reducing overall cell velocity (96). Lateral movement of blebs, circus blebbing, can lead to direction changes of the cell (95, 127). It is possible that blebs are simply a by-product of contractility that do not contribute positively to cell motion. Combined with the observation that non-polarised blebbing enhances cell invasion (105), these factors clearly demonstrate there to be a gap in the understanding of the driving mechanisms behind amoeboid blebbing motility. There is a need to dissect the roles played by the geometry of and addition to the ECM, myosin II driven actomyosin contractility, and membrane blebbing. There are significant limitations in the current experimental approaches to uncouple the contributions made to blebbing motility, from partitioning the effects of regulators pathways on adhesion to quantifying the effects of polarised contraction. A theoretical approach to investigate the contributions of cell and ECM properties to amoeboid blebbing motility is therefore essential.

1.5.2.4 An Evolutionary Perspective

As the systems where amoeboid blebbing motility is identified as a valid motility mechanism accumulate, it is becoming clear that blebbing is not a case specific event, or just the sign of a death sentence for a cell. Rather it is a conserved motility mechanism from amoebae to vertebrates (108). At the simplest level, the only requirement for initiation and growth of membrane blebs in cells is cortical contractility. On the other hand, an actin polymerisation based motility mechanism requires detailed regulation of nucleation, elongation, branching and crosslinking (see Section F-actin 1.3.2.1 for details). In other words, membrane blebbing is an emergent physical phenomena of the existance of an actin cortex, while actin polymerisation based protrusions require further orchestration of the cortex assembly machinery. Additional to the differing requirements of complexity, there is evidence to suggest membrane blebbing may require less energy compared to lammelipodia formation (113). This comparison suggests membrane blebbing may be more ancestral as a mechanism for cell surface extension, than actin polymerisation.

Fundamentals of cell motility, and to some extent a primitive form of chemotaxis, have been investigated in non-living systems, based on oil droplet in water systems. These oil drop-water systems aim to mimic a primitive life, protocell, which can self-assemble, sense and respond to the environment it resides in, *via* simple active chemical mechanisms driven by its chemical composition (128). Studies on such an oil droplet system showed blebbing with elastic material accumulation on the surface of the oil drop (129). The proposed model is that with constant accumulation of an elastic aggragate at the oil drop water interface, previously formed layers are pushed out of the drop surface. This pushing will require stretching of the older layers, and with its elastic nature, the outer shell will apply forces towards the oil drop, increasing its internal pressure. The failure of the accumulated material under stress from stretching results in formation of a bleb on the surface of the drop (130). Under conditions where the oil droplet is small (<30 μL) and the bleb can grow as big as the remaining body of the oil drop, the whole drop trasnslocated (131). This observed behaviour and proposed model has striking resemblance to oscillatory bulge formation based on actin cortex rupture (97), and indicates a possible step in the evolution of plasma membrane blebbing as a cell motility mechanism.

1.6 Computational Models of Cell Motility

Modelling tumour environments and the behaviour of cancer cells has been a topic of utmost interest. The spreading of cancer cells and the related field of cell motility have been investigated by a range of computational approaches, from continuous reaction-diffusion equation based models of the whole tumour environment, to models of deformation and movement of a single cell with detailed morphology. Almost all levels of modelling have been combined, and over a variety of scales, such as grid based single cell/multi-cellular systems within continuous ECM with diffusive nutrients; elastic network models in continuous fluid environments; or models of morphology and motility of the cell together with cellular protrusions and protein level regulation. In the collective intellectual process of probing cancer invasion mechanisms, the model cell has been reduced to a point, defined on a grid, given flexible morphology, or put together from semi-independent sub-cellular entities. Further, it has been dissected, with individual motility related phenomena being modelled independent of the rest of the cell, such as dynamics of filopodia formation, force velocity relationships of lammelipodia formation, and initiation of plasma membrane blebs. Both stochastic simulations and analytical models have aided our understanding of underlying regulators of cell motility and cancer cell invasion.

In the following sections a number of modelling methodologies are described, starting with the classical continuum modelling of the tumour environment, then moving on to cell centred models. For describing the cell centred models, increasingly detailed morphological information is gradually introduced into the discussion, from point representation of a single cell, through single cell or multi-cellular vertex models, to models incorporating sophisticated morphology modelling. Then models for individual motility related phenomena are briefly covered, with particular attention paid to the available plasma membrane blebbing models. Here both stochastic simulations and analytical models are exemplified. Finally, the last section focuses on the hybrid finite element-agent based model of single cell motility that is the subject of this thesis. Although the list of models discussed cannot be a complete summary of all available modelling approaches, it aims to provide a thorough picture with examples for each scale of modelling, and justifies the modelling approach adopted in this study.

1.6.1 Continuum Models of the Tumour Environment

Continuum models are utilised to understand the global behaviour of tumours, such as the growth of the tumour and the emerging invasive profile. The tumour environment is traditionally represented in the form of reaction-diffusion equations, and the partial differential equation sets are solved by well-established techniques. Continuum models are less computationally demanding than cell based approaches for investigation of biological phenomena on the same scale (132). This approach has been used to investigate numerous tumour contexts. For instance, the transformation of the environment acidity by cancer cells, resulting in the tumour boundary becoming less viable for non-cancerous cells, and prone to cancer cell invasion, have been identified from a continuum model of tumour growth and invasion (133). Another study, a continuum model for breast ductal carcinoma in situ, proposed the mechanical stress the cancer cells are exposed to upon overpopulating the duct is the dominant factor leading to increased extracellular matrix degradation enzyme synthesis, and eventually cancer invasion (134). Despite the well-established solution techniques, and speed of calculation, this modelling approach has its drawbacks. In these models, the individual properties of cells can not be investigated, as a cell density is substituted for the information at the cell level (135). Moreover, for small numbers of cells the density representation loses validity (132). To account for these shortcomings, hybrid approaches have been developed, where individual cell information is introduced in the form of a grid-based representation of cells, with each cell occupying a single grid point, and moving stochastically, under the influence of the environmental conditions (136).

1.6.2 Cell Centred Models: From Centre of Mass to Flexible Morphology

While there are hybrid modelling initiatives to incorporate information at the individual cell level into existing continuous reaction-diffusion models, there are numerous studies that start with a focus on the individual cell. For cell centred models, the definition of the cell can be stripped of all morphology data, such as in the case of cell centre of mass based models (137). From this lower limit, the morphology definition of a cell can move up to be highly sophisticated as in the continuous definition of cell shape in 3D (15). More often than not, these cell

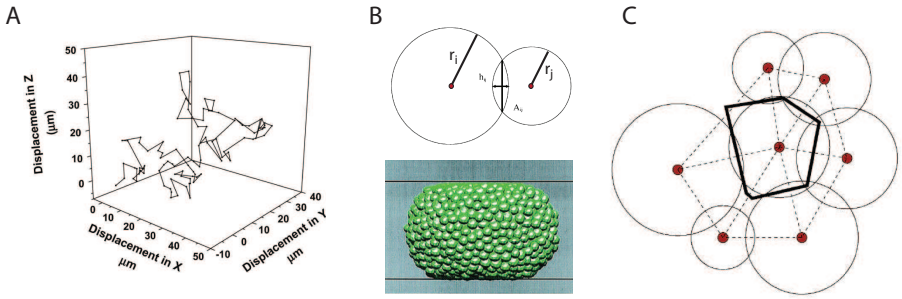

Figure 1.10: A) A Cell motility profile for a cell centre of mass model, where maximum velocities are predicted for intermediate cell–ECM adhesion levels. Image taken from (137). B) Top, schematic representing the interaction area between two cells in a contact theory approach. The area is calculated form the overlap of neighbour cell radii. Image taken from (135). Bottom, cell cohort in between two plates, with cell centre of mass based modelling and where cell morphology is defined by cell radii. Image taken from (139). C) Voronoi diagram approach for the calculation of cell-cell contact area in a packed environment. Image taken from (135).

centred models move into hybrid modelling zones, with the reaction-diffusion models for the extracellular environment being incorporated.

1.6.2.1 Cell Centred Models: Centre of Mass and Simple Morphology

In the simplest form of cell centred models, the cell position is modelled as the centre of mass of the cell. In other words, the cell is a point in 3D or 2D space, which can respond to changes in its environment. These models are successful for investigating the dependency of cell motility on extracellular properties (137), and the rates of environment remodelling by the cell (Figure 1.10A) (138).

When multi-cellular systems are to be investigated in cell centre of mass models, principles of contact theory can be utilised to allow each cell the space to accommodate its mass, which is a simple form of morphology definition (135, 139). Here, the cells are defined by their centres and radii, and they can be assumed to be circular/spherical, or morphology information can be enhanced by ellipse/ellipsoid definitions (Figure 1.10B). Studies of *Dictyostelium dicoideum* demonstrate a good example of modelling the cell morphology in this approach, where cells are represented as ellipsoids in three dimensions. Under the influence of external signals,

the cells regulate their orientation and have chemotactic response (139). In models based on contact theory, the current distance between the centre of masses of any two cells and the sum of their corresponding radii is used to calculate the contact area (Figure 1.10B). Although well established for the calculation of the contact area between two bodies, multi-body contact area calculations are prone to errors in this approach. An alternative modelling technique yielding contact zone geometries in cell centre of mass based models is to employ Voroni diagrams constructed from the cell centers, from which to calculate contact areas (Figure 1.10C). Although effective in modelling cell-cell contacts in densely packed systems, this approach has a very high error margin for cells that are not in immediate contact with their closest neighbours. There are examples in the literature, where a hybrid methodology of contact theory and Voronoi tessellation has been used to accurately model cell-cell contacts. In dense zones the contact areas are obtained *via* the Voronoi diagram, while areas from contact theory are utilised at smaller contact zones (135).

Models combining cell centre of mass with a simple morphology definition *via* cell radii are not limited to multi-cellular systems. A 2D model of *Dictyostelium dicoideum*, where the cell is modelled as an ellipse and the rhythmic cell contractions have been modelled as shrinkage and growth of the ellipse radii, proven to be very informative on adhesion dynamics of the system (140). Indeed, this model of cell motility with simple morphology incorporation was successful in explaining the preferential motility of the *Dictyostelium dicoideum* cells towards stiffer ECM.

1.6.2.2 Cell Centred Models: Advanced Flexible Morphology

Increasing detail in the definition of cell morphology brings a distinct separation in modelling methodologies: grid-based and continuous models. Grid-based models define cell shape as a set of points the cell occupies on the grid. These models are computationally less expensive than models employing continuous methodologies but have certain limitations in their representation of cell shape. One clear example is the lack of surface curvature information for a grid-based model of the cell, and the change of circumference (2D) or surface area (3D) depending on the orientation of the cell in the environment (136). On the other hand, depending on the system of interest, the benefits of the computational

efficiency can be higher than the loss of information due to the listed shortcomings of grid-based approaches. Moreover, parallel to the stochastic cell movement modelling being incorporated into continuous tumour environment models (136), a number of continuous properties of extracellular environment can be included in grid-based models. Indeed, grids on which the cell morphology is defined, are mostly used for the solution of ordinary or partial differential equations, defining for example, properties such as nutrient gradients. A good representative, and one of the most well known, of the grid based modelling frameworks is the Cellular Potts Model (CPM). In CPM, each grid point within the simulation environment defines part of a cell or the extracellular medium. All cellular properties, such as volume conservation or chemotactic response are defined by energy terms, and the overall system is simulated towards a lower energy state. Taking its roots from ferromagnetism, CPM defines the shape changes and emerging movement of the cells *via* probabilistic ”spin flips”. Spin flips are trials for each grid point to copy itself to a neighbouring grid point. The acceptation or rejection of the trial depends on the energy change of the system associated with the copy event. This modelling technique have been used to investigate a range of biological phenomena from crawling of a single keratocyte (141), to investigating motility of T-cells in a multi-cellular environment on the scale of thousands of cells and a complex ECM (Figure 1.11) (142).

For non-grid based methods, cell morphology can be introduced *via* defining sub-cellular agents; representing the cell as an elastic or viscoelastic element network; or solving the partial differential equations defining the cell shape in continuous space. The approaches where the cell is defined by a number of sub-cellular agents; and where it is postulated as a network of elastic/viscoelastic elements; are similar at the basics. They both generate cell morphology and emerging motility *via* solving for the positions of vertices forming the cell, depending on the governing equations that define the interactions between cell subsections. In a sub-cellular agent model, the vertices are the agents themselves, while in a network model the vertices are the junction points of the elastic/viscoelastic elements forming the network.

In most of the sub-cellular agent models, the agents undergo random motion,

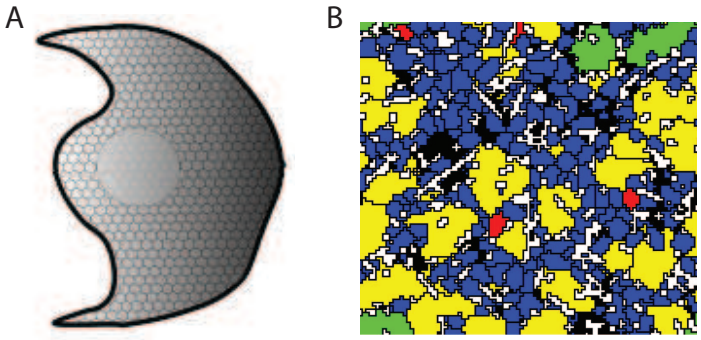

Figure 1.11: A) Schematic of a keratocyte crawling, modelled on a hexagonal grid using the Cellular Potts Model (CPM). Gray scale represents F-actin distribution, darker the colour, higher the catin concentration. Image taken from (141). B) Cross-section of a snapshot from a 3D simulation of a lymph node using an orthogonal grid. The ECM is in black, reticular matrix in grey, dendritic cells in green and yellow, T-cells in red and blue. Image taken from (142).

with some constraints from equations governing motion of different parts of the cell body (143). As an example, cell surface nodes can have stronger interactions with neighbouring cell surface nodes, compared to cell interior nodes, representing the surface tension of the cell from the plasma membrane and F-actin cortex. Similarly, interactions with the environment can be defined individually for different sub-cellular agent types, for example cell surface nodes forming adhesion with the ECM (144). In other words, the agents are under the influence of stochastic fluctuations, and active forces depending on their position within the cell and the cell's environment. These approaches have been used to model streaming profiles of chemotaxis in epithelial sheets, movement of platalets in blood, and cellular microrheology (Figure 1.12A) (143–145).

Models where the cell has been postulated as a network of elastic/viscoelastic elements can take many forms. Shape can be represented with a range of nodes, from multi-cellular systems with a small number of nodes per cell to high resolution networks for a single cell. The cell interior can be included in the network, or the effects of the bulk cell body can be introduced through continuous definitions, with a detailed representation of the cell boundary: the F-actin cortex and the plasma membrane. Modelling methods to ascertain the effects of the environment upon a cell can vary from the use of a simple damping factor to the incorporation of com-

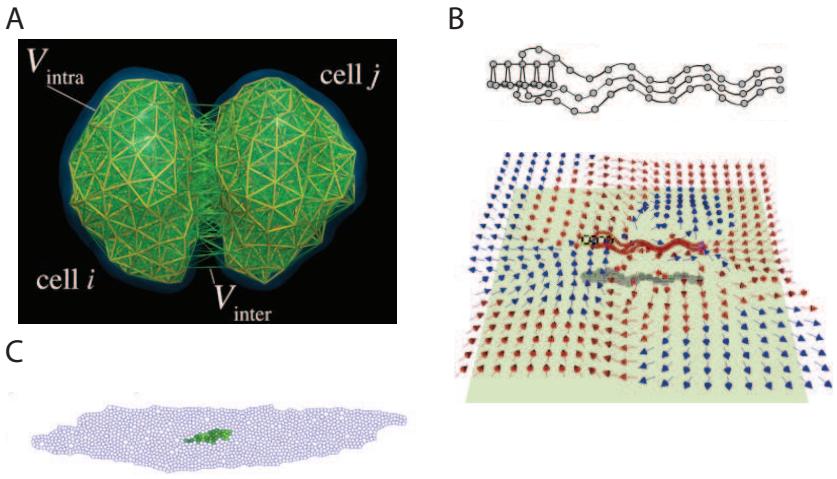

Figure 1.12: A) Modelling of two cells in contact with a sub-cellular element agent modelling approach. Image taken from (145). B) Top, schematic of the model for bacteria swimming, with a simple network definition of the cell body and flagella. Bottom, the flow field of the fluid in the vicinity of the bacterium. Images taken form (146). C) Vertex model of *Drosophila* wing disc (147). Image courtesy of Dr.Yanlan Mao.

plete fluid dynamics in continuous space. The decision on the level of resolution, and degree of model sophistication, is purely dependent on the biological system to be modelled and the question(s) the model intends to seek answers to.

A published model of bacteria swimming is a good example for a system where the cell body is defined in low resolution, while the dynamics of the cellular protrusions driving motility and the dynamics of the extracellular environment are implemented (146). Although the cell body and flagella shape of the bacterium are almost rigid in this model, the motion of the flagella is modelled in detail, together with the motion of the surrounding fluid (Figure 1.12B). Albeit with low levels of flexibility, incorporation of the cell body and flagella morphology reveals detailed information on the flow fields in the immediate neighbourhood of the cell. Another well-established method where the cells are represented by a low number of nodes connected with elastic elements are the vertex based modelling of multi-cellular environments. In this approach, each cell is defined by a set of vertices in either 2D or 3D, with the links between intercellular vertex couples representing the contour of the two cells in contact (Figure 1.12C). As with the Voroni diagram-based methodology described above for modelling multi-cellular systems, this approach

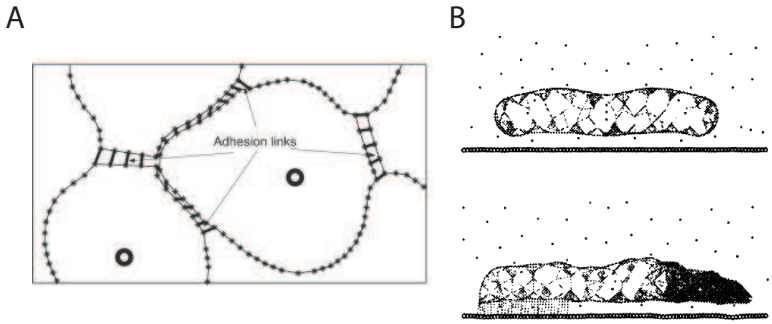

Figure 1.13: A) Immersed boundary model of tumour growth, with each cell defined as a contour of elastic elements. Image taken from (148). B) Immersed boundary method defining an amoeboid cell cytoskeleton, boundary and interior, as a network of elastic elements. Top frame: resting cell; bottom frame: protrusion extension. Images taken from (14).

is more successful in densely packed tissues as it does not allow gaps between cells, therefore, the method cannot be called upon to model single cell motility or the motility of small cohorts of cells. On the other hand, this method has proved to be particularly useful in modelling tissues of packed cells, such as epithelial sheets, and has been rigorously used in clarifying the forces at play in development (147).

Progressing further up the cell morphology complexity scale, the cell can be modelled as a network of elastic elements with properties that allow for significant deformations in cell shape. One of the key studies at this complexity level investigates crawling of nematode sperm cells on surfaces (13), which in essence is a simplified biological system for polymerisation based motility, similar to amoeboid spreading motility discussed in Section 1.5.1, if not using actin but major sperm protein. This model has a simplified interaction with the environment, where adhesions to the underlying surface function as dampers. For biological problems that require a more detailed representation of the fluid environment, immersed boundary models are postulated. This methodology is most suitable for systems where the cell behaviour is closely linked with the hydraulics of the surroundings. Immersed boundary models define cells as a network of elastic elements embedded in the viscous fluid of the medium. This methodology have been used in both modelling of multi-cellular systems defining each of the cells as a contour of elastic linkers (Figure 1.13A) (148), and modelling the motility of a single amoeboid cell,

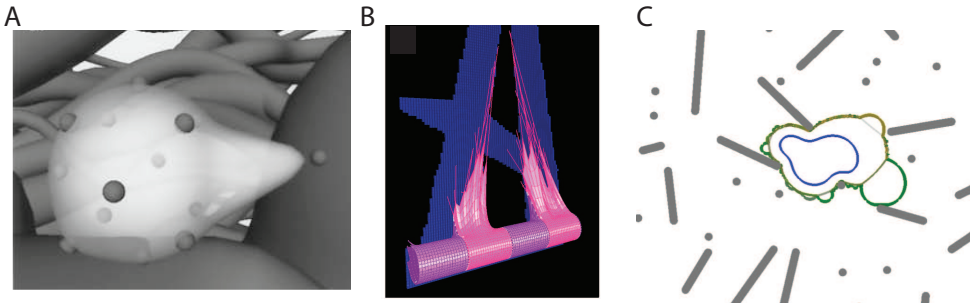

Figure 1.14: A) Snapshot from the model of amoeboid motility with pseudopod elongation. The cell is represented as a network of elastic elements, with pseudopod initiation restricted to eight points on the cell surface (marked in dark grey. Image taken form (151). B) Model of angiogenesis, with cell-cell signalling and filopodia formation. Tip cells in light pink. The pathways cells can elongate and move along are marked in blue. Image taken from (152). C) A multiscale model of single cell motility, the subject of this thesis. The cell cortex is represented with overlaid F-actin in green, myosin in red and plasma membrane in grey. Nuclear lamina is in blue. ECM filaments are shown in grey.

where the whole cell body, including the cell interior, is modelled as an elastic element network (14) (Figure 1.13B). Although there are complications with the fluid flows through the cell boundaries, this approach is particularly useful for systems where interactions of the cell with the flow in the environment are under investigation, such as leukocyte rolling and adhesion in blood vessels (149, 150).

Following the introduction of cell body flexibility, network models of cell motility can incorporate explicit definitions of cellular protrusions, such as filopodia, pseudopodia, and plasma membrane blebs. A limited number of such studies can also include an explicit definition of the ECM, with individual filaments or migration pathways defined. A model of amoeboid cell motility with pseudopod formation, in an environment of explicitly defined ECM fibres, has been used to reproduce the random walk of amoeboid cells (Figure 1.14A) (151). This study defines the cell boundary as a network of springs. There are strict limitations on the position of protrusion initiation on the cell surface, and the cell can have only one protrusion at a time. Albeit the limitations, the framework is open to improvement, and a suitable starting point for modelling of amoeboid motility. Preceding this model, in a study focusing on angiogenesis, flexible cell morphology, filopodia

formation and explicit definition of pathways for the cell to crawl on have been incorporated into a single model (Figure 1.14B) (152). This model is distinct from the models described above, in that it incorporates an agent based definition of cell shape on a grid, with cell shape change constraints by elastic linkers in continuous space. Protein levels regulating filopodia formation and cell-cell signalling are simulated *via* the agents defining the cell on the grid, while the forces regulating the changes in cell shape are simulated *via* the positions of the agents in continuous space. The model predicts the patterning of endothelial cells *via* cell-cell signalling, the movement of cells forming new blood vessels, as well as the morphology of the new blood vessel.

One last example for defining the cell as a network of viscoelastic elements comes from the study presented in this thesis. In this model, the cell contour is represented as a set of agents linked with viscoelastic elements (Figure 1.14C). Similar to grid-based agents of the angiogenesis model described above, the model simulates the protein levels over the agents. Here the whole system, including the agents are moved in continuous space. The protein levels regulate many processes included in the model, such as cell–ECM adhesion, actin polymerisation based protrusion formation, plasma membrane blebbing and local myosin II driven contractility. The ECM filaments are explicitly defined, and the roles of both the geometry and rigidity of filaments are investigated together with a range of intracellular states and polarities. A detailed summary of this model is given in Section 1.6.3, and Chapter 2 describes the development of the model.

Finally, cells can be modelled free from postulation of a network, by either sub-cellular elements or elastic/viscoelastic network models. In such an approach, the dynamics of the cell body are defined by governing ordinary or partial differential equations, and the equations are solved by finite element methods to generate the dynamics of the cell shape and motility. This approach have been used to investigate the possible mechanisms of leukocyte motion in capillaries, namely cytoskeleton-membrane interactions in terms of polymerisation, or cytoskeleton-cytoskeleton interactions in terms of swelling (Figure 1.15A) (153). Recently, the same research group have also produced a modelling framework for cell shape determination for a crawling cell (15) (Figure 1.15B). This form of modelling is

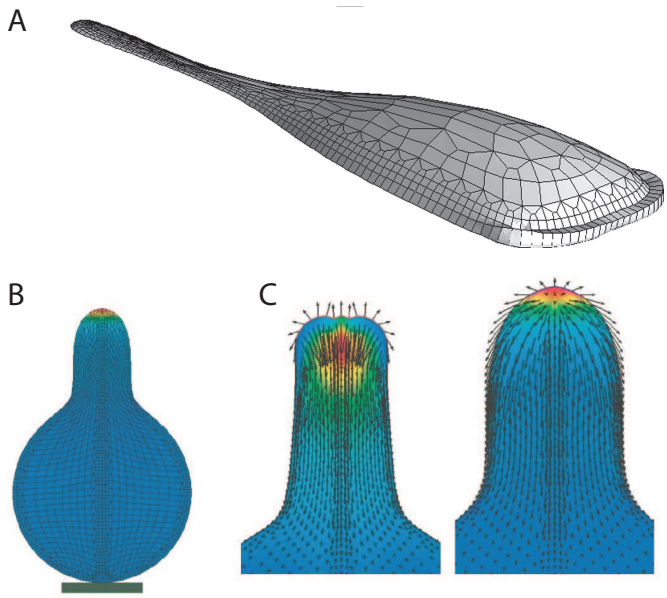

Figure 1.15: A) A finite element model (FEM) of a crawling cell on a flat surface. Image taken from (15). B) Preceding versions of same model in 2D, applied to model pseudopod elongation. Actin intensity is colour coded in the image; red high, blue low. Image taken form (153). C) Same cell and colouring scheme as for B, left: model for elongation of pseudopod by actin polymerisation model, right: model for elongation by F-actin network swelling. Image taken from (153).

particularly successful for understanding the contribution fluid-like behaviour of the cytoskeleton and cytoplasm make to cell motility and morphology changes. On the other hand, in this methodology, complex extracellular matrix geometries require complex boundary conditions for contact zones, and the computational load increases significantly.

1.6.2.3 Cell Centred Models: Bits and Pieces of the Cell

In the pursuit of understanding the underlying mechanisms of different cell motility modes, mesenchymal, amoeboid spreading and amoeboid blebbing, specific phenomena have been investigated detached from the actual movement of the cell, and sometimes detached from the whole cell body. There have been several studies investigating protrusion/retraction of filopodia and lammellipodia without including the cell body into the model (154). The formation and dynamics of plasma membrane blebbing too have been modelled in this manner. For example, the roles of actomyosin contractility in plasma membrane bleb formation have been studied by an analytical analysis of the cell body. These analyses provided accurate predictions of actomyosin cortex tension thresholds for bleb formation, but lacked simulations of bleb growth dynamics and cell movement (27). Single bleb models have also been constructed, which have proven useful in interpreting fluid flow, both within the bleb and cell body, upon bleb expansion and retraction. (155). In an sub-cellular agent based model of blebbing, the roles of contractility and excess membrane have also been investigated, albeit with limited biological relevance (156).

In detailed models of lammelipodia and filopodia formation, individual actin filaments in assembled bundles and individual branched actin filaments have been investigated. Models of single filopod growth have been utilised to probe the rate of elongation, and thermodynamic limits of an unsupported filopod's geometry. For instance, minimum and maximum number of actin filaments in a filopod have been shown to be limited respectively by buckling under membrane tension and insufficient G-actin diffusion to sustain growth (63). The same study revealed, in between the limitations of buckling and G-actin availability, an unsupported filopodia can grow up to approximately ~2 μm. A similar study emphasised the role of retrograde flow in filopodia protrusion, suggesting myosin generated tension and

associated retrograde flow as an important mechanism regulating protrusion rates (157). Models of lammelipodia growth showed the mechanical load of protrusion elongation is overcome by the collective performance of the branched filaments, and that the flexibility of the membrane contributes to the stability of growth (158). Another study successfully produced the experimentally observed force velocity relationship of lammelipodia growth - the growth rates of these protrusions under an opposing external force (154). This work highlighted the role of crowding effects amongst the branched actin filaments of lammelipodia, where branching of the filaments and the necessary volume exclusion leads to swelling of the F-actin network, thereby significantly contributing to protrusion elongation.

Models of actin polymerisation based protrusion formation, and elongation have been combined with ECM adhesion models. In such a study, the mode of interaction of the protruding filopod is shown to be linked with the stiffness of the underlying substrate (159). Stiff substrates allow for rapid accumulation of tension at adhesion points, leading to detachment of engaged bonds. Meanwhile, flexible substrates lead to slow tension accumulation, which provides the timeframe for multiple bonds to engage with the substrate, decreasing the load on any single bond, and hence reducing the likelihood of detachment. On a related topic, analogous modelling of stress fibers revealed myosin generated tension on these fibre prevents crack like propagation of detachment form the ECM (160).

Analytical models have been used to probe plasma membrane blebbing process, revealing the importance of myosin II generated contractility, and the interplay between myosin and the F-actin cortex–plasma membrane linker dynamics. Relating the pressure generated in a cell of given dimensions to the cortical tension *via* Laplace's Law (Eq. 1.1), the threshold tension on the actomyosin cortex for initiation of a membrane bleb have been calculated in the range ~200 $pN\mu m^{-1}$; this value has been subsequently validated by experimentation to be in the range 200-240 $pN\mu m^{-1}$ (27). Another analytical bleb dynamics study, on *Entamoeba histolytica* revealed that cyclic blebbing under micropipette suction occurs as a result of the interplay between tension accumulation rate, and F-actin cortex plasma membrane linker accumulation rate, at the F-actin cortex (102). The tension necessary in bleb formation due to cortex rupture has also been analytically investigated (99).

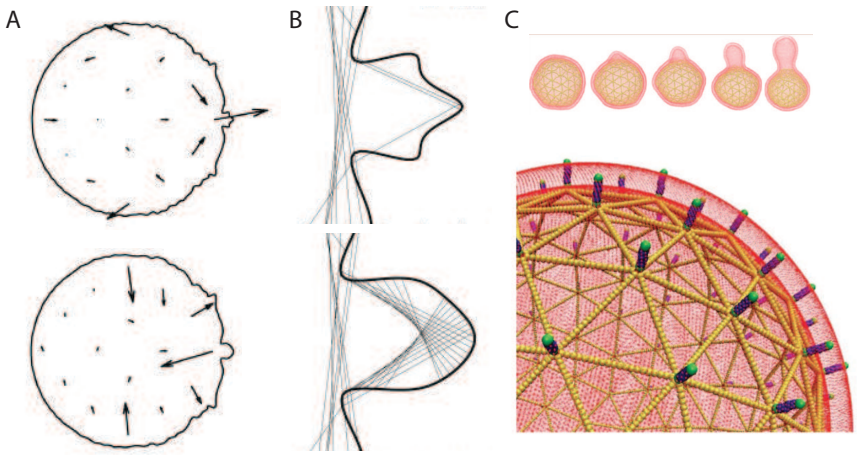

Figure 1.16: A) Model of plasma membrane blebbing, where the cell membrane is modelled with taking into account the influence of the intracellular flow and forces generated by the F-actin cortex. Top: plasma membrane expansion; bottom: plasma membrane retraction. Arrows represent the fluid flow. Image taken from (155). B) Close-up view of A, elastic elements modelling the F-actin cortex can be seen. C) Particle based model of plasma membrane blebbing. Top: Expansion of a bleb. Bottom: Close-up view of the model setup. Lipid particles shown in red, cortex particles in yellow, linker particles in blue and green. Images taken from (156).

Only two model frameworks are currently available that include the simulation of plasma membrane dynamics. One such model approaches the blebbing problem in a similar methodology to the immerse boundary framework discussed above. The study investigates the dynamics of a single bleb that is initiated at a selected point, and reveals useful insights into the dynamics of the pressure profiles and G-actin concentrations during bleb expansion and retraction (Figure 1.16A) (155). However, there are simplifications of this model, that will have significant influences on the dynamics of the bleb growth, such as the deterministic and symmetric definition bleb neck growth.

The second available study on simulations of plasma membrane blebbing adopts a particle based approach (156). The model includes three sets of particles, lipids of the plasma membrane, cortex subunits, and plasma membrane-cortex linkers. The plasma membrane particles themselves are formed from hydrophilic and hydrophobic subunits. The model is constructed in three dimensions (Figure

1.16B). Albeit the detailed definition of the sub-cellular elements, this study fails to capture a biologically relevant conclusion. Volume effects are not included in the model, and the key parameter determining blebbing dynamics have been identified as the ratio of the available membrane to the size of the cell: An excess amount of membrane leads to stretching of the underlying cortex, force accumulation on the linkers, and initiation of a membrane bleb (156). Both of the models discussed above for plasma membrane blebbing do not include the cell motility aspect or the interaction of membrane blebs with the surrounding extracellular environment.

1.6.3 A Hybrid Agent Based/Viscoelastic Network Approach

Multitudes of modelling techniques, a subset of which are listed above, are available to investigate any selected biological phenomena. Although the choice of the most suitable technique is not always apparent, the list can be narrowed down focusing on the needs of the problem at hand. To investigate the relative efficiency of different cell motility modes, a detailed definition of cell morphology is necessary. The motility modes of the cell strongly depend on ECM geometry, therefore, a study aiming to dissect the modes of cell motility needs to incorporate complex ECM geometry. A continuum model would not be of interest as the aim is to investigate the motility mode of each cell. Low detail morphology models would not be sufficient for the aims of this study, and a continuous definition and solution of the governing PDEs of the cell shape would become overly expensive with the explicit definition of ECM filaments. Hence the possible methods suitable for the aims of this thesis are reduced to viscoelastic element network models or sub-cellular element modelling techniques. Here, the properties that are necessary for the investigating a continuous spectrum of motility modes are obtained by merging these two approaches, into a multiscale model of cancer cell motility.

In the model, the cell cortex and the nucleus are defined as sets of agents connected by viscoelastic linkers. Protein levels, namely F-actin, myosin, cortex-membrane linkers and cell–ECM adhesion proteins, are recorded at each agent. The dynamics of local protein levels regulate the properties of the viscoelastic linkers, making it possible to define local heterogeneities of the cell surface. The effects of the internal cell body, cell cytoskeleton and cytoplasm, are taken into account as internal pressure regulation and a viscous drag, in the model. As the

aim of the work reported in this thesis is to investigate the roles of these protrusions under a multitude of intracellular and extracellular conditions, the dynamics of actin polymerisation-based protrusions are simplified compared to some of the finer detailed models discussed above. Similarly, the fluid effects on the plasma membrane bleb dynamics are simplified compared to the study investigating single bleb formation with fluid dynamics of the cytoplasm. This simplification is essential, since the presented study investigates the dynamics and roles of multiple plasma membrane blebs, in the context of how a cell navigates the ECM, with a highly flexible morphology; and a detailed fluid dynamics model would simply be computational intractable. On the other, the presented model has detailed stochastic dynamics of membrane bleb formation, bleb neck growth, interactions with the environment, and bleb retraction, that is not available in previous models. The analysis includes a range of intracellular states, in terms of overall contractility and cell–ECM adhesion; and a range of cellular polarities, in terms of contractility and F-actin cortex plasma membrane linkers. A series of snapshots of the model within an *in vivo* mimetic environment is given in Figure 1.17.

To be able to quantify the effects the ECM geometry has upon the motility, an explicit representation of the ECM fibres is selected, rather than a continuous representation as a concentration. A range of ECM geometries are investigated, from single and double surfaces, to *in vivo* mimetic topologies generated in the light of experimental measurements of interstitial collagen matrices in mice.

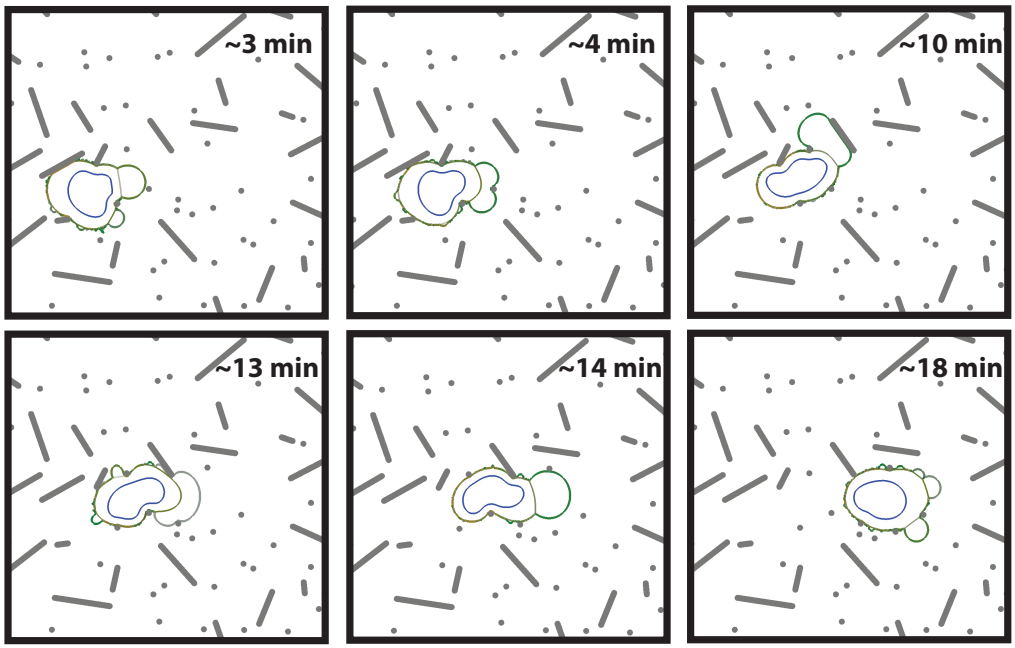

Figure 1.17: A melanoma (A375M2) cell simulated in an *in vivo* mimetic environment, with 40 percent increased contractility at the cell rear and 30 percent reduced cortex-plasma membrane linker strength at the cell front. F-actin cortex in green, myosin intensity in red, plasma membrane in grey. The colors are overlayed during visualisation of the model cell. The explicit ECM filaments in grey. Approximate times of the frames are indicated on each image. An protrusion unable to reach an ECM filemant can be seen in the snapshot at 3 minutes, the different stages of blebs and the behaviour of the bleb necks are visible in all frames. The frame at 13 minutes shows a bleb in expansion state before actin accumulation has started. Frame at 18 minutes shows three blebs at the cell front, at different actin accumulation states.

Chapter 2

Model Construction

2.1 Introduction

This chapter presents the detailed methodology of the single cell model of cancer cell motility. The model incorporates changes in matrix geometry, and rigidity of the ECM filaments, together with a complex cell. The model cell has flexible morphology, local cortex heterogeneity, actin polymerisation based protrusions, plasma membrane blebs, and variable cell–ECM adhesion strength (Figure 2.1). The cell is modelled as a set of agents, linked with viscoelastic elements representing finite segments of cell body.

The viscoelastic F-actin cortex is modelled as a Kelvin-Voigt body, resisting stretching/compression scales and rates. Myosin generated compression is introduced as a parallel spring of zero ideal length. Levels of key proteins are recorded on the agents, and the protein levels feed back to local properties of the linkers. For example, the average myosin concentration of two linked agents determines the strength of the myosin spring in between them. The plasma membrane resists stretching when the total cell surface rises above the available membrane pool limit. The bending resistance of the cortex and the membrane is also included. The cell interior behaves as a viscoelastic material and the action of the cortex coupled to the plasma membrane generates internal hydrostatic pressure. The cell nucleus is defined with a similar setup to the cell cortex and internal cell body, with different parameters values: the nucleus is more rigid than the cell cytoskeleton, and nuclear lamina is stiffer than the cell cortex. Throughout each of the simulations, agents are added and deleted from the cell surface to ensure homogenous discretisation

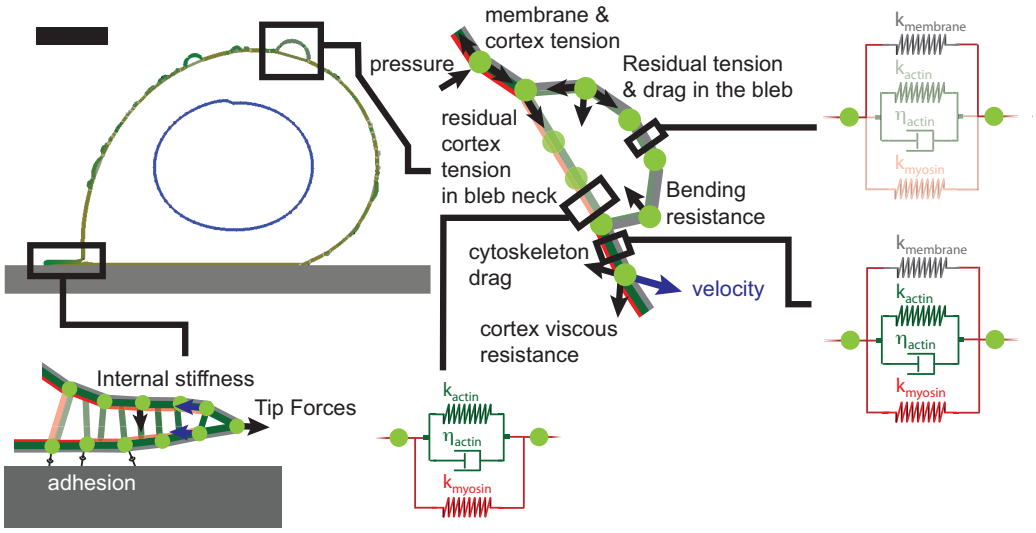

Figure 2.1: Schematic of the modelling framework displayed on a model snapshot, scale bar 5 μm. The actin cortex is represented by a Kelvin-Voigt body (green). The myosin driven contractility (red) ane membrane tension are modelled as parallel springs (grey). The agents are moved in the over-damped system, under the influence of cortex forces, intracellular pressure, and viscous damping from both cytoskeleton and cortex.

of the cell surface by the agents. In other words, the agents are deleted from regions where agent density reaches above a given threshold, and are added to regions where agent density is below the lower threshold. To ensure agent number modifications do not effect the dynamics of the system, upon each addition and deletion event, the protein concentrations, and ideal length of F-actin linkers are redistributed in the modified region.

F-actin protrusions are initiated stochastically, with a probability dependent on local myosin concentration. During un-supported growth, their probability for termination of elongation is constant; on the other hand, if a protrusion starts spreading on a surface, the probability of termination is significantly reduced. When an F-actin protrusion stops elongating, it begins to retract back into the cell body, *via* the forces generated by the accumulating myosin that arrives inside the protrusions with normal diffusion rules.

When the hydrostatic pressure inside the cell exceeds the local strength of cortex-membrane linkage at any point on the cell surface, the membrane detaches

from the cortex, forming a plasma membrane bleb. Membrane blebs grow with the hydrostatic pressure pushing the detached patch. The membrane can be torn of the cortex at bleb borders, facilitating the growth of bleb necks, if the pulling of the detached membrane together with the pressure is higher than local adhesion forces. The expansion phase of a bleb is followed by new F-actin polymerisation underneath the detached membrane along with depolymerisation of F-actin at the bleb neck, the rates for which are fitted to experimental data. Once a new F-actin cortex starts to form, a bleb can form adhesions with the environment, but not during the expansion phases.

The model cell is placed in a variety of ECM geometries. The interaction of the cell with the ECM filaments is defined by probabilistic adhesion/detachment events and volume exclusion. The geometries of *in vivo* mimetic environments are generated based on intravital imaging data of interstitial collagen of mice. The ECM filaments themselves are viscoelastic materials, modelled as a network of elastic elements able to move and change the filament shape according to forces imposed upon them, against the viscous drag of the material.

2.2 Actomyosin Cortex and the Membrane

2.2.1 Viscoelasticity of the Actin Cortex

In differential constitutive models of viscoelasticity, the stress and strains at a given time t, are combined using constant coefficient linear differential equations. Combining elastic elements (springs, Figure 2.2) and viscous elements (dashpots, Figure 2.3), in series or in parallel, one can obtain the differential model for the desired specific rheological phenomena (161). The selected model for the scope of this study needs to capture the complex viscoelastic responses of the actin cortex, while remaining simple enough to be solved simultaneously for each finite segment of the cell in the model.

The stress strain relationship for the spring as defined by Hooke's Law (Eq.2.1),

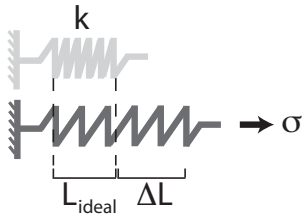

Figure 2.2: Elastic element - Spring. k represents the spring constant, and σ represents the stress.

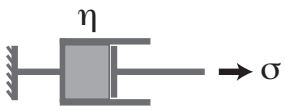

Figure 2.3: Viscous element - Dashpot. σ is stress, and η is the Newtonian viscosity.

where σ is stress, ε is strain and k is the spring constant:

$$\sigma = k \times \varepsilon. \tag{2.1}$$

For a dashpot the relationship follows Newton's Law (Eq.2.2), η being the Newtonian viscosity:

$$\sigma = \eta \times \frac{d\varepsilon}{dt}. \tag{2.2}$$

The success of the resulting rheological behaviour in modelling viscoelastic creep, time dependent increase in strain of viscoelastic materials under constant stress; viscoelastic recovery, the partial recovery of the creep upon release of the stress; and relaxation, time dependent decrease in stress under constant strain; will depend on the selection and combination of these basic elements (161).

2.2.1.1 Maxwell Material

The Maxwell material consists of a dashpot and a spring in series (Figure 2.4).

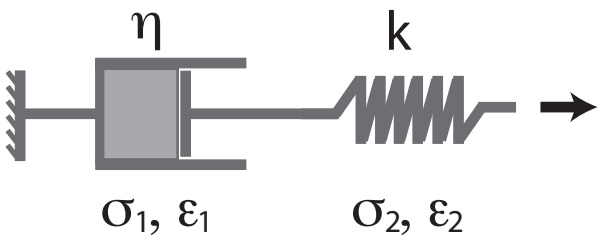

Figure 2.4: Maxwell model of viscoelastic response. η is the Newtonian viscosity of the dashpot, k is the spring constant, σ is the stress and ε is strain. The subscripts 1 and 2 represent the dashpot and the spring, respectively.

The stress of the two elements, spring and the dashpot, are equal in a Maxwell material. The corresponding stress and strain are:

$$\begin{aligned} \sigma &= \sigma_1 = \sigma_2 \\ \varepsilon &= \varepsilon_1 + \varepsilon_2. \end{aligned} \tag{2.3}$$

Using Eq.2.1 and 2.2 with Eq.2.3, the stress-strain relation for a Maxwell material becomes:

$$\frac{d\varepsilon}{dt} = \frac{1}{k} \times \frac{d\sigma}{dt} + \frac{1}{\eta} \times \sigma. \tag{2.4}$$

Under sudden deformation, and constant strain ε^0 thereafter, the stress in a Maxwell material decays with a characteristic time of η/k (Eq.2.5):

$$\sigma(t) = k\, \varepsilon^0 e^{(-\frac{k}{\eta}t)}. \tag{2.5}$$

Upon release of the element at any given time t_1, the elastic element will return to its original length, causing a length change given in Eq.(2.6), the viscous element will not return to its original length, leaving the Maxwell material with a plastic deformation as given in the following:

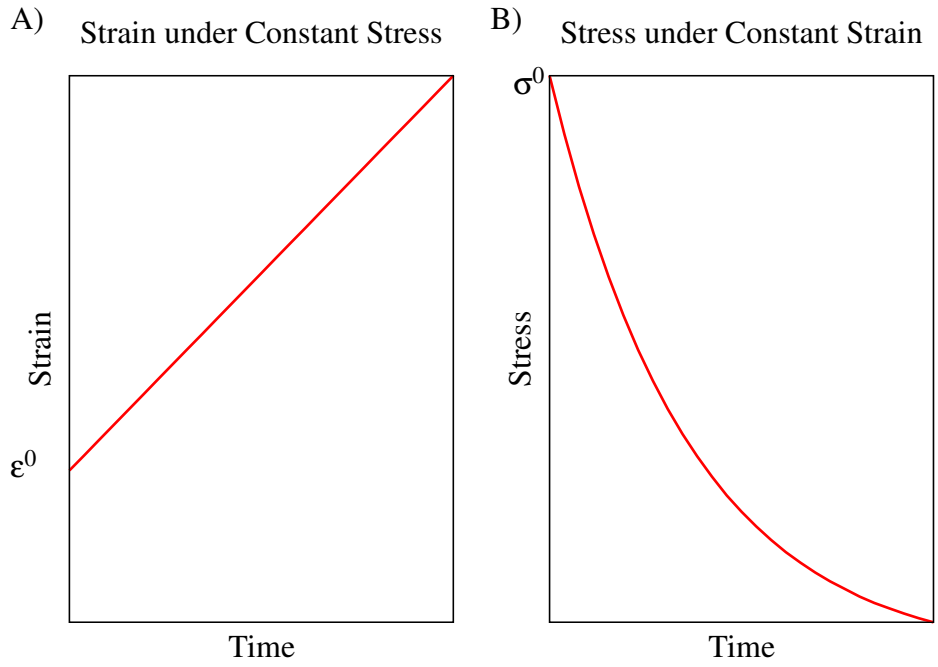

Figure 2.5: Maxwell model time responses. A) Strain under constant stress (creep), B) Stress under constant strain (relaxation).

$$\Delta\varepsilon = -\frac{\sigma(t_1)}{k} = \varepsilon^0 e^{(-\frac{k}{\eta}t)}$$
$$\varepsilon_{final} = \varepsilon^0\left(1 - e^{-\frac{k}{\eta}t_1}\right). \tag{2.6}$$

If a sudden stress, σ^0, is applied, the Maxwell elastic element (spring) will suddenly deform, while the viscous element (dashpot) will deform over a time period. Strain is a linear function of time in a Maxwell material, hence the material does not exhibit creep behaviour. The time dependent stress and strain curves for a Maxwell material are given in Figure 2.5. The Maxwell model is strong in predicting the relaxation viscoelastic response, whereas it is weaker in modelling creep or recovery.

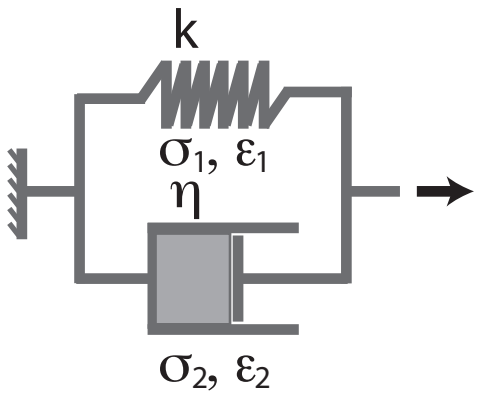

Figure 2.6: Kelvin-Voigt model of viscoelastic response. k is the spring constant, η is the Newtonian viscosity of the dashpot. σ is the stress and ε is strain. The subscripts 1 and 2 represent the spring and the dashpot, respectively.

2.2.1.2 Kelvin-Voigt Material

The Kelvin-Voigt material consists of a dashpot and a spring in parallel (Figure 2.6).

Strain on the elements of the model are equal in a Kelvin-Voigt material. The corresponding stress and strain are:

$$\begin{aligned} \sigma &= \sigma_1 + \sigma_2 \\ \varepsilon &= \varepsilon_1 = \varepsilon_2. \end{aligned} \tag{2.7}$$

Similar to above, using Eq.2.1 and Eq.2.2 with Eq. 2.7, the stress strain relationship for a Kelvin-Voigt material becomes:

$$\sigma = k \times \varepsilon + \eta \times \frac{d\varepsilon}{dt}. \tag{2.8}$$

Under constant strain ε^0, the elastic element in Kelvin-Voigt material results in constant stress, while the viscous element does not contribute to stress. Thus, a constant stress persists on the material, with no relaxation. With a sudden stress applied to a Kelvin-Voigt material, the strain response approaches that of a purely

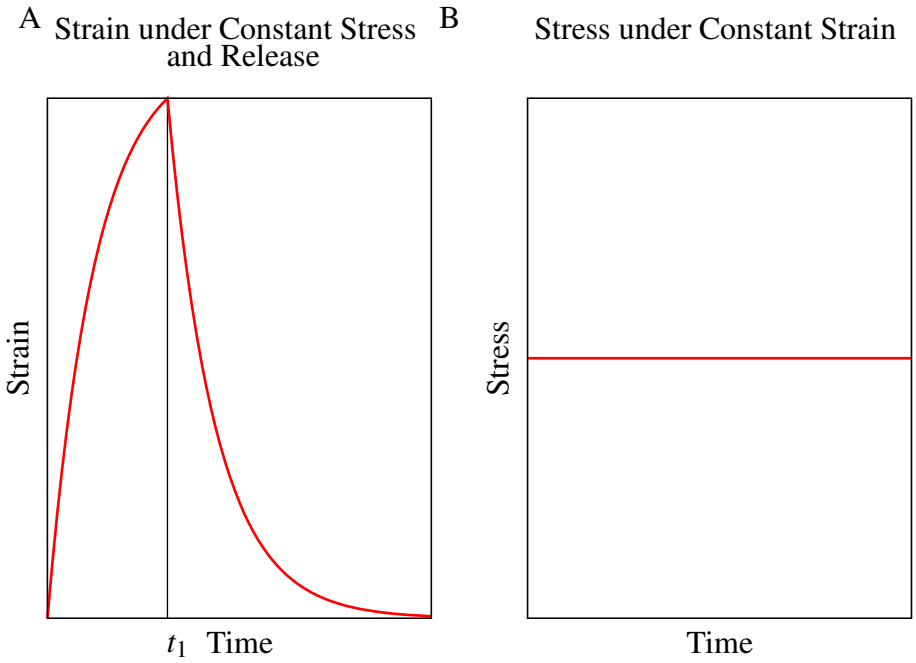

Figure 2.7: Kelvin-Voigt model time responses A) Strain under constant stress (creep) up to t_1 and release (recovery). B) Stress under constant strain (relaxation).

elastic material over time (Eq. 2.9):

$$\varepsilon(t) = \frac{\sigma^0}{k}\left(1 - e^{\frac{k}{\eta}t}\right) \tag{2.9}$$

If the stress is relased at a given time t_1, the material recovers back to its initial length, *via* the response of the elastic element, with no plastic deformation. The recovery follows Eq.2.10:

$$\varepsilon(t > t_1) = \varepsilon(t_1)\, e^{-\frac{k}{\eta}(t-t_1)}. \tag{2.10}$$

The resulting time dependent stress-strain response for a Kelvin-Voigt material is given in Figure 2.7. Kelvin-Voigt materials are successful at representing the viscoelastic response during creep and recovery, but are weaker in modelling relaxation.

2.2.1.3 Model Implementation

Emerging from the internal driving forces of the cell, and the interacitons with the environment; the cortex of the model cell is dynamic and is under constant stress. The ability to represent the dynamic responses under changing stresses are of priority in the model, therefore the viscoelastic actin cortex is represented as a Kelvin-Voigt material. The contribution the actin cortex makes to the dynamics of each linker between agents, is modelled as a Kelvin-Voigt body (Figure 2.1).

The weak aspect of Kelvin-Voigt materials, the relaxation period, is supplemented in the model by defining an actin cortex turnover rate, Eq.2.11. Actin renewal brings the ideal length of the spring defining the elastic response of the cortex to its current length, with a turnover time of τ_a.

$$L_i^{0,t+dt} = L_i^{0,t} + \frac{L_i^t - L_i^{0,t}}{\tau_a} \times dt. \tag{2.11}$$

After addition of actin renewal, under a constant deformed length, L_{def}, the ideal length of the elastic element and the relaxation response of a Kelvin-Voigt body implemented in the model becomes as in Figure 2.8.

The density, and hence the physical response of the F-actin cortex is not uniform in the model cell. The physical properties of the F-actin cortex, the spring constant k_{cor} and the dashpot viscosity η_{cor}, are dependent on the current density of actin at any finite segment of the cortex, represented by each of the Kelvin-Voigt bodies. The strength of spring and the dashpot in each Kelvin-Voigt body is scaled from the resting strengths, with the normalised fraction of actin in the corresponding segment:

$$k_{cor} = k_{cor}^0 \times f_{cor}^0 \tag{2.12}$$

$$\eta_{cor} = \eta_{cor}^0 \times f_{cor}^0, \tag{2.13}$$

where k_{cor} is the current spring constant, and η_{cor} is the current dashpot viscosity for F-actin cortex segment, k_{cor}^0 and η_{cor}^0 are the corresponding resting values, and

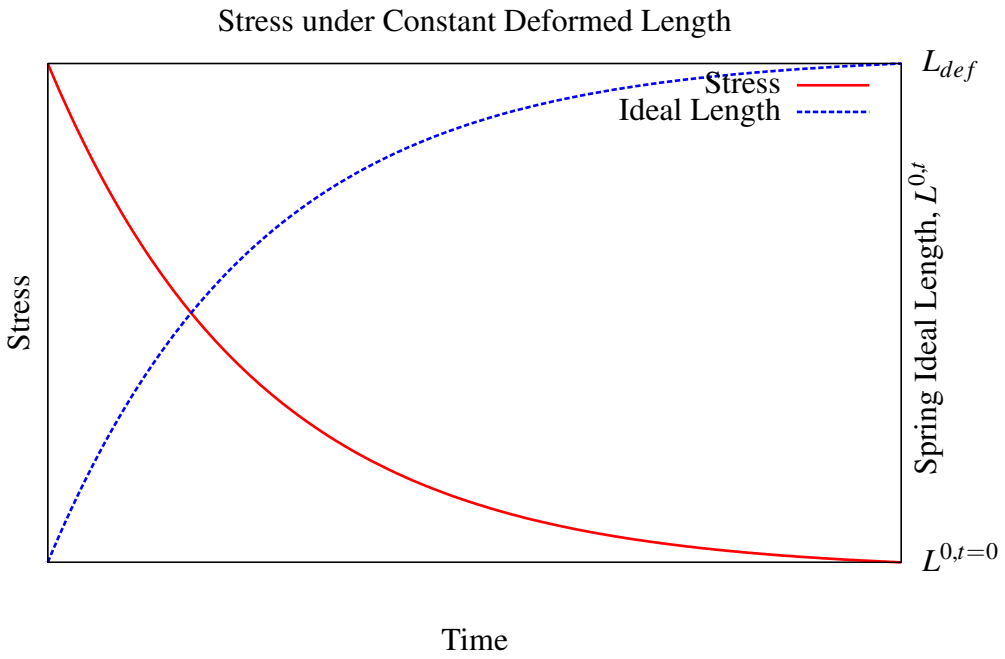

Figure 2.8: The implementation of actin turnover in the model changes the stress response of the Kelvin-Voigt bodies at a constant deformed length. The change in ideal length of the elastic element of the Kelvin-Voigt body relaxes the stress in the system.

f_{cor} is the density of actin in the segment, as normalised to cortex density at the resting state of the cell. The value of f_{cor} is modulated for cortex reassembly at bleb rims, cortex decay at bleb necks, and cortex decay at actin polymerisation based protrusion bases. During cortex reassembly, the value of f_{cor} increases towards the resting value from the initial reduced cortex density of the bleb. During cortex decay, it is reduced towards the value of zero from a resting density. The details of actin density modulation are given is Sections 2.7.1, 2.7.3 and 2.7.4.

2.2.2 Myosin II Driven Contractility

The compression myosin motors generate within the F-actin cortex is modelled as a spring in parallel to each of the Kelvin-Voigt bodies for finite segments of the cortex (Figure 2.1). The strength of the myosin spring is dependent on the local concentration of myosin in agents on either side of the spring:

$$k_{myo} = k^0_{myo} \times c_{myo}, \tag{2.14}$$

where k_{myo} is the current myosin spring constant, k^0_{myo} is the spring constant corresponding to the resting state of the cell, and c_{myo} is the average myosin concentration of the two linked agents, normalised to the myosin concentration at the resting state.

The concentration of myosin in any given agent is modulated upon state changes of the cell surface segment, and is updated according to the equilibrium concentration of myosin signalled at that point on the cell cortex. For instance, a blebbing surface loses all myosin II activity, setting the concentration of c_{myo} to zero at all agents that are parts of an expanding bleb; and the actin polymerised at the tips of an actin polymerisation based protrusion is devoid of myosin initially. The concentration of myosin is updated in the agents as myosin diffuses from the cytoplasm, into the cell cortex segment. Using the Fick's Law to model the flux of myosin molecules from the cytosol to the cortex, with diffusion coefficient D_{myo}:

$$J_{myo} = -D_{myo}\frac{dc_{myo}}{dx}, \tag{2.15}$$

and discretisation of the Eq. 2.15 with h for cortex thickness, and defining the effective diffusion constant $D_{eff} = D_{myo}/h^2$, the myosin update function is obtained

as:

$$\frac{\Delta c_{myo}}{\Delta t} = -D_{myo}\frac{\left(c_{myo} - c_{myo}^{eq}\right)}{h^2}, \tag{2.16}$$

$$c_{myo}(t+dt) = c_{myo}(t) + D_{eff}\left(c_{myo} - c_{myo}^{eq}\right)dt. \tag{2.17}$$

The effective myosin diffusion constant represents the sum effect of diffusion and activation for the accumulation of active myosin II at the cortex, depending on the concentration in the cytoplasm, at the vicinity of the segment of interest. c_{myo}^{eq} is a local property. It is dependent on the overall contractility of the cell, the state of the agent – set to zero for expanding blebs and protrusion tips – and the position of the agent on the cell cortex, together with the postulated polarity of the cell. In a working example, in a cell with twenty percent increased overall contractility with respect to the resting control state, and a polarity of twenty percent increased contractility at the cell rear, the equilibrium myosin concentration of a non-blebbing cortex segment at the cell rear with no protrusion elongation will have c_{myo}^{eq} of 1.44; while a similar agent at the cell front would have an equilibrium myosin level of 1.2. For a detailed definition of polarity as an input to the simulation platform, see Section 2.10.2.

2.2.3 The Plasma Membrane

The plasma membrane is a layer phsically covering the actin cortex, and thus, the tension from the membrane is implemented as a spring, in parallel to the actomyosin cortex, in each of the linkers defining the cell surface (Figure 2.1). In the resting state of the cell, the membrane is not limited, and its effects on surface tension are neglected. When the surface exceeds the limits of the available excess membrane, tension starts to increase, as the membrane itself starts stretching. Once the membrane pool is depleted, the membrane tension, namely the membrane spring constant, linearly increases, and reaches the rupture threshold within the stretch limit (Eq. 2.18). Here k_{mem} is the current membrane spring constant, k_{tear} the spring constant at tearing, S_{mem}^{pool} the total size of the resting cell membrane including the available membrane pool, $\delta_{stretch}$ the stretch limit of the membrane as a fraction, and S_{mem} the current cell membrane size. δ_{pool} is the step function defining the state of the cell, 1 if the cell exceeds available membrane pool and 0

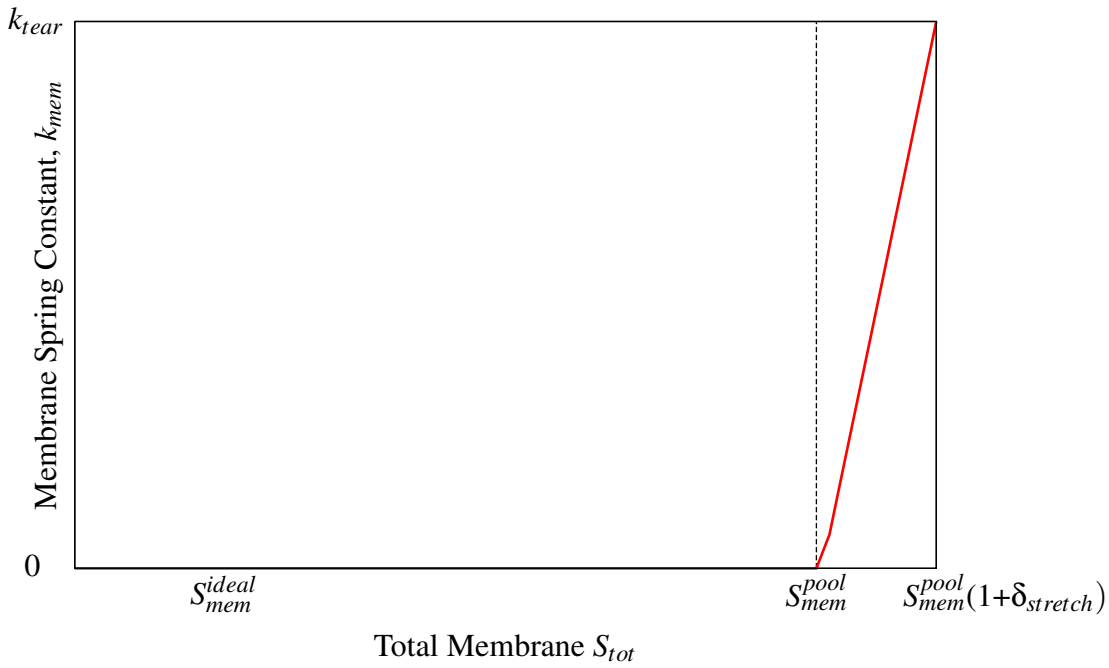

Figure 2.9: Membrane spring constant profile as a function of total cell membrane.

otherwise:

$$k_{mem} = \frac{k_{tear}}{S_{mem}^{pool}\delta_{stretch}} \times \left(S_{mem} - S_{mem}^{pool}\right) \times \delta_{pool}$$
$$\delta_{pool} = \begin{cases} 0 & if \quad S_{mem} < S_{mem}^{pool} \\ 1 & if \quad S_{mem} > S_{mem}^{pool}. \end{cases} \tag{2.18}$$

The exact shape of the increasing function is not of significance, as long as there is a sharp increase from resting state to rupture tension as the total surface area of the cell reaches the rupture stretch limit (15). As referenced in Section 1.3.1.4, the membrane pool is a global property of the cell, and the membrane spring constant is regulated over the whole cell surface, rather than being a local property which was the case for actin and myosin. The resulting membrane spring constant profile of the cell is given in Figure 2.9.

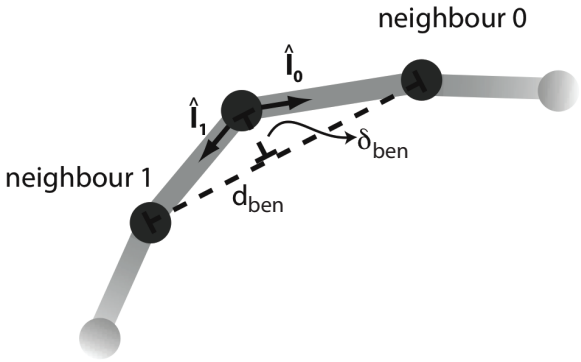

Figure 2.10: Schematic showing the terms used in calculation of the bending resistance. Agents of a non-blebbing cell surface is represented in black, representation of the viscoelastic linkers of actomyosin cortex and membrane are simplified to grey lines. d_{ben} is the distance between the two neighbours of the current agent, δ_{ben} is the agent's deflection, $\hat{\mathbf{l}}_i$ are the unit vectors in the direction of neighbour i of the agent.

2.2.4 Bending Resistance

The forces resisting to the bending of the cortex are calculated over the agents, taking into account the local curvature information. The magnitude of the force for bending of each cell surface segment is dependent on the local bending rigidity, the distance between the two neighbours of the current agent (d_{ben}), and the agent's deflection (δ_{ben}) (Figure 2.10). The direction of the bending resistance force is obtained from $\hat{\mathbf{l}}_i$, the unit vector in the direction of neighbour i of the agent. The force for each agent is calculated as:

$$\mathbf{F}_{BEN} = B_{ben}\frac{\delta_{ben}}{d_{ben}^2}\frac{\sum_{i=0:1}\hat{\mathbf{l}}_i}{\left|\left|\sum_{i=0:1}\hat{\mathbf{l}}_i\right|\right|}. \tag{2.19}$$

For each agent i, a bending force equal in magnitude but opposite in direction is distributed over its neighbours. As calculation of forces continues over all the agents of the cell in each time step, bending forces accumulate on each agent i, and its neighbours, such that:

$$\mathbf{F}^i_{BEN} = \mathbf{F}^i_{BEN} + \mathbf{F}_{BEN} \tag{2.20}$$

$$\mathbf{F}^{i\pm1}_{BEN} = \mathbf{F}^{i\pm1}_{BEN} - \mathbf{F}_{BEN}/2. \tag{2.21}$$

The bending modulus B_{ben}, is linearly dependent on the aforementioned actin cortex fraction, f_{cor}. The magnitude of the bending modulus is obtained from experimental measurements of blebbing and non-blebbing surfaces (35), using the residual cortex fraction at the onset of bleb initiation and the current cortex fraction:

$$B_{cor} = \left(f_{cor} - f_{cor}^{bleb}\right) \frac{B_{cor}^{0}}{1 - f_{cor}^{bleb}} + B_{cor}^{bleb}. \tag{2.22}$$

In the above Eq. 2.22, B_{cor}^{bleb} is the bending modulus of an expanding bleb, f_{cor}^{bleb} is the fraction of residual cortex at the bleb rim at the onset of bleb initiation, and B_{cor}^{0} is the bending modulus of the non-blebbing cell cortex at resting state.

2.3 The Cell Interior

2.3.1 The Cytoskeleton and the Cytoplasm

The internal cell body is modelled as a viscoelastic material, the elastic response is modelled *via* internal pressure modulation, and the viscous effects are introduced as a viscous drag felt by the moving agents of the cell cortex.

At the resting state of the cell, there is an ideal internal pressure, P_{CELL}^{0}, generated by the actomyosin cortex. Deviations from the ideal total area of the 2D model cell, A_{CELL}^{0}, are reflected as changes in the internal pressure. The magnitude of the response is dependent on the bulk modulus of the cell, according to the relation:

$$P_{CELL} = P_{CELL}^{0} + K_{cyt} \ ln\left(\frac{A_{CELL}^{0}}{A_{CELL}}\right) \tag{2.23}$$

Here, P_{CELL} and A_{CELL} are the current internal pressure and area of the cell, superscript 0 indicates resting state value, and K_{cyt} is the bulk modulus of the internal cell body.

The effect of the internal cell pressure on each agent is dependent on the fi-

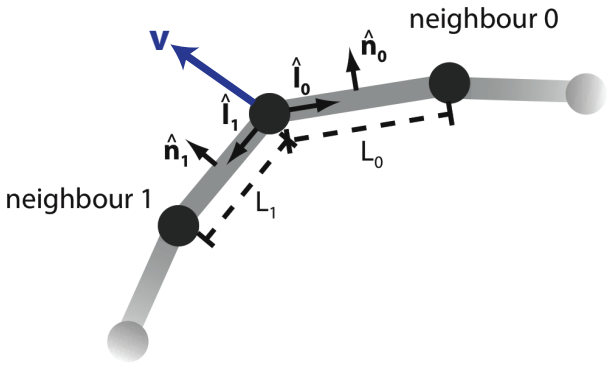

Figure 2.11: Schematic showing the terms used in calculation of the internal pressure effects. Agents of a non-blebbing cell surface are represented in black, representation of the viscoelastic linkers of actomyosin cortex and membrane are simplified to grey lines. $\hat{\mathbf{n}}_i$ are the normal unit vectors in the direction of each neighbour i: $\hat{\mathbf{l}}_i$. L_i are the distances to the neighbour i, and $\mathbf{v}$ is the velocity of the agent.

nite segment lengths associated with each agent:

$$\mathbf{F}_P = w_{model} \sum_{i=0:1} P_{CELL} \frac{L_i}{2} \hat{\mathbf{n}}_\mathbf{i}, \tag{2.24}$$

where $\hat{\mathbf{n}}_i$ are the normal unit vectors to $\hat{\mathbf{l}}_i$, the direction of neighbour i. L_i are the distance to each of the neighbours i, and finally, w_{model} is the defined cross-section width of the 2D model cell (Figure 2.11).

The viscous drag from the internal cell body, the cell cytoskeleton, is introduced with a viscous damping coefficient, η_{cyt}, and is calculated for each agent as:

$$\mathbf{F}_{CIN} = \eta_{cyt} \ \mathbf{v} \sum_{i=0:1} \frac{L_i}{2}. \tag{2.25}$$

Here, $\mathbf{v}$ is the velocity of the agent, and the sum over half distances to neighbouring agents defines the length associated with the current agent (Figure 2.11).

2.3.2 The Nucleus

The nuclear lamina is represented with the same modelling technique as the F-actin cortex; and the nucleus body has the same viscoelastic responses as the cell cytoskeleton and cytoplasm.

The nuclear lamina is formed by a set of nucleus agents, and the viscoelastic linkers in between. Differing from the modelling of the cell surface, the nuclear lamina does not have myosin driven contractility. The deformations of the nucleus are significantly limited compared to the cell body, and the nucleus is not likely to be deformed into a shape that will cause depletion and stretching of its membrane, thus membrane tension acting on the nuclear lamina is not implemented in the model. The parameters defining the stiffness, the viscosity, and the bending modulus of the nuclear lamina are scaled form the stiffness of F-actin cortex, based on experimental observations (see Section 1.3.1.5). Bending resistance forces acting on nucleus agents are calculated with the same approach described for agents of the cell cortex in Section 2.2.4.

Similar to the cell cytoskeleton and cytoplasm, the nucleus has an ideal area, A^0_{nuc}, and deviations from this ideal size causes changes in the internal pressure of nucleus, in a relation analogous to Eq. 2.23:

$$P_{nuc} = P^0_{nuc} + K_{nuc} \ ln\left(\frac{A^0_{nuc}}{A_{nuc}}\right). \tag{2.26}$$

Here, P^0_{nuc} is the hydrostatic pressure difference between the nucleus and the internal cell body, and the value of P^0_{nuc} is set to zero. K_{nuc} is the bulk modulus of the nucleus, which, similar to nuclear lamina, is parameterised scaled to the bulk modulus of the cell, K_{cyt}, based on experimental data.

Experimental observations of the Tumour Cell Biology Laboratory in LRI–CRUK, reveal that the movements of the nucleus correlate with the movement of the cell centre of mass. Moreover, during the cell's course within the ECM, in areas of high confinement, the cell nucleus can be pushed, and deformed. The contribution of the cell movement to movement of the nucleus is incorporated

into the model by using the relative velocity of the nucleus agents with respect to the cell centre of mass velocity, $\mathbf{v}_{CELL}$, during the calculation of the viscous drag felt by nucleus agents. In a relation analogous to Eq. 2.25, the force calculation becomes:

$$\mathbf{F}_{CIN} = \eta_{nuc}\,(\mathbf{v} - \mathbf{v}_{CELL}) \sum_{i=0:1} \frac{L_i}{2}. \tag{2.27}$$

Here, $\mathbf{v}$ is the velocity of the nucleus agent, and η_{nuc} the viscous damping coefficient, representing the drag from both the interior of the nucleus, and the surrounding cytoskeleton. For the interactions with the cortex, when the cell is under confinement and the nucleus is packed against a part of the cell cortex, the compression of cytoskeleton in between the nucleus and the cortex is reflected on each of the nucleus and cortex agents:

$$\mathbf{F}_{NCP} = w_{model}\hat{\mathbf{l}}_{kj}K_{cyt}\ \ ln\left(\frac{r_{nuc}}{L_{kj}}\right) \times \frac{1}{2}\sum_{i=0:1}\frac{L_{ji}}{2} + \frac{L_{ki}}{2} \tag{2.28}$$

The terms used in Eq. 2.28 are represented in Figure 2.12. The force term $\mathbf{F}_{NCP}$ represents the nucleus–cortex packing. Here, r_{nuc} is the cut-off distance under which the cortex begins to have an effect on the shape and position of the nucleus - obtained from experimental observations. The subscript k indicates the nucleus agent of interest, subscript j indicates the cortex agent. $\hat{\mathbf{l}}_{jk}$ is the unit vector in the direction from the nucleus agent k to cortex agent j, and L_{jk} is the distance between the cortex agent j and the nucleus agent k. L_{ji} are the distances between the cortex agent j and its neighbours, similarly, L_{ki} are the distances between the nucleus agent k, and its neighbours. The pressure accumulated in the segment due to compression is calculated analogous to Eq. 2.23 and 2.24, with K_{cyt} the bulk modulus of the internal cell body, and w_{model} is the defined cross-section width of the 2D model cell. The force calculated above is applied to the cortex agent j and a force of equal magnitude and opposite direction is applied to the nucleus agent k. For every nucleus agent k, The force calculation is repeated for all cortex agents that are within r_{nuc}. Bleb neck agents are included in this calculation, while blebbing membrane agents are not.

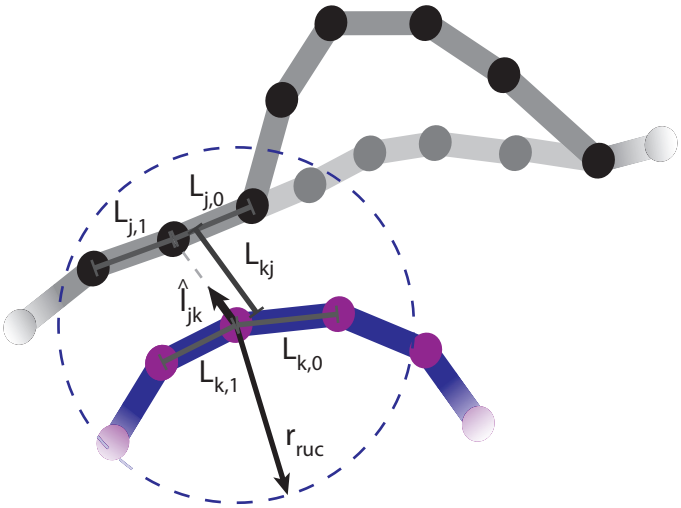

Figure 2.12: Schematic showing the terms used in calculation of the nucleus packing against the cortex, refer to text for detailed descriptions. Nucleus agents are shown in magenta, and nuclear lamina in blue. Agents of the cell surface are represented in black, and bleb neck agents are represented in grey. Representation of the viscoelastic linkers of actomyosin cortex and membrane are simplified to grey lines.

2.4 Mathematical representation

At this point, with the calculation methodology for all the forces from the cell interior introduced, the mathematical representation for the position update function can be given, for a normal surface of the cell, i.e. a region that is not a part of a bleb or an actin polymerisation based protrusion. At the length scale of a cell, and the velocities involved in cell motility, the flow of the cells are within low Reynolds number range; and the system can be assumed over-damped. This means that the forces acting on each agent of the cell body are equilibrated by the dissipative forces due to viscous damping from the cell interior, and the F-actin cortex. Then

the velocity of each agent in the system can be calculated such that:

$$\eta_{CELL}\mathbf{v}\sum_{i=0:1}\frac{L_i}{2}+\sum_{i=0:1}\eta_{cor}\hat{\mathbf{l}}_i.\left(\mathbf{v}-\mathbf{v}_i\right)\hat{\mathbf{l}}_i \tag{2.29}$$
$$=\sum_{i=0:1}\left(k_{cor}\left(L_i-L_i^0\right)+k_{myo}L_i+k_{mem}L_i\right)\hat{\mathbf{l}}_i+\mathbf{F_P}+\mathbf{F_{BEN}}+\mathbf{F_{NCP}}.$$

2.5 F-actin Cortex–Plasma Membrane Linkers

To best represent the dynamic nature of membrane cortex adhesion, the membrane-cortex attachment protein, ERM, levels are initiated and updated through the simulation employing a stochastic rather than a deterministic methodology. The methodology used is a combination of a random walk on the probability domain of the ERM concentration distribution, and inverse transform sampling.

2.5.0.1 Random Walk

A random walk in mathematical terms can be represented by a trajectory, generated by taking successive random steps, in random directions of the defined space. For the problem at hand, a random walk on the probability domain of a given cumulative distribution function (CDF) is utilised, which is a simple random walk in one dimension. A simple random walk in one dimension, initialised at a starting point P_0, is the sequence S_n, with independent increments ζ_i, sampled from a common distribution F, is represented in Eq. 2.30:

$$S_n = P_0 + \sum_{i=1}^{n}\zeta_i. \tag{2.30}$$

For the case of interest, the increments ζ_i are randomly selected from a uniform distribution with defined upper and lower bounds $\pm\delta_{fluct}$. The walk on the probability domain is illustrated in Figure 2.13 for model parameters.

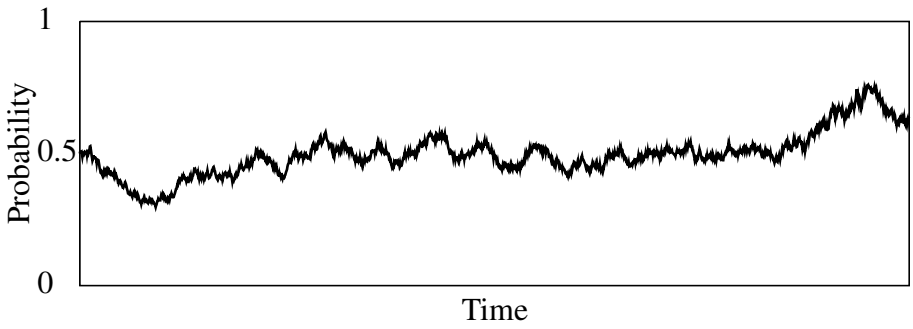

Figure 2.13: A simple random walk in one dimension - probability domain of a given CDF. The step size ζ_i are randomly selected from a uniform distribution in the range [-δ_{fluct},+δ_{fluct}].

2.5.0.2 Inverse Transform Sampling Method

For a distribution with a probability density function (PDF) f(x), the cumulative distribution function F(a) gives the probability $x < a$ (Eq. 2.31) (162).

$$F(a) = \int_{-\infty}^{a} f(x)\,dx \tag{2.31}$$

The CDF F(a) is a random variable, with a uniform probability distribution in the interval [0,1]. For a given u $\in$ [0,1], a unique "a" can be calculated, such that:

$$F(a) = u. \tag{2.32}$$

With the condition we can generate the inverse of the CDF, $F^{-1}(u)$:

$$a = F^{-1}(u) \tag{2.33}$$

Thus, we can sample a distribution of interest by generating uniformly distributed random variables in the interval [0,1], the probability domain, and finding the corresponding "*a*" *via* Eq.2.33. This inverse transform sampling method is efficient under the condition that inverse of the CDF can be evaluated, and the evaluation has low computational costs.

A gamma distribution best represents the experimentally measured distribution of ERM levels (see Section 3.7). The cumulative distribution function $F(x;k\Gamma,\theta_\Gamma)$ of a gamma distribution is given in Eq.2.34, with θ_Γ the scale parameter and k the size parameter of the fitted gamma distribution, $f(x;k_\Gamma,\theta_\Gamma)$ is the probability density function, $\Gamma(x_\Gamma)$ is the gamma function, and $\gamma(k_\Gamma,x/\theta_\Gamma)$ is the lower incomplete gamma function:

$$F(x;k_\Gamma,\theta_\Gamma) = \int_0^x f(u;k_\Gamma,u)du = \frac{\gamma(k_\Gamma,x/\theta_\Gamma)}{\Gamma(k)} \tag{2.34}$$

$$f(x;k_\Gamma,\theta_\Gamma) = x^{k_\Gamma-1}\frac{e^{-x/\theta_\Gamma}}{\theta_\Gamma^k\Gamma(k_\Gamma)} \tag{2.35}$$

$$\Gamma(x) = \int_0^\infty t^{x-1}e^{-t}dt \tag{2.36}$$

$$\gamma(s,x) = \int_0^x t^{s-1}s{-}tdt. \tag{2.37}$$

With the aim of increasing the efficiency in the model implementation, rather than calculating the function and its inverse during the simulation, the CDF of the fitted gamma distribution is pre-calculated at 10^3 points on the ERM concentration domain. The CDF values are interpolated and read accordingly from this fine discrete map of the function.

2.5.0.3 Model Implementation

Upon initiation of each model simulation, the cumulative distribution function (CDF) of the desired ERM distribution is set. Then, all agents on the cell surface are initiated with attachment protein concentrations selected from the CDF representing the ERM distribution over the cell surface, *via* inverse transform sampling.

At each time step of the simulation, the ERM levels are updated at the agent level, in two steps, first based on the size changes at the region; and second, according to the expected stochastic fluctuations in ERM concentration levels. In the first step, from the length attributed to the agent in the previous time step, and the ERM concentration in the agent, the number of ERM proteins is obtained, and the new concentration is calculated with the new length associated with the agent.

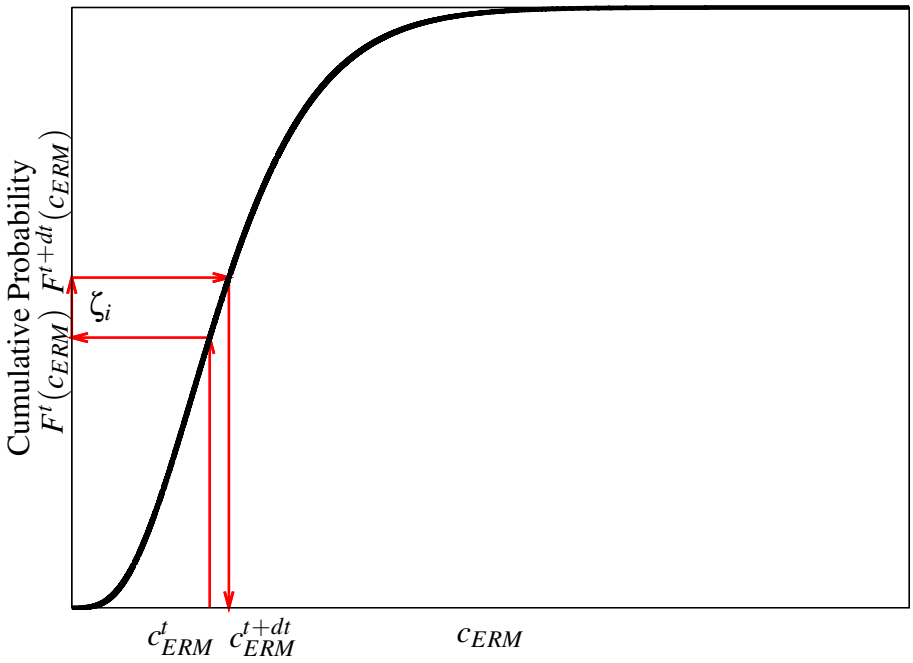

Figure 2.14: Stochastic update of ERM concentrations for each agent. c^t_{ERM} is the ERM concentration for the agent after update due to size change. The corresponding cumulative probability is calculated, and updated with random step size ζ_i, from which the new ERM concentation in agent is calculated. The step size ζ_i demonstrated in the figure is not to scale with model parameters.

For the stochastic sampling, the probability corresponding to the concentration calculated from the first step above is read from the cumulative distribution function. A uniform random percentage shift is selected within the range [-δ_{fluct},+δ_{fluct}], which defines the step size - and direction - of the random walk. Then the probability of the ERM proteins is updated, with the selected percentage. The new concentration corresponding to the updated probability is obtained from the inverse cumulative distribution function (Fig. 2.14).

This approach allows for the natural stochastic fluctuations in ERM levels while also taking into account the ERM concentration level changes due to rapid changes on cell surface, such as rapidly expanding or contracting cell surface regions.

2.5.0.4 Special Cases

(i) During the assignment of the random step size to the random walk, the probability of the current ERM concentration, the calculated probability can reach beyond 1.0. In such cases, instead of capping the probability at 1.0, the probability is reflected with respect to 1.0. This approach avoided over sampling the concentration value corresponding to the probability of 1.0.

(ii) Upon bleb initiation, membrane-cortex attachment proteins are set to zero within the blebbing region, not updated during the expansion phase, and re-set upon the start of retraction phase. The concentration of ERM proteins are not necessarily zero during bleb expansion, as a matter of fact, it is known that ezrin arrives the bleb rim before actin (see Section 1.3.2.2). From a modelling point of view, the ERM levels inside a bleb during the expansion phase are not relevant to any particular calculation in the course of the simulation. On the other hand, with the knowledge on the arrival time of ezrin to the bleb, it is assumed the ERM levels reached their normal values by the time actin accumulation starts, thus the levels are re-set with random concentrations from the ERM probability distribution upon the start of retraction, and are updated normally thereafter.

2.6 Interactions with the Environment

The model cell has no slip binding to ECM filaments, i.e. while an agent is adhered to a filament surface, it has zero velocity for simulations with rigid ECM, and it moves only with the velocity of the deformation of the ECM surface in simulations with flexible ECM. In this study, binding events are treated as reversible, with cell–ECM binding modelled using the well established Bell Model (163). The Bell model of cell-cell and cell-substrate adhesion is a simple yet successful representation of the complex adhesion phenomena, and has been utilised in numerous studies (102, 154).

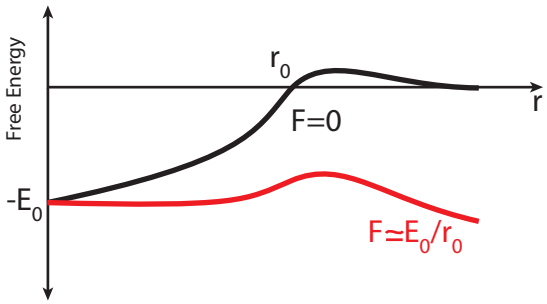

Figure 2.15: Potential energy between ligand and receptor as a function of distance. y-axis gives the energy, x-axis is the deviation in distance between the ligand and the receptor, from the minimum energy orientation. When a force is applied to the bond, the shape of the energy landscape is altered (red).

2.6.1 The Bell Model of Cell-Cell and Cell-Substrate Adhesion

Cells adhere to extracellular substrates, such as collagen, by multiple bonds. At the protein level, the ligand-receptor couples participating in cell adhesion have a reduced energy state in their complex form; hence complex formation is favoured. When the proteins are separated from each other, the free energy change with the distance between the proteins follows a trajectory qualitatively represented in Figure 2.15. The complex has a minimum energy state at the equilibrium binding distance, deviations from which are energetically unfavourable. Here, E_0 is the free energy change upon binding, and r_0 is the range of the minimum, a term defining the shape of the energy well. When an external force is applied to the system to separate the proteins, the energy landscape changes shape, the height of the dissociation energy barrier being reduced by $\sim r_0 f$ (164), and with sufficiently high force, the energy minimum disappears (163). The force required to eliminate the minimum of the energy landscape becomes $f_0 = E_0/r_0$. The values of the parameters defining the energy landscape are protein complex dependent.

The Bell model finds its roots in the kinetic theory of strength of solids, where the lifetime of a bond is defined as:

$$\tau = \tau_0 \, exp\left(\frac{E_0 - \gamma f}{k_b T}\right). \tag{2.38}$$

Here τ_0 is the reciprocal of the natural frequency for atomic oscillations in solids.

T is the temperature, k_b is the Boltzmann constant, E_0 is the bond energy, f is the force per bond, and finally, γ is an empirical factor defining the solids structure (163). In application of this theory to ligand-receptor bonding for cells, the dissociation rate constant k_{off} becomes relevant in place of τ. Moreover, when the minimum of the energy landscape vanishes, $\tau \backsimeq \tau_0$, and thus , at $f = f_0 = E_0/r_0$, we can relate γ and r_0 to be approximately equal. Then following Eq. 2.39, we obtain the reverse rate constant of a ligand-receptor bond under an applied force f:

$$\begin{aligned} \frac{1}{k_{off}} &= \tau_0 \, exp\left(\frac{E_0 - r_0 f}{k_b T}\right) \\ k^0_{off} &= \frac{1}{\tau_0 \, exp\left(\frac{E_0}{k_b T}\right)} \\ k_{off} &= k^0_{off} exp\left(\frac{r_0 f}{k_b T}\right), \end{aligned} \tag{2.39}$$

where k^0_{off} is the unstressed dissociation rate constant of the binding reaction. When there is a number of ligand-receptor pairs, N_b, adhering the cell surface to its substrate, the definition for the dissociation rate constant of a cell patch, under the force F becomes:

$$k_{off} = k^0_{off} exp\left(\frac{r_0 F}{k_b T N_b}\right). \tag{2.40}$$

Here, it is assumed that the stress is distributed equally among the bonds of the adhered patch, which is valid as long as the considered patch is sufficiently small.

2.6.2 Cell–ECM Association and Dissosiation, a Monte Carlo approach

Cell adhesion to the ECM is modelled at the agent level, where the adhesion formation or breakage is updated for each agent with a Monte Carlo process. The probability of association of a given agent with the ECM is modelled with probability P_{on} as in Eq 2.41, dt the model time step and k_{on} the association rate constant (165). The association rate constant is a function of the distance between the agent and the

ECM filament (Eq. 2.42) where δ_{on} is a step function, 1 when the distance to the closest filament, d_{ECM}, is below a given binding threshold, d^{on}_{ECM}, and 0 elsewhere.

$$P_{on} = \delta_{on}\left(1 - exp\left(-k_{on}dt\right)\right) \tag{2.41}$$

$$\delta_{on} = \begin{cases} 0 & if \quad d_{ECM} > d^{on}_{ECM} \\ 1 & if \quad d_{ECM} < d^{on}_{ECM} \end{cases} \tag{2.42}$$

In a similar manner to P_{on}, breakage events are modelled with probability:

$$P_{off} = 1 - exp\left(-k_{off}dt\right). \tag{2.43}$$

Here, the k_{off} is calculated *via* Eq. 2.40, and the resultant force acting on the agent, excluding the component force directed towards the adhered surface, is taken into account. The number of ligand-receptor pairs involved in the adhesion of an agent, N_b, is defined by the units of adhesion proteins within the agent, and variable levels of cell–ECM adhesion could be investigated by changing the units of adhesion cell surface agents have. It is important to note that the unit of adhesion defined for the model does not necessarily correspond to a defined number of binding molecules on the cell surface. For a detail description of the relation between adhesion strength and units of adhesion, see Section 3.11.

At each time step, the probability of association for non-adhered agents and the probability of dissociation for adhered agents are calculated. Then a series of random numbers are generated, and the relevant event carried out for each agent, if the generated random number is less than the calculated probability. For dissociation events, the probability check is done for a single unit of adhesion only, and the agent is considered detached in the event the probability check is successful. Although this may seem a contradiction at first glance, detachment events are catastrophic by nature. When one unit of adhesion is dissociated within the agent, the force per receptor-ligand couple increases for the remaining units, making the probability of dissociation higher. Thus we define our probability check for dissociation to be for all the adhesion units within the agent, if one unit

of adhesion breaks, so to do the remaining units.

2.6.3 Elimination of Cell–ECM Penetration

The Bell model and the Monte Carlo procedure defined above represent the attractive interactions between the cell and ECM. A hard wall potential is used to model the repulsive forces between the filaments and the cell, and to prevent the cell from penetrating into ECM filaments. This is implemented in the form of an exponentially growing repulsive force, pushing the agent away from the filament, when the agent penetrates into a pre-defined cut-off distance, r_{cut}, from the filament surface (Fig. 2.16). Upon contact, when an agent of the cell pushes towards a filament, the reaction force applied by the filament to the agent is equal in magnitude and opposite in direction. Hence the exponential growth of the hard-wall force is capped at F^{CAP}, which is defined with relation to the current driving force $F_{drive,j}$, pushing the agent j towards the filament. For stability purposes, the force is capped slightly higher than the driving force:

$$F_{HW} = \begin{cases} 0 & if \quad d > r_{cut} \\ a_{HW} \times \left(\frac{r_{cut}-d}{db_{HW}}\right) & if \quad d < r_{cut} \;\; and \;\; a_{HW} \times \left(\frac{r_{cut}-d}{db_{HW}}\right) < F^{CAP} \\ F^{CAP} & if \quad d < r_{cut} \;\; and \;\; a_{HW} \times \left(\frac{r_{cut}-d}{db_{HW}}\right) > F^{CAP} \end{cases} \tag{2.44}$$

The exact shape of the hard wall forces are not of importance, as long as the parameters can prevent the cell from penetrating into filaments, while not interfering with adhesion events, i.e. preventing the agent from coming close enough, within d^{on}_{ECM}, to adhere to the filament.

2.6.4 Flexible ECM Filaments

The model can incorporate flexibility of ECM filaments. In simulations where the filaments are treated non-rigid, each filament is defined as a network of elastic springs (Figure 2.17).

Each node of the filament is also attached to its resting position by a spring, ensuring the filament will relax to its original position when the deforming forces

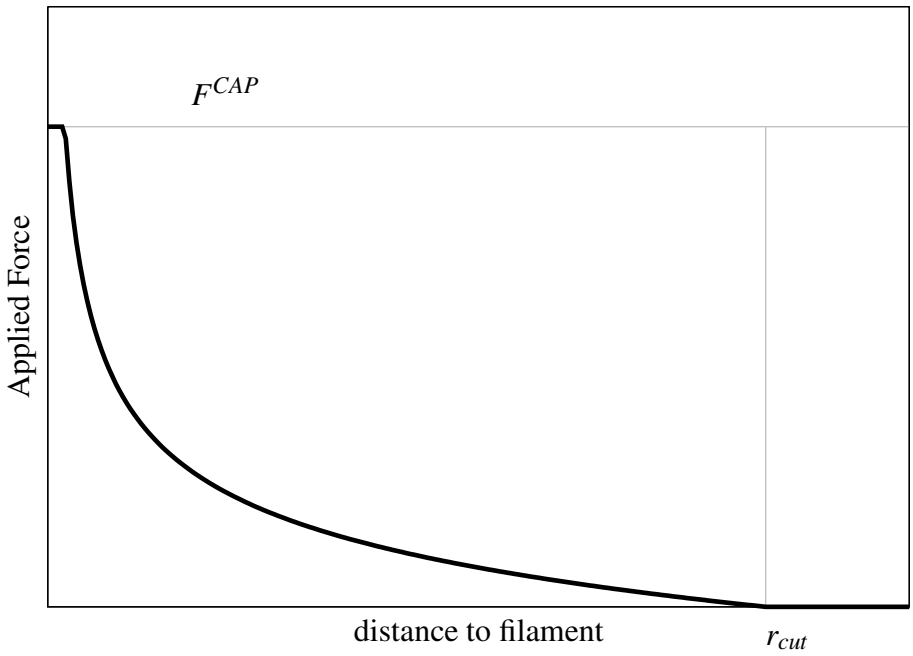

Figure 2.16: Hard wall forces are utilised to prevent cells penetration into the ECM filaments.

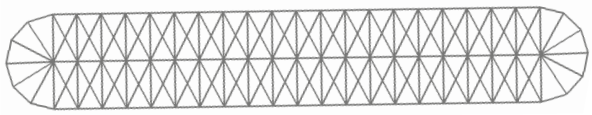

Figure 2.17: The network of springs used to construct an elastic ECM filament. The filament is at its resting state with no deformation.

are removed, i.e. the cell stops pushing against the filament. This definition is necessary to model the effect of the connectivity of filaments in the third dimension, as the model represents cross-sections of these filaments in 2D. The forces on each node are calculated from the spring deformations. When a cell surface agent is adhered to the neighbourhood of a filament node, the forces acting on the cell surface agent are transferred to the filament node, including the viscous damping forces, and the velocities of the two nodes are coupled.

$$\mathbf{F}_{FIL} = k_{fil}\left(\hat{\mathbf{l}}_{disp}L_{disp} + \sum_{i=0:n}\hat{\mathbf{l}}_i\left(L_i - Li^0\right)\right) + \mathbf{F}_{CARR}. \tag{2.45}$$

Here, $\mathbf{F}_{FIL}$ represents all the active forces on the filament node, and $\mathbf{F}_{CARR}$ represents all the forces carried on the filament node from adhered cell surface agents. k_{fil} is the spring constant for each of the linkers, L_i and L_i^0 are the lengths, and ideal lengths towards each of the neighbouring filament nodes. $\hat{\mathbf{l}}_i$ are unit vectors in the direction of the neighbours i, n is the number of neighbours the filament node has, L_{disp} is the displacement of the filament node from its resting position, and $\hat{\mathbf{l}}_{disp}$ is the unit vector in the direction of the resting position of the node. After obtaining all the driving forces, the position of the filament nodes are updated by obtaining the velocity of each node *via*:

$$\mathbf{F}_{FIL} = \eta_{fil}\mathbf{v}\frac{1}{n}\sum_{i=0:n}L_i, \tag{2.46}$$

where η_{fil} is the viscous damping coefficient of the filament, and $\mathbf{v}$ is the velocity of the filament node.

2.7 Membrane Blebs

2.7.1 Bleb Formation

Bleb initiation events are controlled *via* the agents in the model. Blebs can be initiated at any agent of the cell that is not a part of an actin polymerisation based protrusion, not part of an already existing bleb, or adhered to an ECM filament. The pressure due to hydrostatic force is calculated *via* Eq. 2.47, and the strength of the adhesion between the F-actin cortex and the plasma membrane is calculated from

the concentration of ERM proteins within the agent:

$$F_P = w_{model} \sum_{i=0:1} P_{CELL} L_i; \tag{2.47}$$

$$F_{att} = \left(c_{ERM} \sum_{i=0:1} \frac{L_i}{2} + \sum_{i=0:1} c_{ERM,i} \frac{L_i}{2} \right) \times F_{unitattach}, \tag{2.48}$$

where c_{ERM} is the concentration of ERM proteins within the agent, and $c_{ERM,i}$ are the concentrations of ERM in neighbouring agents. L_i are the distance to each of the neighbours i, $F_{unitattach}$ is the adhesion force associated with one unit of adhesion protein, and w_{model} is the defined cross-section width of the 2D model cell. The whole region from the agent under consideration to its neighbours is detached from the cortex, thus forces acting on the whole length are taken into account. When the force from the hydrostatic pressure exceeds the strength of cortex-membrane adhesion, the agent is detached from the underlying cortex, and a bleb is initiated (Figure 2.18).

Upon bleb initiation, the cortex and local cytoskeleton properties are set to expanding bleb levels. At the bleb rim, cortex density is set to f_{cor}^{bleb}, resulting in a reduction of cortex driven forces and resistance *via* Eq. 2.12. The bleb rim is initially devoid of myosin, and by setting the concentration of myosin II to zero, and the resulting contractile forces in this region are reduced to zero according to Eq. 2.14. During the expansion phase, blebs are mainly filled with cytosolic fluid that lacks large organelles and structured cytoskeleton, thus the cytoskeletal damping coefficient of the region is reduced to η_{cyt}^{bleb} according to Eq. 2.49:

$$\eta_{cyt}^{bleb} = f_{cor}^{bleb} \times \eta_{cyt}. \tag{2.49}$$

Blebs cannot adhere to ECM filaments during their expansion phases.

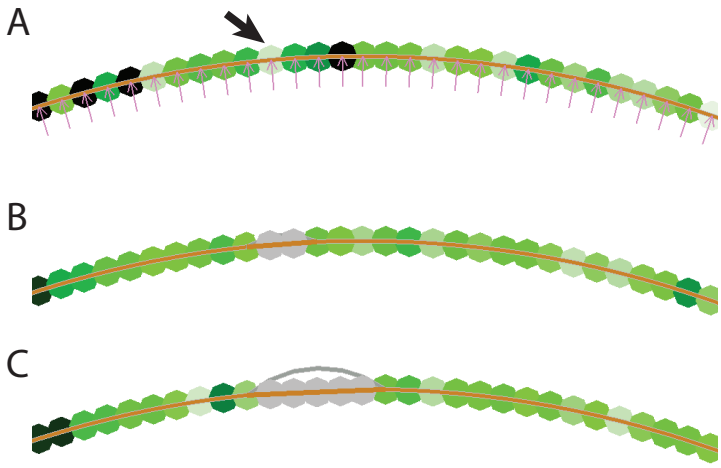

Figure 2.18: A) The cell surface with hydrostatic pressure forces acting on agents shown in pink, the density of ERM proteins is colour coded on the agents, higher the concentration, darker the green. B) A bleb is initiated at the agent marked by the black arrow in (A). On the linkers, the density of F-actin cortex is colour coded in green, myosin in red and plasma membrane in grey, the colours are overlaid, a non-blebbing cell surface with high actin and myosin density showing as orange.

2.7.2 Bleb Tearing

During the expansion phase, blebs can tear the membrane off the cortex at their borders. This tearing facilitates growth of the bleb neck, and contributes to membrane allocation into the expanding bleb. Tearing is driven by cellular pressure acting on bleb border and pulling forces from the blebbing membrane. In the case of the pulling force from the blebbing membrane, the component of the force that is pulling the attached surface off the cortex is taken into account (Figure 2.19).

Similar to initiation of blebs, once the summation of forces from the internal cell pressure and membrane tension of the expanding bleb exceeds the cortex-membrane adhesion force, the border is torn off the cortex, and incorporated into the bleb body (Figure 2.20A/B).

During their expansion phases, two neighbouring blebs can tear the membrane in between them, resulting in a larger single bleb (Figure 2.20C/D).

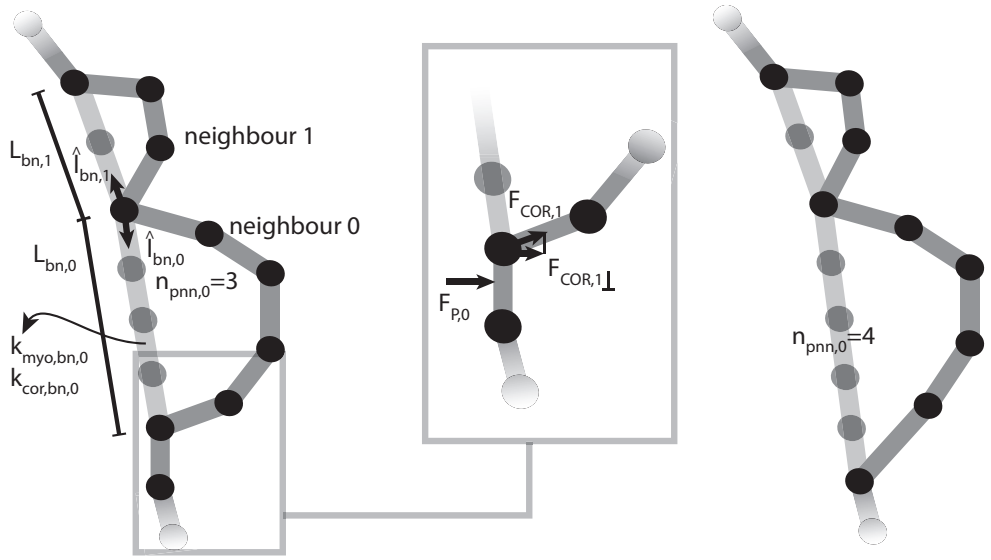

Figure 2.19: A) Schematic showing the parameters involved in calculation of forces for the simple bleb neck definition. B) Forces that are facilitating tearing of the membrane, at the bleb borders. The force from pressure on the attached side is fully taken into account. For the force from the expanding membrane pulling, only the component pulling on the attached surface is taken into. C) The same bleb schematic after the neck is torn. The realignment of the simple bleb neck, and addition of the *pseudo* bleb neck node is demonstrated.

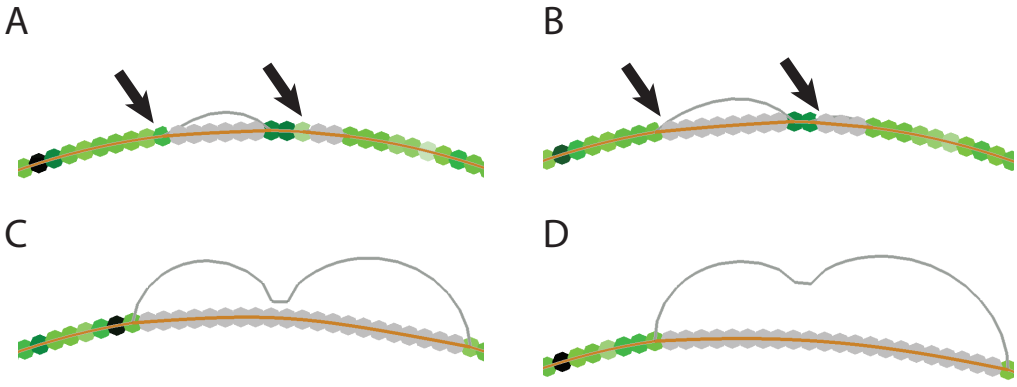

Figure 2.20: A) Two adjecent expanding blebs, colour coding same as Figure 2.18. B) The agents indicated by the blacks arrow in (A) are torn off the cortex, and incorporated into each bleb body. The bleb necks are extended upon tearing of the bleb borders, with the bleb neck nodes marked by black arrows in (B). C) The whole patch of membrane in between the two blebs is detached from the cortex, and the two blebs merged into a single bleb. D) Continuing expansion of the single bleb.

2.7.3 Bleb Retraction

The expansion phase of a bleb ends when actin starts to re-accumulate at the bleb rim. The accumulation starts with a delay Δt_{cor}, after initiation of the bleb. The delay time is randomly selected form the experimentally measured distribution of the start of actin polymerisation. The rate of actin density increase is *via*:

$$f_{cor} = f_{cor}^{bleb} \frac{g(t_{bleb}) - g(0)}{g(\infty) - g(0)}, with \qquad g(t) = \frac{a}{b + exp(ct)} \tag{2.50}$$

where the function $g(t)$ is fitted to experimental data, giving $a = 2.5$, $b = 1.3$ and $c = -0.26$. The variable t_{bleb} represents the time period since the initiation of actin accumulation in the bleb. The details of the fit are given in Section 3.3.1 together with the experimental data. The damping coefficient from the cell interior is restored to normal cell values at the same time with actin accumulation rate at the bleb rim, following Eq. 2.49. As there is sufficient cortex to bind integrins, blebs can form adhesions with ECM filaments during the retraction phase. Blebs cannot tear at the borders during retraction phase.

Myosin accumulation starts in the bleb significantly later than initiation of actin accumulation, the delay Δt_{myo} is randomly selected in the range of experimental measurements, $7.3 \pm 2.4s$ (31). The dynamics of myosin accumulation are regulated *via* aforementioned diffusion rules, initiation of myosin accumulation being marked by setting equilibrium myosin levels from zero to the level determined by the polarity and overall contractility of the cell.

A bleb can be declared fully retracted with two alternative sets of criteria: (i) To account for blebs that grow and retract back into the cell body, the bleb is declared retracted if the size of the bleb is smaller than fifty percent of its maximum size and the retraction velocity is below a selected threshold of 0.005 $\mu m\ s^{-1}$. (ii) To account for blebs that expand to large sizes, and that become stabilised as a part of the cell body instead of retracting back to small enough sizes to qualify for criteria (i), blebs can be declared fully retracted if the residual cortex at the bleb neck has depolymerised completely. Once a bleb is declared fully retracted, it is

deleted and removed from further calculations, and from there on, the blebbing membrane is treated as regular cell surface.

2.7.4 Bleb Necks

Bleb necks are the residual cortex leftover once a membrane patch has detached from the cortex, and formed a bleb. The model includes two definitions of bleb necks, one simplified and one detailed approach.

2.7.4.1 Simple Definition

In the simple definition, the two borders of a bleb are linearly connected. The number of agents that are supposed to construct the neck is recorded, starting from one upon bleb initiation, and increasing by one for each tearing event. These nodes are assumed to be distributed equally on the linear connection between the bleb borders, and the forces acting on the borders due to the bleb neck are calculated accordingly (Figure 2.19).

The ideal length per link at the bleb neck is necessary for calculation of elastic resistance forces. This value is assigned at bleb initiation, as the average of the ideal lengths of linkers in the detached region:

$$L^0_{bn} = \frac{1}{2} \sum_{i=0:1} L^0_i, \tag{2.51}$$

where L^0_{bn} is the ideal linker length for the bleb, and L^0_i are the ideal lengths of linkers towards neighours i. Then the forces due to the elastic response of the bleb neck cortex and myosin activity are calculated as;

$$F_{BN} = \sum_{i=0:1} \left(\frac{L_{bn,i}}{n_{pnn,i}+1} \times k_{myo,bn,i} + \left(\frac{L_{bn,i}}{n_{pnn,i}+1} - L^0_{bn,i} \right) \times k_{cor,bn,i} \right) \times \hat{l}_{bn,i}, \tag{2.52}$$

where the $k_{cor,bn,i}$ and $k_{myo,bn,i}$ are the spring constants for cortex elasticity and myosin activity on the side i of the bleb neck, respectively. $n_{pnn,i}$ is the number of pseudo nodes along bleb neck on side i, and $L_{bn,i}$ is the total length of the bleb neck on the side i (Figure 2.19).

Calculation of the velocities for the pseudo agents along the bleb neck is required for the contribution the bleb neck makes to the viscous drag felt by the bleb border. The velocity of the closest pseudo agent is calculated from the velocity of the second border of the bleb, and the viscous damping becomes:

$$\mathbf{F}_{BN,visc} = \sum_{i=0:1} \eta_{cor,bn,i} \times \left(\hat{\mathbf{l}}_{bn,i} . \left(\frac{\mathbf{v} - \mathbf{v}_{bn,i}}{n_{pnn,i}} \right) \right) \times \hat{\mathbf{l}}_{bn,i}. \tag{2.53}$$

Here, $\mathbf{F}_{BN,visc}$ is the viscous damping force felt by the bleb border agent, $\eta_{cor,bn,i}$ is the viscous damping coefficient of the bleb neck that neighbour i is a member of, $\hat{l}_{bn,i}$ is the direction of the bleb neck that neighbour i is a member of, $\mathbf{v}$ is the velocity of the agent, $\mathbf{v}_{bn,i}$ is the velocity of the other border of the bleb, and $n_{pnn,i}$ is the pseudo neck node number of the bleb (Figure 2.19).

The viscous damping coefficient $\eta cor, bn$, cortex elasticity $k_{cor,bn}$ and myosin activity $k_{myo,bn}$, for any bleb, is decayed in time, with the activity of myosin being directly proportional to the density of actin. The decay is carried out with similar time constraints to those used to regulate the renewal of actin at regular cell surfaces (Eq. 2.11), this time with the values decaying towards zero:

$$k_{cor,bn}(t) = k_{cor,bn}(0) \times \left(1 - \frac{t}{\tau_a}\right), \tag{2.54}$$

$$\eta_{cor,bn}(t) = \nu_{cor,bn}(0) \times \left(1 - \frac{t}{\tau_a}\right), \tag{2.55}$$

$$k_{myo,bn}(t) = k_{myo,bn}(0) \times \left(1 - \frac{t}{\tau_a}\right), \tag{2.56}$$

where t is the time since the initiation of the bleb, and τ_a is the actin turnover time.

2.7.4.2 Improved Definition

In the improved definition, the linkers defining the membrane and the actomyosin cortex are separated from each other for all the regions where the adhesion between the cortex and the membrane is lost, and each entity (the cortex and the membrane) continues to be represented as explicit agents. Once a bleb is initiated, the first

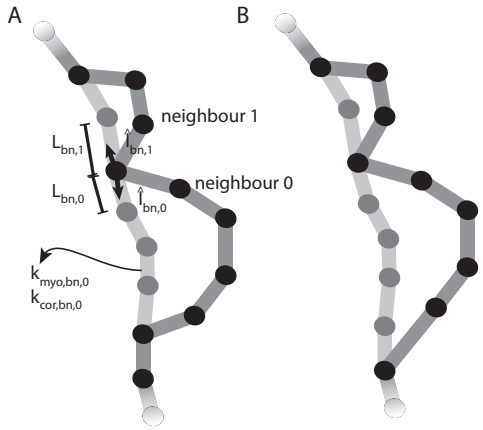

Figure 2.21: A) Schematic demonstrating the parameters involved in calculation of forces in improved bleb neck definiton. B) Same blebs, upon tearing of the border for the lower bleb, a new bleb neck agent is added to the neck, at the position of the torn agent.

bleb neck node is positioned at the position of the agent where the membrane patch detached from the surface. At each tearing event, a new bleb neck agent is added to the bleb neck, at the position of the torn agent (Figure 2.21). The elastic forces and viscous damping are calculated in the same manner as for the simple bleb neck definition. However, in this definition, there is no need to scale the lengths and velocities, since each node is moved and traced individually. The equations then simplify to:

$$\mathbf{F}_{BN} = \sum_{i=0:1} \left(L_{bn,i} \times k_{myo,bn,i} + \left(L_{bn,i} - L^0_{bn,i}\right) \times k_{cor,bn,i}\right) \times \hat{\mathbf{l}}_{bn,i}, \tag{2.57}$$

$$\mathbf{F}_{BN,visc} = \sum_{i=0:1} \nu_{cor,bn,i} \times \left(\hat{\mathbf{l}}_{bn,i}\left(\mathbf{v} - \mathbf{v}_{bn,i}\right)\right) \times \hat{\mathbf{l}}_{bn,i}. \tag{2.58}$$

Where $L_{bn,i}$, $v_{bn,i}$ and $\hat{l}_{bn,i}$ becomes the length towards, the velocity of, and the the direction to the bleb neck agent in the direction of neighbour i ((Figure 2.21A). The decay of actin cortex and myosin motor activity is calculated for the bleb same as the simple definition (Eq. 2.54) and updated in each bleb neck agent. In the position update of bleb necks, the elastic component of the cortex resistance and myosin driven contractility, $\mathbf{F}_{BN}$ are added to the right hand side of Eq. 2.29, and the contribution of the damping forces of the bleb neck, $\mathbf{F}_{BN,visc}$, are added to the left hand side of Eq. 2.29.

2.8 Actin Polymerisation Based Protrusions

2.8.1 Protrusion Formation and Elongation

Actin polymerisation based protrusions can be initiated at any point on the cell surface that is not adhered to an ECM filament, nor a part of an existing membrane bleb, and not within the 1 μm neighbourhood of an existing protrusion. The occurrence of protrusion initiation at any agent is dependent on the local myosin concentration:

$$\begin{aligned} P^0 &= 1 - exp\left(-k_f^0 dt\right); \\ P &= P^0 exp\left(-b_{prot}\left(c_{myo} - c_{myo}^0\right)\right), \end{aligned} \tag{2.59}$$

where k_f^0 is the protrusion formation rate per agent under normal myosin concentration ($c_{myo} = c_{myo}^0 = 1$), c_{myo} is the current myosin concentration in the agent, and c_{myo}^0 is the normal myosin concentration (set equal to 1). The normal protrusion initiation rate is fitted to the experimental data. Similarly, the shift in occurrence rate of protrusions is fitted to experimental data at multiple levels of myosin expression (see Section 3.10). At the onset of initiation, each protrusion is randomly assigned an angle of elongation, θ_{prot} in the range $[-30, 30]$ degrees, determining the angle it will form with the cell surface at that point; the angle between the protrusion direction and a vector joining agents either side of the protrusion point (Figure 2.22A). Secondly, each protrusion is randomly assigned a lifetime from a uniform distribution, that will dictate the instant the protrusion will stop elongating, if it has not attached to an ECM filament. The model does not have detailed modelling of actin polymerisation at the molecular level, and the time threshold is selected to fit with the thermodynamic limits of unsupported actin protrusion elongation: the time limit is selected in the range $[5, 10]$ s, leading to $[1, 2]$ μm maximum lengths for unsupported protrusions.

The agent where the protrusion is initiated becomes the tip of the protrusion. During the elongation phase, the protrusion tip is pushed with a tip force, $\mathbf{F}_{TIP}$

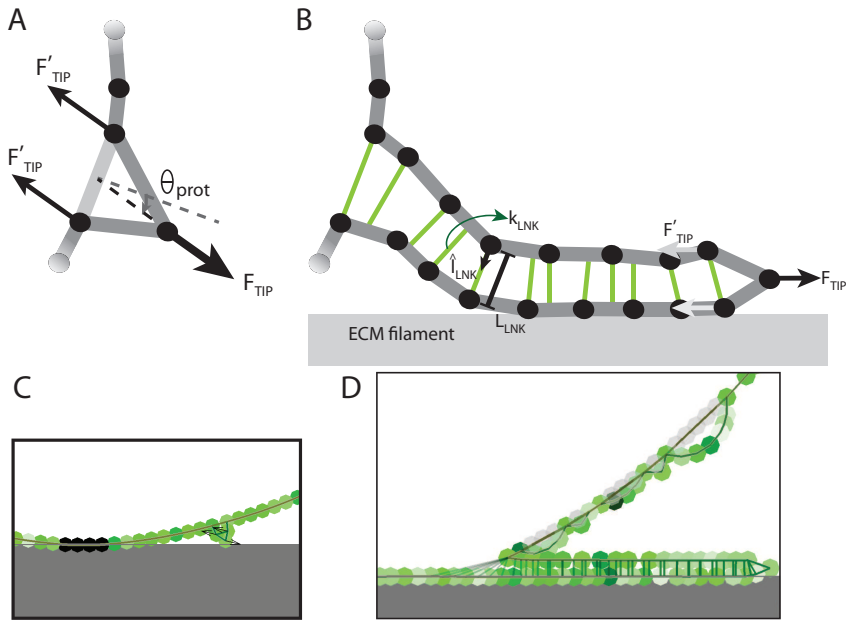

Figure 2.22: A) Schematic of a newly initiated protrusion with orientation angle θ_{prot}. B) Schematic showing a protrusion spreading on a surface. The terms used in calculation of the protrusion tip elongation, and protrusion linker forces are shown. C) Model snapshot for a newly initiated protrusion, at the onset of spreading. D) Model snapshots for a spreading protrusion. In the linkers between the cell surface agents, actin density is colour coded in green and myosin concentration colour coded in red. The myosin gradient within the protrusion can be observed.

in the direction of its elongation angle. This tip force models the force applied to the membrane by the polymerising actin. To balance internal forces, a force equal in magnitude and opposite in direction is distributed on the two neighbours of the protrusion tip. As the elongation of these protrusions is facilitated by polymerisation of actin at the tip, within the limits of the actin polymerisation velocity range, the tip should not experience a resistance to stretching. If the ideal lengths of the springs attached to the protrusion tip are shorter than the current lengths, and the rate of elongation is below the selected maximum polymerisation velocity, v_{prot}^{max}, the ideal lengths are updated to be equal to the current lengths. If the current length of one of these springs increases faster than the upper limit imposed by the maximum polymerisation velocity, its ideal length is updated to be as high as the size it would reach with the maximum polymerisation rate. If the ideal length is larger than the current length, as can be the case during the retraction phase of these protrusions, the ideal length is not updated. These criteria can be summarised in:

$$L_i^0(t+dt) = \begin{cases} L_i(t) & \text{if} \quad L_i(t) > L_i^0(t) \,\&\, \left(L_i^0(t) - L_i(t)\right) < v_{prot}^{max} dt \\ L_i^0(t) + v_{prot}^{max} dt & \text{if} \quad L_i(t) > L_i^0(t) \,\&\, \left(L_i^0(t) - L_i(t)\right) = v_{prot}^{max} dt \\ L_i^0(t) & \text{if} \quad L_i^0(t) = L_i(t) \end{cases}$$

As the protrusion elongates, new agents are added between the protrusion base and tip, forming the sides of the protrusion. Differing from blebs, the actin polymerisation based protrusions are filled with a meshwork of actin. Moreover, while elongating by polymerisation at the tip, these protrusions disassemble the actin meshwork at the base. Thus, for each agent forming the sides and base of a protrusion, it is necessary to keep track of the time since their addition. Elastic linkers can then be defined to model the finite segments of the meshwork inside the protrusion, with an ideal length that is equal to the width of the protrusion, and with a spring constant based on the density of the meshwork, similar to the strength of cortex at the rim of an expanding bleb.

This calculation is carried out as follows: For each agent on the sides of the protrusion, the minimum distance to the opposing side is calculated, and the agent(s) closest to the current agent on the opposing side are selected. The closest

point can correspond to either a single agent, or to the linker between two agent on the opposing side. The average age of the actin meshwork, in between the current agent and its closest neighbours on the opposite side of the protrusion, is calculated as the average age of these agents - the time since addition of the agents to the protrusion. The elastic force is then calculated according to:

$$\mathbf{F}_{LNK} = k_{LNK}\left(L_{LNK} - w_{prot}\right)\hat{\mathbf{l}}_{LNK}. \tag{2.60}$$

Here, $\mathbf{F}_{LNK}$ is the force applied on an agent forming the protrusion side, k_{LNK} is the spring constant for the elastic link defining the inner mesh of the protrusion, L_{LNK} is the closest distance to the opposing side, w_{prot} is the defined thickness of actin polymerisation based protrusions in the model, and $\hat{\mathbf{l}}_{LNK}$ is the unit vector in the direction of the closest point on the opposing side (Figure 2.22B). The strength of the link is calculated form:

$$k_{LNK} = k^0_{cor} \times \left(1 - \frac{\langle t \rangle}{\tau_a}\right) \tag{2.61}$$

where, k^0_{cor} is the strength of the actin cortex at its resting state, $\langle t \rangle$ is the average time passed since agents involved in the interaction have become part of the protrusion, and τ_a is the actin turnover time.

The protrusion tip is formed by recently polymerised actin, which is devoid of myosin, and is kept devoid of myosin as long as the protrusion elongates. Myosin diffuses into the agents of forming the sides of the protrusion through the protrusion life time, and the tip of a retracting protrusion, by normal diffusion rules. This generates a gradient of myosin within each protrusion (Figure 2.22C).

In terms of interactions with the environment, the actin polymerisation based protrusions differ from membrane blebs such that they can form adhesions with the surrounding ECM filaments at any part of their life cycle, with the exception of the protrusion tip. Moreover, these protrusions can spread on filament surfaces, which stabilises their growth, and prevents spontaneous retraction initiation, which would happen due to thermodynamic limitations.

2.8.2 Protrusion Spreading

Once encountering an ECM filament, and provided the angle between the axis of protrusion and the filament surface is below 85 degrees, an actin polymerisation based protrusion can begin to spread on the filament surface. If the protrusion hits the filament with an angle above 85 degrees, than it will stop elongating and switch to the retraction phase. Provided there are no physical barriers, a spreading protrusion will keep elongating. During the spreading phase, the orientation of the protrusion, and hence the tip force direction, is set in the orientation towards the closest node of the ECM filament, the protrusion is currently spreading on (Figure 2.22). Once the protrusion tip reaches the vicinity of the target node, the target node is reassigned to the next closet node that is in line with the direction of elongation. Hence, the protrusion follows the surface of the filament (Figure 2.22).

During the prolonged elongation phase of a spreading protrusion, the regions at the base of the protrusion where all the internal meshwork of actin disassembled according to Eq. 2.61, are declared not to be part of the protrusion, and are set back to having regular cell surface properties. This transition allows initiation of blebs and new protrusions to take place on these surfaces, while the original protrusion keeps spreading.

2.8.3 Protrusion Retraction

Depending upon a protrusion's interaction with the environment, its retraction phase can be initiated for a variety of reasons. The retraction phase itself is simply defined as elimination of the tip force, $\mathbf{F}_{TIP}$. Then with the accumulation of myosin, the actin polymerisation based protrusion is pulled into the cell body, or the cell body is pulled towards the protrusion, effectively shortening its length in both cases. Once a protrusion shrinks below a set length of $0.2\mu m$, the cell surface it occupied is once again declared a regular cell surface.

Depending upon its randomly assigned lifetime, a protrusion with no support from the surrounding ECM will eventually undergo spontaneous retraction. In the case of a protrusion spreading on a filament with adhesions to its surface, there are two possible ways retraction can be initiated. i) During spreading, the

protrusion tip has a target ECM filament node that defines the orientation of the tip force. However, the protrusion tip can move away from its target ECM filament node which indicates that the summation of the remaining cell forces acting on the tip has overcome the polymerisation driven tip force. The forces that can overcome the protrusion tip force can be due to an increase in membrane tension as a consequence of membrane depletion, or accumulation of myosin within the protrusion that pulls the tip backward. Under these conditions, a protrusion is declared retracting, and the tip force is removed. ii) It is not realistic for protrusions to buckle above certain limits during their spreading on filament surfaces. If a protrusion's current orientation defined by the ECM filament has a 90 degree or higher deviation form the protrusion's initial orientation, then the protrusion is shifted into its retraction phase. This retraction initiation criteria allows for the bending limit of bundled actin filaments, which is not explicitly modelled. Here, it is important to note that spreading on a surface is not sufficient for the stabilisation of a protrusion, and that spontaneous retraction initiation will be blocked only if the protrusion can form adhesions with the filament.

2.9 Conservation of Momentum, a Minimisation Approach

Understanding cell motility within low to zero adhesion environments, is one of the major research aims of this work. In a friction free environment, where the cell cannot form any form of adhesion or anchorage to the extracellular matrix, cell shape can change, but the shape changes cannot result in translocation of the cell body, since due to the law of conservation of momentum, the cell centre of mass would stay at the same position. In other words, a cell cannot swim in an inviscid fluid, or in a zero adhesion environment where no form of anchoring is possible.

An over-damped system approach, which is utilised in the model, does not inherently conserve the momentum of the cell. Moreover, the diffusion and mixing of materials within the cell, such as diffusion of G-actin from the rear to the front of the cell following depolymerisation, is not explicitly modelled. Neglecting this movement of material is justifiable in an environment where the cell is always anchored to its environment, however, some form of conservation for

the overall momentum of the cell is required for accurate modelling of adhesion free environments. Thus, conservation of momentum is introduced in the model in the form of a minimisation layer.

The minimiser approach is utilised to determine the translocation of cell body in simpler models (140). Here, this approach is parameterised to work in conjunction with the over-damped model system, with the purpose of avoiding cell body motion unless the cell has ability to have some form of adhesion or anchorage to the environment, rather than defining the cell body translocation or changes in cell morphology. During minimisation the cell is treated as a rigid-body. The minimum of the local energy landscape is searched for by varying the position of the cell's centre of mass and rotation of the cell's body. The objective function of the minimisation (Eq 2.62) includes energy penalty terms for translocation of the cell centre of mass from the previous time step, the overlaps with extracellular filaments, and deformation of adhesion points (Eq 2.63-2.65). The energy penalties from clashes of the cell body with the filaments and deformation of adhesion points are significantly higher than the penalty for translocation of the cell body. The relative magnitudes of the energy penalties ensures the minimiser prevents the cell from swimming, while not interfering with cell movement when the cell has anchors or adheres to the environment. The energy definitions used in minimisation are given as:

$$E_{total} = E_{DISPLACEMENT} + E_{ADHESION} + E_{CLASH} \tag{2.62}$$

$$E_{DISPLACEMENT} = e_1 \times \left(d_{CM}^2 + d\theta\right) \tag{2.63}$$

$$E_{ADHESION} = \sum_{i}^{agents} \delta_j^{Ad} \times \left[\frac{e_2}{1 + exp(-12 \times d_{Ad,j})} - \frac{e_2}{2}\right] \tag{2.64}$$

$$\delta_i^{Ad} = \begin{cases} 1 & \text{if agent adhered} \\ 0 & \text{otherwise} \end{cases}$$

$$E_{CLASH} = \sum_{i}^{agents} \delta_i^{Clash} \times e_3 \times d_{Clash,i}^2 \tag{2.65}$$

$$\delta_i^{Clash} = \begin{cases} 1 & \text{if agent penetrates into filament} \\ 0 & \text{otherwise} \end{cases}$$

In the above equations, d_{CM} is the displacement of cell centre of mass from the previous time step, and $d\theta$ the rotation of the cell body in radians. e_1 is the displacement energy multiplier utilised by the minimiser. The adhesion energy, $E_{ADHESION}$, is summed over all adhered agents of the cell, with $d_{ad,j}$ being the distance each agent has to its adhesion point. e_2 is the adhesion energy multiplier of the minimiser. Lastly, $d_{Clash,j}$ is the distance agent j penetrated into an ECM filament, and e_3 is the ECM clash energy multiplier of the minimiser.

In the process of minimising the defined objective function, the search for the minimum energy position needs to be local, avoiding large jumps in position. Meanwhile, the selected method should work with energy function evaluations, rather than numerical derivatives, as this would introduce a computational burden and higher error rate. Lastly, the method should be able to minimise a multidimensional search space and be easily scalable to minimise at even higher dimensions when required. Nelder and Mead Simplex method (also known as amoeba method) fits the required criteria (166), and is utilised in the model.

2.9.1 The Nelder and Mead Simplex Method

A simplex in N dimensions is a polytope consisting of N+1 vertices. In 1D, the simplex is a line segment; in 2D, a triangle; in 3D, a tetrahedron; etc. The method starts from N initial guess points, which can be generated by taking one initial guess point, and generating N-1 random vectors with a given step sizes, s_i for each of the independent variables of the objective function, to define the remaining points taking the initial guess point as the origin. The method then cycles through the following steps:

i) Vertices are ordered according to the value of the objective function, and

the centre of gravity, $\mathbf{x_0}$, of the simplex calculated excluding the worst point, $\mathbf{x_{N+1}}$.

$$f(\mathbf{x_1}) \leq f(\mathbf{x_2}) \leq ... \leq f(\mathbf{x_{N+1}}) \tag{2.66}$$

ii) Reflection: Taking the worst point - the point with the largest value of objective function - a reflection point is calculated with respect to the centre of gravity of the simplex:

$$\mathbf{x_r} = \mathbf{x_0} + \alpha_{min}(\mathbf{x_r} - \mathbf{x_{N+1}}) \tag{2.67}$$

If the reflected point is better than the second worst, but not better than the best point, the worst point is replaced by the reflection point and the algorithm returns to step (i), else continues to (iii).

iii) Expansion: If the reflected point is better than the best vertex of the simplex (has a lower value of the objective function), the simplex is expanded in the direction of the reflected point.

$$\mathbf{x_e} = \mathbf{x_0} + \gamma_{min}(\mathbf{x_0} - \mathbf{x_{N+1}}) \tag{2.68}$$

If the expanded point is better than the reflected point, the worst point is replaced with the expanded point, else the worst point is replaced with the reflected point. Then the algorithm returns to step (i), else continues to step (iv).

iv) Contraction: If the reflected point is not better than the second worst point, a contracted point is calculated.

$$\mathbf{x_c} = \mathbf{x_{N+1}} + \rho_{min}(\mathbf{x_0} - \mathbf{x_{N+1}}) \tag{2.69}$$

If the contracted point is better than the worst point, then the worst point is replaced with the contracted point. And the algorithm returns to step (i), else continues to

step (v).

v) Reduction: All points except the best point are replaced according to Eq. 2.70. And the algorithm returns to step (i).

$$\mathbf{x_i} = \mathbf{x_1} + \sigma_{min}(\mathbf{x_i} - \mathbf{x_1}) \text{for all i } \in \mathbf{2}, ..., \mathbf{N+1} \tag{2.70}$$

Here α_{min}, γ_{min}, ρ_{min}, and σ_{min} are the reflection, expansion, contraction and shrink coefficients, respectively. The reflection step tries to find a lower value of the objective function on the opposite face of the simplex with respect to the worst vertex. After reflection, if the new point is the minimum of the simplex, the methods searches for a lower point further in the same direction of the search space. In the contraction step, the calculations indicate a better value of the objective function might lie within the simplex. The selected termination criteria is when the simplex contracts below a threshold size, when the average of the distance of all vertices to the cell centre of mass is lower than selected threshold δ_{tol}. A schematic representation of the process for three dimensions is given in Figure 2.23. The Nelder and Mead Simplex minimiser available in the GNU Scientific Library (gsl_ multimin_ fminimizer_ nmsimplex2rand) is used (167) in this study.

2.9.2 Model Parameters and Effects of Minimiser

The energy parameters of the objective function are selected with the following criteria: avoiding cell movement in environments where there are no filaments that the cell can adhere or anchor to, while not interfering with movement elsewhere, not causing clashes with the fibres, stable convergence of the minimiser and computational performance. In short, parameter selection is based on performance, within the limits that the cell position is corrected accurately.

The effects of the minimiser for a number of test cell simulations are summarised in Figure (2.24). The trajectory of a polarised cell, suspended in media

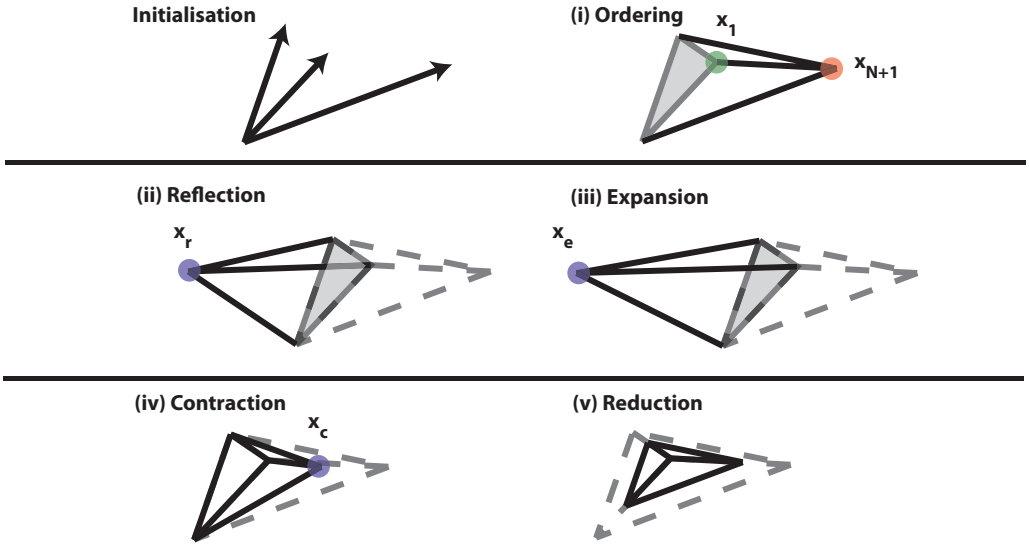

Figure 2.23: A schematic representation for steps of the Nelder-Mead minimisation procedure

with no ECM fibres is demonstrated, where simulations equivalent of ten minutes are carried out, with (Fig. 2.24 A) and without (Fig. 2.24 B) minimiser. Similarly, model trajectories for a cell on a surface with adhesion are given with (C) and without (D) the minimiser. It can be seen that the minimiser alters the trajectory where momentum conservation dictates the cell should stay stationary, while it has no effect on the cell motion when the cell has the ability to adhere to the environment. The values used for minimiser parameters are given in Table 2.1.

Table 2.1: Parameters and their values used by the minimiser

Diplacement Energy Multiplier:	e_1	10^{-5}
Adhesion Energy Multiplier:	e_2	2
ECM Clash Energy Multiplier:	e_3	10^{-5}
Simplex Reflection Coefficient:	α_{min}	-1.0
Simplex Expansion Coefficient:	γ_{min}	-2.0
Simplex Reflection Coefficient:	ρ_{min}	0.5
Simplex Shrink Coefficient:	σ_{min}	0.5

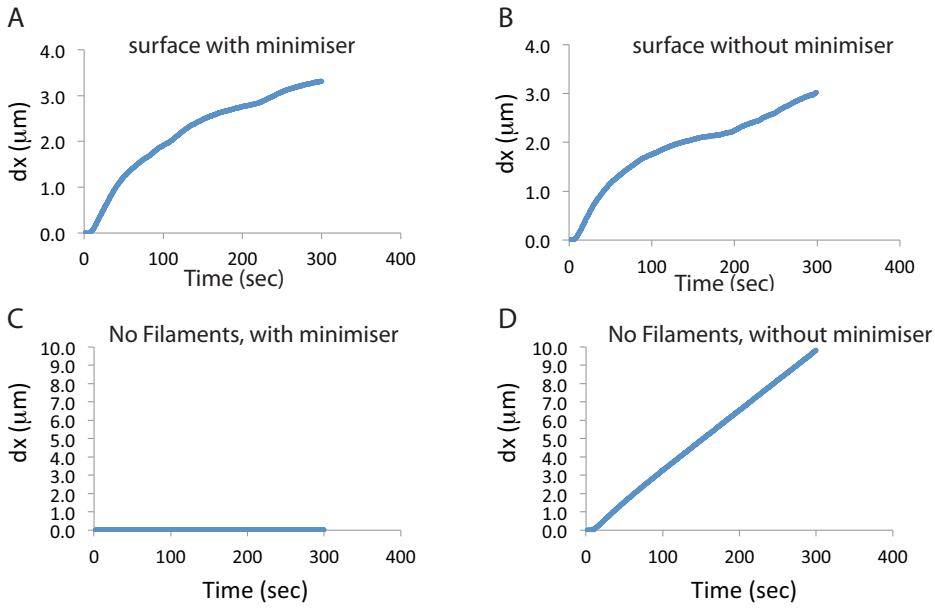

Figure 2.24: Displacement (in x-dir) plotted as a function of time, in 600 second simulations, with and without the minimiser. A) Displacement profile of a cell crawling on a surface, with minimiser utilised. B) Displacement profile of a cell crawling on a surface, without the minimiser. C) Displacement profile of a cell with no filament interactions, with minimiser utilised. D) Displacement profile of a cell with no filament interactions and without the minimiser. As demonstrated, in environments where the cell can anchor to the filaments, the minimiser does not affect the velocity profile. However, the minimisation procedure eliminates cell drift, conserving momentum, when there are no interactions with ECM filaments.

2.10 Investigated Scenarios

2.10.1 The Modelled Motility Types

In the model, the features of mesenchymal, amoeboid crawling and amoeboid blebbing cells are incorporated. Since the aim of the study is to dissect the efficiency of these motility modes, simulations are ran for (i) a cell that has only polarised contractility, with neither blebs, nor protrusions, (ii) a cell that has only the ability to form actin polymerization based protrusions but not membrane blebs, (iii) a cell that has the ability to form membrane blebs but not actin polymerization based protrusion, and finally (iv) a cell with the ability to form both actin polymerization based protrusions and plasma membrane blebs. Cells (i) to (iv) have been simulated for a range of cell polarity levels in all protein levels. As demonstrated in the following chapters, the cell listed in (iv) reproduced the plasticity of cell motility, i.e. demonstrated the ability to adapt its motility mode to the most effective motility upon changes in the geometry of the ECM.

2.10.2 Definition of Polarity

The polarity of the cell in terms of its myosin II driven contractility, ERM levels and actin polymerization based protrusion initiation frequency are investigated. It should be noted that in the model, the myosin levels and actin polymerization based protrusion initiation are inherently coupled (Eq. 2.59), however, the scenarios where the cell possessed polarity in protrusion formation, but without contractile polarity, are also investigated.

Polarity of any protein, m, is provided as an input to the simulations, with four parameters: The strength of polarity - f^m_{polar}, the origin of polarity - θ^m_{ori}, the extent of polarity - θ^m_{ext}, and the range of the transition - θ^m_{trn}. The strength of a protein's polarity is defined as its percentage increase with respect to the overall expression level. The origin, extent, and transition range of polarity are defined as angles in degrees. To assign the extent of protein polarity to cell surface agents, the positions of each agent is projected on a circle centred at the cell centre of mass (Figure 2.25A). Then the corresponding protein level is calculated from the four parameters listed above (Figure 2.25B). During simulations, depending on

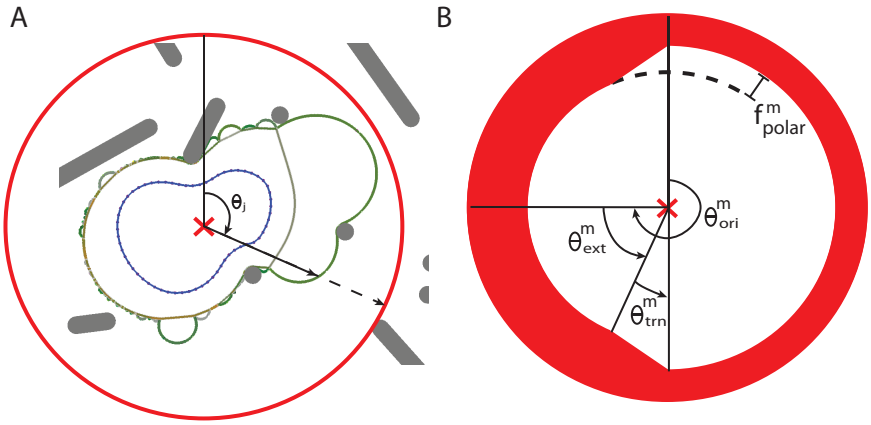

Figure 2.25: A) Mapping of the cell surface agents to their positions on the cell polarity scale. An agent on the surface of a retracting bleb, pointed by the black arrow, is projected on the circle, centred at the centre of mass of the cell. The polarity orientation of agent j is read as θ_j, the angle its position forms with respect to (+)ve y-direction. B) Schematic representing the terms used in defining polarity, see text for details. The thickness of the red contour represents the concentration of the protein of interest, m.

the environments, cells can adapt the origin of polarity of any given protein, as a response to readouts of the extracellular environment.

For myosin II driven contractility, the magnitude of the equilibrium myosin concentration is shifted by the obtained polarity. Then the equilibrium myosin levels are utilised to define the dynamics of the actual myosin levels within the cell surface agents (Eq. 2.16). For ERM proteins, the read value represents the mean ERM concentration within the agent. The CDF curve, from which the probabilities are sampled and ERM levels updated accordingly, is shifted, to bring the mean to the value dictated by polarity. For protrusion initiation rates, the calculated occurrence rate is scaled according to the dictated polarity.

2.10.3 Extracellular Matrix Geometries

The environments investigated by the model start form simple unconfined 2D surfaces (Figure 2.26A). Simulations then progress to investigating the movement of a cell confined between two parallel surfaces, and multiple setups with variations in the gap size d_{TUBE}, the distance between the two surfaces (Figure 2.26B). Initial discontinuity is introduced to the ECM in the form of regular matrices, with the

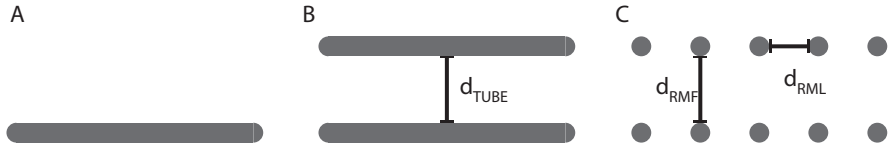

Figure 2.26: Simple extracellular environment topologies investigated in this work. A) An unconfined surface. B) Two surfaces between which the cell is confined. C) A regular matrix setup. The diameter of the filament cross-section is obtained from experimental data. For environments in (B) and (C), a range of simulations are carried with changing gap sizes marked on the schematics.

filament cross-section diameter obtained from experiments (Figure 2.26C). For these regular matrices, multiple setups with variations in both frontal and lateral gap sizes, d_{RMF} and d_{RML} respectively, have been investigated.

In vivo collagen matrices can have aligned fibres, but in most cases, there will be variation in orientation of the fibres of a tissue. Therefore 2D slice of this environment will generate filament cross-sections in a variety of angles, resulting in circular and ellipse like filament slices. Following the characterisation of the relation between cell motility modes and ECM geometry within the above setups, *in vivo* mimetic ECMs are generated, initially with constant filament shape (Figure 2.27A), and then in the final, most realistic setup, with variation in 2D cross-section slice angles of the 3D fibres, generating both circular and surface like filaments (Figure 2.27B). To ensure a range of ECM gap sizes are sampled, multiple such environments are constructed. The gap size distribution in these *in vivo* mimetic environments are matched to an experimentally derived distribution of interstitial collagen gap sizes taken from an *in vivo* murine tissue sample.

Due to the stochastic nature of the simulations, the velocity of the cell under the same intracellular conditions, and within the same environment, can show variation between repeated simulations. All of the velocity values reported throughout this thesis are averaged values taken from at least ten simulation runs under the same intra- and extra- cellular conditions.

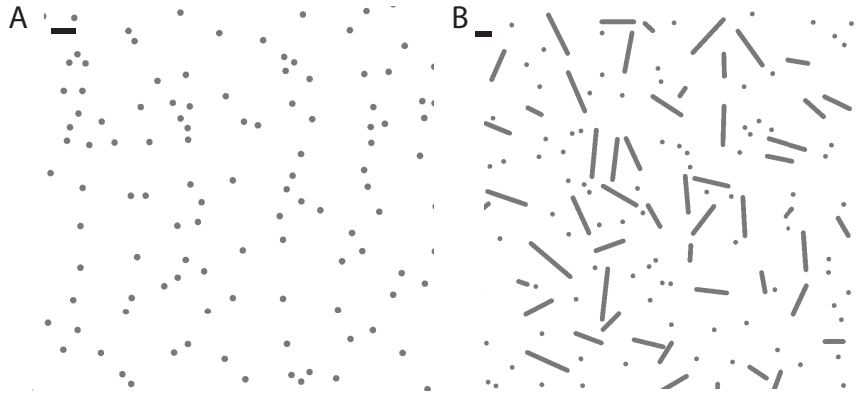

Figure 2.27: *in vivo* mimetic extracellular environment geometries used for simulations. A) Simple random matrix, constructed from circular ECM fibre cross-sections only B) Complex *in vivo* mimetic random matrix, with embedded surfaces, representing variable cross-section angles for ECM fibres. Scale bars indicate 5 μm.

2.11 The Front End of the Simulation Platform

For visualisation purposes, and for ease of use of the developed simulation platform, a front end package is developed (Figure 2.28). Simulations can be run in visualisation mode, with on the run display, simulation snapshot recording, and recording the state of the simulation environment (cell and ECM)every 1s. Alternatively, the simulations can be run without the visual interface, with only the state of the environment recorded. The recorded states include coordinates, all protein levels, bleb/actin polymerisation based protrusion states, and polarity levels. The visualisation interface can be utilised to visualise the saved simulation, and save snapshots if desired.

The visualisation interface is interactive, with multiple display options, making it possible to observe the dynamics of any specific protein, or any selected subset of forces. The visualisation package is developed using the programming language OpenGL.

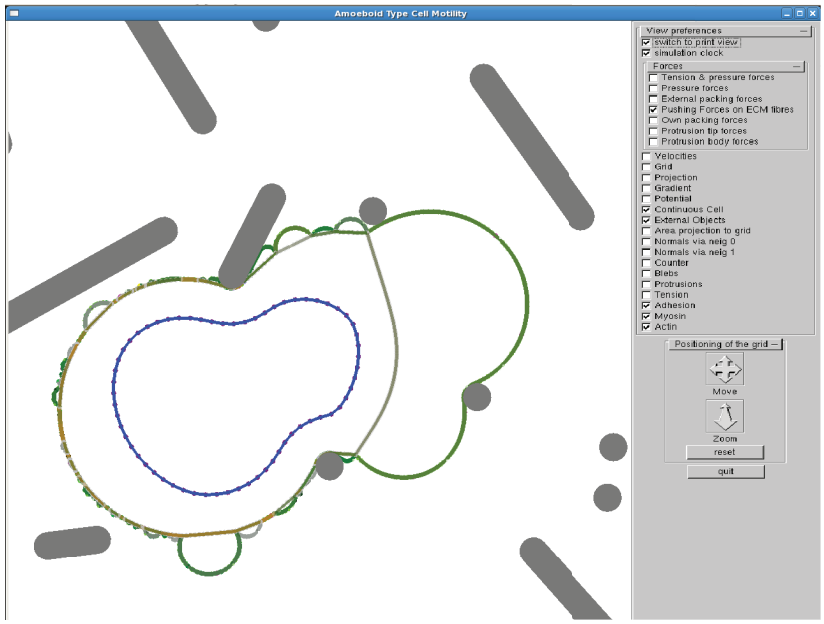

Figure 2.28: A screen snapshot from the visualisation interface of the simulation package. On the left, display options can be seen. The choices of force display options are given on the top panel. Actin, myosin and membrane levels in each linker of the system can be displayed individually, or overlayed. On each of the agents, ERM densities or the state of the agent, such as its adhesion or blebbing state, can be marked. Display of the tension/compression state of the actin linkers is also available.

Chapter 3

Model Parameterisation

3.1 Introduction

This chapter describes the selection of models parameters, which were introduced in Chapter 2. Some of the model parameters are calculated from measurements available in the published literature. The rest are obtained from measurements taken from the experiments introduced in this chapter. Some parameter values could be directly measured, such as cell size, the probability distribution of ERM proteins on the cell surface, and the actin accumulation rate at plasma membrane bleb rims. Others, such as the cell internal viscosity and the average adhesion strength of the ERM proteins are not directly measured, but fitted to measurements of bleb and actin polymerisation based protrusion dynamics. Wherever possible, model parameter optimisations begin with parameter values obtained from experiments. The model is parametrised against the A375 melanoma cell line. A list of all model parameters is given in Table 3.1.

The experimental data associated with the model development that is presented in this chapter is generated by Tumour Cell Biology Laboratory, based within the London Research Institute of Cancer Research UK. The author of this thesis has taken part in the analysis of the experimental data, but the experiments were not conducted by her.

Table 3.1: Model Parameter Descriptions and Values

Model Parameter	Parameter Description	Value Used in Simulations	Reference
Cell diameter	-	$18\mu m$	This study
F-actin cortex parameters			
k^0_{cor}	Cortex spring constant at resting state	$240 pN\mu m^{-1}$	Calc. (27)
η^0_{cor}	Cortex damping coefficient at resting state	$6000 pNs\mu m^{-1}$	Calculated from (27, 168)
τ_a	Actin renewal time	$40s$	(15)
B^0_{cor}	Bending modulus of the cortex and the membrane, resting state	$0.215 pN\mu m$	(35)
B^{bleb}_{cor}	Bending modulus of the cor. and the mem., onset of blebbing	$0.047 pN\mu m$	(35)
Myosin parameters			
k^0_{myo}	Myosin II driven contractility spring constant, rest. state	$720 pN\mu m^{-1}$	Calc. (27, 35)
D_{eff}	Effective diffusion constant of myosin II	$0.099 s^{-1}$	Calc. (23)
Membrane parameters			
S^{pool}_{mem}	Total membrane pool normalised to resting cell size	1.4	This study
$\delta_{stretch}$	Maximum stretch percentage for the membrane	4 %	(42)
k_{tear}	Maximum membrane spring constant	$20000 pN\mu m^{-1}$	Calc. (22)
The cytoskeleton and the cytoplasm (internal cell body) parameters			
K_{cyt}	Internal cell body bulk modulus	$2250 Pa$	Calc. (27)
P^0_{CELL}	Hydrostatic pressure of the cell at resting state	$80 Pa.$	Calc. (27, 35)
η_{cyt}	Internal cell body damping coefficient at resting state	$100 pNs\mu m^{-2}$	Fitted to data
Nucleus parameters			
Diameter	–	$10\mu m$	This study
K_{nuc}	Nucleus bulk modulus	$6750 Pa$	Calc. (27, 45, 46)
P^0_{nuc}	Pressure difference of the nucleus and cyt. at resting state	$0\ Pa.$	Calc. (27, 45, 46)

Table 3.1 continued on next page

Table 3.1 continued from previous page

Model Parameter	Parameter Description	Value Used in Simulations	Reference
η_{nuc}	Damping coefficient of the internal nucleus body	$200 pN s \mu m^{-2}$	Calc. (45, 46)
k_{lam}	Nuclear lamina spring constant	$720 pN \mu m^{-1}$	Calc. (27, 45, 46)
η_{lam}	Nuclear lamina damping coefficient	$18000 pN s \mu m^{-1}$	Calc. (27, 45, 46)
B_{lam}	Nuclear lamina bending modulus	$0.645 pN \mu m$	Calc. (27, 35, 45, 46)
ERM parameters			
$F_{unnitattach}$	Adhesion force per unit cortex–membrane linker protein	$10 pN$	Fitted to data
Plasma membrane bleb parameters			
f_{cor}^{bleb}	Residual cortex fraction of the bleb rim at bleb initiation	0.2	Fitted to data
Δt_{cor}	Delay for actin accumulation initiation at the bleb rim	$3 \pm 2.85 s$	This study
Δt_{myo}	Delay for myosin accumulation initiation at the bleb rim	$7.3 \pm 2.4 s$	(31)
Protrusion parameters			
k_f^0	Protrusion initiation rate per agent at resting state	4×10^{-4}	Fitted to data
Un-supported growth time	–	$7.5 \pm 2.5 s$	Calc. from (63)
Cell-ECM adhesion parameters			
k_{off}^0	Unstressed dissociation rate constant	$0.01 s^{-1}$	Fitted to data
r_0	Range of the binding potential energy well	$0.5 nm$	(163)
k_{on}	association rate constant	$1000 s^{-1}$	Binding limited with d_{ECM}^{on} only.
k_b	Boltzman constant	$1.3806503 \times 10^{-23} m^2 kg s^2$	(22)
T	Temperature	310 K	Body temperature
d_{ECM}^{on}	Binding threshold	$1 nm$	Double r_0
k_{fil}	Elastic ECM fibre spring constant	$60 pN \mu m^{-1}$	Calc. from
η_{fil}	Elastic ECM fibre damping coefficient	$1500 pN s \mu m^{-2}$	Calc. from

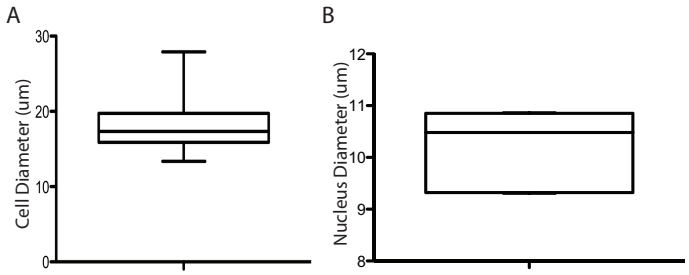

Figure 3.1: Experimental measurements of melanoma cells. A) Cell diameter. B) Nuclei diameter.

3.2 Cell and Nucleus Size

Cell diameters are measured from A375P cells, $18.12 \pm 3.34 \mu m$ (Figure 3.1A), and cell nuclear sizes, $10.3 \pm 0.7 \mu m$ (Figure 3.1B), from A375M2 cells. For modelling, a cell diameter of $18 \mu m$, and a nuclear diameter of $10 \mu m$, is selected.

3.3 The F-Actin Cortex

The actin cortex is defined by four parameters: the spring constant modelling the elastic response, k_{cor}; the damping coefficient defining the viscous response, η_{cor}; bending modulus of the cortex and the membrane, B_{cor}; and the actin renewal time, τ_a. The stiffness of the actin cortex have been measured in multiple systems, and has a wide range of $130 - 4100 pN\mu m^{-1}$, depending on the cell type (27, 35–37). In a study investigating the role of cortical tension in plasma membrane formation, the effective F-actin cortex elastic modulus, $E_c h$, has been reported to be $240 pN\mu m^{-1}$; here E_c represents the Young's modulus and h the thickness of the F-actin cortex shell (27). The model parameter k_{cor} is obtained by relating the cortex elastic resistance in the model to this measured effective elastic modulus. The magnitude of the force due to the F-actin elastic response, on a finite segment of the F-actin cortex, defined in spherical coordinates, is given as:

$$F_{cortex} = E_c \times \frac{\Delta L}{L^0_{cortex}} \times (h \times w_\phi), \tag{3.1}$$

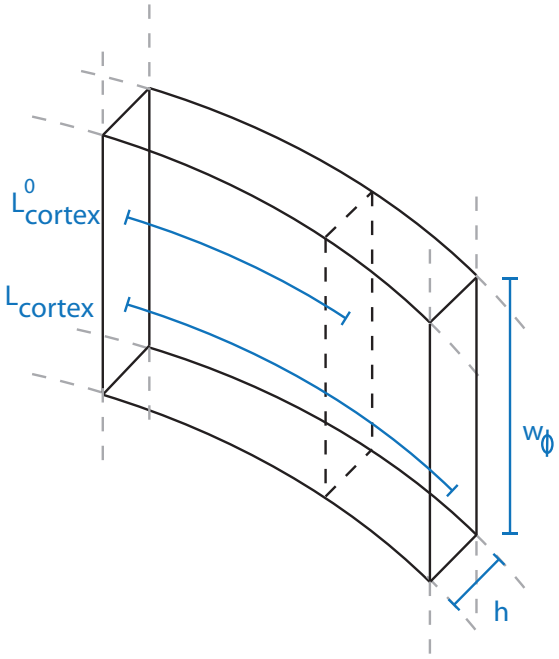

Figure 3.2: Schematic representing the discretisation of the F-actin cortex shell, in spherical coordinates. The parameters used in the calculation of the F-actin cortex spring constants, values for which were obtained from the literature (27), are illustrated. See text for more details.

where ΔL is the deviation from the ideal length of the finite segment and L^0_{cortex} is the ideal length of the segment in θ axis. w_ϕ the width of the finite segment along the ϕ axis (Figure 3.2).

The same relation for the elastic response force magnitude in the 2D model is:

$$F_{cortex} = k_{cor}\Delta L, \tag{3.2}$$

where k_{cor} is the F-actin cortex spring constant. Then combining Eq. 3.1 and 3.2, the spring constant relates to the measured effective cortex elastic modulus as:

$$k_{cor} = \frac{E_c h w_\phi}{\langle L^0_{cortex} \rangle}. \tag{3.3}$$

Here, $\langle L^0_{cortex} \rangle$ corresponds to the average ideal spring length of the linkers in

the model, and w_ϕ corresponds to w_{model}. The model cell is initially discretised by cell surface agents at 0.2 μm intervals, and the agent distribution is regulated by addition and deletion of agents, to prevent strong deviations from the initial distribution, leading to an average linker ideal distance of 0.2 μm. The model width is selected as 0.2 μm. Then, the relation in Eq. 3.3 simplifies to:

$$k_{cor} = E_c h. \tag{3.4}$$

Therefore, the spring constant of the F-actin cortex in the model is defined as $240 pN\mu m^{-1}$. The viscous damping coefficient of the F-actin cortex is scaled from the spring constant. In a study of inverse mapping of images of crawling cells to an amoeboid cell model, the ratio of viscous to elastic resistance is defined as $25s$ (168). The viscous damping coefficient of the F-actin cortex, η_{cor} is selected as $6000 pNs\mu m^{-1}$. The bending modulus at resting state in the model, B^0_{cor} and at the onset of bleb initiation, B^{bleb}_{cor} are selected from values reported for HeLa cells, $0.215 pN\mu m$ and $0.047 pN\mu m$ (35). Actin turnover time, τ_a is selected as 40 s (15).

3.3.1 Actin Reaccumulation at Bleb Rims

The actin accumulation rate at bleb rims is measured from experimental data generated by the Tumour Cell Biology Laboratory. The intensity of GFP tagged actin is measured at the bleb rim throughout the lifetime of each bleb; the intensity at each time point is normalised by the intensity of the cell background. The procedure to obtain the effective F-actin intensity of the bleb rim at any time point is given as:

$$I^{eff}_{act} = \frac{I_{act}}{I^{bg}_{act}}. \tag{3.5}$$

Here, I_{act} is the measured average actin intensity at the bleb rim, and I^{bg}_{act} is the actin intensity of the background at the same time point. The actin accumulation curve obtained by this methodology is given in Figure 3.3. The time point where the minimum actin intensity is reached is $3 \pm 2.85s$ after bleb initiation, which defines Δt_{cor}, and from this point on, the intensity increases with the fitted curve given in Eq. 2.50. The parameters reported in Section 2.7.3 are obtained from the

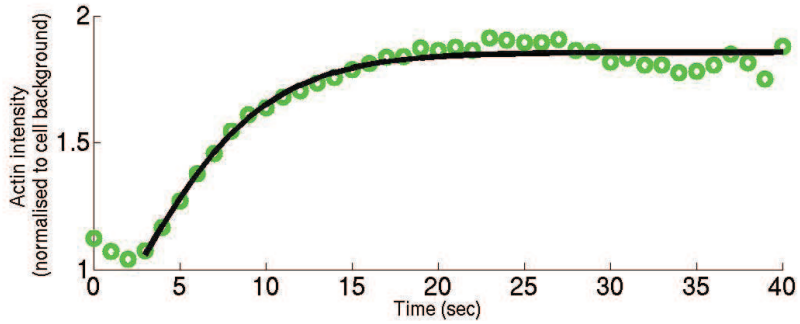

Figure 3.3: The LifeAct-GFP intensity was quantified from multiple blebs every second following bleb initiation. The normalised average values are shown in green circles and the fitted rate of actin polymerisation used in the model is shown in black.

fitted curve in Figure 3.3.

3.4 The Cytoskeleton and the Cytoplasm

The physical response of the internal cell body, the cell cytoskeleton and the cytoplasm, is defined by a bulk modulus, K_{cyt}, a viscous damping coefficient η_{cyt}, and the resting hydrostatic pressure of the cell P^0_{CELL}.

The bulk modulus of the inner cell body is calculated from the effective cytoplasmic elasticity of $6750Pa$, reported in the same publication that the actin elastic response is based on (27). This effective cytoplasmic elasticity is given as $E_{CYT}/(1-2\nu_{CYT})$, where E_{CYT} is the Young's Modulus, and ν_{CYT} Poisson's ratio of the inner cell body. The bulk modulus of the inner cell body is obtained as $2250Pa$ from the relation between the bulk modulus, Young's modulus and Poisson's ratio of elastic solids:

$$K_{CYT} = \frac{1}{3}\frac{E_{CYT}}{1-2\nu_{CYT}}. \tag{3.6}$$

The viscous damping coefficient of the internal cell body is fitted to plasma membrane dynamics, the procedure of which is given in Section 3.9.1. The starting

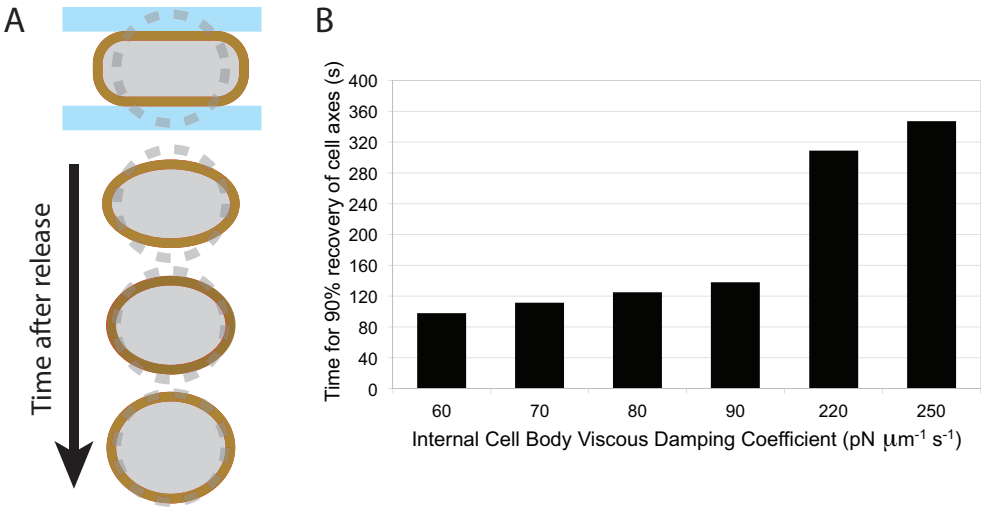

Figure 3.4: The computational experiment mimicking experiments carried out on macrophages for measurement of internal cell body viscosity. A) Schematic describing the computational experiment. Cells are released form $10\mu m$ tubes, and the time required for 90 per cent recovery to resting cell size is measured. The resting cell size is indicated by dashed lines. B) The relaxation time as a function of internal cell body viscous damping coefficient.

point for parameterisation is based on computer experiments that mimic *in vitro* experiments utilised to measure the cell body viscosity. In these experiments, the cells are sucked into tubes of diameters smaller than the cell size, then the time for each cell to recover back to its original shape upon release is measured (37, 169, 170). Recovery times are then utilised to calculate the internal cell viscosity. For macrophages of $15-18\mu m$ diameter, sucked into $10.5\mu m$ pipettes, the time required for the cells to recover their axes within 90 per cent of their resting size lie in the range $2-5min$ (37). Running these experiments in the computer model, for macrophages with the reported physical properties, the range that fits with the recovery time has been obtained as $80-200pN\ s\ \mu m^{-2}$ (Figure 3.4). Starting the parameterisation within this initial estimate rage, the internal cell viscosity is obtained as $100pN\ s\ \mu m^{-2}$.

The resting hydrostatic cell pressure for HeLa cells has been measured to be in the range, 17-110Pa. Additionally, the study to which the F-actin cortex elastic response and inner cell body bulk modulus parameterisation is based on, reports

a cortical tension of $413 pN\mu m^{-1}$ and cell diameter of $8.5\mu m$. From these values, and using Laplace's Law (Eq. 1.1), the resting pressure for the cell type of interest in their study (mouse fibroblasts) is calculated to be $97Pa$. The resting hydrostatic pressure within the cells is taken as the midpoint of these available measurements, $80Pa$.

3.5 The Myosin II Driven Contractility

The myosin II driven contractility is characterised by the myosin spring constant, k_{myo}, and the effective diffusion constant of myosin from the cytoplasm into the F-actin cortex, D_{eff}.

The internal hydrostatic pressure accumulation within the cell is driven by actomyosin contractility. The spring constants for myosin II driven contractility are selected to produce an internal pressure of $80Pa$ for an inner cell body bulk modulus of $2250Pa$, for the resting state of the cell, resulting in k^0_{myo} of 720 $pN\mu m^{-1}$.

The value of the effective diffusion constant is obtained by fitting Eq. 2.16 to the myosin recovery time obtained from photo bleaching studies, $7.01 \pm 2.62s$ (23), the value used is $0.099s^{-1}$.

3.6 The Plasma Membrane

The plasma membrane is characterised by the total membrane pool available to the cell, S^{pool}_{mem}, the maximum spring constant that membrane springs can reach, the tension that can accumulate on the membrane without rupture, k_{tear}, and the stretch limit - the fraction of membrane area increase that is necessary to increase the tension from zero to its maximum value, $\delta_{stretch}$. During the simulations, membrane spring constant, k_{mem}, is obtained from these parameters *via* Eq. 2.18.

The available membrane pool is measured experimentally. The diameters of cells with reduced adhesion are measured, such that cell spreading is avoided, and

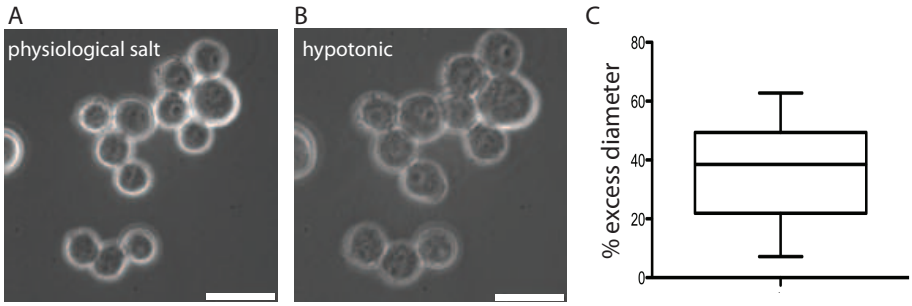

Figure 3.5: Measurement of available membrane pool for A375M2 cells. Images show A) A375M2 cells under a physiological salt concentration and B) after exposure to severe hypotonic conditions leading to cell swelling and bursting. Scale bar is 40mm. C) Average excess cell membrane, calculated in terms of per cent increase in cell diameter, by comparison of the cell diameter in physiological salt compared to the diameter at the time of bursting due to hypotonic shock.

the cell has a round morphology at its resting state. Then water is gradually added to the experimental setup, causing the cells to swell. The final diameter before the plasma membrane of the cells are torn, resulting in cell death, revealed the amount of plasma membrane available to A375P cells (Figure 3.5). As a result of these experiments, the model parameter S_{mem}^{pool} is set be 40 per cent higher than the amount necessary for the model cell circumference at resting state.

The membrane stretch limit was selected as 4 per cent (42). The tension lipid bilayer can withstand before rupture is reported to be $0.01 Jm^{-2}$ (22). The pressure such a tension level would generate on the cell is calculated from Laplace Law (Eq. 1.1). Similar to myosin II driven contractility parameterisation, the spring constant that would generate the equivalent pressure is taken to be k_{tear}, $20000 pN\mu m^{-1}$. The increase from zero to this tension is linear with increasing cell circumference length, as given in Eq. 2.18.

3.7 The F-Actin Cortex–Plasma Membrane Linkers

ERM proteins are characterised by a cumulative distribution function (CDF) curve used for modelling their fluctuations; the range of the step size used in sampling the CDF, ζ; and the adhesion force per unit adhesion protein, $F_{unitattach}$.

The cumulative distribution function used in sampling for the ERM fluctuations is obtained by measuring the PIP_2 protein intensity (see Section 1.3.2.2). The intensities on non-blebbing cell surfaces are measured from a number of images. The background intensity is then subtracted from the measurements to account for time dependent bleaching of the fluorescent protein, and the values normalised with the membrane marker channel. The procedure to obtain the effective PIP_2 intensity is given as:

$$I^{eff}_{PIP_2} = \frac{I_{PIP_2} - I^{bg}_{PIP_2}}{I_{mem} - I^{bg}_{mem}}. \tag{3.7}$$

Here, I_{PIP_2} is the measured intensity of PIP_2, and $I^{bg}_{PIP_2}$ the PIP_2 intensity of the image background. Similarly, I_{mem} and I^{bg}_{mem} are the measured intensities of the plasma membrane marker on the cell surface and at image background, respectively. The data points are normalised relative to the mean, and the probability distribution, sampled by the inverse transform sampling method as explained in Section 2.5.0.2, is obtained (Figure 3.6).

During each concentration update event, the step size, ζ, is randomly selected within the range $\pm 5\%$ of the current local concentration.

The adhesion strength per unit adhesion protein is fitted to an analysis of the dynamics of blebbing. The starting point for parameterisation is based on experiments where membrane tethers are pulled from the cell membrane and the forces required to generate these tethers measured. The formed tethers have a radius in the range $0.2 - 0.3\mu m$, and the forces necessary to pull these tethers vary in the range $10 - 22\ pN$. In the model, the cortex–membrane adhesion protein unit is defined as being normalised per agent, i.e. the number does not necessarily correspond to the number of linker proteins. At the resting state of the cell, the mean value of adhesion protein unit per agent is set to unity. Since the average length associated with an agent of the model is $0.2\mu m$, $F_{unnitattach}$ should then be in the range $7 - 22pN$. Starting the fitting procedure from this initial point, the final value of $10pN$ is assigned to $F_{unitattach}$.

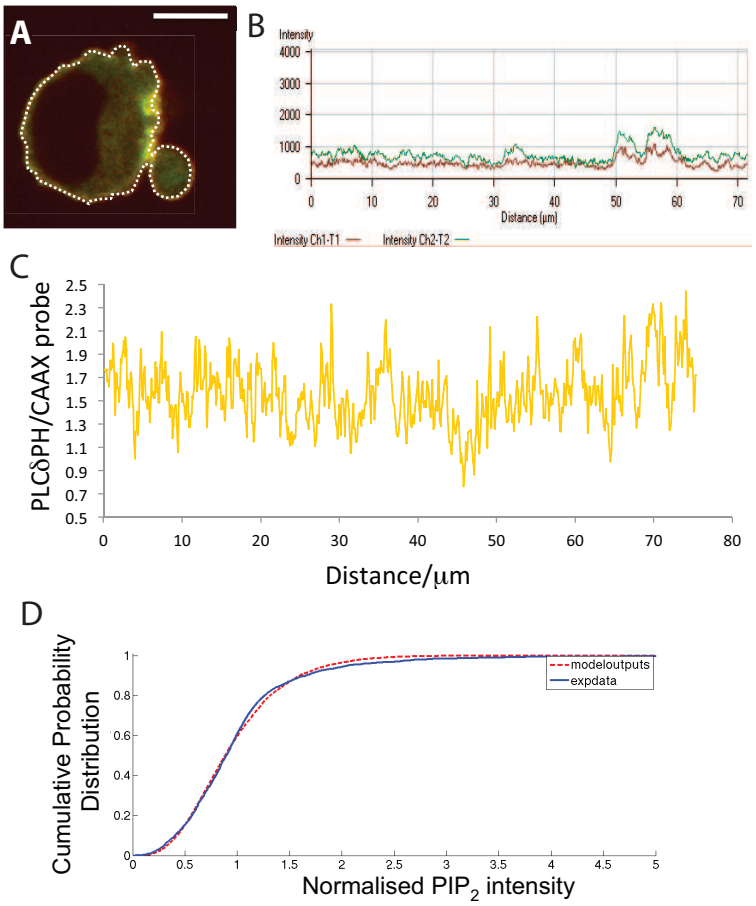

Figure 3.6: A) Fluctuations in the PIP_2 levels over the cell surface. Image shows merged PLCdPH-GFP (labelling for PIP_2), mRFP-CAAX (labelling for the lipid plasma membrane), and line tracing of the cell membrane. Scale bar is 10 microns B) Plot showing PLCdPH-GFP and mRFP-CAAX intensity along the line traced in the left hand side image. C) Profile of the PLCdPH-GFP signal divided by the mRFP-CAAX signal along the line traced in image (A). D) Experimentally derived cumulative probability distribution of PIP_2 in A375 cells, normalised and shown in blue. Distribution was derived only from the plasma membrane and not internal areas of the cell. The resulting distribution obtained from the model simulations is shown in red.

3.8 The Nucleus

The physical responses of the nucleus are characterised by the spring constants of the nuclear lamina, k_{lam}; the viscous damping coefficient of the nuclear lamina η_{lam}; the viscous damping coefficient, ηnuc; and the bulk modulus of the inner body of the nucleus, K_{nuc}.

All the parameters of the nucleus are scaled from the properties of cell F-actin cortex and the cytoskeleton. The nucleus is set to be three times stiffer than, and twice as viscous as, the cell cortex and internal cell body, setting k_{lam} at $720pN\ \mu m^{-1}$, η_{lam} at $18000pN\ s\ \mu m^{-1}$, B_{lam} at $0.645pN\ \mu m$, η_{nuc} at $200pN\ s\ \mu m^{-2}$, and K_{nuc} at 6750 Pa.

Although this scaling is reported in the literature, the parameters are also tested with a cell spreading analysis. Spreading cells obtain a pancake shape, their nucleus being pushed against the surface and being deformed from its spherical shape (Figure 3.7A). The diameter of the nucleus for a spread cell depends on the physical properties of the cell, and can be used as a crosschecking point for the validity of selected nucleus parameters. The nuclear area of A375M2 melanoma cells allowed to spread on collagen surfaces *in vitro*, were measured for the control state, for Y27632 treated cells with reduced myosin II driven contractility and for Dasatinib treated cells with increased myosin II driven contractility (Table 3.2). The average nuclei diameters are calculated for the equivalent circular areas. With the contractility values listed in Table 3.2, computational experiments are carried out and the maximum nuclei diameters are measured. The values obtained from experiments give a mean nucleus diameter of $11.67 \pm 2.11 \mu m$, $13.10 \pm 1.47 \mu m$, and $10.30 \pm 0.70 \mu m$ for control, Y27632 treated and Dasatinib treated, respectively. Equivalent computational experiment results are $10.94 \pm 0.56 \mu m$, $11.79 \pm 0.58 \mu m$, and $10.12 \pm 0.27 \mu m$, in the same order (Figure 3.7B).

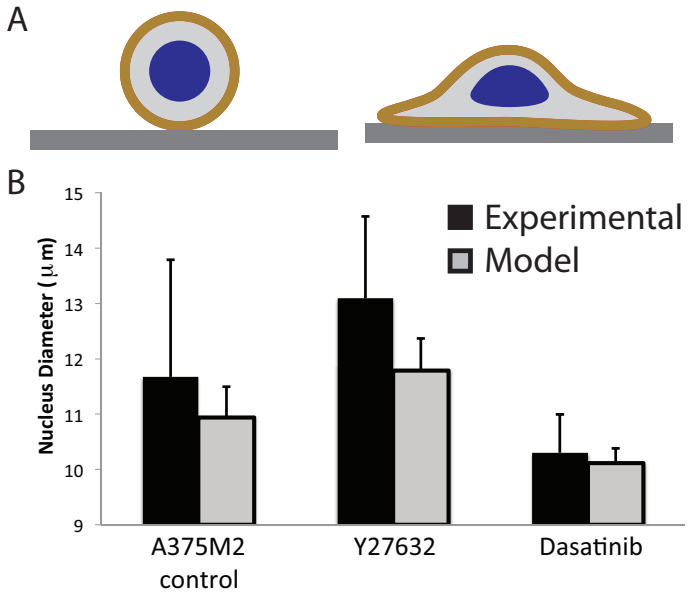

Figure 3.7: A) Schematic showing the nuclei diameter increase upon spreading of a cell. B) The experimental measurements (black) and model outputs (grey), for the nucleus size of A375M2 cells. Control conditions, treatment with reduced (Y27632) and increased (Dasatinib) myosin II driven contractility are demonstrated (see Table 3.2 for the numerical representation of the contractility scaling after treatments.).

Table 3.2: Overall contractility of A375M2 cells under biochemical perturbation for nucleus size measurements

	Contractility scaled to A375P cells
A375M2 control	1.4
+Y27632	0.59
+Dasatinib	1.95

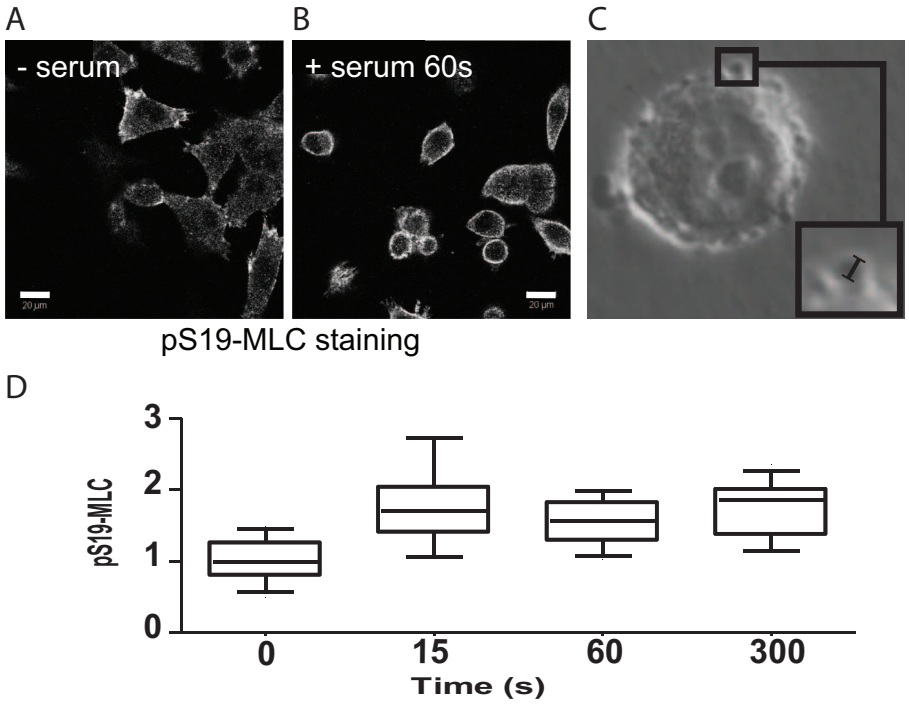

Figure 3.8: A) A375P cells on collagen, in serum-free media. B) A375P cells after addition of 1 % serum. Plasma membrane blebbing can be seen. Scale bars 20 μm C) A blebbing cell, inset shows the measurement of the size of a bleb. D) Quantification of myosin II activity increase upon 1 % serum stimulation.

3.9 Plasma Membrane Bleb Dynamics

The dynamics of plasma membrane blebbing is measured in experimental setups, and model parameters that cannot be measured directly, or calculated form data available in the published literature, are fitted to reproduce the measured bleb dynamics. The fitted parameters are the viscous damping coefficient of the internal cell body, η_{cyt}; adhesion strength per unit cortex-membrane attachment protein, $F_{unitattach}$; and residual actin cortex at the bleb rim at the onset of bleb initiation, f_{cor}^{bleb}.

In the experimental setups, A375P melanoma cells are allowed to spread on collagen in serum-free media. Then these cells are stimulated by one per cent serum, resulting in increased myosin II activity, rounding up of the cells on the collagen, and plasma membrane blebbing (Figure 3.8).

Bleb sizes are measured from their base, to the furthest point on their rim (Figure 3.8B, inset). Image analysis was done using the ImageJ software. Bleb expansion and retraction velocities are obtained *via* three-point averaged bleb size measurements taken from time-lapse image data. Retraction velocity is defined as the rate of shrinkage of the bleb size, i.e. the directions of expansion and retraction velocities are defined in reference frames of opposite directions. Model parameters are fitted to maximum bleb size, maximum bleb expansion velocity and maximum bleb retraction velocity.

Computational experiments mimicking serum-stimulated cells were carried out, with a myosin concentration increase of one hundred per cent. The analysis of blebs in the computational experiments is based on the same rules as experimental measurements. In the simple definition of bleb necks, tearing of the bleb results in re-alignment of the bleb-neck, i.e. the bleb base where the bleb size measurements are referenced. To avoid measuring artificially high bleb expansion velocities due to this reference point change, bleb size measurement of a bleb at the time step of a tearing event are not included in the analysis.

For the computational experiments, all membrane detachment areas can be measured, even those too small to be detected experimentally from light microscopy imaging. To confirm the existence of small blebs, SEM images of blebbing cells under the same experimental conditions are taken (Figure 3.9). Following the confirmation of small blebs in real cells, bleb dynamics data generated by the model for only blebs of sufficient size are included in comparison with the experimental measurements. The threshold of size is selected as the minimum bleb size that could be measured in light microscopy experiments, which is $0.51\mu m$.

3.9.1 Parameter Fitting Procedure

For maximum bleb size, maximum bleb expansion velocity and maximum retraction velocity measurements, for both experimental and computational experiments, cumulative distribution functions are prepared. Bin sizes for generating the cumulative distributions are selected as $0.0025\mu m$ for maximum bleb size, and $0.005\mu m s^{-1}$ for bleb expansion and retraction rates. Then the R^2 fit between

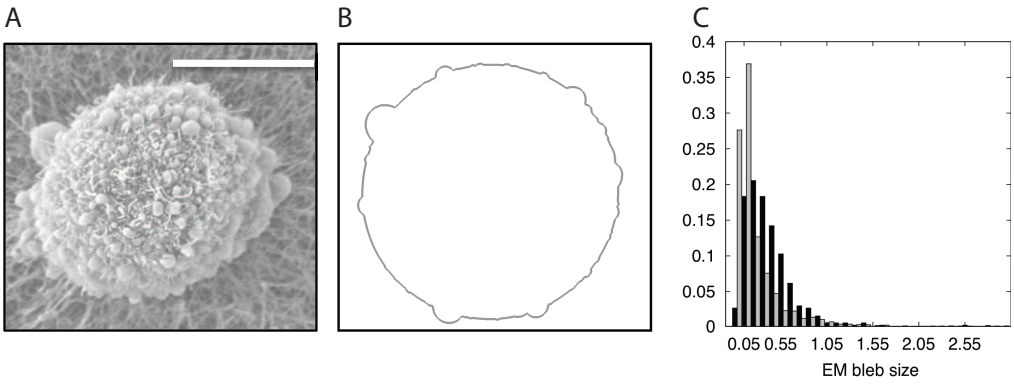

Figure 3.9: A) SEM image of a blebbing cells, showing numerous small blebs under the resolution limit for which blebs can be observed in videos generated from light microscopy. B) Image showing a snapshot of bleb sizes from a simulation under equivalent level of contractility relative to the experimental conditions of (A). C) Histogram showing bleb size distribution from random snapshots taken during simulations (grey), and experimental measurements (black). The sizes are reported above the threshold of $0.067\mu m$, below which it is not possible to distinguish actin polymerisation protrusions from plasma membrane blebs in SEM data.

experimental data, and data from each of the parameter sets from the computational experiments are calculated (171). For this, the total sum of squares, SS_{tot} and residual sum of squares SS_{res} are calculated from each bin point value y_i of the cumulative distribution function obtained from the computational experiment, and each bin point value f_i of the cumulative distribution function of the experimental data. The formulation is then:

$$SS_{tot} = \sum_i (y_i - \bar{y})^2, \tag{3.8}$$
$$SS_{err} = \sum_i (y_i - f_i)^2,$$

where $\bar{y}$ is the average of all bin point. Then R^2 is calculated as:

$$R^2 = 1 - \frac{SS_{err}}{SS_{tot}}. \tag{3.9}$$

The parameter set with the highest R^2 score for the average of all three cumulative distributions (size, expansion and retraction velocities), is selected as the fitted

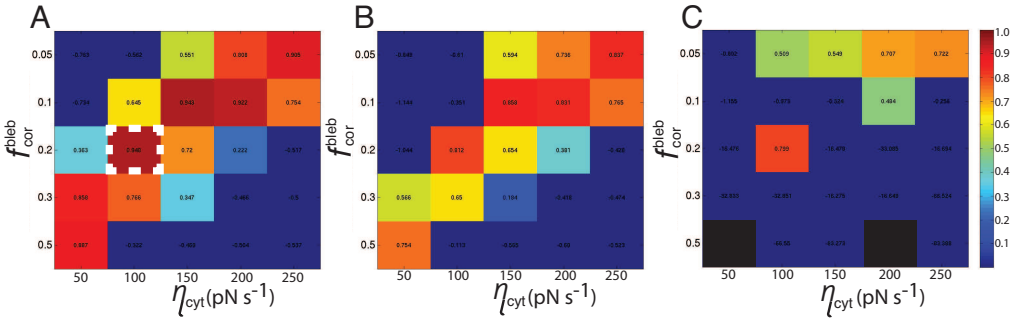

Figure 3.10: The average of R^2 for maximum bleb expansion velocities, maximum bleb retraction velocities and maximum bleb sizes, reported as a function of η_{cyt} and $f_{cor}bleb$. A) $F_{unitattach}$ is 10 pN, B) 20 pN and C) 30 pN. Black marked regions indicate the computer model simulations did not form blebs for analysis. The selected parameter set is marked by the dashed white box.

model parameter set. The results for the scanned parameter ranges are reported in Table 3.3 in descending order with respect to the average of the three R^2 scores. All results are an average of ten independent simulations, summing up to 100$mins$ of simulation time. The effects of different parameters can be seen from the heat-maps of average R^2 in Figure 3.10.

Table 3.3: Parameterisation of the model with bleb dynamics data. first three columns give the values of model parameters for a given parameter set. R^2 - $\mathbf{v}_{EXP}$ is the R^2 fit score for maximum bleb expansion velocity, R^2 - $\mathbf{v}_{RET}$ is the R^2 fit score for maximum bleb retraction velocity, and R^2 bleb size is the R^2 fit score for maximum bleb size. The parameter sets are ranked in ascending order for the average of three R^2 values, reported in the rightmost column.

η_{cyt} ($pN\ s\ \mu m^{-2}$)	$F_{unitattach}$ ($pN per\ unit\ adesion$)	f_{bleb}^{frac}	R^2 - $\mathbf{v}_{EXP}$	R^2 - $\mathbf{v}_{RET}$	R^2 bleb size	# of bleb ($10 min^{-1}$)	$< R^2 >$
100	10	0.2	0.95	0.96	0.93	91.67	0.948
150	10	0.1	0.91	0.97	0.95	124.83	0.943
200	10	0.1	0.89	0.95	0.93	117	0.923
250	10	0.05	0.8	0.98	0.95	134.5	0.909
50	10	0.5	0.82	0.97	0.88	69.33	0.889
50	10	0.3	0.72	0.95	0.92	91.17	0.864
150	20	0.1	0.75	0.95	0.89	36.83	0.862
250	20	0.05	0.65	0.96	0.94	53.5	0.85
200	20	0.1	0.74	0.91	0.86	36	0.834
200	10	0.05	0.57	0.98	0.94	139	0.831
100	20	0.2	0.78	0.91	0.76	15.5	0.815
100	30	0.2	0.91	0.84	0.67	1.67	0.806
100	10	0.3	0.53	0.94	0.9	83.83	0.791
200	20	0.05	0.44	0.98	0.93	57.17	0.783
250	10	0.1	0.52	0.89	0.93	114.5	0.779
250	20	0.1	0.6	0.85	0.88	34	0.776
150	10	0.2	0.44	0.91	0.92	94.67	0.76
50	20	0.5	0.75	0.82	0.7	4.5	0.756
200	30	0.05	0.41	0.96	0.89	18.5	0.756
250	30	0.05	0.47	0.93	0.87	15.33	0.754
100	10	0.1	0.29	0.96	0.96	124	0.737

Table 3.3 continued on next page

Table 3.3 continued from previous page

η_{cyt} ($pN\ s\ \mu m^{-2}$)	$F_{unitattach}$ ($pN per\ unit\ adesion$)	f_{bleb}^{frac}	R^2 - $\mathbf{v}_{EXP}$	R^2 - $\mathbf{v}_{RET}$	R^2 bleb size	# of blebs ($10 min^{-1}$)	$< R^2 >$
150	20	0.05	0.23	0.97	0.92	58.67	0.71
150	10	0.05	0.18	0.97	0.94	142.67	0.699
150	20	0.2	0.42	0.85	0.79	18.33	0.684
150	30	0.05	0.2	0.96	0.85	16.83	0.67
100	20	0.3	0.48	0.82	0.7	12.5	0.665
100	30	0.05	0.16	0.96	0.85	17.67	0.656
50	20	0.3	0.27	0.94	0.71	12.33	0.64
50	10	0.2	0.06	0.9	0.94	104	0.634
100	20	0.1	-0.05	0.97	0.89	32.33	0.602
150	10	0.3	0.05	0.84	0.9	76.67	0.6
200	30	0.1	0.18	0.85	0.74	5.67	0.59
200	10	0.2	0.02	0.82	0.89	88.83	0.575
100	10	0.5	-0.05	0.86	0.85	64.67	0.552
100	10	0.05	-0.21	0.93	0.93	145.83	0.551
200	20	0.2	0.1	0.75	0.75	13	0.534
100	20	0.05	-0.27	0.93	0.89	59.67	0.516
150	30	0.1	-0.05	0.89	0.71	6.33	0.513
250	30	0.1	-0.03	0.79	0.75	6.17	0.505
200	10	0.3	-0.16	0.74	0.88	72.5	0.489
150	20	0.3	0.01	0.73	0.73	13.33	0.488
250	10	0.2	-0.21	0.75	0.88	84	0.476
50	10	0.1	-0.47	0.88	0.96	130.33	0.458
150	10	0.5	-0.17	0.7	0.84	62.83	0.456

Table 3.3 continued on next page

Table 3.3 continued from previous page

η_{cyt} ($pN\ s\ \mu m^{-2}$)	$F_{unitattach}$ ($pN per\ unit\ adesion$)	f_{bleb}^{frac}	R^2 - $\mathbf{v}_{EXP}$	R^2 - $\mathbf{v}_{RET}$	R^2 bleb size	# of blebs ($10 min^{-1}$)	$< R^2 >$
250	10	0.3	-0.23	0.62	0.86	70.5	0.416
100	20	0.5	0	0.63	0.57	5.67	0.401
250	20	0.2	-0.18	0.64	0.68	15.67	0.379
200	10	0.5	-0.27	0.58	0.82	53.17	0.377
50	30	0.05	-0.68	0.87	0.87	17.83	0.351
250	20	0.3	-0.27	0.53	0.76	7.83	0.339
200	20	0.3	-0.21	0.56	0.63	8.67	0.327
250	10	0.5	-0.45	0.42	0.82	57.67	0.262
150	20	0.5	-0.5	0.5	0.71	4.83	0.237
50	20	0.05	-1.02	0.74	0.81	54.33	0.179
50	10	0.05	-0.93	0.59	0.8	106.33	0.157
200	20	0.5	-0.91	0.5	0.69	4.17	0.093
100	30	0.1	-1.37	0.91	0.73	6.83	0.091
50	20	0.2	-1.53	0.95	0.78	19.67	0.068
50	20	0.1	-1.75	0.93	0.92	33.83	0.032
250	20	0.5	-1.26	0.22	0.51	3.83	-0.176
50	30	0.1	-2.29	0.93	0.72	6.67	-0.213
150	30	0.3	-16.74	-16.01	-16.08	4	-16.278
150	30	0.2	-17.22	-16.03	-16.21	5	-16.486
50	30	0.2	-17.49	-15.92	-16.06	5.67	-16.491
200	30	0.3	-17.74	-16.11	-16.15	4.17	-16.665
250	30	0.2	-17.76	-16.18	-16.19	5	-16.71
50	30	0.3	-32.84	-32.78	-32.88	7.17	-32.833

Table 3.3 continued on next page

Table 3.3 continued from previous page

η_{cyt} ($pN\ s\ \mu m^{-2}$)	$F_{unitattach}$ ($pN per\ unit\ adesion$)	f_{bleb}^{frac}	R^2 - $\mathbf{v}_{EXP}$	R^2 - $\mathbf{v}_{RET}$	R^2 bleb size	# of blebs ($10 min^{-1}$)	$< R^2 >$
100	30	0.3	-32.88	-32.8	-32.88	7	-32.851
200	30	0.2	-33.4	-32.86	-32.99	7.33	-33.086
250	30	0.3	-66.79	-66.42	-66.36	13.17	-66.524
100	30	0.5	-66.69	-66.48	-66.48	13.17	-66.55
150	30	0.5	-83.44	-83.2	-83.18	16	-83.273
250	30	0.5	-83.64	-83.27	-83.25	16.17	-83.388
200	30	0.5	–	–	–	–	–
50	30	0.5	–	–	–	–	–

From these parameter sets, the highest scoring one is selected, giving η_{cyt} as $100pN\ s\ \mu m^{-2}$, $F_{unitattach}$ as $10pN$, and f_{cor}^{bleb} as 0.2. The histograms for maximum bleb size, maximum bleb expansion velocity and maximum bleb retraction velocity are given for the experimental measurements, and the computational experiments for the selected parameter set are given in Figure 3.11.

3.10 The Actin Polymerisation Based Protrusion Dynamics

Protrusion initiation rate is characterised by protrusion initiation rate constant under resting myosin levels, k_f^0, and the function relating the protrusion occurrence rate on myosin II concentration, Eq. 2.59, both of which are fitted to experimental data generated by the Tumour Cell Biology Laboratory.

Cells with varying levels of myosin II activity are generated my serum stimulation (increased contractility) and Y27632 treatment (reduced contractility) (Figure 3.12A). It is necessary to translate the protrusion formation data observed from the experiments to the 2D cell cross-section in the model. To mimic these cross-sections, four lines were constructed, bisecting the cell at 45 degree angles. The presence or absence of a protrusion at each intersection point of the cell cortex at these lines are counted. The number obtained for each cell is divided by four, to give a protrusion occurrence rate that can be fitted with the model. In the equivalent computational experiments, the number of protrusions spreading on the surface are counted for a range of myosin II levels. The resting protrusion initiation rate constant that best fit the protrusion occurrence rate at control conditions is obtained as 4×10^{-4}, and the parameter b_{prot} in Eq. 2.59, is fitted as 1.39 (Figure 3.12B).

3.11 Cell–Extracellular Matrix Adhesion Levels

Adhesion events are characterised by the association rate constant, k_{on}; binding threshold, d_{on}; unstressed dissociation rate constant k_{off}^0; and the range of the

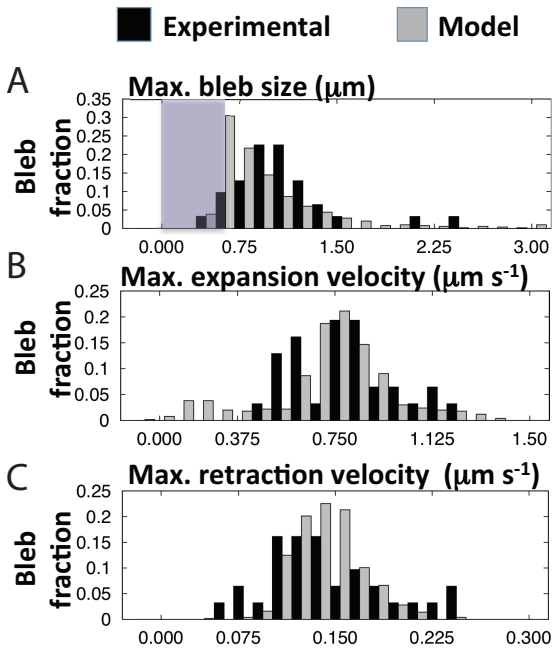

Figure 3.11: The histograms show the maximum bleb size, bleb expansion velocity and bleb retraction velocity values from experiments (black) and the model outputs, with the selected parameter set (grey). Experimental measurements done at 1 % serum stimulation. A) Maximum bleb sizes. The blue shading indicates the bleb size range where the accuracy of measurements are effected by the resolution of light microscopy. B) Maximum bleb expansion velocities and C) Maximum bleb retraction velocities.

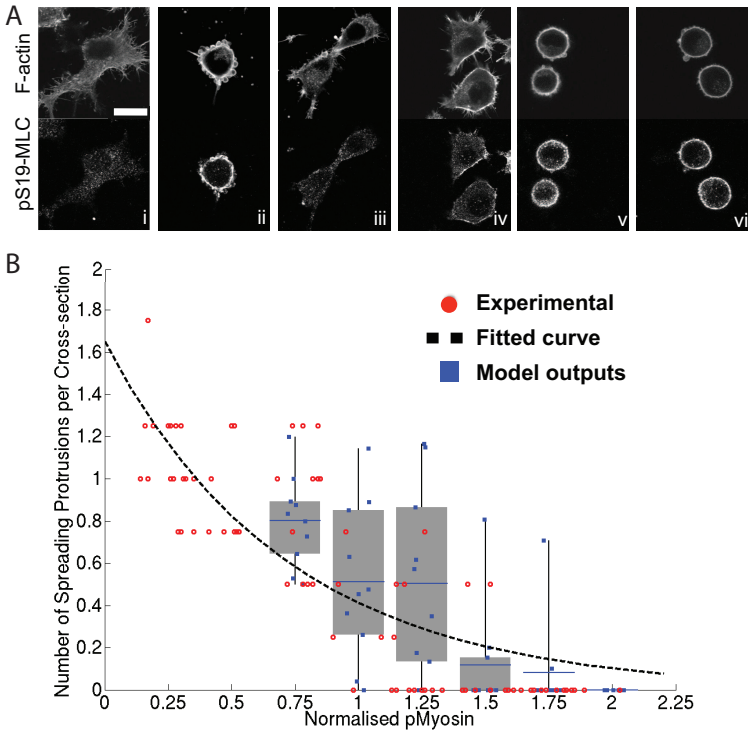

Figure 3.12: A) Images show representative examples of A375P cells with varying levels of F-actin protrusions and pS19-MLC. Image i shows cells treated with 10mM Y27632, images ii-iv show cells under serum starved conditions, and images v& vi show cells stimulated with 1 % serum. Scale bar is 20 μm. B. Quantification of the relationship between protrusions and pS19MLC. Experimental data points are extracted from images such as those shown in 'A'. Cortical pS19-MLC fluorescence was quantified in each cell along with the average numbers of protrusions per cross-section of the cell. Four lines bisecting the cell are drawn at 45 degree angles. The presence or absence of a protrusion at each point where the line intersected the cell periphery is scored (four lines gave a total of eight intersections per cell). The number of protrusions is divided by 4. Model outputs are the number of spreading protrusions taken at random time intervals. Each data point represents the mean protrusion number from one simulation (blue), boxes and whiskers represent upper and lower quartiles, and range, with mean of ten independent simulations marked on the box plot.

binding potential energy well, r_0. The values for these parameters are selected as $1000s^{-1}$, $1.0nm$, $0.01s^{-1}$ and $0.5nm$, respectively. A high association constant is selected to limit binding events only by the availability of adhesion proteins, and the interaction distance between the ligands and receptors. The threshold distance itself is selected as double r_0. The range r_0 is based on previous studies utilising the Bell model for cell–ECM adhesion (163). The calculation of cell–ECM detachment is probabilistic, and the adhesion protein units described in the model do not correspond to a specific number of adhesion proteins. As the affects of adhesion change are investigated in the model, the precise value of the dissociation rate constant is not of significance. However, the selected parameters should reproduce realistic force values, covering the range necessary to break focal contacts, and detach cells from the surfaces they adhere.

Two methods are used to map the adhesion units defined for the model to real life forces at cell–ECM adhesion sites. First, using adhesion force data available for focal contacts, the range of adhesion units for an agent of the model that would fit with realistic focal complex strengths is determined. Second, computations are performed which mimic atomic force microscopy experiments aimed at measuring the whole cell–ECM adhesion force. A map relating adhesion units to the forces necessary to detach the whole cell from its substrate is then compiled.

As discussed in Section 1.3.2.3, the cell–ECM adhesion structures relevant for the multiscale model of single cell motility are focal complexes, strengths for which have been measured to be $1-3nN\mu m^{-2}$ (172). The average area per cell surface agent, calculated from w_{model} and the average length associated with an agent, is $0.04\mu m^2$. Therefore, for an adhesion strength equivalent to a focal complex, the forces necessary to detach an adhered agent from its substrate should be within the range $0.04-0.12nN$. Adhesion maturation to focal complexes takes approximately $60s$, a period which is not included in the model. If a $60s$ period is allowed for adhesion and another $60s$ for possible detachment, the force per adhesion unit protein within an agent resulting in a 90 per cent probability that the agent will detach within 120s, $(F/N_b)\,|^{P_{off}=0.90}$, can be calculated from Eq. 2.40 and 2.43. Fitting this force term to the range $0.04-0.12nN$, the adhesion protein units per agent, defining a cell forming focal contacts with its substrate under

control conditions should be in the range $7-21$ *adhesion units*.

This scaling gives a rough estimate of the adhesion level for the cell with un-perturbed cell–ECM adhesion. However, considering the stochastic nature of binding and detachment events, and the multiple cell surface agents involved in adhering the model cell to ECM filaments, a further mapping of the adhesion units to the forces necessary to detach cells from the ECM is required. Computational experiments are carried out with this purpose, where spread cells are pushed against a surface for $20s$, with a force of $1nN$, applied over a range of $15\mu m$. After this pushing period, the pushing force is released, and the cells are allowed to stabilise their shape for $2min$. Following this resting period, cells are pulled from the surface with forces applied over a $5\mu m$ cell surface patch (Figure 3.13A). Detachment events are reported as percentages over at least ten simulations, for variable adhesion levels and pulling forces (Figure 3.13B). Forces reported in Figure 3.13 are for a 2D model cell, where the represented adhesion area is:

$$S_{AFM}^{2D} = L_{AFM} \times w_{model}, \tag{3.10}$$

here w_{model} is the width of the cross-section defined by the model, and L_{AFM} is the total length represented by the adhered agents of the model. Assuming a continuous, circular adhesion surface in 3D, the adhered area of the model can be approximately scaled to a 3D adhesion area *via*:

$$S_{AFM}^{3D} = \pi \frac{L_{AFM}^2}{4}. \tag{3.11}$$

Then with w_{model} being 0.2 μm, and the average adhesion length of the cells, $\langle L_{AFM} \rangle$, obtained as $18\mu m$ from the computational experiments, comparing Eq. 3.10 and 3.11, the area represented by the computational experiments can be scaled to a 3D adhesion area of a real cell, with an approximate 70 fold increase. This scaling should be considered when comparing the forces necessary to detach cells, reported in Figure 3.13. With this scaling, the adhesion levels investigated in the model still falls within the wide range of adhesion strengths reported for different cell types: MDCK cells $20nN$, keratocytes $45nN$ and fibroblasts $2000nN$ (90, 173).

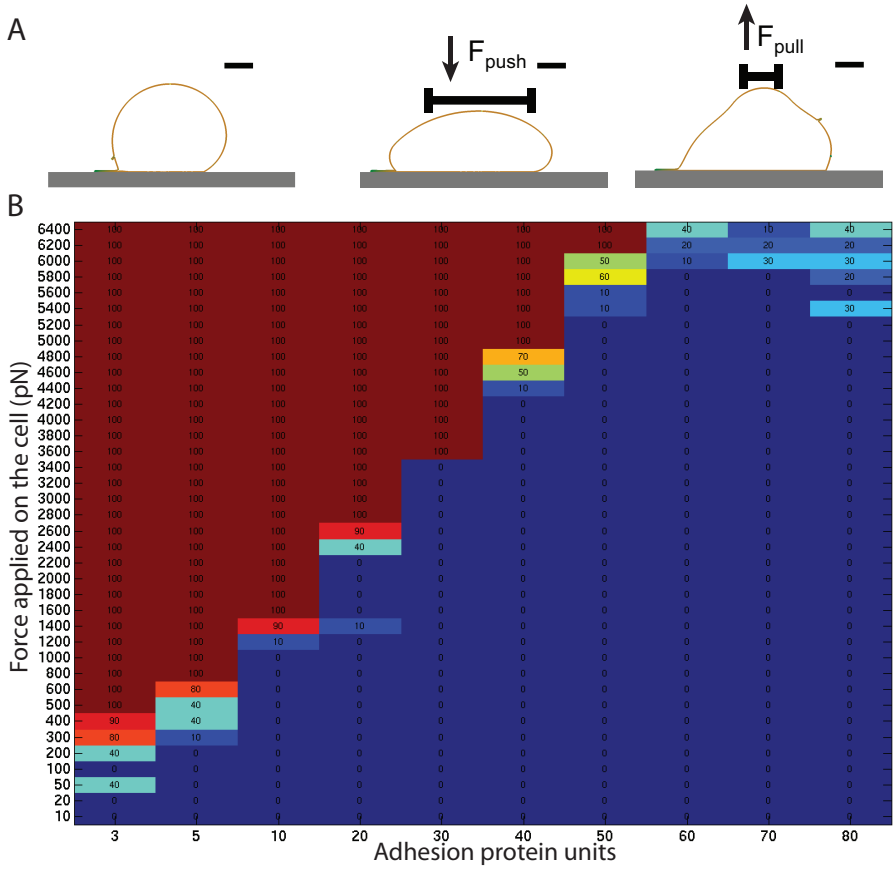

Figure 3.13: A) Model snapshots from the computational experiments. Cells are allowed to spread on surfaces. Then the cells are pushed against the surface for 20*s*, with a force of 1*nN* applied over 15*μm*. The pushing force is removed, and after a resting period, cells are pulled from the surface with a range of forces, applied over 5*μm*. Scale bar 5*μm* B) Heatmap reporting the percentage of cells detached, x-axis: adhesion protein units, y-axis: applied pulling force. Each data point is obtained from a minimum of ten independent simulations.

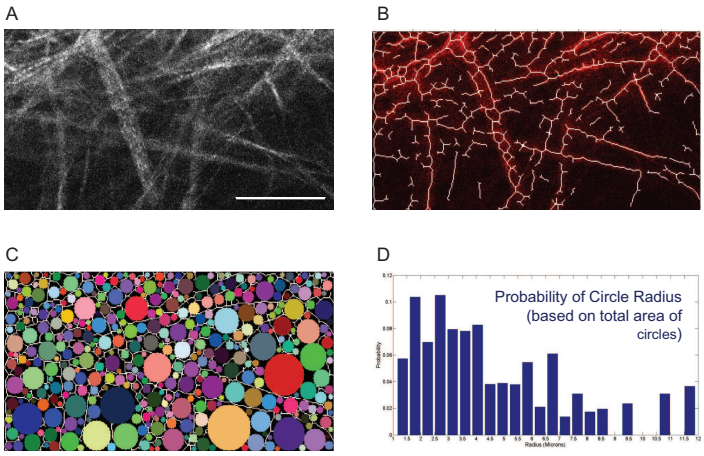

Figure 3.14: A) Image showing collagen fibres around the margin of an A375 tumour. Scale bar is 50 microns. B) Automated tracing of collagen fibres. C) Circles fitted into the gaps between collagen fibres. D) Histogram showing the frequency of different radial spacing sizes (diameter of fitted circles) between collagen fibres. Figure courtesy of Tumour Cell Biology Laboratory.

3.12 Extracellular Matrix Geometry

3.12.1 *in vivo* Mimetic ECM Generation

The extracellular matrices that mimic the *in vivo* collagen fibres are generated based on the gap sizes of mouse interstitial collagen. *In vivo* gap size distribution is measured by an automated analysis of images obtained from interstitial collagen matrix (Figure 3.14A). Initially, lines are fitted to the fibres of the image (Figure 3.14B), then overlapping circles are fitted into the gaps between the line segments (Figure 3.14C), diameter distribution of which gives the gap size distribution of the matrix (Figure 3.14D). This analysis has been carried out by the Tumour Cell Biology Laboratory.

After obtaining *in vivo* distribution of gaps in the range $1 - 12\mu m$, random matrices with similar size distributions are generated by the following procedure: Uniformly distributed random points are generated within a $200\mu m$ by $200\mu m$ square region. At each new point generation, the system is triangulated, and the point is accepted

if it is not closer than $1\mu m$ to any other existing point, and refused otherwise. This sequential addition is continued until a highly packed distribution of points is obtained. Then a histogram of the point-to-point distances is generated with a bin size of $1\mu m$. At his stage, almost all points of the packed mesh belong to the interval of $1-2\mu m$. Then an iterative procedure is initiated, where (i) the gap interval with highest frequency is determined, (ii) a point is randomly selected among the points that contribute gaps to the network within this selected interval, and the point is removed from the set, (iii) the histogram is re-calculated. For instance, at the initiation of the iteration, the selected interval of the highly packed point distribution is $1-2\mu m$, and the subset for random point deletion includes almost all points of the set. The iteration is continued until the generated mesh contains gap sizes for all $1\mu m$ increments within the gap range $1-12\mu m$, as determined from experimental observations (Figure 3.15A-C). Then twenty per cent of the points are then randomly selected, and are connected to one of their neighbours in triangulation. Thereby, the surfaces that are necessary to represent the random filament cross-section orientations are generated (Figure 3.15D-F).

3.12.2 Flexible ECM Characterisation

The spring network constructing the flexible ECM filaments is characterised by two parameters, the spring constant for each spring of the network, k_{fil}, and the viscous damping coefficient of the material, η_{fil}. The bulk modulus of the tumour environment have been reported in the range 1-5 kPa (174, 175). To estimate the bulk modulus of the constructed spring network, computational experiments are performed by placing filaments of variable sizes under pressure, and measuring the resulting area change. To fit the bulk modulus of the model filaments with the measured bulk modulus of the tumour environment, the elasticity and viscous damping of the filaments are varied scaled to the cell F-actin cortex parameters (Figure 3.16). The parameter set corresponding to 0.25 times the cortex parameters reproduced a bulk modulus within the reported range of 1-5 kPa, with variations in the calculated bulk modulus with changing initial filament size. The simulations of elastic ECM fibres are carried out with $60pN\mu m^{-1}$ for k_{fil} and $1500pNs\mu m^{-1}$ for η_{fil}.

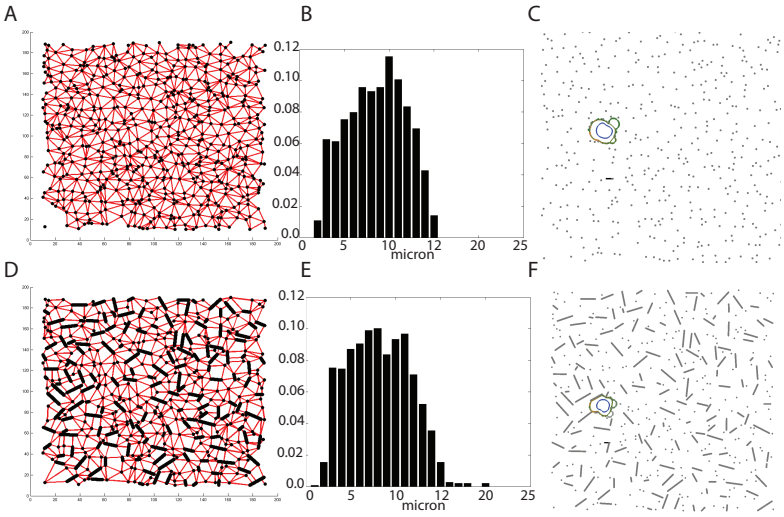

Figure 3.15: A) Triangulation of the randomly generated point set, without inclusion of surfaces generated by random cross-section orientations of filaments. B) Gap size distribution of the random matrix in (A). C) Snapshot of a model simulation with the cell moving in ECM generated by using point distribution in (A). D) Gap size calculation after introduction of the surfaces representing random cross-sections of ECM fibres. E) Gap size distribution of the random matrix in (D). F) Snapshot of a model simulation with the cell moving in ECM generated by using point distribution in (D).

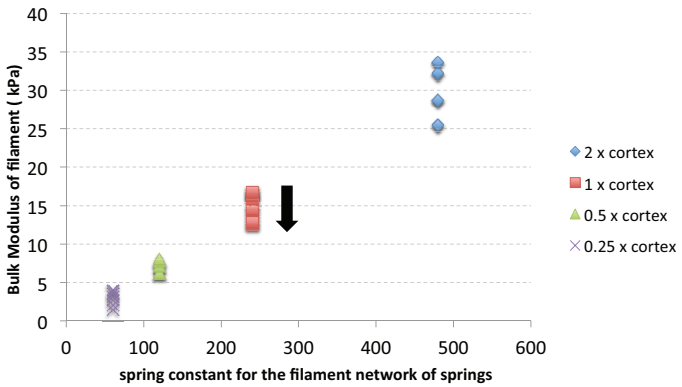

Figure 3.16: The calculated bulk modulus of ECM fibres in computational experiments, as a function of fibre size, and the parameters of the spring network, k_{fil} and η_{fil}, as scaled to cell F-actin cortex values.

Chapter 4

Optimum Motility Mechanism and the Extracellular Matrix Geometry

4.1 Introduction

In this chapter, the influence of the extracellular matrix geometry in determining the most effective cell motility mode is investigated. Initially, the emergent behaviours of the model cell (i) in its resting state, and (ii) under serum stimulation, are demonstrated. Then the results in the motility context, the behaviour of the polarised cell in a set of ECM geometries, are presented.

Cells are simulated in the variety of environments introduced in previous chapters: unconfined continuous, confined continuous and confined discontinuous environments. At the end of these simulations, the model successfully predicts the well established bell-shaped curve for the relationship between adhesion and velocity in unconfined continuous environments. Introduction of confinement reveals profound changes in the contractility velocity relationship, and finally, within a confined discontinuous environment, a fundamentally different relationship between adhesion and velocity is revealed. The model predicts that in environments with sufficient confinement and discontinuity, such that the cell body is able to anchor to the gaps within the ECM, direct cell-ECM adhesion is expendable. The model provides an explanation to the long observed, but not fully understood phenomenon of cell motility without adhesion. Meanwhile, cell motility modes are dissected, with simulations where the model cell can utilise only actin polymerisation based protrusions, only plasma membrane blebs, and

finally, both actin protrusions and blebs. This investigation reveals that different motility modes are effective in different environments. Moreover, the cell with the ability to perform both a spreading and a blebbing mode of motility utilises the more effective cell motility mode in each environment, highlighting a possible physical feedback mechanism between the ECM geometry, and distinct cell motility machinery.

The chapter continues with investigation of the relations between local regulation of myosin II and ERM proteins, highlighting a role for plasma membrane blebbing in cell rear detachment in continuous environments, and cell forward propuslsion in discontinuous environments. The two state solution of the relation between ERM and myosin II polarities depending on the extracellular matrix geometry signifies that the cells may be required to alter the regulatory mechanisms between cortex-membrane adhesion and cortical contractility, depending on the extracellular matrix they interact with.

It should be noted that the author of this thesis has taken part in the analysis, but not the collection of experimental data associated with the prediction validation of the computational model; data was collected by the Tumour Cell Biology Laboratory, based within the London Research Institute of Cancer Research UK.

4.2 The Emergent Behaviour of the Model Cell

After rigorous model development and parameterisation, the simple emergent behaviour of the cell is examined. Placed on a flat surface, with myosin levels of a serum starved A375 cell, the model cell spreads on the surface (Figure 4.1A-C). One per cent serum stimulation of A375 cells results in an overall contractility increase of two fold (Figure 3.8C). Upon mimicking this stimulation on the spread model cell, the cell rounds up, cell surface area is decreased, and the cell starts blebbing (Figure 4.1A/D). Detailed investigation of the blebbing phenomenon reveals a strong correlation with contractility levels. Moreover, the transition form a non-blebbing to a blebbing cell demonstrates a threshold-like behaviour, in agreement with experimental observations (Figure 4.1D-E).

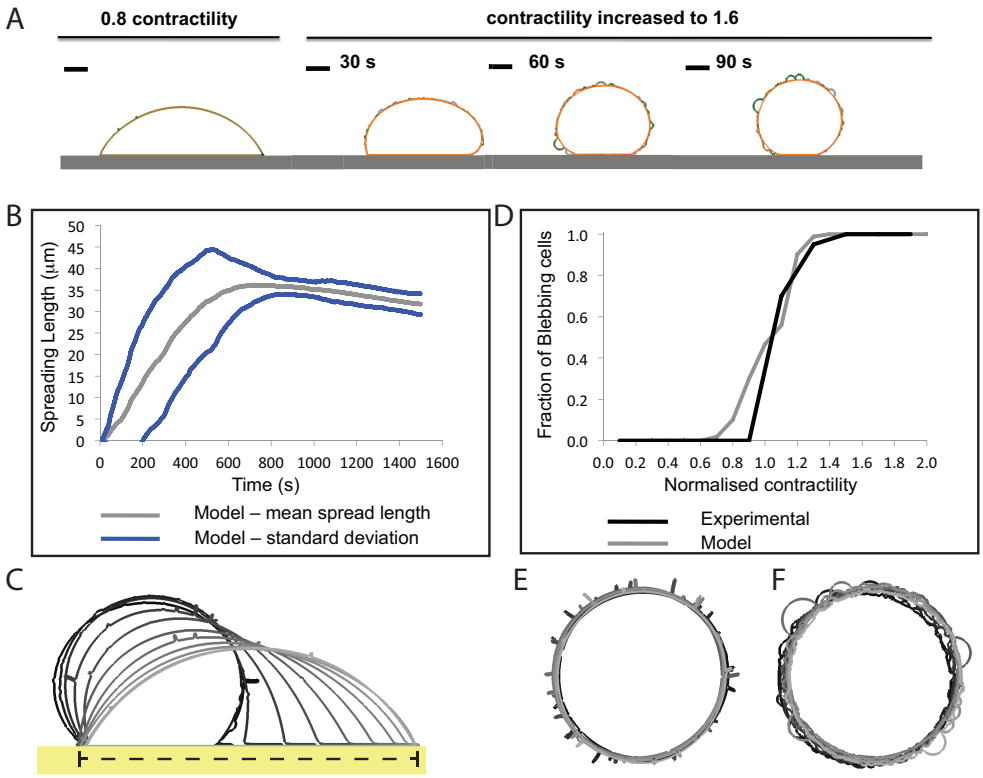

Figure 4.1: A) Model snapshots for a serum starved cell, spreading on a 2D surface, followed by 1 % serum stimulation. Scale bar 5 μm. Times indicated on the images are after serum stimulation. Serum starved cell has a normalised cortical contractility level of 0.8, serum stimulation increases the normalised contractility level to 1.6, initialising plasma membrane blebbing. B) Model outputs for increase in cell spread area as a function of simulation time. Each value is an average of ten independent simulations of 1500s each, for cells with normalised contractility level of 0.8. Mean of all simulations is plotted in grey; blue lines mark the standard deviation range for each time point. C) Snapshots from a simulation within the range of simulations described in (B). ECM surface shown in yellow. Overlaid snapshots taken every minute; time colour coded in the grey scale, lighter the colour, longer the simulation time. The dashed line marks the length plotted in (B) for the last snapshot. D) Frequency of blebbing cells, as a function of overall contractility. The model outputs are given in grey, experimental outputs in black. For the experimental data, normalised myosin expression levels are binned in intervals of 0.2, and the fraction of blebbing cells within the bin plotted. E,F) Snapshots from simulations within the range of simulations described in (D). Overall normalised contractility levels 0.6 in E, and 2.0 in F. Snapshot frequency and colour coding same as C.

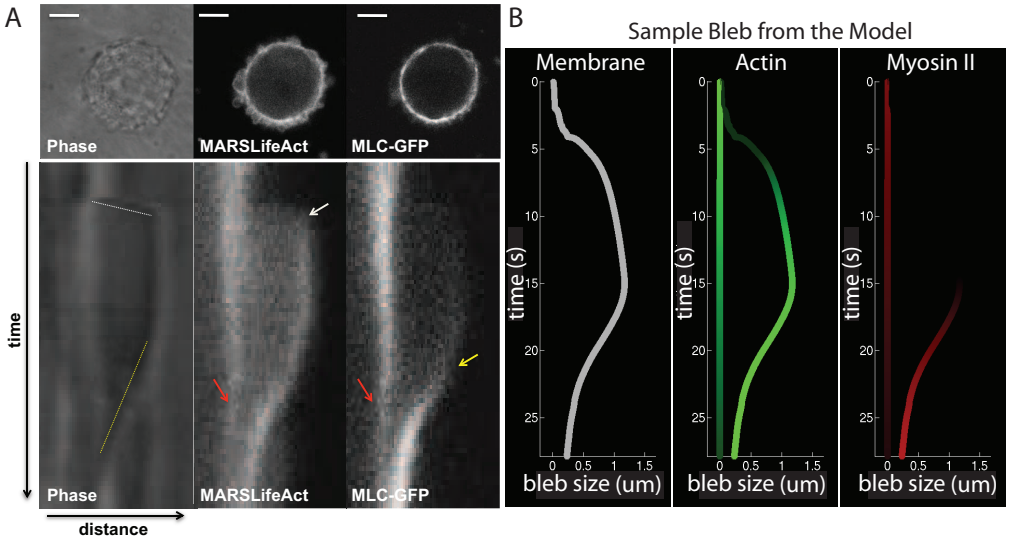

Figure 4.2: Bleb kymographs from experimentation and simulation outputs. A) Bleb kymographs: t axis spans 150 seconds and d axis spans 5.5 $\mu\, m$. Phase gives the position of the plasma membrane, MARSLifeACT labels actin and MLC-GFP is the GFP tagged myosin light chain, marking the active form of myosin II. The rapid expansion (indicated with white line), stabilisation, and slower retraction (indicated with yellow line) can be seen. Increased F-actin levels are roughly coincident with stabilisation of the bleb (white arrow) and increasing MLC levels are coincident with retraction of the bleb (yellow arrow). The decay of the residual cortex at the neck of the bleb is indicated with red arrows. Upper panels show snapshots of the time series from which the kymographs were generated. B) Sample kymograph from model simulations. Plasma membrane represented in grey, actin in green and myosin in red, concentration levels of each component are indicated by colour intensity. Bleb neck decay, together with the accumulation of actin and myosin at the bleb rim, can be observed. Stabilisation of the bleb size is correlated with the arrival of actin, while arrival of myosin facilitates bleb retraction.

For individual blebs, termination of bleb expansion is marked by actin accumulation at the bleb rim, and myosin arrival is linked with the initiation of bleb retraction. The relationship between plasma membrane bleb size, and protein levels at the bleb rim, is demonstrated for both experimental measurements and model outputs in the form of kymographs (Figure 4.2).

Directed cell migration is guided by extracellular cues, that induce asymmetry in cytoskeletal properties (176, 177). Moreover, asymmetries induced in myosin II levels are coupled to actin polymerisation based protrusion, *via* Rac-RhoA

cross-talk (79). Introducing polarity into either actin polymerisation-based protrusions or myosin II driven contractility individually, can generate cell motility: actin polymerisation based protrusions move the cell in the direction of enhanced protrusion formation, while increasing myosin II driven contractility in one region of the cell generates forward motion towards the opposite direction. Coupling these two mechanisms, with an experimentally derived inverse correlation function, results in enhanced cell motility (Figure 4.3). Together, these observations confirm that cell protrusion at the front and myosin contractility at the rear cooperate during cell migration. This emergent motility profile is in agreement with the widely accepted model for the process of cell crawling on surfaces (See Section 1.5.1).

4.3 Extracellular Matrix Geometry and the Optimum Cell Motility Mode

As outlined above, the computational model is able to accurately recapitulate real cell behaviour, and generate persistent cell motility. The next step is to probe the relationship between the extracellular matrix geometry and the optimal cell migration strategy. In other words, searching the levels and distribution of intracellular parameters that produce the maximum cell velocity, for a given ECM geometry. Three environments, which are introduced in Section 2.10.3, are systematically searched: i) an unconfined continuous environment, a planar surface, ii) a confined and continuous environment, analogous to cell movement in a tube, and iii) a confined and discontinuous environment, analogous to the environment a cell encounters while traversing a network of fibres. In each of these environments a range of contractile forces, F-actin protrusion rates, cortex-plasma membrane linker strengths and cell-ECM adhesion levels are explored. In the simulations presented through Sections 4.3.1 to 4.3.3, the cell has a mild polarity in cortical contractility, with a thirty per cent increased myosin at the cell rear, and where applicable, a twenty per cent PIP_2 reduction at the cell front. Results for higher degrees of polarities are presented in Appendix B, and an investigation of the spatial distribution of polarity is presented in Section 4.4.

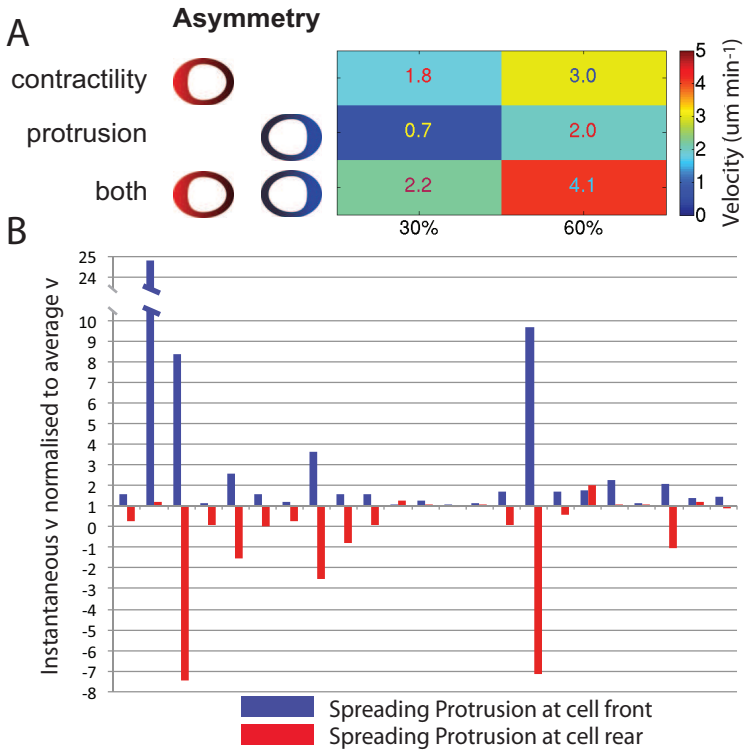

Figure 4.3: A) Velocity ($\mu m\ min^{-1}$) heatmap for cell with only polarised contractility; only polarised protrusions; and both. The velocities are reported at 30 % and 60 % increased myosin, equivalent protrusion suppression, or both, at the rear of the cell. B) Plot shows that the spreading protrusions drive cell motility in the direction of their spread. A subset of simulations on surfaces, where the cell formed spreading protrusions towards both the cell front and the cell rear (cell rear defined by increased contractility) are selected. Instantaneous velocities, taken over $1s$ intervals, over the time periods of protrusion spreading to front (blue) or rear (red) are calculated. Plot shows the average instantaneous velocity for each simulation, as normalised to the overall velocity of the cell during the same simulation. Instantaneous velocities are higher than the average velocity during protrusion spreading to the front, and lower during protrusion spreading to the rear.

4.3.1 Unconfined Surfaces: Benefits of Mesenchymal Motility and the Bell-shaped Curve Reflecting the Relationship Between Cell Adhesion and Velocity

For unconfined continuous surfaces, simulations generate the well established bell-shaped curve for the relationship between cell–ECM adhesion and cell velocity (Figure 4.4). At high adhesion levels, the cells remain adhered to the surfaces at all points of contact and are unable to detach their rear. At low adhesion levels, the cells fail to maintain contact with the ECM, and cannot therefore maintain a persistent motility. The contractility-velocity relationship is closely linked with adhesion levels. At low adhesion levels, increased contractility reduces cell velocity due to reduced actin polymerisation based protrusion formation and increased rate of complete cell detachment. At high adhesion levels, with a lower likelihood of complete cell detachment, increasing the overall contractility of the cell rescues cell motility, by facilitating cell rear detachment. The shift in the peak of the bell-shaped cell velocity-ECM adhesion curve clarifies this relationship (Figure 4.4D).

In agreement with expectations, among the simulated cell motility strategies, cells with actin protrusion formations are established as the most efficient cells in terms of their ability to move on unconfined surfaces (Figure 4.4A). The simulations reveal that polarised plasma membrane bleb formation at the cell front leads to reduced velocities in unconfined surfaces, with blebbing reducing the probability of protrusion spreading at the cell front, and increasing the probability of complete cell detachment from the surface (Figure 4.5). For the tested parameter space, protrusion-alone strategies, coupled with contractility of the cell rear, are the most effective. The velocity of a cell with the ability to form both plasma membrane blebs and actin protrusions (Figure 4.4C) falls back of the protrusion alone cell velocity (Figure 4.4A), while being higher than that of a blebbing only motility strategy (Figure 4.4B). The comparison presented in Figure 4.4 comprises cells with a thirty per cent increased contractility at the cell rear, and a twenty per cent reduced cortex-plasma membrane linkers at the cell front. A broader investigation of cell polarities show that the relationships presented in detail here are valid for increased levels of polarity. Cell velocities for higher

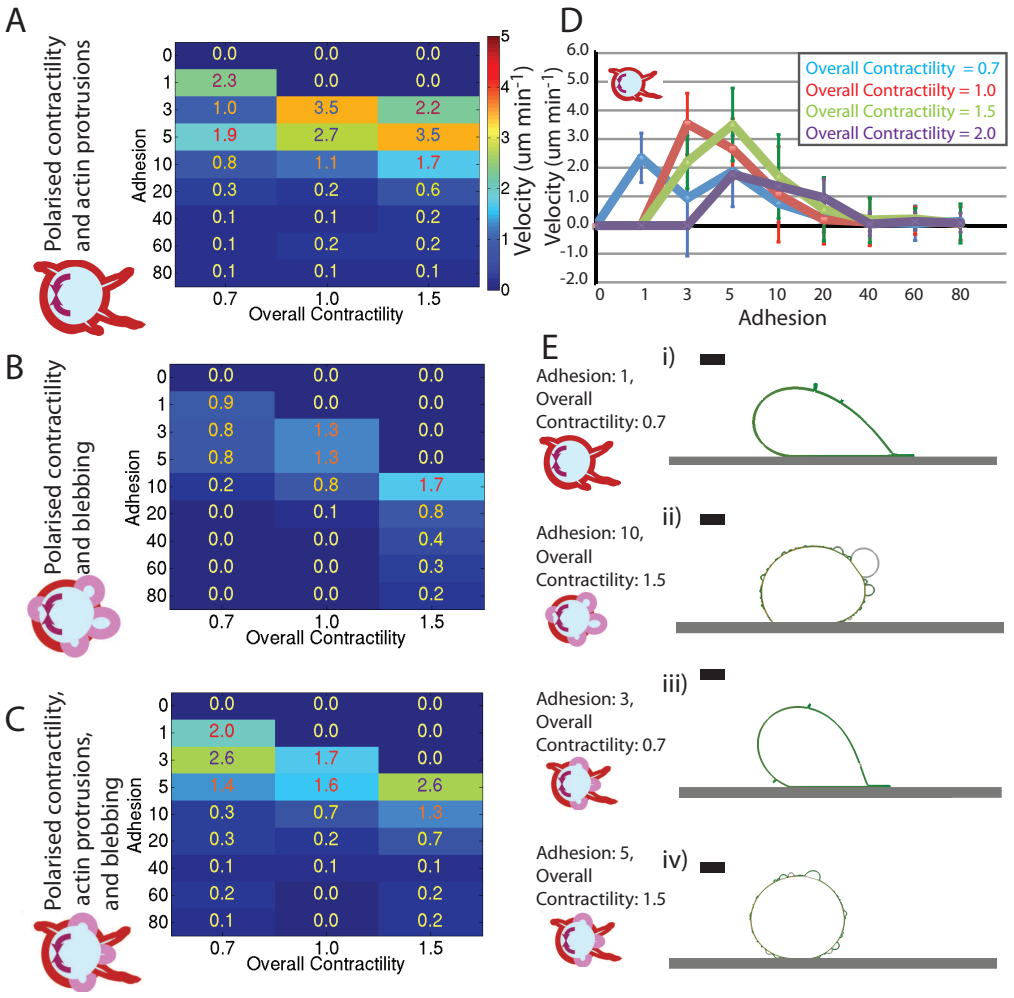

Figure 4.4: Velocity Heatmaps for cells moving on unconfined continuous surfaces, with 30 % polarised contractility at the cell rear, and 20 % reduced cortex-membrane adhesion at the cell front, where applicable. All displayed data is averaged from a minimum of ten independent simulations, 15 minutes each. A) Cell with only actin polymerisation based protrusion formation, B) Cell with only plasma membrane bleb formation, and C) Cell with the ability to form all protrusions. Velocities are given in $\mu m\ min^{-1}$, the colour bar in (A) is valid for all three heatmaps. D) Cell velocity profiles vs. adhesion for cell in (A), plotted for individual overall contractility values, with standard deviations marked at each data point. The bell-shaped curve, and the shift of the curve with increasing cell contractility can be seen. E) Model snapshots for each motility strategy. Top to bottom: i) Cell with only actin protrusions, with an overall contractility of 0.7 and cell-ECM adhesion level of 1.0. ii) Cell with only bleb formation, with an overall contractility of 1.5, and cell-ECM adhesion level of 10. iii) Cell with blebs and actin protrusions, overall contractility 0.7 and adhesion 3. iv) Cell with blebs and protrusions, overall contractility 1.5, adhesion 5. In all snapshots, F-actin cortex density is indicated by the colour intensity in green, myosin in red, membrane in grey. ECM filaments are shown in dark grey. Scale bar 5 μm.

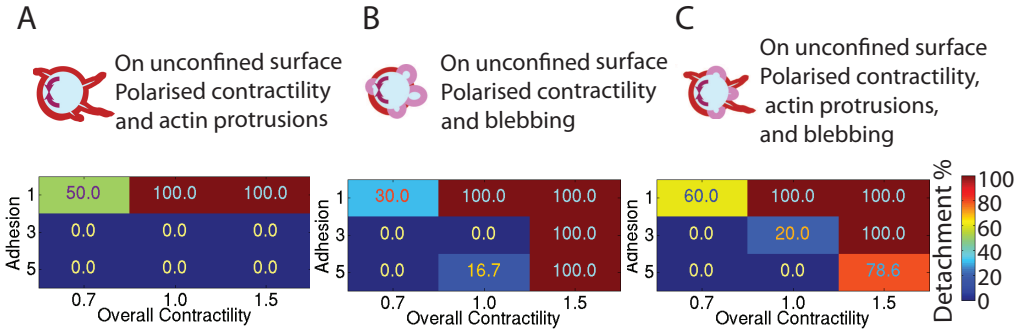

Figure 4.5: Heatmaps for percentage cell detachment from surfaces. A) Cell with only actin polymerisation based protrusion formation, B) Cell with only plasma membrane bleb formation, and C) Cell with the ability to form all protrusions. The colour bar is valid for all three heatmaps. Simulations carried out for 30 % increased contractility at the cell rear for all motility mechanisms, and 20 % reduced PIP_2 at the cell rear where applicable. Under these conditions, there is no detachment observed for adhesion levels above 5.

levels of polarity, and cell motility strategies excluding any form of protrusion formation, or lacking polarised contractility, are provided in Appendix B. These simulations reveal that on an unconfined surface, plasma membrane blebbing at the front of the cell does not increase cell velocity compared to a cell with only polarised contractility, but increases cell detachment and leads to loss of motion (Figure B.1A/E). The importance of polarised contractility for a cell without actin protrusions is emphasised by lack of movement of a cell with polarised blebbing, but without polarised contractility (Figure B.1B). In the case of polarised actin protrusions without polarised contractility, the cell is able to move on unconfined surfaces at high levels of polarity (Figure B.1D), albeit significantly slower than a cell with polarised contractility. Although the simulations reveal detrimental roles for increased blebbing at the front of the cell on unconfined surfaces, variable correlations between myosin and ERM polarity are investigated in Section 4.4, and suggest alternate roles for plasma membrane blebbing, which does enhance cell velocity.

4.3.2 Confined Surfaces: Confinement Determines the Contractility-Velocity Relationship

In the confined continuous environments, with the cell sandwiched between two continuous surfaces, two different high cell velocity strategies emerged. At moderate levels of myosin II driven contractility (overall contractility values 0.7 and 1.0), a cell with polarised contractility and actin protrusions only, is the most effective (Figure 4.6A). The moderate levels of contractility are sufficient to facilitate cell rear detachment, and protrusion formation is not hindered *via* increased myosin levels, or plasma membrane bleb formation.

In contrast, with an increase in overall contractility levels (contractility value 1.5), blebbing based strategies become the most effective strategies. The ability to form blebs brings a shift in the relation between contractility and velocity (Figure 4.6B/C). Differing from cell motility on unconfined surfaces, increasing myosin activity, hence overall cell contractility, generates an increase in cell velocity. This can be observed across a wide region of parameter space, covering blebbing-based and bleb and actin protrusion based motilities, for all cases where there is adhesion to the environment (all adhesion values > 0). For the cells with protrusion only strategies, cell velocity profiles remain affected by the trade-off between increased contractility and reduced protrusion formation. The functional relationship between contractility and protrusion remains the same as previously described, the highest velocity obtained at intermediate levels of myosin. Increase in adhesion strength increases the limitation of cell rear detachment. The shift of the contractility-velocity curve can be observed in Figure 4.6D, where the peak of velocity is obtained at higher contractility levels as adhesion increases.

The main source of change in the contractility-velocity relationship for cells with blebbing is driven by the geometry of the environment: cells displaying high levels of contractility cannot cause loss of contact with the environment in a confined space, whereas cells do get completely detached from unconfined surfaces. Further investigation reveals the level of confinement regulates the balance between beneficial and detrimental effects of contractility. The beneficial effects are higher force generation and larger bleb formation, while the detrimental effects are loss of adhesion to the surface, and the trade-off between myosin levels and actin protrusion formation.

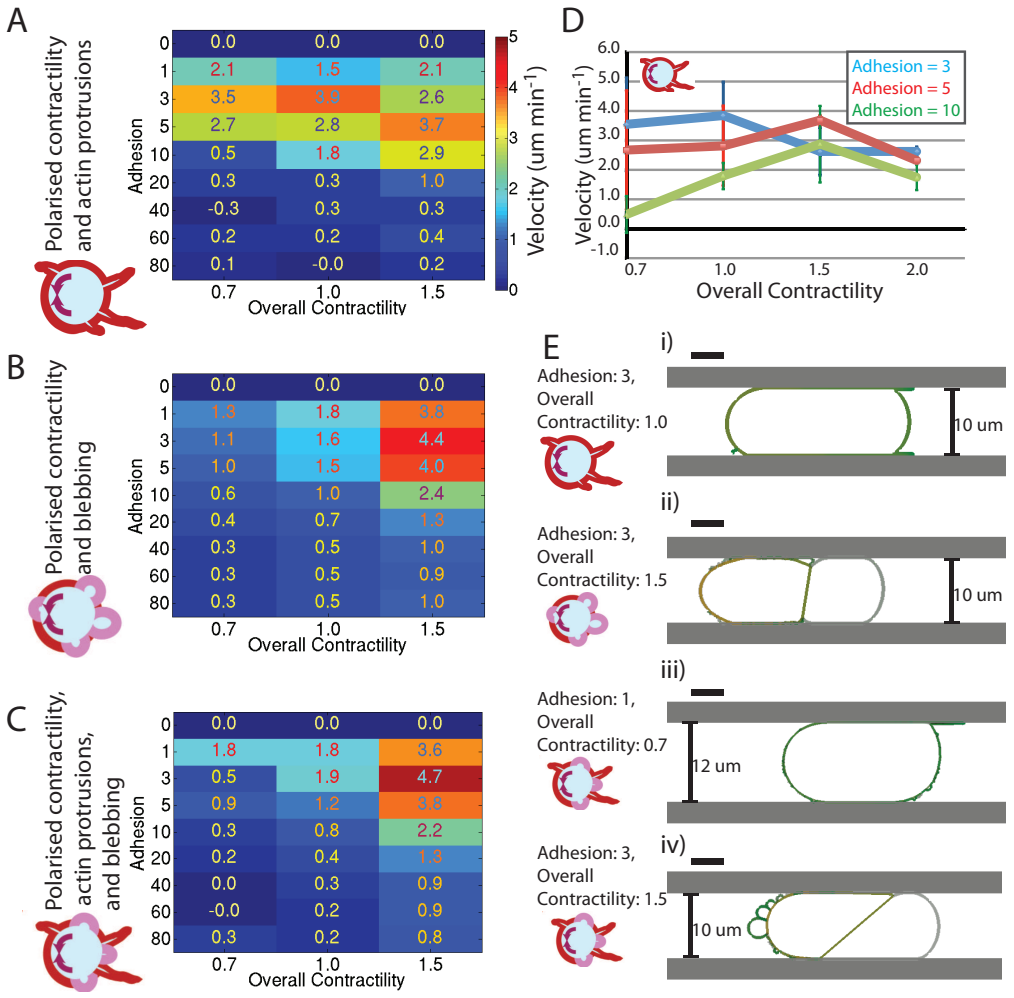

Figure 4.6: Velocity Heatmaps for cells moving within confined continuous surfaces, with 30 % polarised contractility at the cell rear, and 20 % reduced cortex-membrane adhesion at the cell front, where applicable. All displayed data is averaged from a minimum of ten independent simulations, 15 minutes each. A) Cell with only actin polymerisation based protrusion formation, B) Cell with only plasma membrane bleb formation, and C) Cell with the ability to form all protrusions. Velocities are given in $\mu m\ min^{-1}$, the colour bar in (A) is valid for all three heatmaps. D) Cell velocity profiles vs. overall contractility for cell in (A), plotted for individual adhesion values, with standard deviations marked at each data point. The shift in the peak of the curve with increasing adhesion can be seen. E) Model snapshots of each motility strategy. Top to bottom: i) Cell with only actin protrusions, with an overall contractility of 1.0 and cell-ECM adhesion level of 3, tube gap size $10\mu m$. ii) Cell with only bleb formation, with an overall contractility of 1.5, and cell-ECM adhesion level of 3, tube gap size $10\mu m$. iii) Cell with blebs and actin protrusions, overall contractility 0.7 and adhesion 1, tube gap size $12\mu m$. iv) Cell with blebs and protrusions, overall contractility 1.5, adhesion 3, tube gap size $10\mu m$. In all snapshots, F-actin cortex density is indicated by the colour intensity in green, myosin in red, membrane in grey. ECM filaments are shown in dark grey. Scale bar 5 μm.

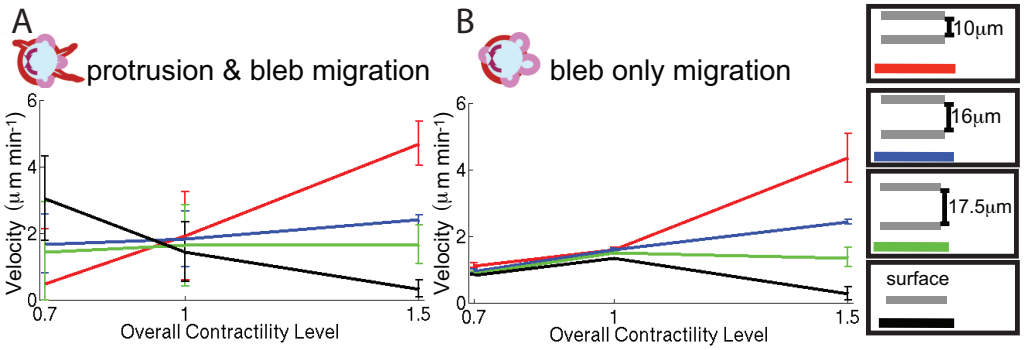

Figure 4.7: Velocity profiles plotted against overall contractility, for increasing confinement levels: from an unconfined surface to a tube of 10 μm gap size. Cell with 30 % increased contractility at the cell rear, and 20 % reduction in PIP_2 at the cell front, cell-ECM adhesion level 3. A) Cell can form actin protrusions and plasma membrane blebs B) Cell can form solely plasma membrane blebs. Resting state cell diameter is 18μm.

The model predicts that on unconfined surfaces, cells move more quickly at low levels of contractility; whereas in a highly confined environment, cells move quicker with higher levels of contractility (Figure 4.7). As confinement levels increase, the benefits of higher cell contractility dominate over the detrimental effects, with cells forming larger, and thus more efficient, blebs. The velocity profile of a blebbing only cell clearly demonstrates this trend, with cell velocity increase directly correlating with increased levels of confinement (Figure 4.7B). For the case of a cell with bleb and actin protrusion formation abilities, the shift in the contractility-velocity relationship can clearly be observed between unconfined surfaces and a tube of gap size 10μm. Over varying frontal gap sizes larger than 10μm, the trade-off between protrusion formation and overall contractility balance each other, generating low variation in cell velocity with increasing contractility (Figure 4.7A).

As for the analysis of cell movement on unconfined surfaces, investigation of higher levels of cell polarities shows the above trends to be maintained. Moreover, the importance of polarised contractility is emphasised: cells that have polarised contractility coupled with polarised blebs or actin protrusions are always faster than the cells with polarity solely in their blebs or actin protrusions (Figure B.2C/D and B/E for a tube of 12μm and Figure B.3C/D and B/E for a tube of 10μm).

One difference form the motility predictions on unconfined surfaces is that cells with only increased blebbing at the cell front can generate motion within confined continuous surfaces at high levels of polarity (Figure B.1B and Figure B.2B, B.3B). Similar to the change in the contractility-velocity relationship with confinement, this can be attributed to the reduced likelihood of complete detachment of the cell from the ECM. In line with the suggestion increased bleb size increases cell velocity, an increase PIP_2 polarity increases cell velocity in almost all cases. Similarly, a higher confinement, i.e. smaller frontal gap size, increases velocity of blebbing cells (Figure B.2B/E/F vs. B.3B/E/F). This can be attributed to the pressure increase within higher confinement levels leading to larger, thus more effective bleb formation.

4.3.3 Discontinuous Matrices: Benefits of Amoeboid Blebbing Motility and Fundamental Changes in the Adhesion-Velocity Relationship

Investigation of confined discontinuous ECM environments reveals a change in dominant cell motility strategy; the fastest cell motility switches from protrusion-based to blebbing-based. The importance of plasma membrane bleb formation is demonstrated by the consistently high velocities for cells with blebbing, compared to cells with the ability to form only actin protrusions, under the same overall contractility levels (Figure 4.8). The results presented in Figure 4.8 are for a cell with mild polarity , in a discontinuous environment of $10\mu m$ frontal gap size and $4.3\mu m$ lateral gap size. The correlations summarised in this section hold for increased polarity levels and variations in confinement levels (Figure B.4 -B.7)

Strikingly, a fundamental change in the adhesion-velocity relationship is observed for confined discontinuous environments. Instead of an intermediate level of adhesion yielding the highest cell velocity, as found for continuous environments, the lower the adhesion, the faster the cell moves in discontinuous environments. This relation is maintained at the theoretical level of zero cell-ECM adhesion. It is important to note here that an adhesion level of zero is deemed ”theoretical”, as it is not testable in an experimental setup. Even in the case that one suggested to have inhibited all linker molecules between the cell cortex and the ECM –which is not

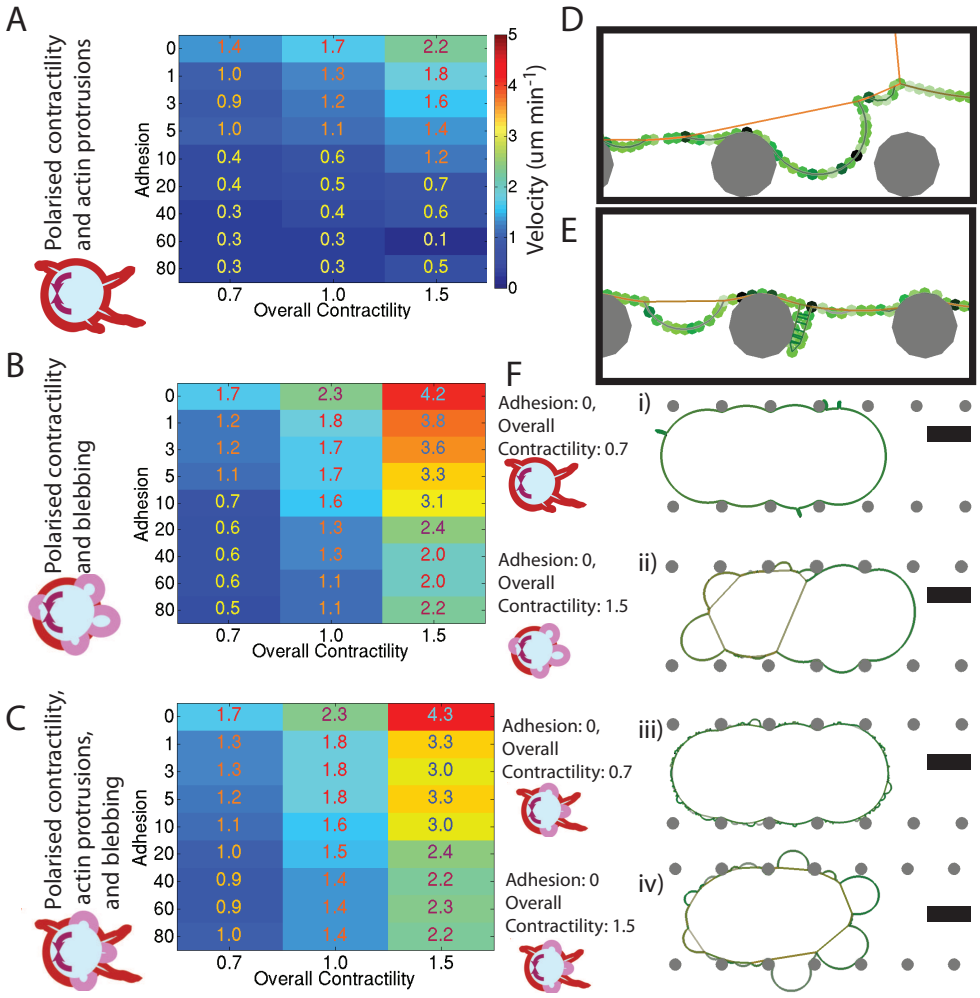

Figure 4.8: Velocity Heatmaps for cells moving within confined discontinuous environments, for cells with 30 % polarised contractility at the cell rear, and 20 % reduced cortex-membrane adhesion at the cell front, where applicable. All displayed data is averaged from a minimum of ten independent simulations, 15 minutes each. A) Cell with only actin polymerisation based protrusion formation, B) Cell with only plasma membrane bleb formation, and C) Cell with the ability to form all protrusions. Velocities are given in $\mu m\ min^{-1}$, the colour bar in (A) is valid for all three heatmaps. D) Model snapshot showing interdigitation of a plasma membrane bleb in a gap of the ECM. The model cell has no adhesion to the ECM. E) Model snapshot showing interdigitation of an actin protrusion to a gap of the ECM. F) Model snapshots of each motility strategy. All snapshots are of model cells with zero adhesion to the ECM. Frontal gap size of the matrix is $10\mu m$, and latheral gap size $4.3\mu m$. Top to bottom: i) Cell with only actin protrusions, with an overall contractility of 0.7. ii) Cell with only bleb formation, overall contractility 1.5. iii) Cell with blebs and actin protrusions, overall contractility 0.7. iv) Cell with blebs and actin protrusions, overall contractility 1.5. In all snapshots, F-actin cortex density color coded in the linkers in green, myosin in red, membrane in grey. ECM filaments are shown in grey. Scale bar 5 μm.

possible with the current knowledge level in cellular biology– all frictional forces between a cell and an ECM filament cannot be eliminated. On the other hand, there is evidence to suggest a significant impairment and reduction in cell-ECM adhesion does not impair cell velocity in a multitude of complex *in vivo* environment.

This unusual observation is further investigated, to reveal the source of the traction generated by cells, in the absence of adhesion. Close inspection of the behaviour of the model cells, as they move through a discontinuous matrix, indicates that their efficient motility at zero adhesion is a consequence of lateral cell protrusions interdigitating with gaps in the matrix (Figure 4.8D/E). These lateral protrusions allow the cell to anchor to the environment, enabling traction in the absence of cell-ECM adhesion. Due to their morphology and size, plasma membrane blebs are more effective in generating this traction than the actin protrusions. A large bleb of amorphous shape is more likely to expand and fill a lateral more effectively (Figure 4.8D), rather than an actin polymerisation based protrusion, which needs to elongate at the right point of the cell surface, and at the correct angle, to facilitate anchoring (Figure 4.8E).

At zero adhesion, the efficiency of the above form of traction generation is dependent on the relative confinement of the cell body. The cell is forms less-effective interdigitations with larger gaps, thus larger lateral gap sizes reduce the efficiency of traction generation (Figure 4.9A). With increasing confinement and reduced lateral gap size, cells with any form of protrusions, either blebs or actin protrusions, start generating movement before a cell with solely polarised contractility. Blebs are more effective, and a cell with increased blebbing at its front, (reduced PIP_2 levels at front) is the fastest. On the other hand, if the confinement of the cell is high enough, even the cell body itself can deform and fill the lateral gaps sufficiently well to facilitate cell motility. This can be seen in the gradual increase in velocity at zero adhesion for cells with no protrusions but only polarised contractility (Figure 4.9B). Interestingly, as the confinement increases and the cell body itself starts forming the necessary anchoring (Figure 4.9B, matrix frontal gap size $10\mu m$), cells with increased blebbing at cell rear become slower. Here, the trade-off between the increased anchoring provided by blebs, and decreased cell velocity due to the blebs propelling the cell body in the opposite direction to that imposed by contractility can be seen. The variable

correlation between myosin and ERM polarity are further investigated in Section 4.4. The changes in anchoring performance are given in detail for altered levels of confinement in Figures B.4-B.7. Overall, these observations demonstrate adhesion ceases to be a limiting factor when considering the efficiency of cell motility within confined discontinuous environments.

4.3.4 The Plastic Cell

Figures 4.4, 4.6 and 4.8 reveal that cells possessing the ability to form both blebs and actin-based protrusions display motility profiles in between that of cells using one of these protrusion mechanisms. Moreover, the cell with the ability to form both types of protrusions has a closer resemblance to the more effective motility strategy for each environment and intracellular state. It is important to note that no enforced preference mechanism to choose between motility modes is included in the model development. The emergent behaviour of the modelled cell emulates the plasticity of real cells, choosing the more effective motility strategy depending on the geometry of the ECM.

This emergent behaviour indicates the existence of purely physical cross–talk between the cell and its environment, the interpretation of which leads the cell to adopt a predominantly spreading or blebbing motility strategy. The model suggests a physical feedback between actin polymerisation based protrusion spreading and plasma membrane blebbing, which would be functioning together with the biochemical feedback mechanisms. An increase in cell spreading leads to an increase in cell area (equivalent of a real cell's volume in the 2D model), and thus a reduction in intracellular pressure. This reduction in pressure reduces the likelihood of plasma membrane bleb formation. Moreover, a spread cell has a larger circumference, using up the available plasma membrane reserves. As a result, due to the lack of available membrane, i.e. increased membrane tension, the unlikely bleb that is initiated grows to a smaller size compared to a bleb on a rounded cell at the same internal pressure. Meanwhile, plasma membrane blebbing reduces the likelihood of actin polymerisation based protrusion formation, as these protrusions require an intact cortex, and cannot be formed on the bleb rims. These purely physical feedbacks between plasma membrane blebs and actin polymerisation based protrusions can facilitate the choice towards the more effective motility

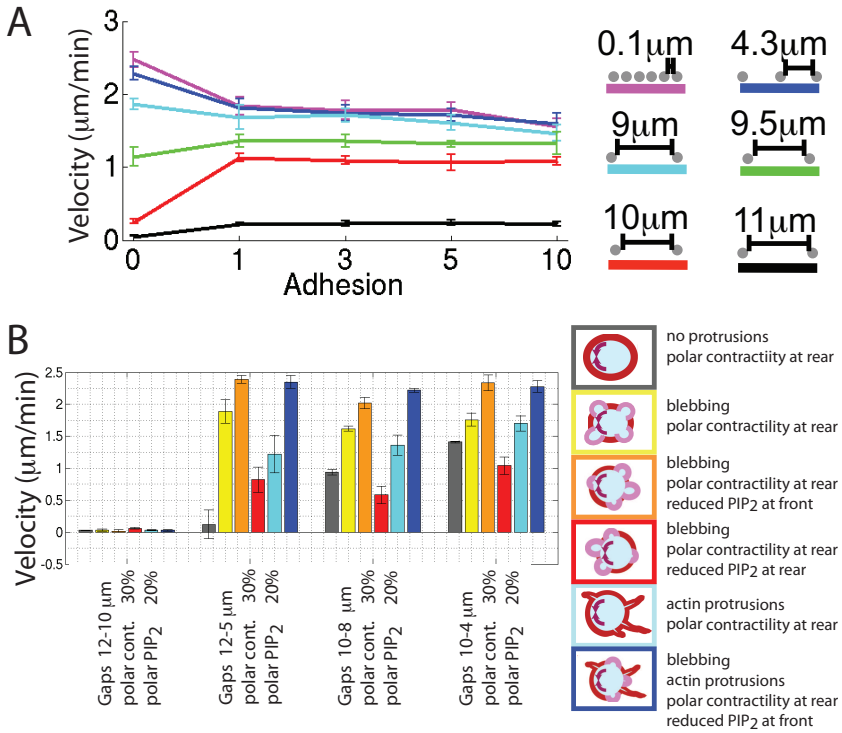

Figure 4.9: Cell velocity at zero adhesion. A) Velocity profiles plotted against adhesion, for variable lateral gap (gap parallel to the cell's direction of motion) sizes of the discontinuous ECM. Frontal gap size is $10\mu m$. Cell is able to form blebs and actin protrusions, with 30 % increased contractility at the cell rear, and 20 % reduced PIP_2 at the cell front, overall contractility level 1.0. The ability of cells to move at zero adhesion is inversely proportional to the lateral gap size, the magnitude of the velocity reducing with increased gap size. This observation is in line with the proposed mechanism of traction generation: interdigitation of cellular protrusions in the gaps of the ECM. B) Cell velocity at zero adhesion, plotted for a range of cell motility modes, polarities, and variable frontal and lateral gap sizes for the discontinuous environment. All cells have an overall contractility value of 1.0, where applicable, polarities are as indicated on the figure. Bars represent different motility mechanisms, all cells have increased contractility at the cell rear: i) Grey: cell with increased contractility at the cell rear only, no protrusions. ii) Yellow: cell with ability to form blebs only, uniform PIP_2 distribution. iii) Orange: cell with the ability to form blebs only, with reduced PIP_2 at front. iv) Red: cell with the ability to form blebs only, with reduced PIP_2 at rear. v) Cyan: cell with the ability to form actin protrusions only. vi) Blue: cell with the ability to form blebs and actin protrusions, reduced PIP_2 at front. In both (A) and (B), all data points are averaged from at least ten independent simulations equicalent to 15 minutes cell motility period each. Standard deviations are marked on the data.

strategy depending on the environment geometry: An environment with continuous surfaces available for actin protrusion spreading will supress bleb formation, drawing the plastic cell closer to an actin protrusion based motility strategy.

4.4 Cross–Talk between Myosin II and ERM proteins

For all of the above simulations, the asymmetry in contractility is positively linked with asymmetry in the distribution of plasma membrane–cortex linker proteins: contractility increases at the rear of the cell are accompanied by a reduction in ERM proteins at the cell front. The basis of this selection is multiple experimental observations. A375 cells have a structure at cell rear with enriched contractile cortex, and ERM proteins. Indeed, increased myosin and PIP_2 (a master regulator of ERM proteins (85)) density at the cell rear is shown in many studies. Nevertheless, there is no *a priori* reason for myosin II driven contractility and cortex-membrane linkage strength to be positively correlated, and there have been studies showing plasma membrane blebs at the front, the sides, and the rear of migrating cells (8, 39, 126).

From an experimental perspective, it is not straightforward to investigate variations in contractility and membrane–cortex linker strengths independently. However, for the computer model, it is possible to explore the consequences of local membrane–cortex linker variations at different regions of the cell, independent of the polarity in myosin. This analysis provides insights to the roles of plasma membrane blebs in cell motility, and the dependency of these roles to ECM geometry.

4.4.1 Continuous Surfaces: Overcoming the Adhesion Limitation with Blebbing at the Cell Rear

On unconfined surfaces, especially at low levels of asymmetry in contractility, blebbing at the cell rear increases cell velocity (Figure 4.10A). For low levels of asymmetry, detachment of the cell rear is the limiting step in cell movement on

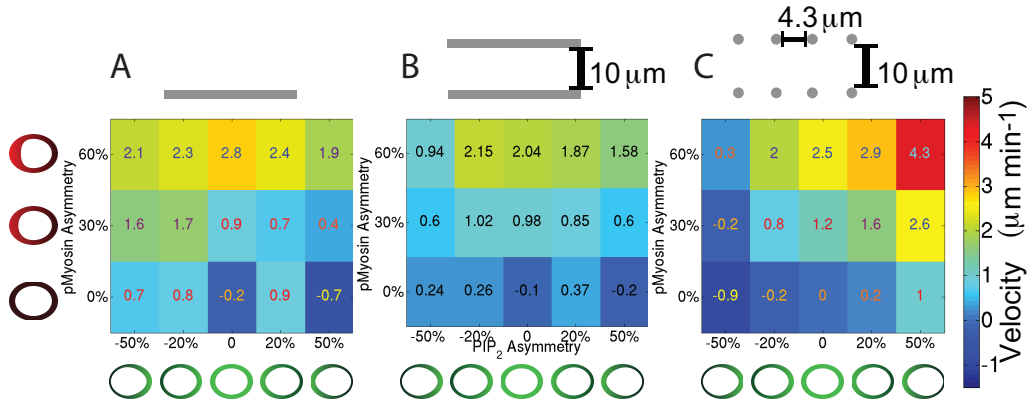

Figure 4.10: Velocity heatmaps for variations in spatial distribution, and magnitude, of PIP_2 and myosin polarities. The schematics represent the magnitude and position of cell polarity, red myosin, green PIP_2. Brighter colours indicate higher protein concentration. Schematics above the heatmaps demonstrate the environments, ECM shown in grey. A) Variation of cell polarity on an unconfined surface, B) in a confined continuous environment of frontal gap size $10\mu m$, and C) confined discontinuous environment of frontal gap size $10\mu m$ and lateral gap size $4.3\mu m$. Colourbar valid for all three heatmaps. Cells have the ability to form blebs and actin protrusions, with overall contractility level of 1.0.

unconfined surfaces, and increased blebbing at the cell rear facilitates this cell rear detachment. In this environment, another aspect of motility at low levels of myosin asymmetry is the formation of spreading actin protrusions in the direction opposite to cell motion. With the increased contractility of the cell rear, actin protrusions are less likely to form and spread towards the rear, and compared to a protrusion at the cell front, they are more likely to be pulled back and terminated due to the local accumulation of myosin. Albeit being less likely to form, spread, and become long-lived, once formed, the actin protrusions towards the cell rear do reduce cell velocity (Figure 4.3B). Another benefit of increased blebbing at the cell rear is that the likelihood actin protrusions at the rear of the cell becoming established is reduced (Figure 4.11A/C), hence the mean cell velocity is increased. At high levels of asymmetry in contractility, the increased levels of myosin can sufficiently suppress the actin protrusion formation at the cell rear due to the feedback between myosin concentrations and actin protrusion formation rate (Figure 3.12). Moreover, increased contractile forces suffice for cell rear detachment. Thus, high levels of contractile asymmetry render increased blebbing at the cell rear redundant in these aspects. Meanwhile, increased blebbing at the cell rear hinders accumulation of

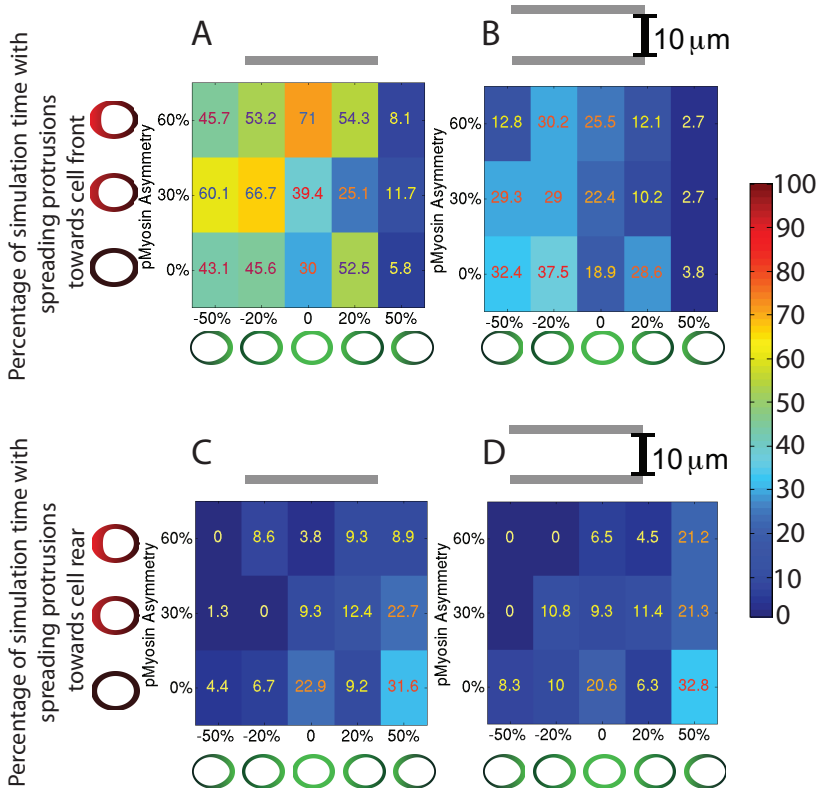

Figure 4.11: Simulation time percentages, where the cells have protrusions towards the cell front (top panels A-B), or towards the cell rear (bottom panels C-D), are shown on unconfined surfaces and within confined continuous surfaces. A) Percentage time spent with protrusion spreading towards cell front, on an unconfined continuous surface. B) Percentage time spent with protrusion spreading towards the cell front, in confined continuous environments; frontal gap size $10\mu m$. C) Percentage time spent with protrusion spreading towards the cell rear on an unconfined continuous surface. D) Percentage time spent with protrusion spreading towards the cell rear, in a confined continuous environment; frontal gap size $10\mu m$. All data from simulations of cells with the ability to form blebs and actin protrusions, with an overall contractility level of 1.0. Increased rear contractility suppresses protrusion spreading towards the cell rear, and increases the likelihood of protrusion formation to the front. Reduced PIP_2 at the cell rear (PIP_2 polarities -50% and -20%) increases protrusion spreading towards the front of the cell, and reduces probability of protrusions spreading towards the cell rear. Similarly, reduced PIP_2 at the cell front (PIP_2 polarities 50% and 20%) increases protrusion spreading probability to the cell rear, while decreasing protrusion spreading probability towards the cell front.

myosin at this region, deteriorating the efficiency of contractile force generation. Overall, when the asymmetry in contractile forces is sufficiently high to substitute for the benefits of rear blebbing that are observed at low asymmetries; increased blebbing at the cell rear brings only adverse effects on cell velocity. Consequently, at high levels of contractile asymmetry, the cells can move fastest with uniform blebbing (Figure 4.10A – sixty per cent myosin asymmetry).

4.4.2 Confined Continuous Environments: The Balance Between Actin Protrusions Towards the Cell Front and Detachment of the Cell Rear

Investigation of variable ERM and myosin asymmetries for cells, within confined continuous environments, reveals the balance between the contribution of blebs and actin protrusions to be the key for effective motility. Blebs that are larger in size are more effective in driving cell motility, and larger bleb sizes can be facilitated by higher levels of PIP_2 reduction, leading to easier detachment of the membrane from the cortex; or increased contractility of the cell, leading to increased pressure driving bleb growth. At low levels of PIP_2 polarity (Figure 4.10 twenty per cent reduction at cell rear), the aforementioned benefits of increased blebbing at cell rear, namely facilitating faster rear detachment and reducing the probability of actin protrusion spreading in the direction opposite to cell movement (Figure 4.11B/D), are dominant. With increasing PIP_2 polarity, the blebs at the cell rear start interfering with contractile force generation, as was the case for unconfined surfaces, and the cell velocity is reduced with higher levels of PIP_2 reduction at the cell rear (Figure 4.10B fifty per cent reduction at cell rear). In the case of reduced levels of PIP_2 at the front of the cell, blebbing interferes with protrusion spreading to the front of the cell; hence the velocities are reduced in line with the increase in the polarity strength. Although this observation is similar to the case for unconfined surfaces, increased blebbing at the cell front is an effective cell motility mechanism in confined environments, and the loss of velocity due to reduced actin protrusions is balanced to some extent, by cell movement driven by expanding blebs, causing the detrimental effects of front blebbing to be less significant (Compare Figure 4.10A and B).

4.4.3 Discontinuous Environments: Blebbing at the Cell Front Prevails

In confined, discontinuous environments, plasma membrane blebbing is the most effective strategy (Figure 4.8). Increased blebbing at the cell front facilitates pushing the membrane and cytoplasm forward, and lateral blebs facilitate traction generation. Moreover, unlike for continuous environments, detachment of the cell from the ECM is not as strong a limiting factor (Figures 4.4, 4.6 and 4.8). Thus, higher cortex-membrane linkage at the cell rear is always more favourable in confined discontinuous environments (Figure 4.10C). With increased efficiency of blebs in driving cell motility, and reduced benefits of blebbing at the cell rear, PIP_2 reduction at cell rear results in slower movement compared to no asymmetry in PIP_2 distribution – zero PIP_2 polarity. In fact, at high levels of PIP_2 reduction at the cell rear blebbing can overcome the effects of polarised contractility, resulting in cell movement towards the ”rear” - here, rear being defined as the region of increased myosin II driven contractility (Figure 4.10C, fifty per cent PIP_2 reduction and thirty per cent myosin increase at rear). Overall, an analysis of spatial variation in cortex-membrane linker and myosin II driven contractility polarities predicts that, mechanisms influencing whether cortex-membrane linkage and myosin contractility locally co-vary or, are inversely related, will differentially effect migration depending on the matrix geometry.

Chapter 5

Predicting Cell Behaviour and Response to Biochemical Perturbations

5.1 Introduction

In this chapter, model predictions for both *in vivo* and *in vitro* cell behaviour, as well as the cell's response to biochemical perturbations, are investigated. Initially, the behaviour of metastatic melanoma cells are probed, and the model predictions validated both *in vitro* and *in vivo*. After demonstrating the model can successfully mimic metastatic melanoma behaviour, the effects of biochemical perturbations are analysed. Predicted cellular responses to a set of perturbations, are again validated both *in vitro* and *in vivo*.

Initially, the metastatic subtype – A375M2 – of the melanoma cell line utilised in model parameterisation – A375P – is investigated. The model predicted the metastatic subtype A375M2 will have significantly higher cell velocities than A375P cells within *in vivo* mimetic environments, but not on unconfined continuous surfaces. Model predictions indicate the morphology of a motile cell to be highly amorphous, with the predominant motility mode being amoeboid blebbing within *in vivo* mimetic environments. Moreover, model cells display cell motility profiles similar to those observed *in vivo*, with periods of fast movement followed by periods of slow movement, and even, at low frequencies of occurrence, periods of statis. The cell nucleus interacts with the cortex in the neck region of

plasma membrane blebs, and since the nucleus can only translocate after the cortex in these regions have disassembled, such interactions are closely coupled to the overall movement of the cell body. In line with the suggestion that a rigid nucleus is a limiting factor for cells movement through small gaps within a complex ECM environment, the model predicts that the nucleus does have significant influence on cell motility profiles within *in vivo* mimetic environments, but not on unconfined surfaces.

Experimental analysis of melanoma cells, both *in vitro* and *in vivo*, validates all model predictions: on the morphology of the motile cell, the movement profile, and the interactions of the nucleus with the plasma membrane blebs. Moreover, in all cases, the magnitude of the predicted cell velocities are in good agreement with those measured experimentally. Metastatic melanoma cells indeed move with an amoeboid blebbing motility mode, and the interaction of the nucleus with the residual cortex of the bleb necks notably influences the translocation of the cell body. In exceptional cases where this cortex does not disassemble, the cell cannot generate movement. The results presented in the previous chapter suggest the amoeboid blebbing motility mode will be effective for a broad range of parameters that are investigated in the model. Following the validation of model predictions on A375M2 cells, other systems are invested to see if a similar motility mode can be observed. Indeed, a similar motility profile is demonstrated by intravital imaging of breast cancer cells, and surprisingly, endothelial cells surrounding melanoma.

Affirming the model can successfully mimic cell behaviour *in vivo*, the model is then challenged to predict the effects of biochemical perturbations on cell velocity. A set of biochemical perturbations reducing cortical contractility (+ Y27632), reducing cell-ECM adhesion (integrinβ1 shRNA), or impairing signalling pathways between the cell-ECM adhesion sites to contractile and protrusive machineries (+ Dasatinib), is selected. The changes induced by these perturbations on actin polymerisation based protrusion initiation, cell contractility, cell-ECM adhesion, and membrane-cortex adhesion are characterised *in vitro*. These effects are mapped to the relevant model parameters, and the emergent cell velocity profiles, within *in vivo* mimetic environments and on unconfined surfaces, investigated. Alongside model simulations, experiments were carried out (Tumour Cell Biology Laboratory) to confirm or refute the predictions of the model by performing

intravital imaging of A375M2 melanoma cells invading into interstitial collagen *in vivo*, and by investigating motility profiles on 2D collagen matrices *in vitro*. The model successfully predicts all treatments will significantly reduce cell velocity on 2D surfaces, but only contractility reduction will have significant effects on cell motility profiles *in vivo*. The model also predicts that a reduction in contractility will lead to an elongated cell morphology, and a reduced plasma membrane bleb formation capacity, accompanied by a reduction in cell velocity *in vivo*. Moreover, the scales of the observed effects are predicted to be dose dependent. The morphology of the integrin depleted and Dasatinib treated cells are predicted to be similar to the control state, with excessive blebbing observed for high levels of cellular asymmetry under Dasatinib treatment. All the listed predictions of the model, cell motility profiles and the morphology of the motile cell, have been validated by experimental observation. In summary, by measuring rather simple variables *in vitro*, the model have been able to predict the melanoma response of three very different putative anti-invasive interventions *in vivo*.

Finally, the effects of the surface segments within the *in vivo* mimetic ECM, and the role of ECM filament flexibily are investigated. The model predictions suggest that the continuous surfaces need to be long enough for the whole cell to spread on, to have a significant improvement effect on cell velocities. Model demonstrates the cells can deform the flaxible filaments, applying pushing forces at the front and pulling forces at the rear, but the flexibility of the ECM does not have a significant influence in cell velocities.

It should be noted that the author of this thesis has taken part in the analysis, but not the collection of experimental data associated with the prediction validation of the computational model; data was collected by the Tumour Cell Biology Laboratory, based within the London Research Institute of Cancer Research UK.

5.2 Model Predicts *in vivo* Behaviour of Invasive Melanoma Cells

As presented in the previous chapter, cell motility in a confined discontinuous environment has distinctive, and somewhat unexpected characteristics. However,

the model environment described in that chapter is highly regular, with constant sized lateral and frontal gaps between aligned filaments. This regularity continuously offers lateral gaps to the cell for anchoring, and does not necessitate any directionality change or any change in the level of confinement, i.e. the cell does not need to squeeze its body into a tighter gap at any point. Therefore, the observed peculiarities of the cell behaviour in confined discontinuous environments, such as increased cell velocity with reduced cell-ECM adhesion and the change of the optimal motility mode from mesenchymal to blebbing, should then be tested in more complex, hence more biologically relevant environments. To investigate cell behaviour in an environment closely resembling the interstitial collagen matrices surrounding melanoma, *in vivo* mimetic matrices are generated *via* the methodology described in Section 3.12.1.

Following the preparation of the environments, the cell type to be investigated by simulation is selected as the metastatic melanoma cell line A375M2. A375M2 cells form a highly metastatic subtype of the cell line utilised in parameterisation of the model (A375P cells) (178), and they have both increased overall contractility and increased cell-ECM adhesion compared to A375P cells (Figure 5.1). Selecting the normal cell-ECM adhesion level as 10 adhesion units for A375P cells, the model parameters are scaled accordingly to reflect the properties of A375M2 cells (Table 5.1).

Table 5.1: Parameters characterising the metastatic melanoma cell line A375M2. The parameters are normalised to A375P cells, the cell line utilised in model parameterisation.

	Protrusion Initiation	Myosin Contractility	Integrinβ1	Membrane-Cortex Linker
A375P	1.00	1.00	1.00	1.00
A375M2	0.57	1.40	1.30	1.00

Following the preparation of the environments and the cell lines, A375P and A375M2 cells are simulated on unconfined surfaces, in confined continuous envir-

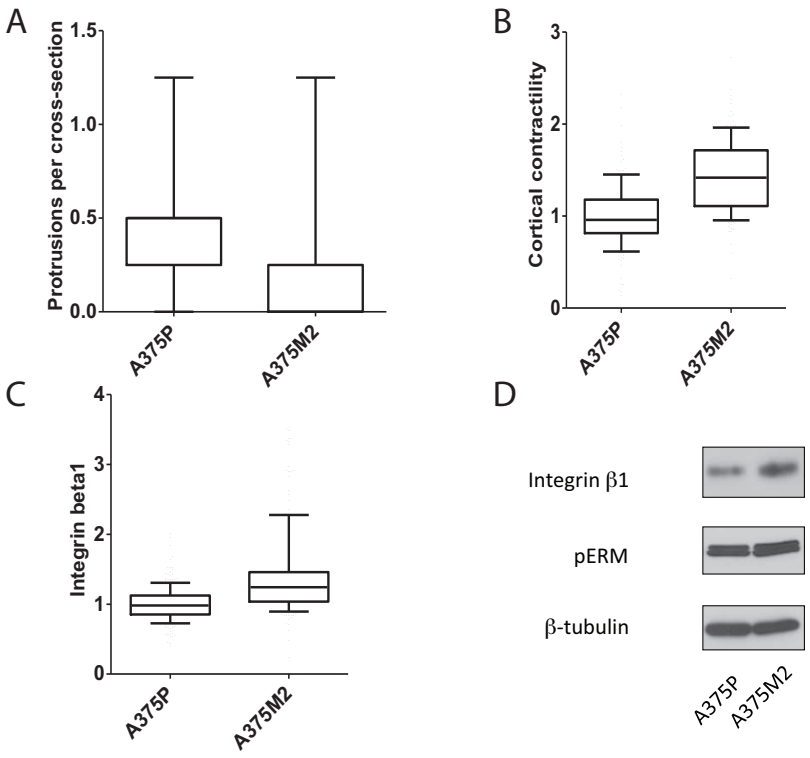

Figure 5.1: Experimental characterisation of the differences between A375P and the metastatic subtype A375M2 cells. A) Difference in protrusion frequency between A375P and A375M2 cells. Average of > 50 cells from two independent experiments. B) Difference in cortical pS19-MLC between A375P and A375M2 cells. Average of > 50 cells from two independent experiments. C) Integrinβ1 levels measured by immune-fluorescence in A375P and A375M2 cells (~50 cells measured for each data point). D) Representative western blots showing integrinβ1, pERM and β-tubulin (loading control) levels in A375P and A375M2 cells.

onments of 12.5μm frontal gap, and within *in vivo* mimetic ECMs. At this point in the development of the computational model, the cell nucleus is incorporated, together with the improved, flexible definition of bleb necks. Throughout all the simulations presented in this chapter, cells are allowed to form both plasma membrane blebs and actin polymerisation based protrusions. For each of the environments, simulations are carried out for a range of polarity levels, with increased contractility at the cell rear and reduced plasma membrane–cortex adhesion strength at the cell front. Moreover, aiming at modelling the cell's response to a chemotactic cue within *in vivo* mimetic environments, the cell is allowed to realign its polarity axis depending on its orientation within the ECM. The preferred direction of the cell is in the positive $x-$direction at all times, and at each time step, the polarity axis is realigned towards the furthermost point of the cell surface in the positive $x-$direction. Expanding blebs are excluded from the furthermost point selection, as there is not sufficient cortex under the bleb rim to host necessary signalling proteins to sense the environment. On the other hand, blebs are included in the selection during their retraction period. The selection of the polarity axis is demonstrated by the schematic in Figure 5.2. It is important to note that the realignment of the polarity axis alters the equilibrium myosin levels for contractility polarity, and shifts the mean of the probability distribution for membrane-cortex attachment protein polarity (see Section 2.10.2). Hence, the realignment of cell polarity induces a gradual shift of protein concentrations by the normal rules governing diffusion and stochastic fluctuations, rather than causing unrealistic, abrupt changes in protein levels.

5.2.1 Model Predictions for Melanoma Motility *in vitro*

On unconfined surfaces, the simulations do not reveal any significant difference between the velocities of A375P and A375M2 cells (Figure 5.3). The antagonistic relationship between cortical contractility and actin polymerisation based protrusion formation dictates that the increased myosin levels of A375M2 cells will lead to an increase in cell velocity due to elevated force generation, while leading to a reduction in cell velocity due to suppression of protrusions. The model predictions suggest that the benefits and impairments of the increased myosin level of A375M2

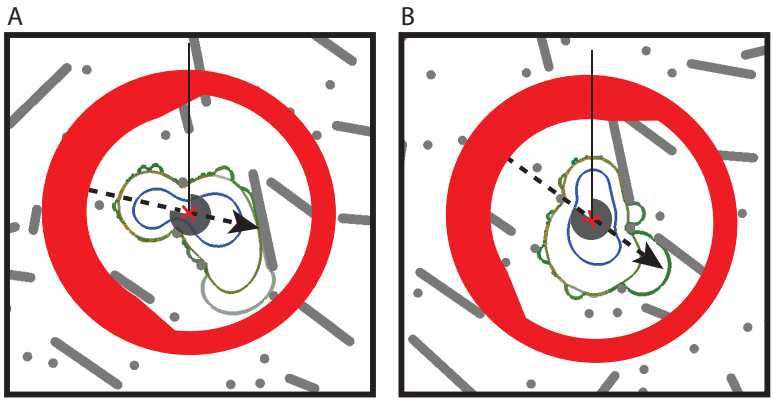

Figure 5.2: Realignment of cell polarity axis as a chemotactic response within *in vivo* mimetic environments is demonstrated. The furthermost point of the cell in the positive x-direction is marked by the dashed arrow. Here, the realignment of the increased equilibrium myosin levels at the cell rear is demonstrated by the thickness of the red circle. The centre of contractility increase is aligned to fit the opposite point on the cell surface with respect to the furthermost point. The angle that marks the origin of polarity (θ^m_{ori}) is shaded in grey at the centre of the cell. A) The expanding bleb is not considered for furthermost point reading, as an expanding bleb lacks the necessary cortex structure to host the proteins of the signalling pathways to sense the chemotactic cue of the environment. B) A retracting bleb has enough actin cortex at its rim, and can sense the environment, hence it is included in the furthermost point calculation.

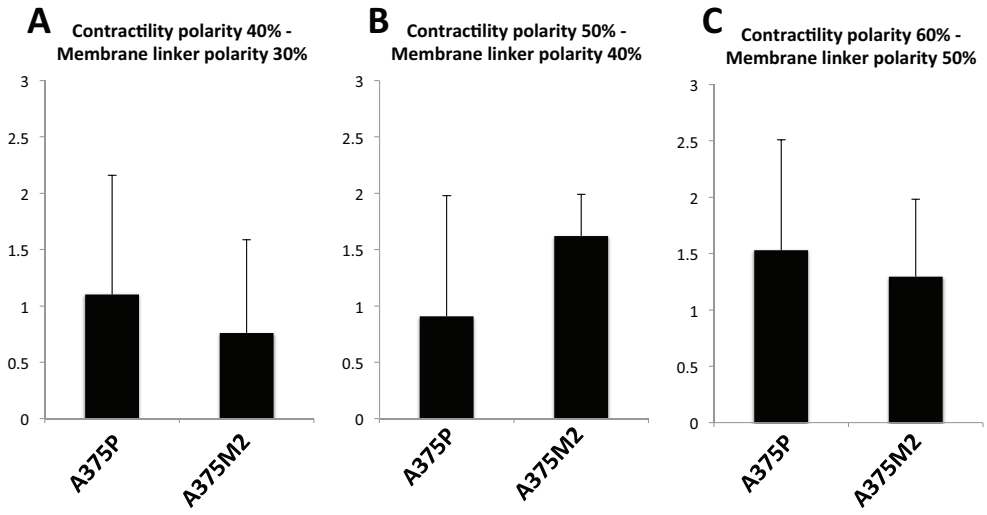

Figure 5.3: Model predictions for the velocities of A375P and A375M2 cells on unconfined surfaces, for a range of asymmetries in cortical contractility and plasma membrane–cortex linker distributions. There is no significant difference identified between the velocities of cell lines, as compared at individual polarities (two-tail t-test, p-values above 0.01). A) 30 % increased contractility at the cell rear, 40 % reduced plasma membrane–cortex linker concentration at the cell front. B) 40 % increased contractility at the cell rear, 50 % reduced plasma membrane–cortex linker concentration at the cell front. C) 50 % increased contractility at the cell rear, 60 % reduced plasma membrane–cortex linker concentration at the cell front.

cells are at a balance, with the final velocity profiles being the same as A375P cells. This can also be seen from the average percentage protrusion spread times for each cell type (Figure 5.4). From these percentages, it is clear that A375P cells have significantly longer periods of actin polymerisation based protrusions pulling the cells forward, while A375M2 cells predominantly rely on the contractile forces. The model predictions also suggest that the simultaneous increase in integrin and myosin levels of A375M2 cells ensure these cells are not completely detaching from unconfined surfaces.

In confined continuous environments, and with moderate to high polarities,

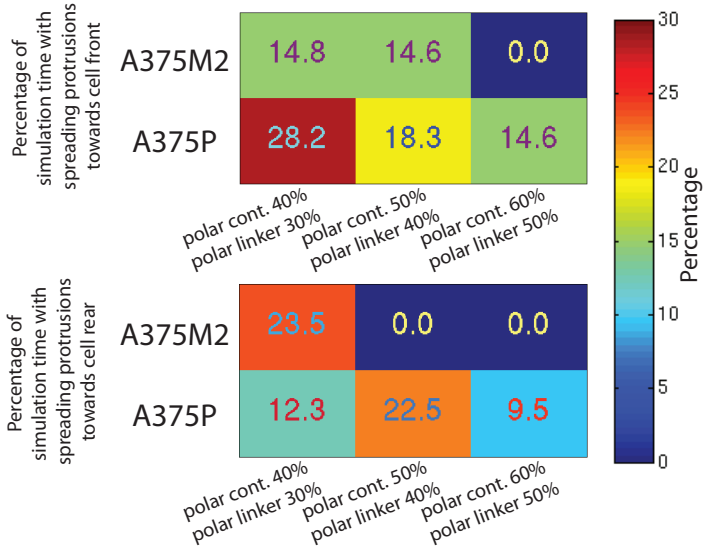

Figure 5.4: Percentage of simulation times with spreading protrusion for A375M2 and A375P cells. Top panel, percentage of simulation time where the cell has protrusions spreading towards the cell front. Bottom panel, percentage of simulation time for protrusions spreading towards cell the rear. The cells are on an unconfined continuous surface.

A375M2 cells become significantly faster than A375P cells (Figure 5.3). This is inline with the observations recorded in the previous chapter, where the velocities of the amoeboid cells are shown to exceed those of mesenchymal cells at high contractility levels (Figure 4.6). The benefits of the elevated contractility of A375M2 cells prevails over the impairment caused by reduced actin polymerisation based protrusions, and A375M2 cells become significantly faster than A375P cells.

5.2.2 Model Predictions for Melanoma Motility *in vivo*

In accordance with A375M2 cells being the metastatic subtype of A375P cells, within the *in vivo* mimetic environments, simulations reveal that A375M2 cells move faster than A375P cells at all polarities, the difference being predominant at low polarities (Figure 5.6). The increased velocities of A375M2 over A375P cells within *in vivo* mimetic environments can be linked with the predicted morphology and motility mode: Within the *in vivo* mimetic environments, the model predicts

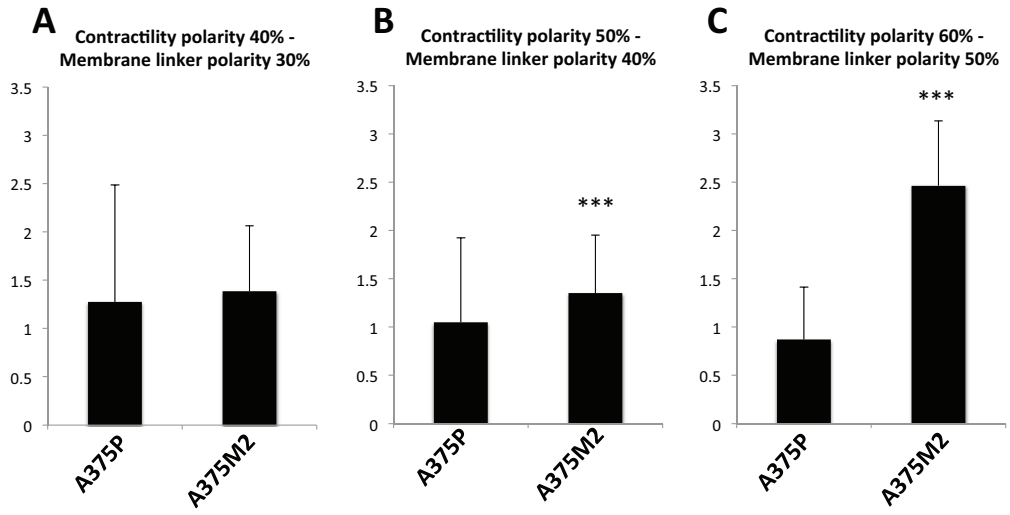

Figure 5.5: Model predictions for the velocities of A375P and A375M2 cells within confined continuous environments of 12.5μm frontal gap size, for a range of asymmetries in cortical contractility and plasma membrane–cortex linker distributions. (***) indicates significant difference from A375P cells under the same conditions, p-value$<$ 0.001, two-tail t-test. A) 30 % increased contractility at the cell rear, 40 % reduced plasma membrane–cortex linker concentration at the cell front. B) 40 % increased contractility at the cell rear, 50 % reduced plasma membrane–cortex linker concentration at the cell front. C) 50 % increased contractility at the cell rear, 60 % reduced plasma membrane–cortex linker concentration at the cell front.

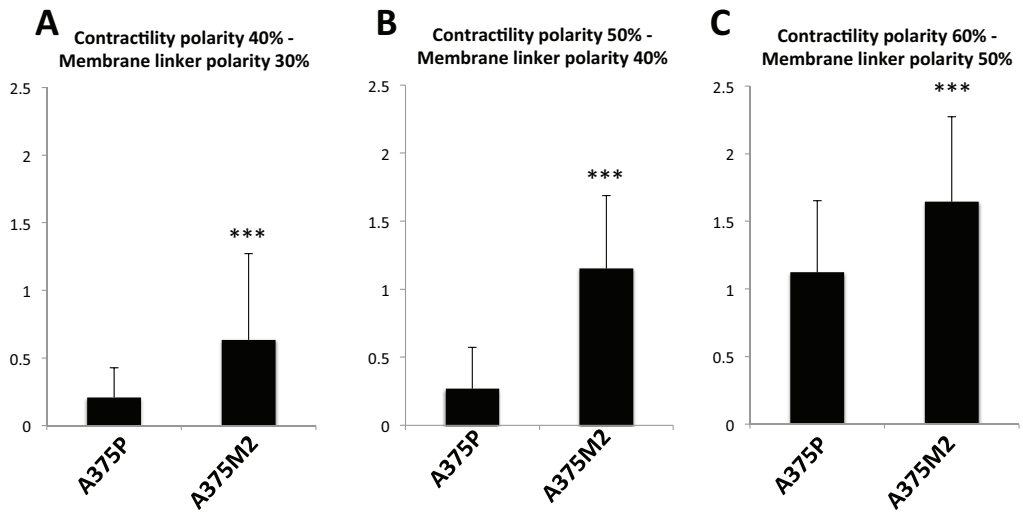

Figure 5.6: Model predictions for the velocities of A375P and A375M2 cells within *in vivo* mimetic environments, for a range of asymmetries in cortical contractility and plasma membrane–cortex linker distributions. (***) indicates significant difference from A375P cells under same conditions, p-value$<$ 0.01, two-tail t-test. A) 30 % increased contractility at the cell rear, 40 % reduced plasma membrane–cortex linker concentration at the cell front. B) 40 % increased contractility at the cell rear, 50 % reduced plasma membrane–cortex linker concentration at the cell front. C) 50 % increased contractility at the cell rear, 60 % reduced plasma membrane–cortex linker concentration at the cell front.

that the cells will adapt an amoeboid blebbing motility mode (Figure 5.7). The identified benefits of increased contractility in confined discontinuous environments explain the higher velocities of A375M2 cells over A375P cells. In the scope of the difference being higher at low polarities, the predicted morphology provides an explanation with the threshold like nature of bleb formation; the non-linear increase in bleb formation probability with increasing contractility (Figure 4.1D).

Considered from a global perspective, model predictions of a cell's motility mode has an even more profound impact. As demonstrated in the previous chapter, the

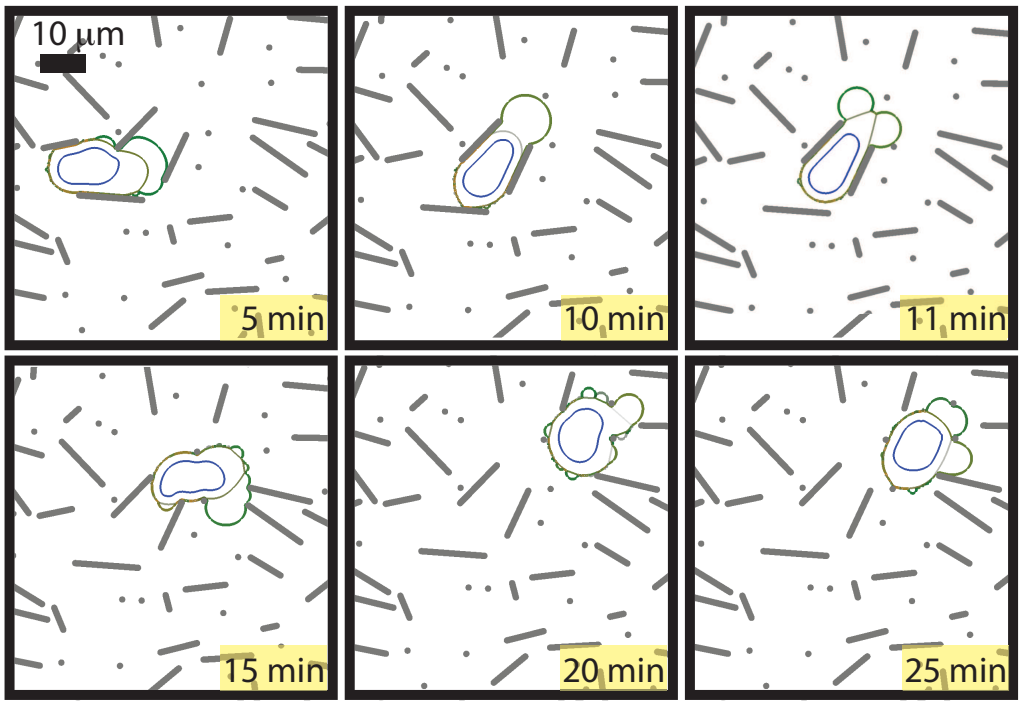

Figure 5.7: Model snapshots for an A375M2 cell within an *in vivo* mimetic environment at 5 minute intervals. Scale bar displayed on the snapshot at 5 minutes is 10 *μm*. The amoeboid motility mode, where the cell protrudes its body forward with large plasma membrane blebs (10 minutes, 15 minutes), and the retracting cell rear (11 minutes) can be seen. The interactions of the nucleus with the cell rear cortex (throughout the snapshots), and the bleb neck cortex (10 and 25 minutes) can be seen. For further examples, see Figure 5.9. The actin cortex is represented in green, myosin in red, the plasma membrane in light grey, with overlay of actin, myosin and membrane generating an orange colour. Nuclear lamina is shown in blue and the ECM filaments are shown in dark grey.

requirements of mesenchymal and amoeboid motility modes are fundamentally different in terms of cortical contractility, plasma membrane cortex adhesion distribution, and cell–ECM adhesion distribution. Consequently, to inhibit these cells from metastasising, different sets of molecular pathways should be modulated. For metastatic melanoma cells within *in vivo* collagen matrices, the model predicts that the predominant mechanism to protrude the cell body forward will be formation of large plasma membrane blebs, followed by pulling of the rest of the cell body *via* increased contractility at the cell rear (Figure 5.7). The morphology of the motile cell is predicted to be highly dynamic, and even though the cells may follow the same chemotactic gradient, the stochastic initiation of the blebs is predicted to generate multiple cell trajectory pathways within the same ECM (Figure 5.8). The model also predicts a saltatory movement profile, where the cell goes through rapid movement phases, followed by slow, in some cases stationary, phases - these profiles are presented side-by-side with the equivalent experimental profiles in Figure 5.13. Moreover, the model indicates that the ability of the cell to rapidly respond to a chemotactic cue, in terms of realigning its polarity axis, is essential. Indeed, simulations with a fixed polarity axis reveal that these cells display small fluctuations in position, but are not able to penetrate through the complex geometry of the *in vivo* mimetic ECM.

Overall, the model suggests that metastatic melanoma is employing a motility mode that, compared to mesenchymal cells, necessitates distinct biochemical pathway perturbations for inhibition of metastasis.

5.2.3 Influence of the Improved Bleb Neck Cortex Definition and the Nucleus

Close investigation of the model cell behaviour within *in vivo* mimetic environments indicates that the nucleus interacts with the residual cortex at the base of the plasma membrane blebs: the bleb necks. Especially during squeezing of the cell through tight gaps, the nucleus is packed towards the residual cortex of the bleb necks (Figure 5.9 red arrows), and forward movement of the nucleus is allowed only upon complete disassembly of these cortex patches (Figure 5.9 blue arrows). At instances of large bleb formation and propelling of a large portion of the cell

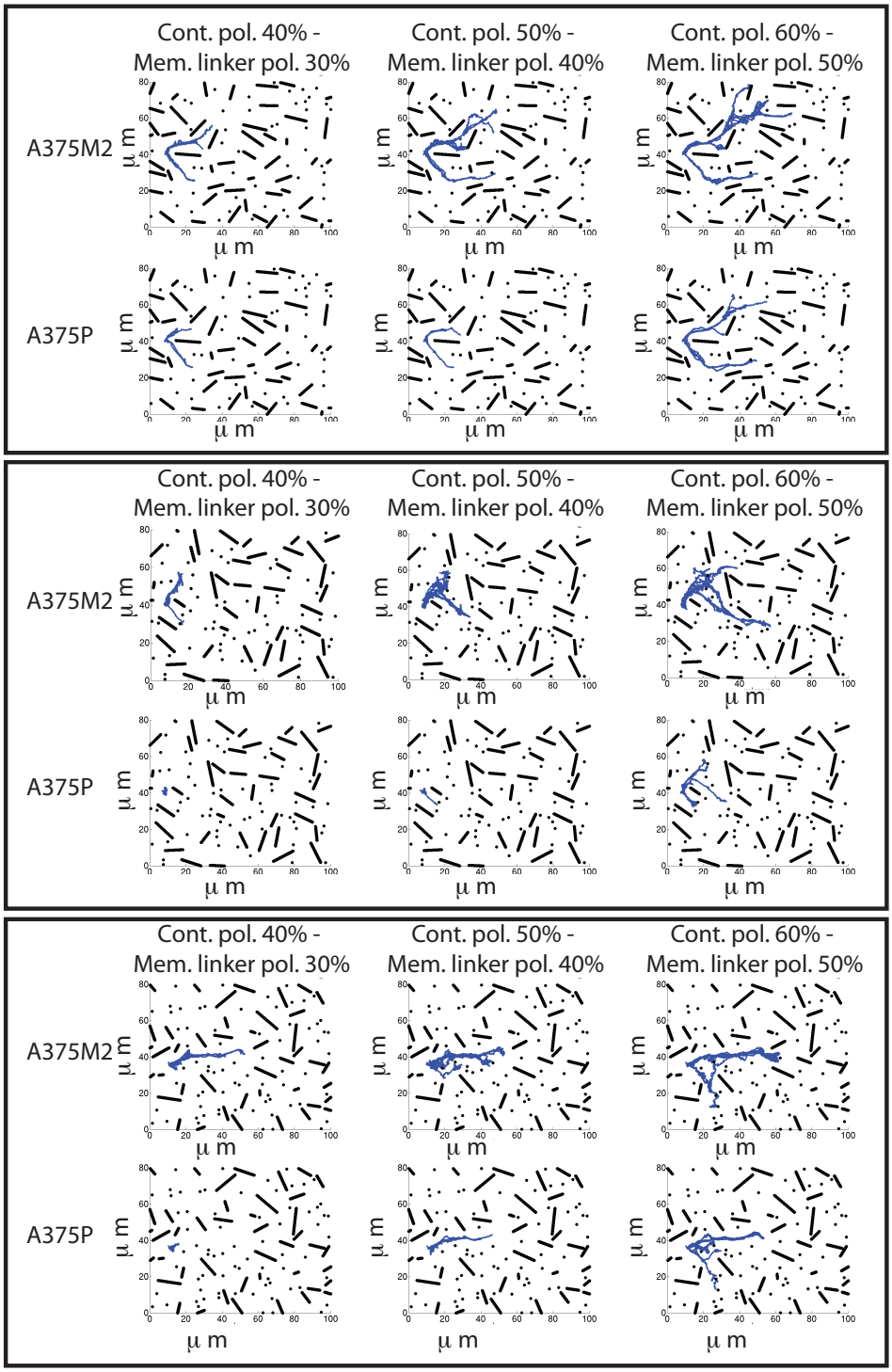

Figure 5.8: Model trajectories for A375M2 and A375P cells. Three different *in vivo* mimetic environments are grouped in panels. The top row in each panel represents the trajectories of A375M2 cells with increasing levels of asymmetry in cortical contractility and plasma membrane–cortex linker distribution. Bottom row displays A375P cell trajectories under the same conditions. ECM filaments are shown in black, cell trajectories in blue. Each panel shows at least ten simulations, twenty minutes each.

volume forward, the cell nucleus is dragged to the rear of the cell, becoming constrained between bleb necks at the cell front and the contractile cortex at the cell rear (Figure 5.9 grey arrows).

Upon observing the interaction of the cell nucleus with other parts of the cell's motile machinery, the contractile cell rear and the plasma membrane bleb necks, the influence of the rigid cell nucleus on predictions of cell velocities is investigated. Simulations are carried out for cells with i) the simple definition of the bleb neck and without a nucleus, and ii) the improved, flexible bleb neck definition and without a nucleus. The resulting velocity profiles reveal that independent of the presence of a cell nucleus, the switch to an improved definition of bleb necks causes changes in the predicted cell velocities only at low polarity levels within the *in vivo* mimetic environments, and high polarity levels on unconfined surfaces. In confined continuous environments, the changes are significant at all polarities (Figure 5.10A-B). This implies that addition of flexible bleb necks introduces minor alterations to bleb dynamics, such that under conditions of moderate blebbing, essentially due to the threshold-like nature of blebbing, significant differences can be seen to occur in cell velocities for cells with and without the modification (Figure 4.1D). For cells with low polarity levels moving on unconfined surfaces, the influence of blebbing is negligible for both setups, hence no significant changes are observed in cell velocity. At the other end of the scale, for *in vivo* mimetic environments, blebs are sufficiently large under all conditions, hence no significant changes in cell velocities are observed.

Addition of the nucleus to the model, together with the improved definition of bleb necks, brings significant changes in the predicted velocities of cell for high polarity levels within the *in vivo* mimetic environment. However, a very limited effect is observed for cells on both unconfined, and confined, continuous surfaces (Figure 5.10C). The predicted effect of the nucleus is in line with the experimental observation that the rigid nucleus becomes a limiting cellular structure for the movement of the cell through gaps within *in vivo* ECMs, and the cell must actively squeeze its nucleus through gaps *via* myosin II driven contractile forces (48–53).

Finally, it should be mentioned here that although the predicted cell velocity magnitudes have changed, the predicted relative effects to the perturbations on the

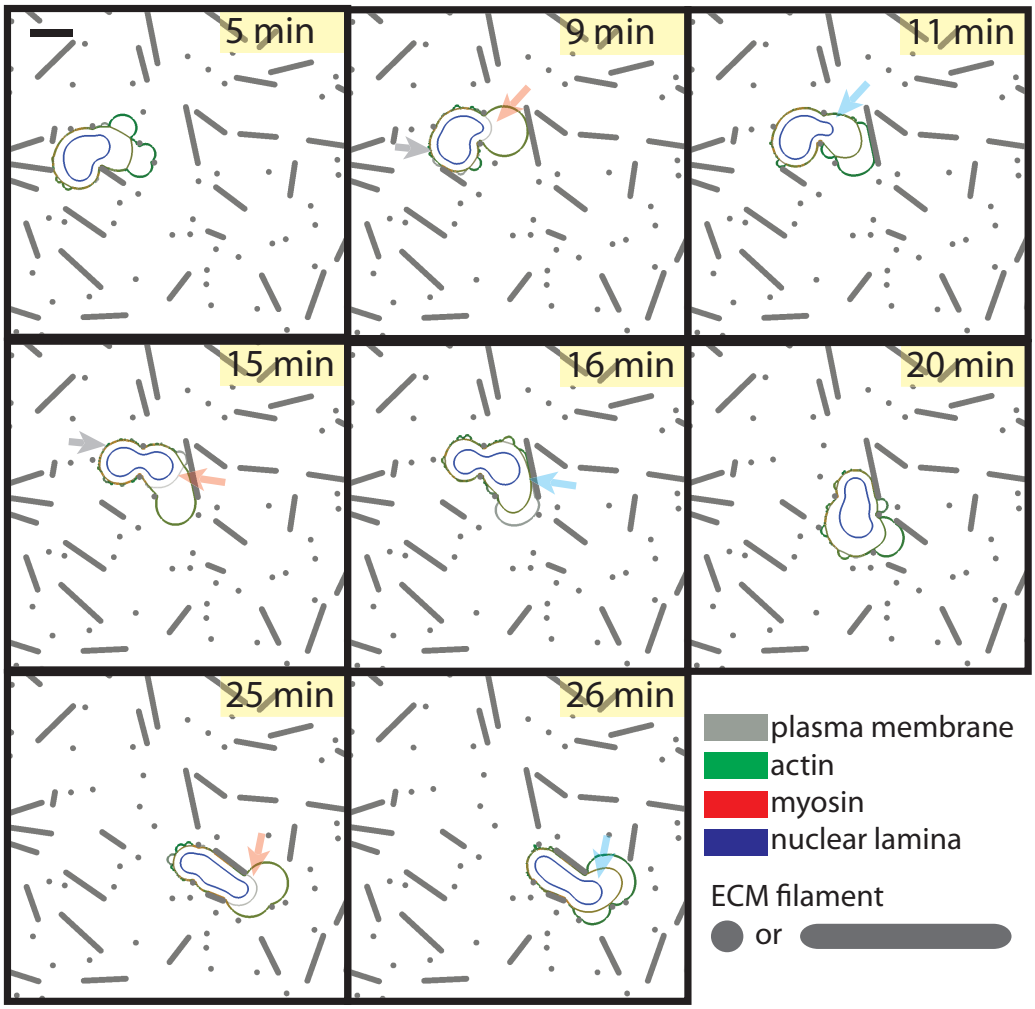

Figure 5.9: Model snapshots for A375M2 cell within an *in vivo* mimetic environment. The red arrows mark the areas where nucleus is packed against the residual cortex at the neck of a bleb. The blue arrows point to the movement of the nucleus upon disassembly of the bleb neck cortex marked in each of the previous snapshots. Grey arrows mark areas where the nucleus is packed against the cortex at the rear of the cell. The nucleus is dragged towards the rear at the beginning of the simulation, and stays at this position relative to the cell body throughout the simulated 30 minutes. The scale bar at 5 minute snapshot is 10μm, and is valid for all snapshots. The actin cortex is represented in green, myosin in red, and the plasma membrane in light grey (see 16 minutes, the frontal expanding bleb). Overlay of actin, myosin and membrane generates an orange colour. Nuclear lamina is shown in blue and the ECM filaments are shown in dark grey.

system are not modified by the addition of the nucleus or the flexible bleb necks to the computational model - presented in Section 5.3.2 and Appendix C.

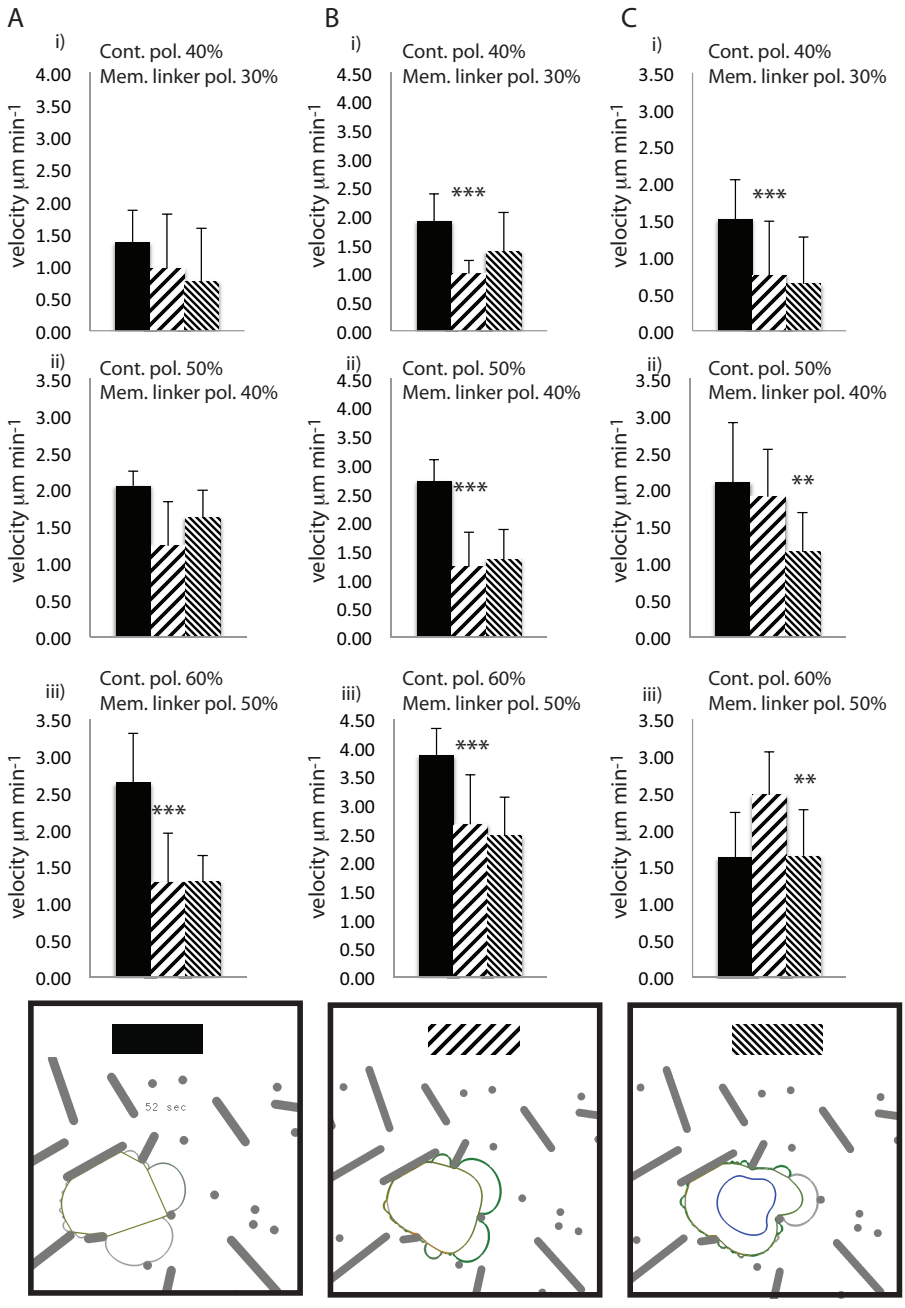

Figure 5.10: Effects of flexible bleb neck cortex and nucleus implementation into the model. Legend continued on the next page.

Figure 5.10: Effects on the magnitude of cell velocities, with the incorporation of flexible bleb neck cortex and nucleus into the model. A375M2 cell simulations are carried out for three model setups of increasing complexity. First with simple plasma membrane bleb necks, second with improved, flexible plasma membrane bleb necks, and third with flexible plasma membrane bleb necks and a nucleus. The differences in predicted cell motility behaviour is investigated in three environments, A) On unconfined continuous surfaces, B) Confined continuous environments, and C) *In vivo* mimetic matrices. For each environment, a range of cellular asymmetry levels are investigated: i) 30 % increased contractility at the cell rear, 40 % reduced plasma membrane–cortex linker concentration at the cell front, ii) 40 % increased contractility at the cell rear, 50 % reduced plasma membrane–cortex linker concentration at the cell front, and iii) 50 % increased contractility at the cell rear, 60 % reduced plasma membrane–cortex linker concentration at the cell front. (***) indicates significant difference between predictions for the flexible bleb neck definition and the linear bleb neck definition, p-value$<$ 0.01, two-tail t-test. (**) indicates significant difference between predictions for the flexible bleb neck definition and for a cell with both flexible bleb necks and a nucleus, p-value$<$ 0.001, two-tail t-test.

5.2.4 Melanoma Motility: Experimental Observations and Validation of Model Predictions

The model predicts metastatic melanoma (A375M2) cells would move with mean velocities in the range $0.76 - 1.29 \mu m\ min^{-1}$ on unconfined surfaces, the magnitude depending on the polarity level of the cell. Within *in vivo* mimetic ECMs, the model predicts that A375M2 cells would adapt an amoeboid blebbing motility mode, with mean cell velocities in the range $0.63 - 1.6\ \mu m\ min^{-1}$, again depending on the cellular polarity level. The cells are also predicted to have a saltatory type of movement *in vivo*, rather than a continuous, constant velocity movement. Furthermore, model predictions for *in vivo* cell motility indicate a close interaction between plasma membrane bleb necks and the cell nucleus.

To test these predictions, experiments are carried out on A375M2 cells *in vitro* on top of collagen matrices forming an unconfined surface. *In vivo* experiments are performed where A375M2 cells are imaged in interstitial collagen of mice. The cell velocities measured in these experimental setups are compared with model predictions. For the comparative analysis, account for the fact that cells respond to chemotactic stimuli in a heterogeneous manner, model cell velocities are averaged over a range of cell polarity levels.

The comparative velocity values for experimental and model setups *in vitro* are presented in Figure 5.11; there is good agreement between model predictions and experimental outputs. The model predictions are presented as the average of a range of polarities, to give a predicted cell velocity of $1.22\ \pm 0.61\ \mu m\ min^{-1}$ on unconfined surfaces, while the experimental observations revels the cell velocity to be $0.89\ \pm\ 0.95\ \mu m\ min^{-1}$ on collagen matrices *in vitro*.

The *in vivo* time lapse images of A375M2 cells clearly show the dominant motility mode to be amoeboid, validating the cell morphology prediction of the model within *in vivo* mimetic environments (Figure 5.14). The images demonstrate the cells are moving with broad, rounded protrusions, which initially lack F-actin, but have a prominent F-actin neck at their base. Repetitive cycles of bleb formation result in a saltatory movement, with bursts of cell centroid movement, in between almost stationary phases (Figure 5.13B), which is in close agreement with instant-

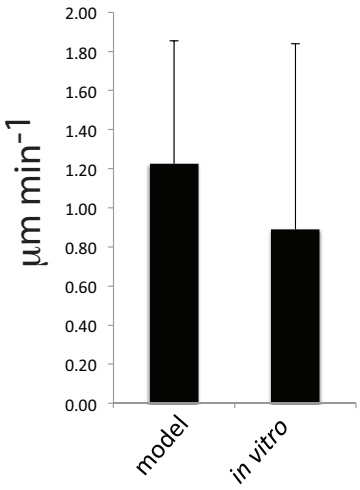

Figure 5.11: The velocities of A375M2 cells as predicted by the model and as measured *in vitro*, on 2D surfaces. The model velocities are reported as the average of all three polarities tested: 40 %, 50 % and 60 % increased contractility at the cell rear coupled with 30 %, 40 % and 50 % reduced plasma membrane–cortex linker concentration at the cell front, respectively. The error bars report one standard deviation.

aneous velocity profiles reported by the model (Figure 5.13A). Compared to the average velocity of 1.14 ± 0.60 $\mu m\ min^{-1}$ predicted by the model, the average velocity for A375M2 cells *in vivo* is measured to be 2.1 $\pm$ 1.8$\mu m\ min^{-1}$ (Figure 5.12). Notably high cell velocities, occasionally observed *in vivo* can be attributed to particularly steep chemotactic gradients leading to higher asymmetry levels than allowed in the model.

Also in good agreement with the model, the *in vivo* time lapse images show the morphological details of how the cell nucleus interacts with the cortex of bleb necks. Following forward protrusion of the cell front with protrusions of a plasma membrane bleb, the nucleus can become packed against the cortex of the bleb neck (Figure 5.14A & B top cell). Translocation of the nucleus, hence the whole cell body, is possible only after the disassembly of this cortex patch. Indeed, in cases where the cell fails to disassemble the cortex at the base of a propelling bleb, the cell front is protruded forward, but the rear fails to follow, and the cell is not able to generate net movement (Figure 5.14B bottom cell)

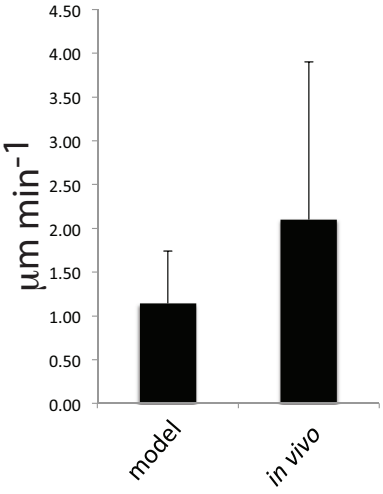

Figure 5.12: Velocities of A375M2 cells as predicted by the model and as measured *in vivo*, within interstitial collagen of mice. The model velocity is reported as the average of all three polarities tested: 40 %, 50 % and 60 % increased contractility at the cell rear coupled with 30 %, 40 % and 50 % reduced plasma membrane–cortex linker concentration at the cell front, respectively. The error bars report one standard deviation.

Overall, model predictions for the velocities of metastatic melanoma cells *in vitro* and *in vivo* are validated by experimental observations, as well as the predictions on cell morphology, and the interactions of the nucleus with plasma membrane blebs.

Although model parameterisation is based on A375P cells and validation is based on their metastatic subtype A375M2 cells, the model suggests the effective motility strategy in discontinuous environments, over a broad range of parameter space, will be an amoeboid blebbing motility (Section 4.3.3). This suggests other cell types, falling within this presented parameter range, may also adapt to a blebbing strategy at tumour margins. To test this hypothesis, behaviours of breast cancer cells and endothelial cells at tumour margins are examined. Intravital imaging of actin labelled MDA MB 231 breast cancer cells clearly demonstrates these cells can utilise an amoeboid blebbing migration mode while progressing through ECM fibres (Figure 5.14C/E). Images from the same system also demonstrate cells spread on ECM fibres, with visible spike like actin protrusion (Figure 5.14C/D),

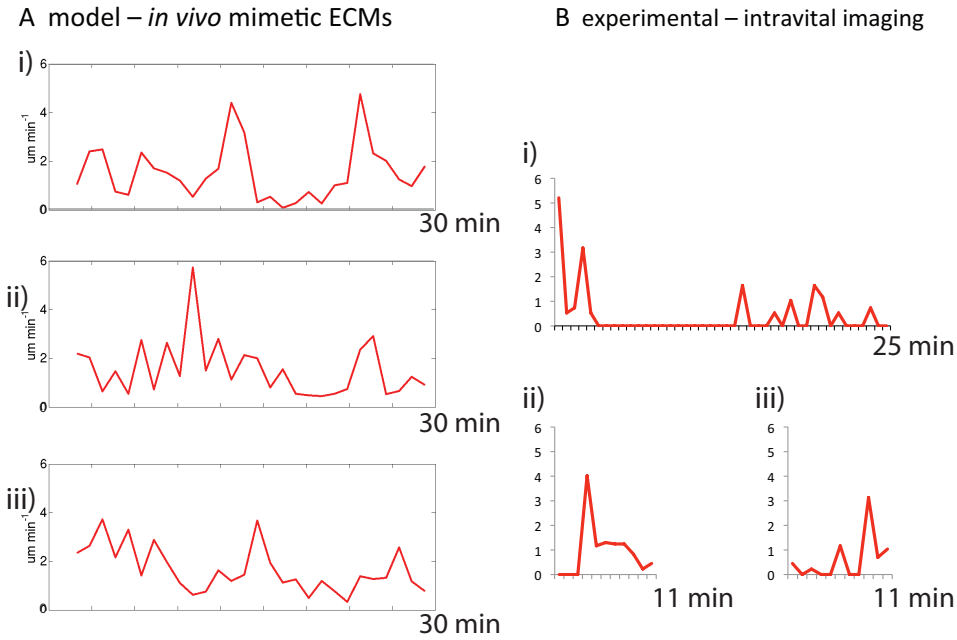

Figure 5.13: Saltatory movement profile as predicted by the model and observed in experiments. The instantaneous velocity profiles of A375M2 cells taken at 1 minue intervals A) For model simulations within *in vivo* mimetic environments, B) in interstitial collagen of mice, *in vivo*. Sample velocity profiles from three independent simulations are shown in (A), i & ii) cell with 50 % increased contractility at the cell rear, 40 % reduced plasma membrane–cortex linker concentration at the cell front, and iii) cell with 60 % increased contractility at the cell rear, 50 per cent reduced plasma membrane–cortex linker concentration at the cell front.

eliminating the possibility that the cells in (D) utilise actin polymerisation based protrusions below the resolution of the images. To investigate the behaviour of endothelial cells, melanoma tumours are generated in transgenic mice that contain an endothelial specific promoter driving the expression of a membrane targeted GFP. An important characteristic of endothelial cells is that they move with actin polymerisation based protrusions in a range of situations, from developmental to pathological, and they have not been reported to utilise other motility modes, such as blebbing. Imaging these cells with the same methodology described for melanoma cells (Appendix A), it is shown that endothelial cells at tumour margins do form plasma membrane blebs. Strikingly, endothelial cells are observed to have a rapid migration with rounded morphology, characteristic of bleb driven motility (Figure 5.15).

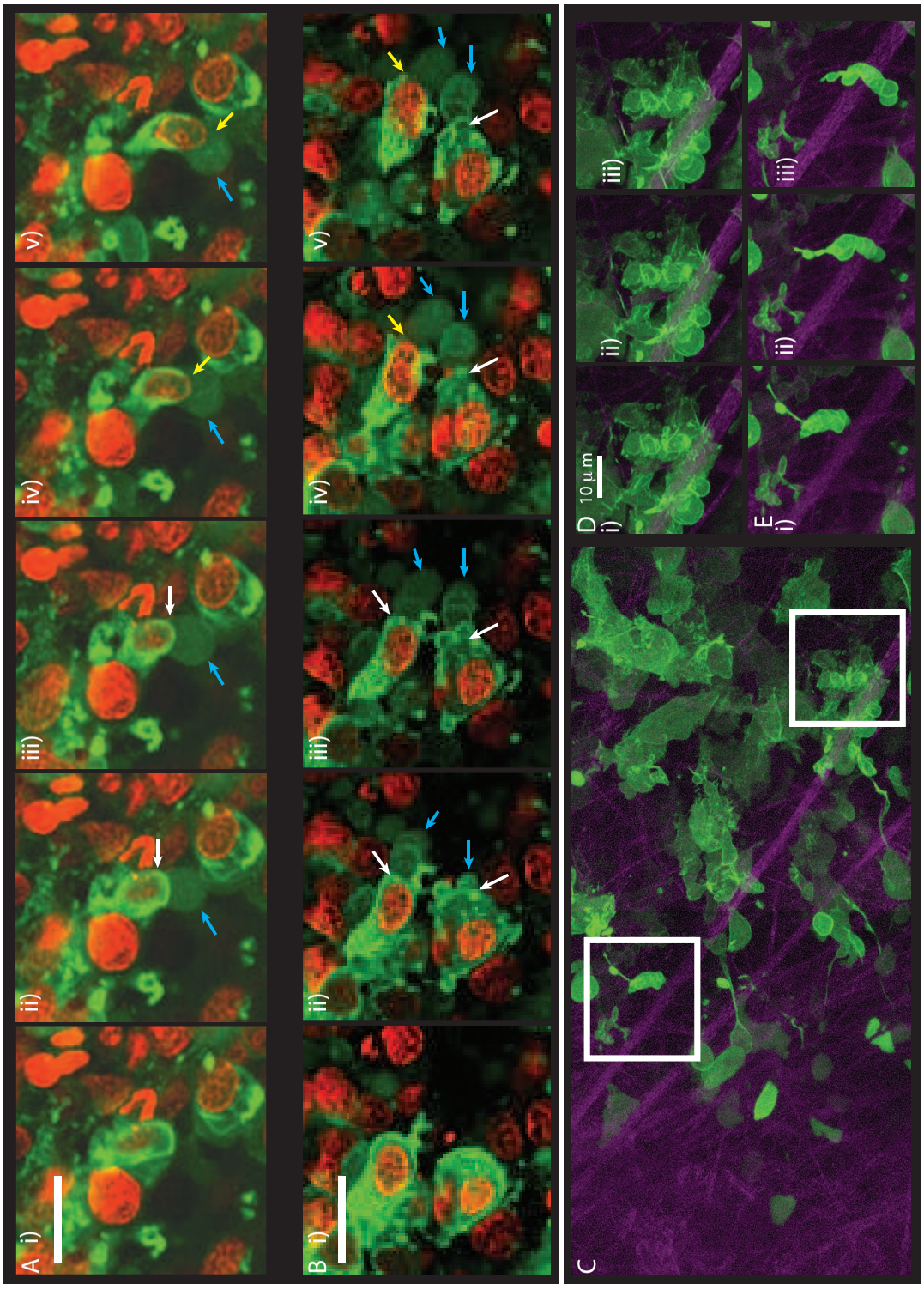

Figure 5.14: Time lapse images of melanoma cells *in vivo*. Legend continued on next page.

Figure 5.14: Time lapse images of melanoma cells *in vivo*. A-B) Intravital imaging of A375M2 melanoma migration. Actin labelled in green, and nucleus labelled in red. Images taken every 5 minutes, Scale bars in the first image (i) of each sequence is 10μm. A) A375M2 cell moving with a large plasma membrane bleb forming at the cell front (blue arrows ii-v). The nucleus is packed to the residual cortex at the bleb neck, white arrows in ii & iii. Translocation of the nucleus is only possible after disassembly of this cortex, yellow arrows in iv & v. B) Bottom cell: The cell forming successive blebs to protrude the cell front (blues arrows in ii-v), but unable to disassemble the residual cortex of the bleb neck (white arrows ii-v). The cell cannot generate any net forward movement. Top cell: Cell protrudes its front with formation of successive plasma membrane blebs (blues arrows in ii-v), and the nucleus is initially packed to the bleb neck (white arrows in ii & iii), translocation of the nucleus is only possible after disassembly of this cortex, yellow arrows in iv & v. C-E) Intravital imaging of MDA MB 231 breast cancer migration, actin labelled in green, and collagen in magenta. Time lapse images in (D/E) are from insets labelled in (C), images taken every 5 minutes. C) Cells spread on the collagen fibre, actin polymerisation based protrusions can be seen. D) MDA MB 231 cell moving through the fibres with blebbing at front. Scale bar in D is valid for all time lapse images in D and E.

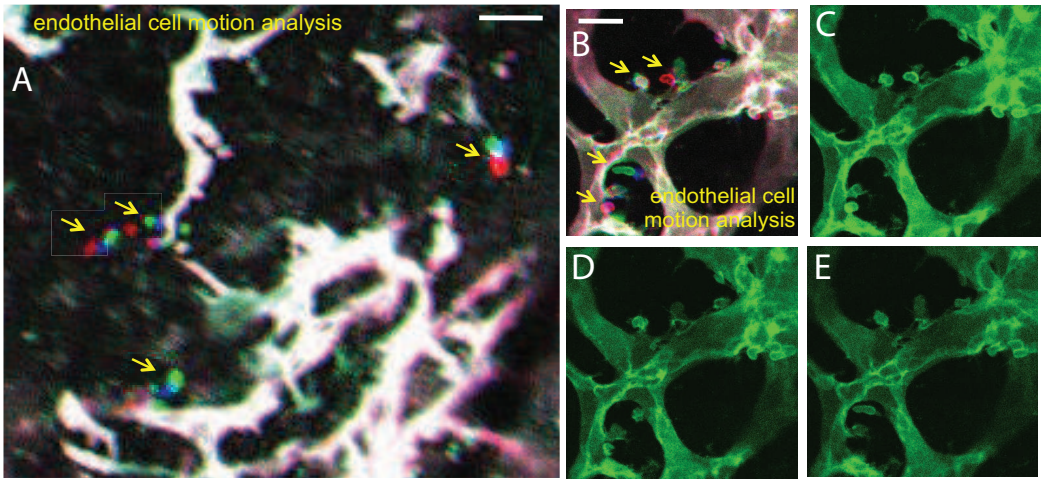

Figure 5.15: Time lapse images of endothelial cells at the tumour margin. Motion analysis of endothelial cells, confocal sections of intravital imaging of endothelial cells are shown overlaid in red, blue and green. Each colour channel is separated by 10 minutes. White indicates static cells whereas separate colours indicate motion. A) Scale bar 40μm, B) Scale bar 10μm C-E) Panels of (B), showing endothelial cells blebbing at the tumour margin.

5.3 Model Predicts the Effects of Experimental Interventions for Different Matrix Geometries

5.3.1 Characterisation of the Biochemical Perturbation Set

Model predictions reveal dramatic ECM geometry dependent differences in interrelationships between cell protrusion, contractility, cell-ECM adhesion, and cell velocity. This suggests that depending on the ECM geometry, the same experimental perturbations will result in different alterations in cell motility. There is much anecdotal evidence to support this, but until the work reported here, no robust basis have been available to ascertain just how different matrix geometries may affect optimal cell migration strategy. Therefore, the model is challenged to predict the response of A375 cells to a divergent set of biochemical perturbations, both on unconfined surfaces *in vitro*, and during movement into interstitial collagen-rich matrices *in vivo*.

Three manipulations are selected for testing: i) integrinβ1 depletion to reduce cell-matrix adhesion, ii) inhibition of ROCK kinases by Y27632 to reduce contractility, and iii) inhibition of SRC and other tyrosine kinases by Dasatinib to disrupt signalling from cell-ECM adhesion sites to protrusion and cortical contractility regulatory mechanisms. The results of these manipulations on F-actin polymerisation based protrusion formation rate, cortical contractility measured by phosphorylated myosin intensity at cortex, cell-ECM adhesion measured by integrinβ1 expression, and plasma membrane-cortex attachment measured by the surrogate phosphorylated ERM are determined experimentally *in vitro*, on 2D collagen substrates (Figure 5.16 and Table 5.2).

To reflect these manipulations, the model parameters are scaled from their values determined for A375M2 cells. Then, to predict the resulting effects of these manipulations on cell motility profiles, simulations are carried out on both unconfined continuous surfaces to mimic *in vitro* 2D substrates, and within *in vivo* mimetic environments to mimic *in vivo* interstitial collagen.

Meanwhile, following experimental perturbations, A375 cell migration is exper-

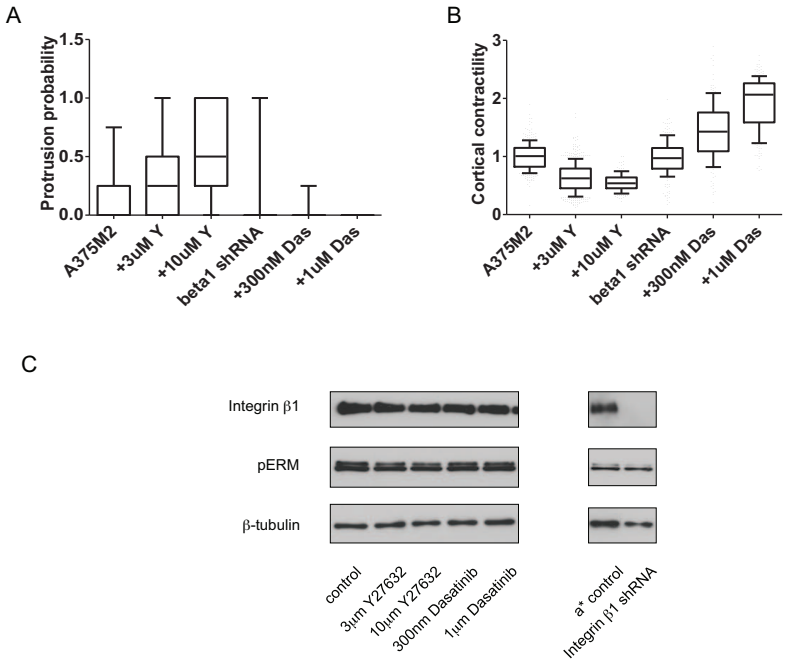

Figure 5.16: Characterisation of the biochemical perturbation effects on protrusion initiation rate, myosin II driven contractility, cell-ECM adhesion, and plasma membrane–cortex adhesion. A) Difference in protrusion frequency in A375M2 cells following the manipulations indicated. Average of > 50 cells from at least two independent experiments. B) Difference in cortical pS19-MLC in A375M2 cells following the manipulations indicated. Average of > 50 cells from at least two independent experiments. C) Representative western blots showing integrinβ1, pERM and β-tubulin (loading control) levels in A375M2 cells following drug treatment or depletion of integrinβ1.

Table 5.2: Paramaters characterising the effects of biochemical perturbations on metastatic melanoma cell line A375M2. The parameters are normalised to A375P cells, the cell line utilised in model parameterisation.

	Protrusion Initiation	Myosin Contractility	Integrinβ1	Membrane-Cortex Linker
A375M2	0.57	1.40	1.30	1.00
+ Y27632 low	1.00	1.00	1.30	1.00
+ Y27632 high	1.50	0.70	1.30	1.00
Integrinβ1 depletion	0.10	1.40	0.10	1.00
+ Dasatinib	0.25	2.00	1.50	1.00

imentally measured on planar substrates *in vitro*, and into interstitial collagen matrices that surround tumours *in vivo*. For the planar substrates, A375M2 cells are plated on collagen I *in vitro*, and the migration efficiency is monitored by time-lapse microscopy. *In vivo* analysis is carried out by generating A375M2 tumours, and then treating the mice with either ROCK or Src-family kinase inhibitors shortly before imaging. To evaluate the effects of integrinβ1 depletion, stably depleted cells that are labelled with a different colour actin probe from controls are generated. These cells are then co-injected with control A375M2 cells to generate 'mosaic' tumours. During imaging and subsequent analysis, the control and integrinβ1 depleted cells are distinguished based on their fluorescence. In the *in vivo* environment, only a minority of cells within a tumour experience the appropriate microenvironment to become motile, hence it is not possible to measure the migration speed of every cell ($> 90\%$ of cells are non-motile). Therefore, the proportion of cells moving with velocities $> 0.5 \mu m\ min^{-1}$ are quantified, and the change in this quantity is utilised as a measure of migratory behaviour.

5.3.2 The Effects of Biochemical Perturbations: Model Predictions and Experimental Validation

For the explored experimental perturbations, the model predicts different effects on cell velocity profiles, depending on the extracellular environment: whether the cells are on unconfined continuous surfaces, or within a confined discontinuous matrix with gap sizes similar to interstitial collagen - the in vivo mimetic matrix (Figure 5.17A). All perturbations are predicted to reduce cell migration on an unconfined continuous surface (Figure 5.17Ai, 5.19A). However, ROCK inhibition is the only perturbation to significantly reduce cell migration within *in vivo* mimetic environments (Figure 5.17Aii, 5.19B). Specifically, integrinβ1 depletion and Src-family kinase inhibition is predicted to have marginal effects *in vivo*. One particularly interesting observation is that the predicted relationship between cell-ECM adhesion and cell velocity within the *in vivo* mimetic environment diverges from that found for regular discontinuous matrix geometries (Section 4.3.3). Reduction in cell-ECM adhesion increases cell velocity in the uniform confined discontinuous environment at all polarities tested; however, for the more

disorganised environments, reduced integrinβ1 levels did not cause significant velocity changes (Figure 5.19B). One possible explanation for this is that the integrinβ1 depleted cells require lateral confinement to be able to anchor to the environment. Within regions of the complex environment where the cell needs to squeeze its body through a relatively small gap, compared to the available lateral confinement, adhesion to ECM may become beneficial. Therefore, although reduction in cell-ECM adhesion may be beneficial in closely packed regions of the ECM, it may hinder the cell's movement within other regions, resulting in no significant increase in overall cell velocity.

As discussed above, two different methods for predicting cell motility profile are used for experiments and model outputs: the direct measurement of cell velocity in the model, and measurment of motile cell percentage in the experimental setups. In order to validate the two different methods demonstrate similar trends, they are compared in the model. The equivalent of percentage of motile cells measurement for the model, percentage of simulation time above the threshold velocity of $0.5\mu m\ min^{-1}$, shows very similar trends to overall changes in cell migration speed (Figure 5.18).

The experimental analysis of cell migration have been carried out on planar substrates *in vitro* and into interstitial collagen matrices surrounding tumours *in vivo*. These analyses reveals that on planar surfaces, as predicted by the model, inhibition of Src-family kinases or depletion of integrinβ1 lead to dramatic reductions in cell migration (Figure 5.17Bi). The velocity reported for integrinβ1 depleted cells *in vitro* is most likely an overestimate as a significant portion of cells did not attach to the surface, and could not be analysed. In other words, the measured value is most likely from a sub-population of cells that were affected by the biochemical perturbation to a lesser extent than the average of the population. For instance, the model predicted all integrinβ1 depleted cells to detach from the surface.

Analysis of the experimentally determined *in vivo* cell migration profiles reveals very similar trends to the overall cell migration profiles predicted by the model (Figure 5.17Bii). Exactly as predicted, only ROCK inhibition leads to

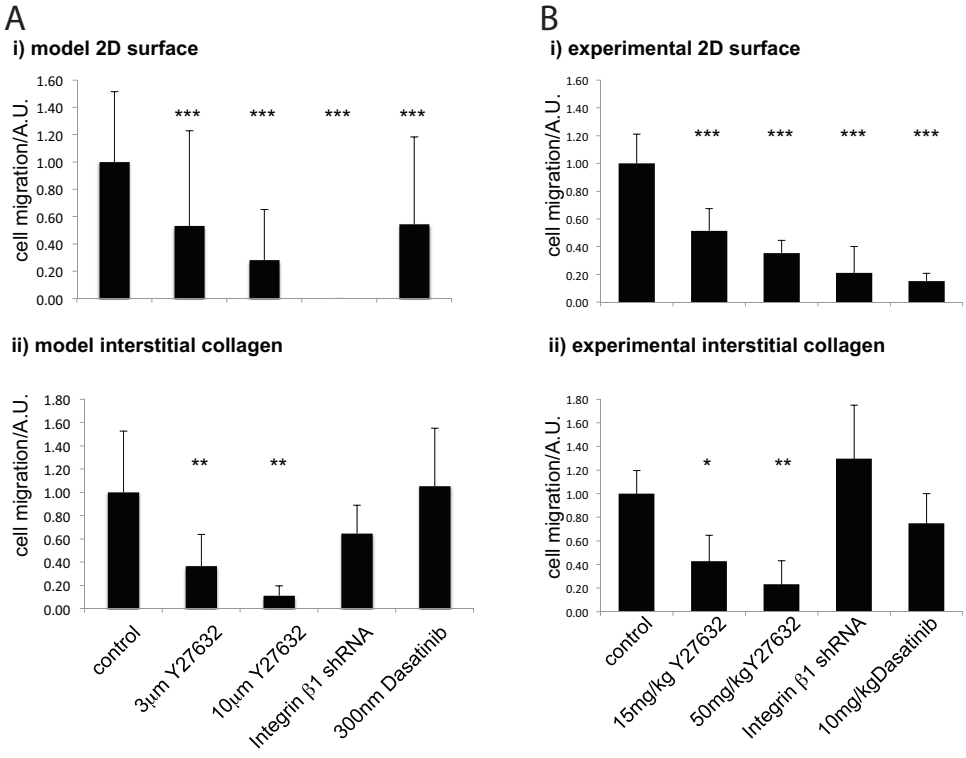

Figure 5.17: Model predictions and experimental measurements on melanoma cell motility upon biochemical perturbation. A) Model predictions of changes in cell migration caused by the experimental manipulations if a cell is moving on a i) 2D continuous surface or ii) within an *in vivo* mimetic environment. $(**)$ mark significant difference from control under the same conditions, two-tail t-test, p-value below $1E^{-12}$; $(***)$ same as $(**)$ with a p-value below 0.01. Model velocities are reported as the average of all three polarities tested: 40 %, 50 % and 60 % increased contractility at the cell rear coupled with 30 %, 40 % and 50 % reduced plasma membrane–cortex linker concentration at the cell front, respectively. The error bars report the average standard deviation. B) Experimental measurements of A375M2 cells moving on i) a collagen surface (average of three movies) or ii) into interstitial collagen in vivo. In vivo analysis is based on the intravital imaging of 36, 15, 20, 11 and 10 tumour volumes for control, Y27632 low, Y27632 high, integrinβ1 shRNA and Dasatinib-treated tumours, respectively. Values are normalised to aid comparison. $(*)$, $(**)$ and $(***)$ mark significant difference from control under same conditions, p-values below 0.05, 0.01, and 0.001 respectively.

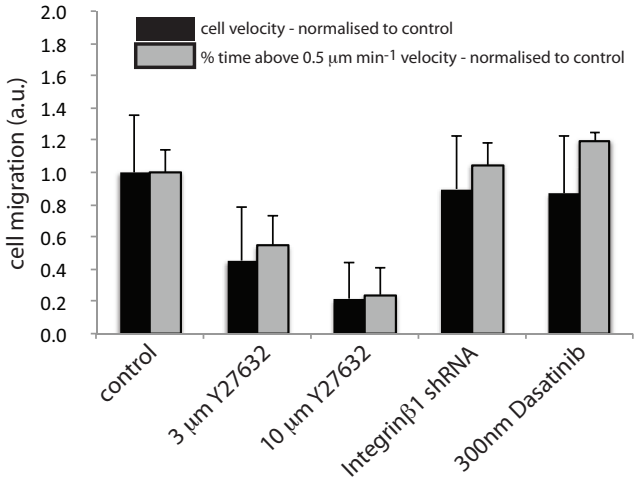

Figure 5.18: The co-variation of cell velocity predictions and percentage of simulation time during which the cell has an instantaneous velocity above the threshold of 0.5 $\mu m\ min^{-1}$. Black bars represent the cell velocity under each treatment normalised to control, grey bars represent the percentage time spent above the threshold velocity, again normalised to control. The measurements are reported as the average of all three polarities tested: 40 %, 50 % and 60 % increased contractility at the cell rear coupled with 30 %, 40 % and 50 % reduced plasma membrane–cortex linker concentration at the cell front, respectively. The error bars report the average standard deviation.

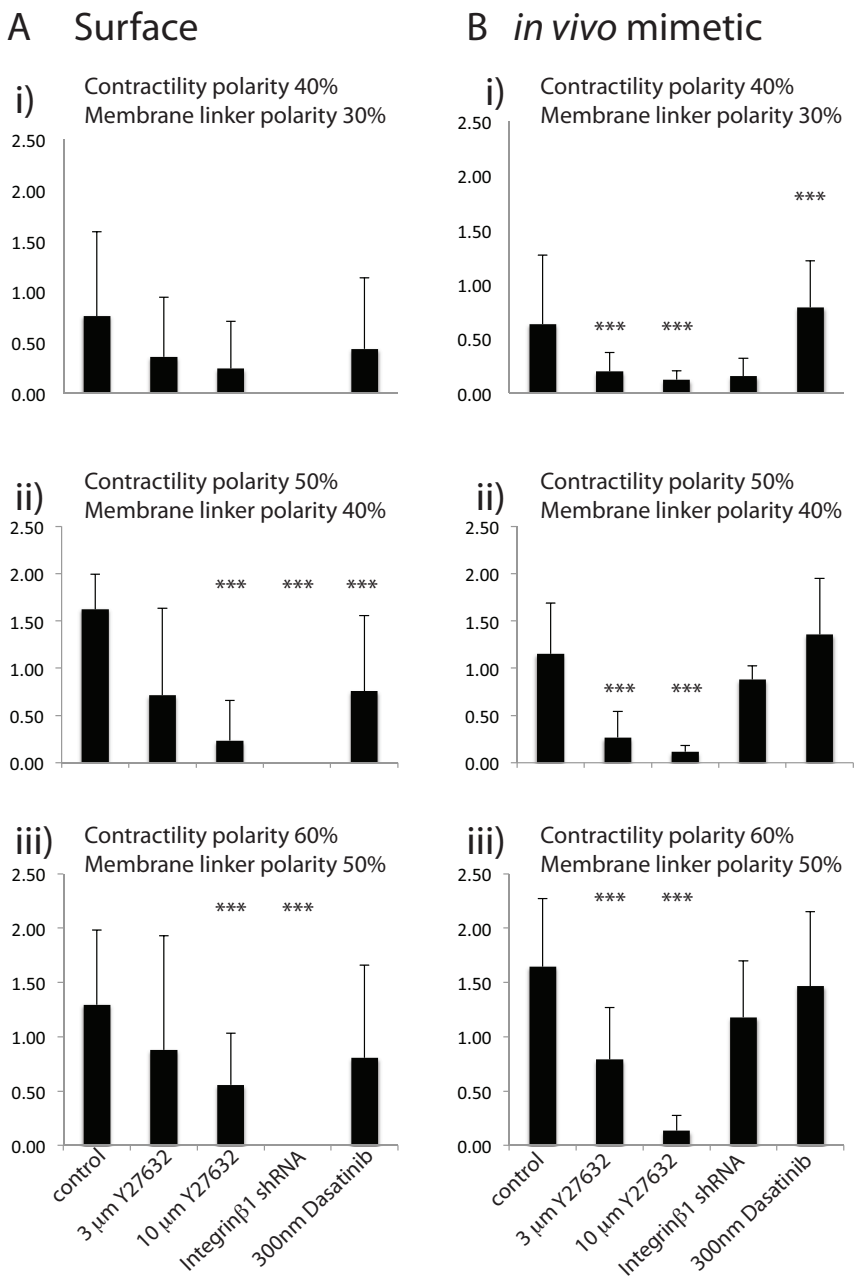

Figure 5.19: Model predictions on melanoma velocity upon biochemical perturbation, reported at individual cell polarities, A) On an unconfined surface and B) Within *in vivo* mimetic ECM. The cellular asymmetries are indicated on each plot. Error bars mark one standard deviation. (***) indicates significant difference from control cells under same conditions, p-value$<$ 0.001 (two-tail t-test)

inhibition of migration, and this effect is dose dependent. With regards to the morphologies of the motile cells under biochemical perturbation, initial observation of the melanoma cells *in vivo* confirmed the predicted increased number of protrusions in ROCK inhibitor treated tumours. Qualitative examination of the cell morphology predicted by the model suggested ROCK inhibition would lead to increased protrusions, an elongated cell morphology and reduced blebbing, while Dasatinib treatment would be associated with "hyper-blebbing" behaviour (Figure 5.20). Intravital imaging confirmed the accuracy of these predictions (Figure 5.20). The migration of integrinβ1 depleted cells is predicted to proceed by the same bleb-driven mechanism as control cells. Figure 5.20E shows *in vivo* imaging of the actin organisation in a migrating integrinβ1 depleted cell. Repeated cycles of bleb-initiation, new polymerisation of the cortex and bleb neck dissolution, are clearly observed. Thus the model accurately predicts both quantitative changes in melanoma cell migration in response to experimental manipulation *in vivo*, and the mechanism of cell migration.

5.3.3 Modifications to the ECM Filaments

The *in vivo* mimetic extracellular matrix environments presented in the previous sections have embedded surface segments, mimicking variable cross-sections of filaments with random orientations. The availability of these segments could influence the velocity profiles of cells, as they provide surfaces to spread actin polymerisation based protrusions. Especially for the biochemical perturbations that induce elongated cell morphology, the roles of these surfaces would indicate possible roles of actin protrusions within complex 3D ECMs. To test the effects of these surfaces, the same environments are simulated stripped from these segments, and only round cross-sections (see Figure 2.27). Surprisingly, the analysis revealed that the surface segments did not have significant effects on velocity profiles, with the only exception of dasatinib treated cells at high levels of asymmetry in their contractility and cortex–membrane linkers (Figure 5.21). This result indicated that for actin protrusion based motility to be an effective motility mode, the continuous surfaces should be at length scales higher that the cell size, such that long protrusions can be established, and start pulling the cell body forward. Moreover, the

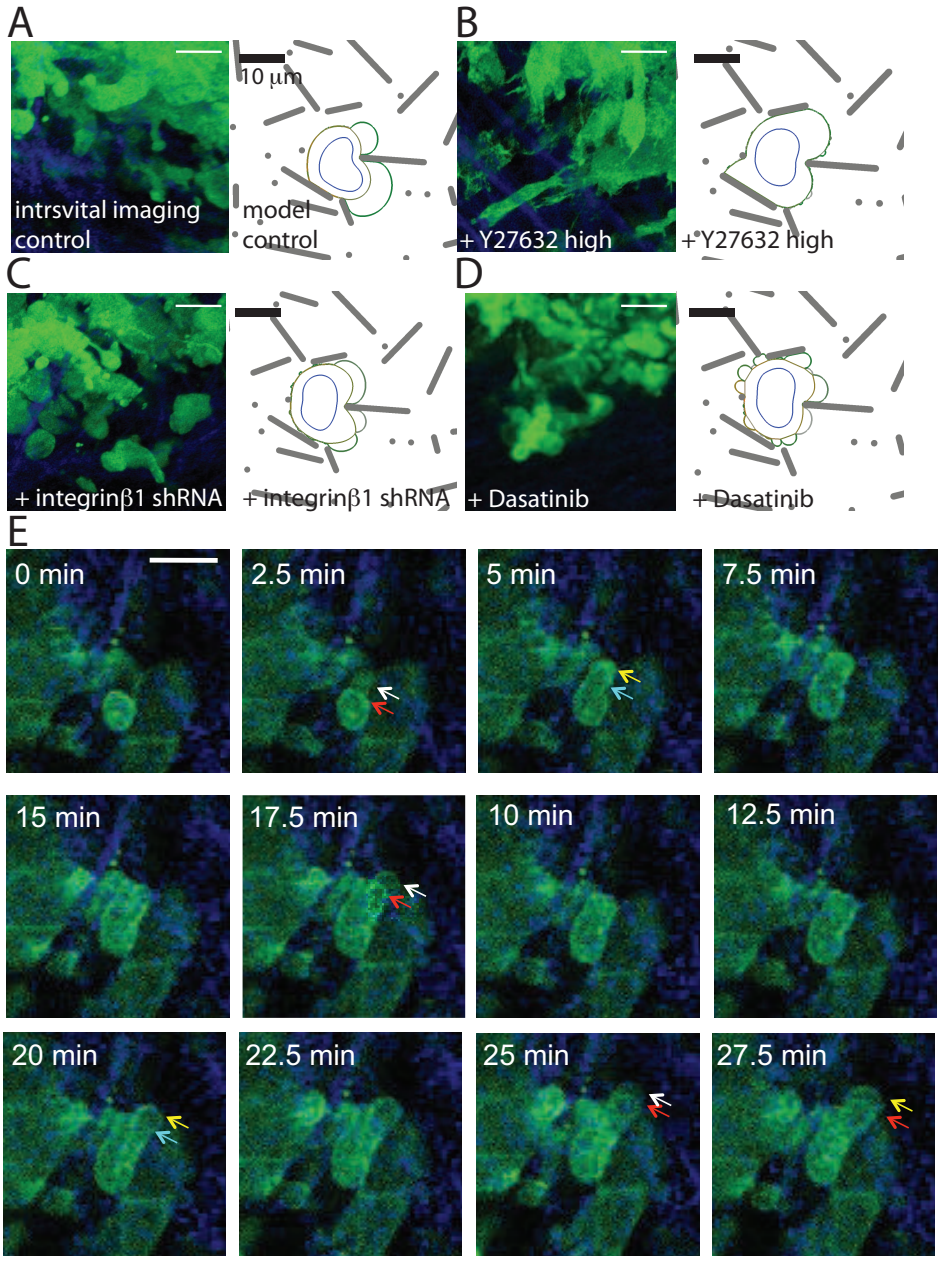

Figure 5.20: Model predictions and the experimental observations on the motile cell morphology, upon biochemical perturbations. A-D) Intravital imaging of melanoma accompanied by model snaphots under the same conditions. Actin labelled in green, and collagen second harmonic generation shown in blue. Colour coding of the model images same as Figure 5.9. The biochemical perturbations are indicated in each panel, scale bars represent 20μm in experimental images and 10μm in model snapshots. E) Images show LifeAct-GFP (green) expressed in A375M2 integrinβ1 shRNA cells and collagen second harmonic generation (blue). White arrow shows F-actin poor bleb initiation, yellow arrow indicates new F-actin polymerisation in a bleb, red arrow shows bleb 'neck' and cyan arrow indicates bleb neck disappearance. Scale bar is 20μm.

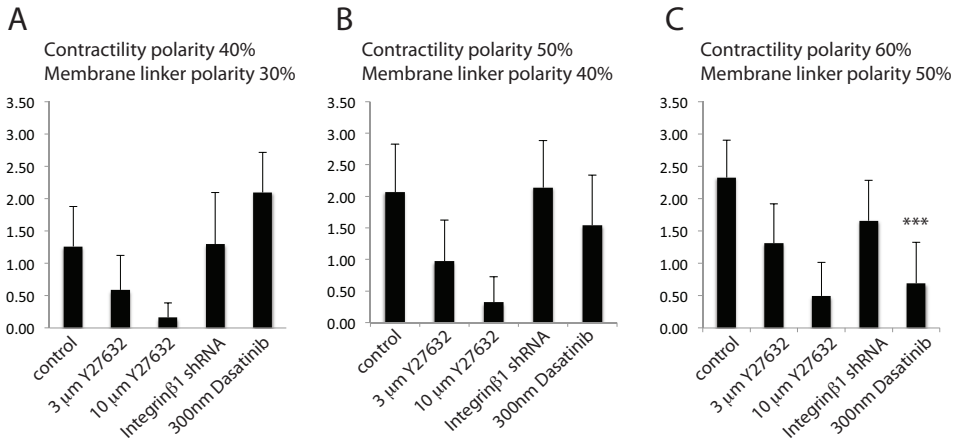

Figure 5.21: Model predictions on melanoma cell velocities upon biochemical perturbations within random ECMs that lack the embedded surface segments. A) Cell with 40 % increased contractility at the cell rear, 30 % reduced plasma membrane–cortex linker concentration at the cell front, B) Cell with 50 % increased contractility at the cell rear, 40 % reduced plasma membrane–cortex linker concentration at the cell front, and C) Cell with 60 % increased contractility at the cell rear, 50 % reduced plasma membrane–cortex linker concentration at the cell front. (***) indicates statistically significant difference from the velocity under same conditions, within an *in vivo* mimetic ECM (two-tail t-test, p-value below 0.01)

reduction in the velocity of dasatinib treated cells at high asymmetries point to a possible stabilising effect of the embedded surfaces. As mentioned in the previous section, dasatinib treatment can induce a hyper blebbing state at high asymmetries, which reduces overall cell velocity. The introduction of the surface segments increases the fibre area available for cell adhesion. This increase in the adhered surface stabilises blebbing dynamics, and lowers the negative effects of excessive blebbing on cell velocity.

The role of the flexibility of the extracellular matrix is also investigated. Keeping the ECM rigidity within the range reported for the rigidity of tumour tissues, the model predicts limited deformation of the ECM filaments, as the cells move through. This is inline with the observations from Tumour Cell Biology Laboratory, where no deformation is observed on the ECM filaments, within the image resolution (~1 μm). Additionally, the velocity of A375M2 cells are not significantly affected by switching from a rigid to a flexible ECM, with the exception of high asymmetries on unconfined surfaces (Figure 5.22A-B). For the case of high asymmetry on sur-

faces, the cells are more likely to detach from surfaces, and the predicted average cell velocity is significantly lower for flexible ECMs, as compared to rigid ECMs. Nevertheless, the model does detect some deformation where the cell surfaces with an intact cortex contact with the filaments. At the cell front, the forces applied by the cell squeeze the filaments, whereas the cell applies pulling forces to the ECM at the rear (Figure 5.22C-F, blue arrows). Unlike the cell body parts with an intact cortex, expanding blebs do not deform the filaments (Figure 5.22C, red arrows)

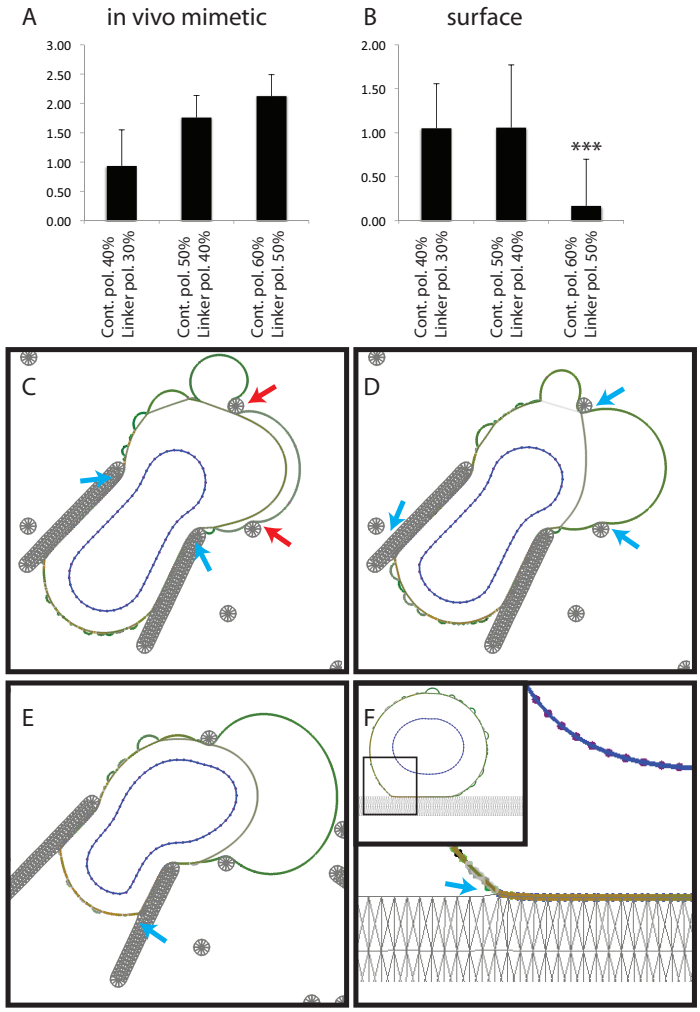

Figure 5.22: Model predictions on melanoma velocity and filament deformation within a flexible ECM. A-B) A375M2 velocities reported at a range of cellular asymmetries in cortical contractility and membrane-cortex linker distribution. The cell is within in vivo mimetic ECM in (A) and on an unconfined surface in (B). (***) indicates statistically significant difference form the cell within a rigid ECM, under same conditions (two-tail t-test, p-value<0.001). C-E) Snapshots from a model simulations demonstrating the deformation of the filaments within an *in vivo* mimetic ECM. The expanding blebs that lack a rigid cortex and are highly flexible, can not deform the filaments (A, red arrows). The cell body with established cortex squeezes the filaments at cell front, and applies pulling forces to the cell rear (blue arrows). E) Cell on an unconfined surface, the figure displays the section marked on the inset. The pulling of the filament surface at the cell rear can be seen (blue arrow).

Chapter 6

Discussions, Conclusions and Future Prospects

6.1 Discussion and Conclusions

Cell motility is essential in a range of biological processes, including cancer cell metastasis. The invasion of the cancer to the surrounding tissue, and formation of secondary tumours, is the cause of the majority of cancer related deaths. Hence, investigation of cell motility, with the purpose of reduction of metastasis, is of great importance.

There is a spectrum of possible motility modes available for cancer cells. It ranges from elongated mesenchymal to amoeboid blebbing, each having different predominant driving factors, such as actin polymerisation based protrusions for crawling cells and cortical contractility for the cells with amoeboid motility. For a number of cell types, including cancer cells, it is now established that depending on the conditions they find themselves in, cells can shift their motility mode within a continuous spectrum of motility mechanisms. This innate cellular plasticity reflects the complexities faced in the fight against metastasis: Depending on the intracellular conditions, and the extracellular matrix (ECM) geometry, the motility mode, consequently, the molecular requirements for migration, and the morphology of the motile cell, can vary considerably. Therefore, predicting the optimal migration mode, or the effect of experimental perturbation in a given environment, is difficult. The regulatory mechanisms behind different modes of motility are coupled, hence from an experimental perspective, it is extremely difficult to study

motility by modulating one cellular pathway at a time. Here, a computational approach, defining a range of cell motility machinery and extracellular environments, becomes an indispensable research aid. A computational approach makes it possible to effectively dissect motility modes, provide explanations for the success of one motility mode over another in a given environment, and predict the effects of perturbations on the efficiency of cell motility.

The multiscale model of cancer cell motility presented in this thesis incorporates variable ECM geometry, flexible cell morphology, actin polymerisation based protrusions, cortical contractility, plasma membrane blebbing, and variable cell-ECM adhesion. Although there have been studies investigating these phenomena individually, the work in this thesis incorporate both actin polymerisation based protrusions and plasma membrane blebbing, on a single platform to investigate cell motility. The presented modelling framework and the simulation platform is based on experimental data obtained solely *in vitro*, and from which emergent cell behaviour strongly mimics the behaviour of cells both *in vitro* and *in vivo*. Moreover, the model successfully predicts the effects of biochemical perturbations on cell velocity *in vivo*.

The initial challenge of the model is to mimic the behaviour of a spreading cell. Once placed on top of a surface, the model cell spreads with actin polymerisation based protrusions. Upon serum stimulation, the cell rounds up, and starts blebbing. The emergent relationship between contractility and blebbing, the sharp transition from a non-blebbing to an excessively blebbing cell within a small contractility range, is in agreement with the experimentally observed profiles (Figure 4.1). Confirming the model cell's emergent behaviour is in line with experimental observations, the model is then tested for emergence of persistent motility (Figure 4.3). Implementing a low level of asymmetry in cortical contractility, and as a consequence the asymmetry in actin polymerisation based protrusion initiation rates (Figure 3.12), the model cell is shown to produce persistent motility. After confirming the model mimics cell behaviour realistically, and is able to produce persistent motility, investigation of variable ECM geometries is initiated.

On unconfined continuous surfaces, the model successfully reproduces the well established bell-shaped curve representing the relationship between cell-ECM

adhesion and cell velocity. Moreover, the optimum motility mode is predicted to be utilisation of actin polymerisation based protrusions at the cell front, coupled with increased contractility of the cell rear (Figure 4.4). This first set of predictions for the dominant cell motility mode, and the relationship between adhesion and velocity, is not surprising. Nevertheless, it demonstrates that the model can reproduce the details of cell motility, in an environment where requirements of cell motility has been well established by decades of accumulated research. Moreover, the model suggests increased blebbing at the cell front does not increase, and that at a high level of blebbing can indeed reduce, cell velocity on an unconfined surface. The reasons for this inefficiency due to increased blebbing at the cell front can be linked to the reduced possibility of forming established actin protrusions, and increased possibility of complete cell detachment from the surface. On the other hand, increased blebbing at the cell rear is shown to increase the velocity of crawling cells, by facilitating cell rear detachment (Figure 4.10). On unconfined surfaces, one of the weaker points of the model is on predicting the extent of the bell-shaped curve for the relationship between adhesion and cell velocity. The adhesion range where the cells can keep in contact with the surface, while still being able to detach their rear and generate motion, is narrow, compared to experimental observations. This implies there are other mechanisms at play that increase the robustness of cell motility on unconfined surfaces, which are not accounted for in the model. The feedback mechanism between the strength of cell-ECM adhesion and the tension on the individual bonds is a possible candidate, and is further discussed in the following paragraphs.

With the introduction of confinement, together with a change in the relationship between cortical contractility and cell velocity, a two state solution to the optimal cell motility mode emerges from the model. Here, a motility mode predominantly based on actin protrusions is predicted to be more effective at low and moderate levels of polarity, whereas an amoeboid blebbing mode is faster at high levels of contractility (Figure 4.6). This two state solution to the optimal cell velocity can be linked to larger blebs becoming more effective in facilitating forward cell movement. At sufficiently high levels of contractility, blebs become large enough to produce a cell velocity that is faster than can be achieved by spreading protrusions under the same conditions. The prediction that larger blebs are more effective is further supported by the investigation of changes

in cell velocity with the confinement level: the amoeboid blebbing motility mode becomes more effective with increased confinement (Figures 4.7, B.2 and B.3). As the frontal gap of the confined continuous environment is reduced, the cell becomes more ”squashed”, creating a higher internal pressure, therefore larger blebs. Moreover, the smaller gap size means that the bleb size required to fill the channel at the front of the cell is smaller. This bleb can form adhesions with the both top and bottom surfaces during the retraction period, which eventually pull the rest of the cell forward. The larger blebs becoming more effective in driving forward cell movement also relates to the second prediction: the marked change in the relationship between cell contractility and velocity. Contrary to a moderate contractility level being optimum on unconfined surfaces, increased contractility increases cell velocity within a confined environment. In a confined environment, the cell does not have the risk of complete detachment from the ECM; the cell is confined to the proximity of the fibres, and can always re-adhere. Then without the possibility of losing contact from the ECM, the cell can freely harness the benefits of increased contractility, with higher hydrostatic pressure driving larger blebs, and increased contractile forces at the cell rear pushing the cell forward faster. Experimental support for this analysis comes from the observation that increased matrix density leads to increasing reliance on contractile myosin function (41). New experimental data presented in this thesis also supports the analysis: Intravital imaging of cell morphology in migrating cells at the tumour margin demonstrates that cancer cells and, surprisingly, endothelial cells, exhibit blebbing-based migration (Figure 5.14).

The most striking feature that emerges from introduction of discontinuity in the environment is the change in the relationship between adhesion and velocity: Instead of the bell-shaped relationship, reducing adhesion simply increases velocity within a confined discontinuous environment (Figure 4.8). At low or zero adhesion to the ECM, the source of traction becomes the interdigitation of cellular protrusions with the gaps of the ECM, these protrusions either being actin polymerisation based protrusions, or plasma membrane blebs. As long as the gaps are smaller than the cell size, a wide rage of gap sizes can be utilised by cells, albeit with lower efficiency for larger gaps. Blebbing-driven migration is predicted to be the most rapid form of migration under all conditions in confined discontinuous environments. Several lines of evidence support the validity of

this analysis: the model very accurately predicts the lack of effect of integrinβ1 depletion on the ability of A375 cells to migrate into interstitial collagen. *In vivo* analysis of dendritic cells moving within similar environments has shown that depletion of all integrins does not significantly perturb cell migration (41). These experiments do not exclude the possibility that other cell–ECM binding proteins may be maintaining some level of adhesion to the environment (179). However, the model enables the conclusion that cell migration can be entirely adhesion independent in certain matrices.

Although many studies have observed blebbing during cell migration, its role has remained contentious (12, 39, 106). Depending on the system, blebbing has been observed at the front, side and rear of migrating cells leading to the proposition that blebbing is merely a consequence of cortical contractility with no actual utility (8, 39, 126). The computational model can investigate asymmetries in contractility, blebbing and actin protrusion formation independent of each other, and dissect the effects of each, within a variety of possible ECM geometries. The model demonstrate that forward blebbing is an effective method for cell protrusion in confined spaces, while on planar surfaces small blebs at the rear of the cell can favour detachment of the cell rear (Figure 4.10). This computational study provides the explanation to the seemingly contradictory range of observations made on the spatial distribution of blebs on migrating cells. Moreover, these predictions of the model imply that effective adaption of migration strategy to the matrix geometry will require the cell to spatially couple and uncouple its regulation of contractility and cortex-membrane linkage.

The predictions of the model on the dependency of optimal migration mode on the ECM geometry suggests that, a cell with the ability to form both actin polymerisation based protrusions and plasma membrane blebs, adapts the more effective motility mode in each environment. The cell displays a spread morphology, and moves predominantly with actin polymerisation based protrusions on unconfined surfaces, while it moves in an amoeboid fashion with plasma membrane blebs within confined discontinuous environments. For the confined continuous environments, the cell utilises actin protrusions at low contractility levels, and switches to a blebbing motility at high contractility levels (Figures 4.4, 4.6, and 4.8). This consistent preference for the more successful motility mode in each

environment implies a biophysical antagonistic feedback between spreading and blebbing, functioning in parallel with the Rho-Rac inhibitory crosstalk at the biochemical level.

When challenged to predict cell morphology and motility *in vivo*, the model successfully predicts the fact that metastatic melanoma cells adapt an amoeboid blebbing motility mode (Figures 5.7 and 5.9). Furthermore, cell velocities are predicted to be in the range $1.14 \pm 0.60 \mu m\ min^{-1}$, later to be measured as $2.1 \pm 1.8 \mu m\ min^{-1}$ by intravital imaging of mice. The interactions of the nucleus with the residual cortex at the plasma membrane bleb necks, and the influence of this residual cortex on the profile of cell velocity, are predicted successfully by the emergent behaviour of the model. Moreover, model simulations, at different levels of complexity, reveal the relatively rigid cell nucleus has influence on cell velocity within *in vivo* matrices, but not on unconfined surfaces (Figure 5.10). This is supported by a range of experimental observations, where the nucleus is shown to be a limiting factor for cells attempting to squeeze through gaps within complex 3D matrices (48–53).

The *in vivo* cell velocity predicted by the model is in the same order of magnitude with the experimental observations. Still, the absolute values of such predictions from computational models are of little importance, and a model's success is in its strength to predict relative changes in a system. With this aim, following the prediction of cancer cell behaviour *in vivo*, the model is challenged to predict the effects of three different perturbations on cell motility. Again, the model successfully predicts the emergent cell velocity profiles of melanoma cells both on unconfined surfaces *in vitro* and during invasion into interstitial collagen *in vivo* (Figure 5.17). Here, the detrimental effects of contractility reduction *in vivo* are predicted alongside the lack of influence of integrinβ1 depletion. As for the roles of the nucleus upon each biochemical perturbation, the model predicts that although the velocity magnitudes are affected by the nucleus, the relative effects of the perturbations are not affected (Figure C.1). This implies that the contractile forces of the cell cortex are indeed responsible for the morphology changes of the nucleus, required for the cell to move through gaps smaller than the nucleus size, but the roles of contractility are not limited to translocation of the nucleus. On unconfined surfaces, the model predicts the depletion of integrin and dasatinib treatment will

have a strictly detrimental effect, causing cell detachment from the surface, and resulting in zero cell velocity. This is an overestimate, as *in vitro* experiments clearly demonstrate some cells can move under same conditions. There are two reasons for this disagreement between the experimental observations and model outputs. First is the aforementioned weak aspect of the model, predicting a narrow range of parameters that can support cell motility on unconfined surfaces, i.e. the sharp transitions between the optimum adhesion–contractility values and the range where the cell either cannot detach its rear, or is detached from the surface completely, hence can not generate motion. This relates to the lack of feedback mechanisms that regulate the adhesion levels of the cell depending on the tension on adhering bonds. Secondly, the cells that can be measured in the experimental setups are the small sub-population of cells that are not detached from the surface. The majority of the cells that do loose contact with the collagen matrix can not be quantified. Then there is an inherent bias in the experimental measurement towards the cells that are affected from the treatment to a lesser extent than the remaining of the cell population, which leads to the measured cell velocity being an over-estimate.

The relatively high speed observed for cells utilising blebbing based strategies within discontinuous environments, including *in vivo* mimetic environments, might suggest that bleb-driven migration would be greatly favoured during evolution. However, it is clear that motility strategies based on actin polymerisation-driven protrusions are widely used. Various reasons, some of which are not accounted for in our model, can be proposed as to why protrusions are not eliminated throughout evolution. Many of the critical environments for cell migration in normal physiology may be continuous surfaces, either confined or non-confined. Blebbing typically reduces cell velocity in these environments; the only exceptions are at high contractility levels. In addition, the energy costs of different types of migration are not investigated, nor too the fidelity of a cell to follow chemotactic cues at a molecular level. Actin polymerisation based protrusions may be more effective in reading the environment, as the continuous tearing of the plasma membrane form the actin cortex, inherent in blebbing migration, is likely to disrupt the formation of signalling complexes that may sense and respond to tactic cues. Bleb dynamics does affect the model cell's readout of the environment, such that the blebs can influence the polarity of the cell only during their retraction phase, but not

during their expansion. However, there may still be long–term effects that are not included in the model, which would influence the performance of a cell that forms successive blebs at its front. There is experimental support for this possibility, for instance, recycling endosomes, which are critical for efficient signal transduction by multiple cell surface receptors, are unable to enter blebs. Moreover, actin polymerisation based protrusions can bring about some of the benefits of plasma membrane blebs at higher actin polymerisation rates. For instance, the model suggests actin protrusions can facilitate the necessary anchoring at zero adhesion and increase cell velocity (Figure 4.9), but the blebs are more effective as the actin protrusion has to elongate at the right position and angle to facilitate anchoring. At a sufficiently high rate of actin polymerisation, this barrier can be overcome, and actin protrusions can be just as effective as plasma membrane blebs at low to zero levels of cell-ECM adhesion. Indeed, dendritic cells provide a good example for the case of cell motility without blebs at highly reduced cell-ECM adhesion (41).

The model takes into account multiple aspects of the cell's motility machinery, and a variety of extracellular matrix geometries. Overall, the model proved to be successful in predicting cell motility within the parameter and environment ranges investigated. On the other hand, there are still several aspects of cell motility that are not included in the model, and could have considerable influence on cell behaviour. For instance, tension at cell–ECM adhesion points influences both the local contractility levels at the adhesion points, and the cell–ECM adhesion strength by inducing clustering of integrins and maturation of adhesion sites (5). Moreover, the time lapse imaging presented in Chapter 5 shows that plasma membrane blebs can form sequentially on top of each other, before the complete disassembly of the cortex at the neck of the first bleb, which is not incorporated into the model. Flexibility of the ECM does not have significant effects in the biological environments that have been investigated; the model predictions do not suggest a significant change in cell velocity, and the experimental imaging does not reveal movement of fibres within the resolution range of imaging (~1 μm). On the other hand, this does not eliminate the possibility that for a larger range of ECM flexibility, which may be relevant to other biological systems, will significantly influence cell motility. Especially coupled to the feedback mechanisms involving tension at the adhesion sites, ECM rigidity can become an important factor influencing cell motility. Last but not the least, possibly the most evident simplification of the model is the

dimensions of the modelled space: The work presented in this thesis demonstrates a multiscale model of cancer cell motility in 2D, which is a simplification from the real world 3D environments cancer cells find themselves in. As presented in the previous chapters, from the beginning of this research, the aim has been to investigate the roles of multiple cell motility modes in a variety of ECM geometries, variable physical properties for the ECM, and a wide range of cellular asymmetries in contractility, cortex-membrane linker distribution, and protrusion initiation rates. With each new data point added to the investigation, the size of the search space to be investigated increases rapidly. Additionally, the stochastic nature of the model necessitates a number of simulations are carried out for each point in the search space, before conclusions can be drawn from the results. Overall, the developed model has to be computationally efficient, and tens of thousands simulations should be feasible within the time frame of this thesis. Hence, the model is developed in 2D, with rigorous parameterisation and cross-checking against experimental data.

In summary, the computational model presented in this thesis, encompassing the complex interplay of actin polymerisation, plasma membrane blebbing, flexible cell morphology, actomyosin contractility, cell-matrix adhesion, hydrostatic pressure, local cortex heterogeneity, the cell nucleus, and variable matrix geometries makes both striking theoretical, and accurate experimental predictions. Confinement of the extracellular environment alters the relationship between cell contractility and velocity. Discontinuous matrices fundamentally alter the relationship between cell adhesion and migration speed, and allow adhesion-independent migration. Computational understanding of the relationship between the cell motility modes and ECM geometries provided by this computational model, enables accurate predictions about cell migration into interstitial collagen, utilising input from only simple *in vitro* measurements. Indeed, by exploring the parameter space in intracellular states, such as cell contractility, or cell asymmetry, the model is able to predict which parameters have the largest effects on cell migration depending on the matrix geometry. This could enable future efforts to identify anti-invasive chemotherapeutic agents be more efficiently targeted. This thesis presents a computational model that utilises measurement of rather simple variables *in vitro*, and has been able to predict the *in vivo* response of three very different putative anti-invasive interventions. This model is a very useful tool to aid more rational drug screening approaches and to determine the likely context in

which anti-invasive agents might act.

6.2 Future Prospects

This thesis presents a modelling framework, and a simulation platform, which incorporates flexible cell morphology, multiple cellular protrusions mechanisms, local protein heterogeneity at the cortex, and an explicitly defined ECM. Throughout this thesis, the modelling framework has been rigorously utilised to investigate single cell motility. There are multiple developments and applications planned for the model, covering improvements to the definition of the single cell, and its interactions with the environment; investigation of cell motility within multi-cellular systems; and focusing on the morphology modelling ability of the framework to investigate other systems where large changes in cell morphology occur, such as during mitosis.

At the single cell level, further biochemical feedback mechanisms, some of which are mentioned in the previous section, can be implemented. It is established in the published literature that tension on cell-ECM adhesion sites influences the strength of adhesion. Increased tension mediates maturation of initial adhesions into focal contacts, and focal contacts to focal adhesion (5). Moreover, local myosin levels have been shown to initially decrease, and then in the long–term (~60min), increase at cell-ECM adhesion sites (180). Considering that the myosin levels predominantly govern the tension accumulating at cell–ECM adhesion sites, these feedback mechanisms; between the adhesion site and local contractility, and the tension at the adhesion point and contractility; are also coupled. Merged with the conclusions of this thesis, that adhesion dependency of the motile cell is strongly linked with the extracellular environment geometry, it can be speculated that the feedback mechanisms between forces at the adhesion sites and local protein concentrations may have environment specific impacts on cell velocity. This hypothesis further emphasises the influence of ECM geometry in determining the optimum cell motility mode and maximum cell velocity; and it can be tested with rather straightforward improvements on the existing modelling framework.

Focusing on cell protrusions, the definition of plasma membrane blebs can

be further improved, by implementing the ability to form new plasma membrane blebs on top of retracting blebs. The interplay between the rigidifying newly formed cortex at the bleb rim, the accumulation of cortex membrane linkers within this cortex, and the hydrostatic forces, can be resolved experimentally. Detailed measurements of the occurrence of blebs upon blebs as a function of increasing contractility should reveal the necessary information for implementing this phenomenon. Furthermore, plasma membrane bleb initiation with cortex rupture due to increased local tension can be implemented. As discussed in Section 1.4.1.1, occurrence of blebs *via* the rupture of the cell cortex is less frequently observed in motile cells. Nonetheless, there is no *a priori* reason why blebs should not form in this manner in a motile cell, and the implementation of this phenomenon may bring new insights into the mechanisms of single cell motility.

In addition to improving the model's single cell functionality, the model can be utilised to investigate collective cell motility. Similar to single cell metastasis, collective invasion of cancer into the surrounding tissue and lymphatic vessels is a significant clinical problem. In the complex environment of the tumour and surrounding tissue, the rate and extent of invasion is dependent on an array of factors, including actin dynamics, matrix proteolysis, cell-cell and cell–ECM adhesions, and paracrine signalling (119, 181, 182). Experimental analyses have made numerous observations regarding the molecular requirements for collective cancer cell invasion; some of which cannot be explained by investigation of the biochemistry or physics of single cells. For instance, increased ECM density only allows collective cell migration, eliminating metastasis as single cells. Moreover, in cell cohorts of collective motility, cell–ECM adhesion becomes less critical in the cells that following a so called leader cell (183). The crosstalk events between the cells can be implemented in the model, such as the release of contractility in the vicinity of cell-cell adhesion sites. Upon the implementation of multiple cells into the model, and the crosstalks between them, the modelling framework presented in this thesis would become an ideal platform to investigate the forces governing the interaction between cell cohorts, and the ECM.

Throughout this thesis, the modelling platform has mainly been utilised to investigate cell motility, while providing accurate predictions on cell morphology. Nevertheless, it is equally possible to focus on morphology modelling within the

same framework. The presented model can be further developed to investigate cell morphology dynamics during cell division. The biochemical events leading to, and driving mitosis have been the subject of rigorous research. However, the physical details of cell division, and the forces at play, still need to be investigated. During mitosis, cortical stiffening with increased contractility, and intracellular pressure increase, enables the cell to round up (33, 184). Moreover, plasma membrane blebbing is suggested to play a role in the regulation of pressure and cortical tension during cytokinesis (116). In the context of modelling the tissue, an additional layer of complexity is the communication between cells, as intercellular contacts do influence internal cell states (181). Even further complexity arises from the physical state of the crowded tissue, where the whole tissue can be under tension or compression (185). The presented modeling framework possesses the functionality to model majority of these regulators, such as cortical contractility, hydrostatic pressure and plasma membrane blebs. Therefore, with the implementation of multiple cells, and the appropriate level of cell-cell communication, the presented modelling framework would become a suitable platform to investigate the physical regulators of cell morphology during mitosis.

Appendix A

Experimental Methods

The experimental methods describe the methodology used by The Tumour Cell Biology (TCB) Laboratory in generation of the experimental data presented throughout the thesis. The author of this thesis received strong guidance from the TCB Laboratory during preparation of this appendix.

A.1 Cell Culture

A375P and A375M2 cells were routinely maintained in DMEM + 10 % Foetal Calf Serum (178). Transfection of MARS-LifeAct, GFP-LifeACT, EGFP-N1 Ezrin, EGFP-N3 MLC, EGFP-PLCδPH domain and pNeo Integrinβ1 shRNA plasmids were carried out using a plasmid DNA concentration of $2\mu g\ ml^{-1}$ and Fugene6 diluted 6:1000 in Optimem. In the case of LifeAct plasmids and pNeo Integrinβ1 shRNA stable transfectants were selected using $500\mu g\ ml^{-1}$ geneticin and purified by FACS. The siRNA and shRNA sequences for integrinβ1 are described in (186).

To investigate cytoskeletal dynamics A375 cells were plated on collagen I ~$4.5mg\ ml^{-1}$ BD Bioscience (# 354249) and then transferred to serum free media. In some cases cell behaviour was modulated by the addition of 1 % serum, $3\mu M$ Y27632, $10\mu M$ Y27632 (Tocris # 1254), 300nM Dasatinib, $1\mu M$ Dasatinib (LCLlabs # 3307) or combinations thereof. *In vitro* time-lapse imaging was performed at 37^oC using a range of platforms: Nikon TE2000 microscopes equipped with environmental chambers and a CCD controlled by MetaMorph software or Zeiss LSM confocal microscopes (either LSM510, 710 or 780). Frame

acquisition rates ranged from 1Hz to 0.25Hz.

A.2 Immunofluorescence

Cells were fixed with 4 % paraformaldehyde, permeabilised with 0.2 % Triton X100 and blocked with 5 % BSA. Primary antibodies (pS19-MLC Cell Signalling or Integrinβ1 Santa Cruz) were incubated overnight at 4^oC and secondary antibodies (Cy5 Anti-Rabbit Jackson Stratech and Alexa 488 Anti-mouse) and TRITC-Phalloidin were incubated for one hour at room temperature. Images were acquired using Zeiss LSM confocal systems. To quantify pS19-MLC and integrinβ1 staining images were opened in the software Volocity. Cells were identified by thresholding based on F-actin staining intensity and selected based on area $> 200\,\mu m$. Mean fluorescent intensities were determined for each cell.

A.3 Western Blotting

Lysates were prepared in Laemlli buffer (without β -mercaptoethanol for integrinβ1 analysis). Following standard SDS-PAGE, proteins were transferred to Nitrocellulose/PVDF membranes and incubated with primary antibodies (pS19-MLC Cell Signalling or Integrinβ1 Santa Cruz).

Appendix B

Velocity Profiles for High Polarities, and Simplified Cell Motility Modes

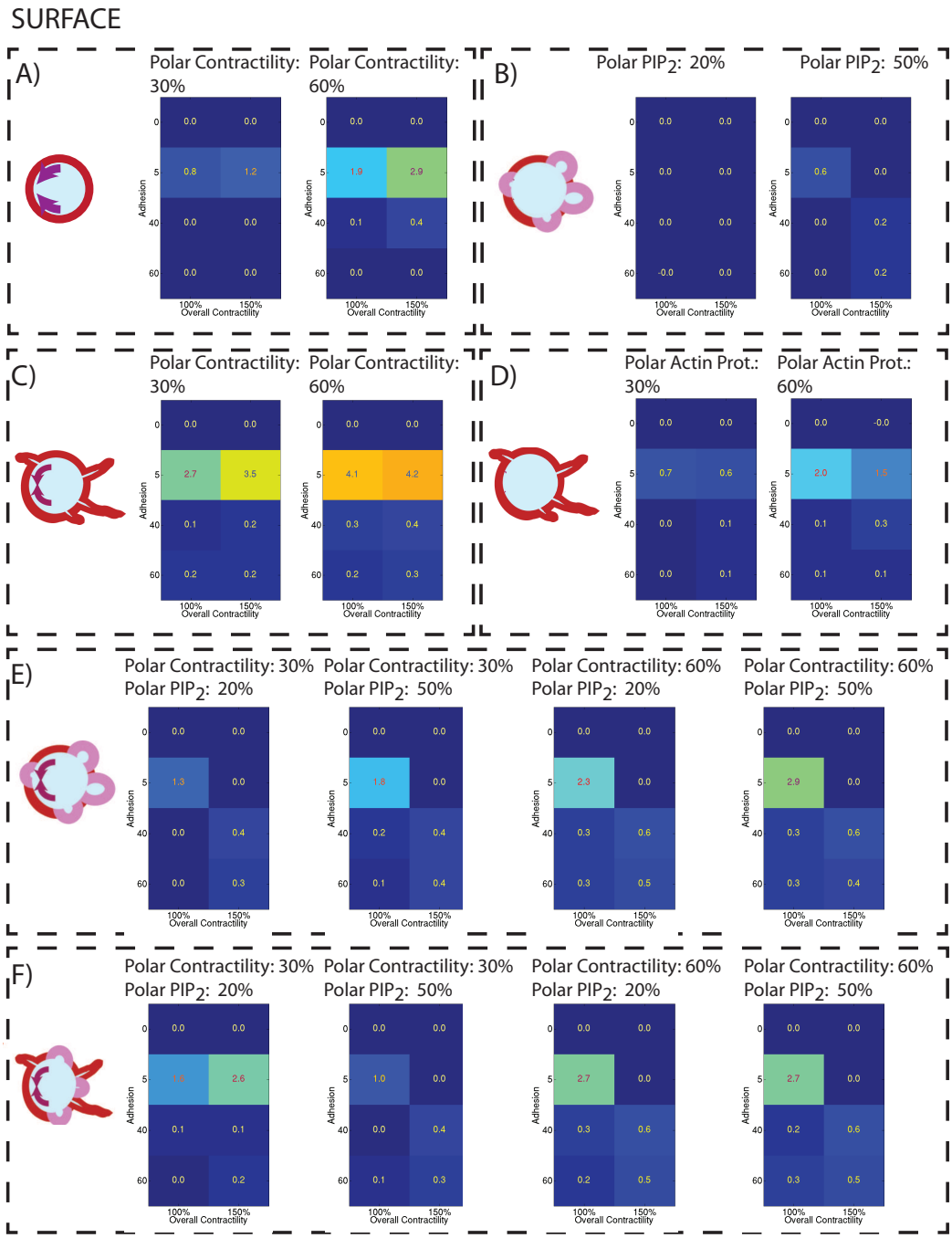

Figure B.1: Heatmaps for unconfined continuous surfaces, reported for higher polarities and additional motility modes. Legend Continued on next page.

Figure B.1: Heatmaps for unconfined continuous surfaces, reported for higher polarities and additional motility modes. Schematic in each sub-figure represents the motility mode. All figures throughout this appendix are colour coded in the same scale. All velocity values are the average of at least 10 simulations of 15min each. A) Simulations for a cell with polarised contractility at the cell rear, and without the ability to form any protrusions. Magnitude of polarised contractility is as indicated in titles. B) Cell without polarised contractilty, with reduced PIP_2 at the cell front, and the ability to form plasma membrane blebs, but not actin polymerisation based protrusions. Magnitude of PIP_2 polarity is as indicated in titles. C) Cell with polarised contractilty at the cell rear, and ability to form actin polymerisation based protrusions, but not plasma membrane blebs. Polarity in contractility is as indicated in titles, protrusion initiation probability is linked to polarised contractility (Figure 3.12). D) Cell without polarised contractility, and the ability to form actin polymerisation based protrusions, but not plasma membrane blebs. The probability of protrusion initiation is reduced at cell rear. The scale of reduction is equivalent to the the level which would be enforced by the contractility increase at the cell rear indicates in the titles (A 30 % polarisation means the protrusion initiation is reduced to a level that would be induced by 30 % contractility increase at the cell rear). E) Cell with increased contractility at the cell rear, with reduced PIP_2 at the cell front, and the ability to form plasma membrane blebs, but not actin polymerisation based protrusions. Magnitude of polarities are as indicated in titles. F) Cell with increased contractility at the cell rear, with reduced PIP_2 at the cell front, and the ability to form plasma membrane blebs and actin polymerisation based protrusions. Magnitude of polarities are as indicated in titles.

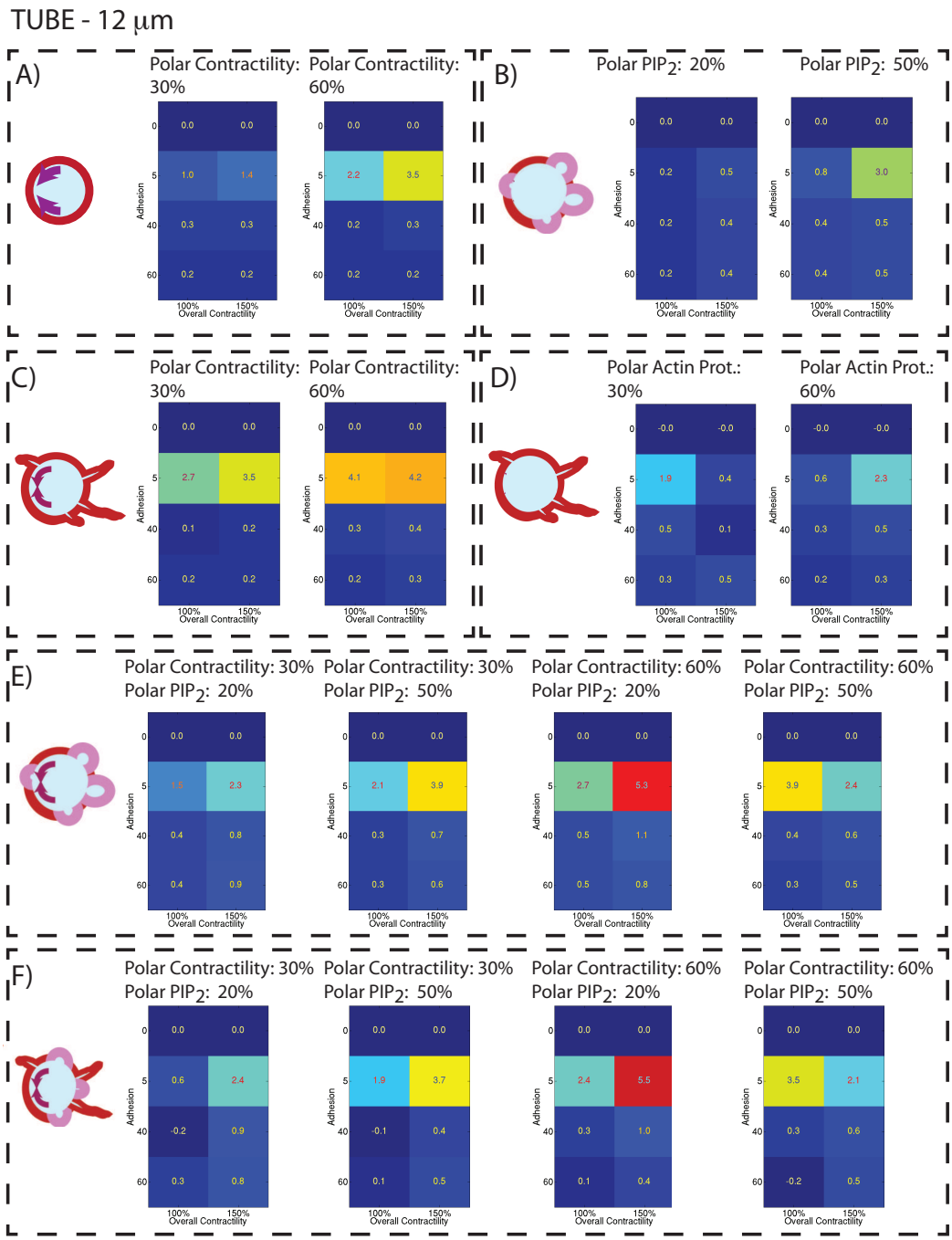

Figure B.2: Heatmaps for confined continuous surfaces with a frontal gap size of 12μm, reported for higher polarities and additional motility modes. Legend Continued on next page.

Figure B.2: Heatmaps for confined continuous surfaces with a frontal gap size of $12\mu m$, reported for higher polarities and additional motility modes. Schematic in each sub-figure represents the motility mode. All figures throughout this appendix are colour coded in the same scale. All velocity values are the average of at least 10 simulations of $15min$ each. A) Simulations for a cell with polarised contractility at the cell rear, and without the ability to form any protrusions. Magnitude of polarised contractility is as indicated in titles. B) Cell without polarised contractilty, with reduced PIP_2 at the cell front, and the ability to form plasma membrane blebs, but not actin polymerisation based protrusions. Magnitude of PIP_2 polarity is as indicated in titles. C) Cell with polarised contractilty at the cell rear, and ability to form actin polymerisation based protrusions, but not plasma membrane blebs. Polarity in contractility is as indicated in titles, protrusion initiation probability is linked to polarised contractility (Figure 3.12). D) Cell without polarised contractility, and the ability to form actin polymerisation based protrusions, but not plasma membrane blebs. The probability of protrusion initiation is reduced at cell rear. The scale of reduction is equivalent to the the level which would be enforced by the contractility increase at the cell rear indicates in the titles (A 30 % polarisation means the protrusion initiation is reduced to a level that would be induced by 30 % contractility increase at the cell rear). E) Cell with increased contractility at the cell rear, with reduced PIP_2 at the cell front, and the ability to form plasma membrane blebs, but not actin polymerisation based protrusions. Magnitude of polarities are as indicated in titles. F) Cell with increased contractility at the cell rear, with reduced PIP_2 at the cell front, and the ability to form plasma membrane blebs and actin polymerisation based protrusions. Magnitude of polarities are as indicated in titles.

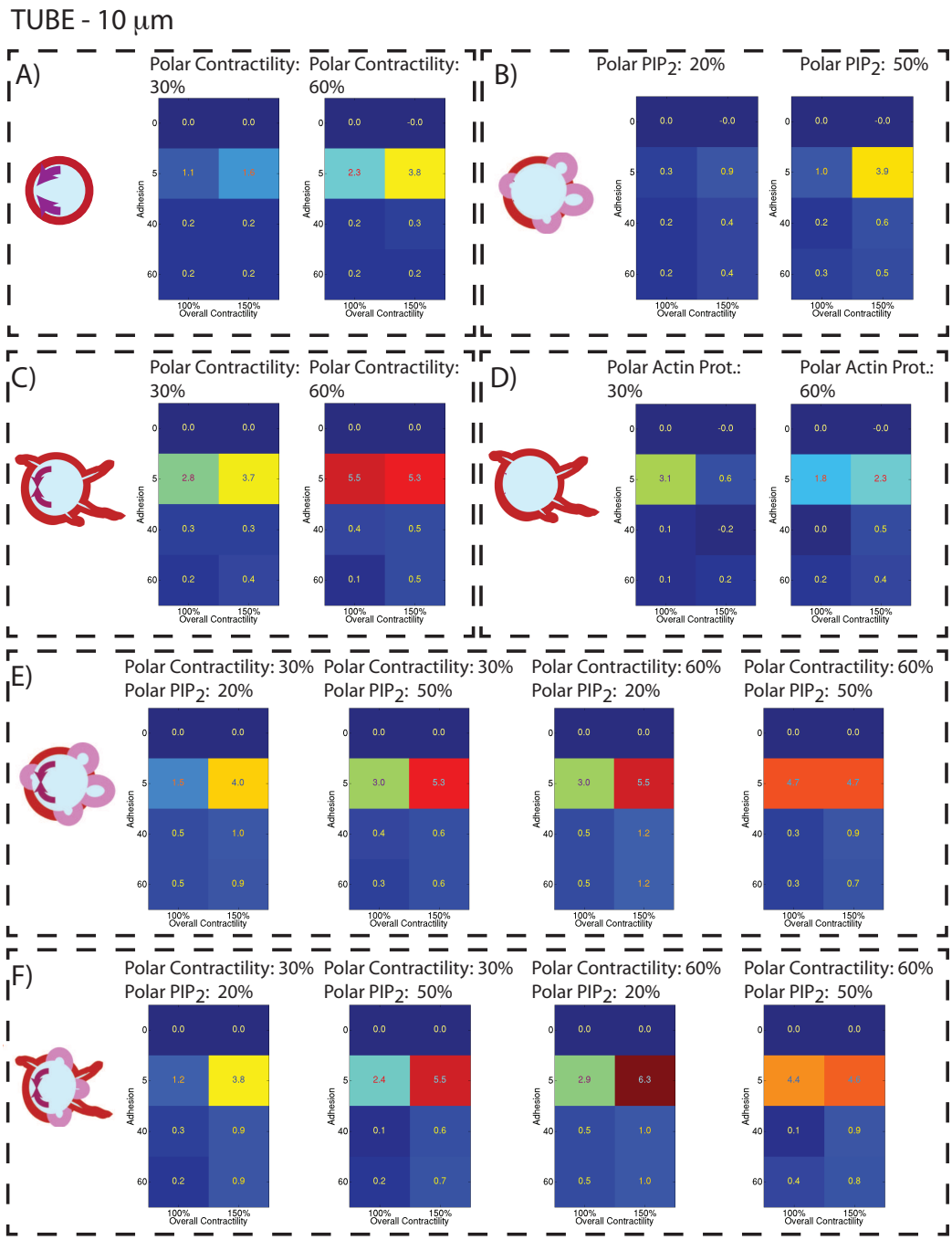

Figure B.3: Heatmaps for confined continuous surfaces with a frontal gap size of 10μm, reported for higher polarities and additional motility modes. Legend continued on next page.

Figure B.3: Heatmaps for confined continuous surfaces with a frontal gap size of $10\mu m$, reported for higher polarities and additional motility modes. Schematic in each sub-figure represents the motility mode. All figures throughout this appendix are colour coded in the same scale. All velocity values are the average of at least 10 simulations of $15min$ each. A) Simulations for a cell with polarised contractility at the cell rear, and without the ability to form any protrusions. Magnitude of polarised contractility is as indicated in titles. B) Cell without polarised contractilty, with reduced PIP_2 at the cell front, and the ability to form plasma membrane blebs, but not actin polymerisation based protrusions. Magnitude of PIP_2 polarity is as indicated in titles. C) Cell with polarised contractilty at the cell rear, and ability to form actin polymerisation based protrusions, but not plasma membrane blebs. Polarity in contractility is as indicated in titles, protrusion initiation probability is linked to polarised contractility (Figure 3.12). D) Cell without polarised contractility, and the ability to form actin polymerisation based protrusions, but not plasma membrane blebs. The probability of protrusion initiation is reduced at cell rear. The scale of reduction is equivalent to the the level which would be enforced by the contractility increase at the cell rear indicates in the titles (A 30 % polarisation means the protrusion initiation is reduced to a level that would be induced by 30 % contractility increase at the cell rear). E) Cell with increased contractility at the cell rear, with reduced PIP_2 at the cell front, and the ability to form plasma membrane blebs, but not actin polymerisation based protrusions. Magnitude of polarities are as indicated in titles. F) Cell with increased contractility at the cell rear, with reduced PIP_2 at the cell front, and the ability to form plasma membrane blebs and actin polymerisation based protrusions. Magnitude of polarities are as indicated in titles.

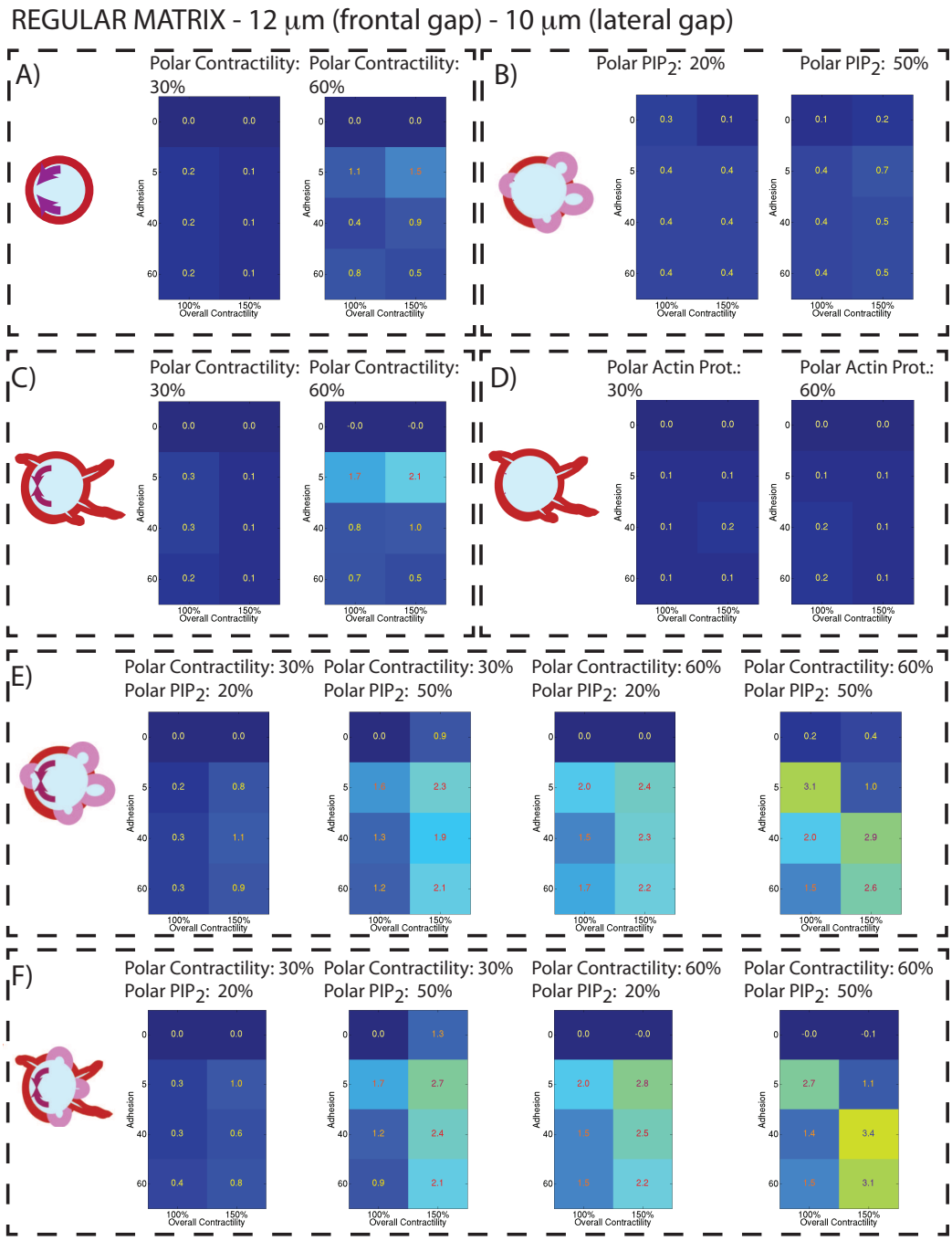

Figure B.4: Heatmaps for confined discontinuous environments with frontal gap size of 12μm and lateral gap size of 10μm, reported for higher polarities and additional motility modes. Legend continued on next page.

Figure B.4: Heatmaps for confined discontinuous environments with frontal gap size of $12\mu m$ and lateral gap size of $10\mu m$, reported for higher polarities and additional motility modes. Schematic in each sub-figure represents the motility mode. All figures throughout this appendix are colour coded in the same scale. All velocity values are the average of at least 10 simulations of $15min$ each. A) Simulations for a cell with polarised contractility at the cell rear, and without the ability to form any protrusions. Magnitude of polarised contractility is as indicated in titles. B) Cell without polarised contractilty, with reduced PIP_2 at the cell front, and the ability to form plasma membrane blebs, but not actin polymerisation based protrusions. Magnitude of PIP_2 polarity is as indicated in titles. C) Cell with polarised contractilty at the cell rear, and ability to form actin polymerisation based protrusions, but not plasma membrane blebs. Polarity in contractility is as indicated in titles, protrusion initiation probability is linked to polarised contractility (Figure 3.12). D) Cell without polarised contractility, and the ability to form actin polymerisation based protrusions, but not plasma membrane blebs. TThe probability of protrusion initiation is reduced at cell rear. The scale of reduction is equivalent to the the level which would be enforced by the contractility increase at the cell rear indicates in the titles (A 30 % polarisation means the protrusion initiation is reduced to a level that would be induced by 30 % contractility increase at the cell rear). E) Cell with increased contractility at the cell rear, with reduced PIP_2 at the cell front, and the ability to form plasma membrane blebs, but not actin polymerisation based protrusions. Magnitude of polarities are as indicated in titles. F) Cell with increased contractility at the cell rear, with reduced PIP_2 at the cell front, and the ability to form plasma membrane blebs and actin polymerisation based protrusions. Magnitude of polarities are as indicated in titles.

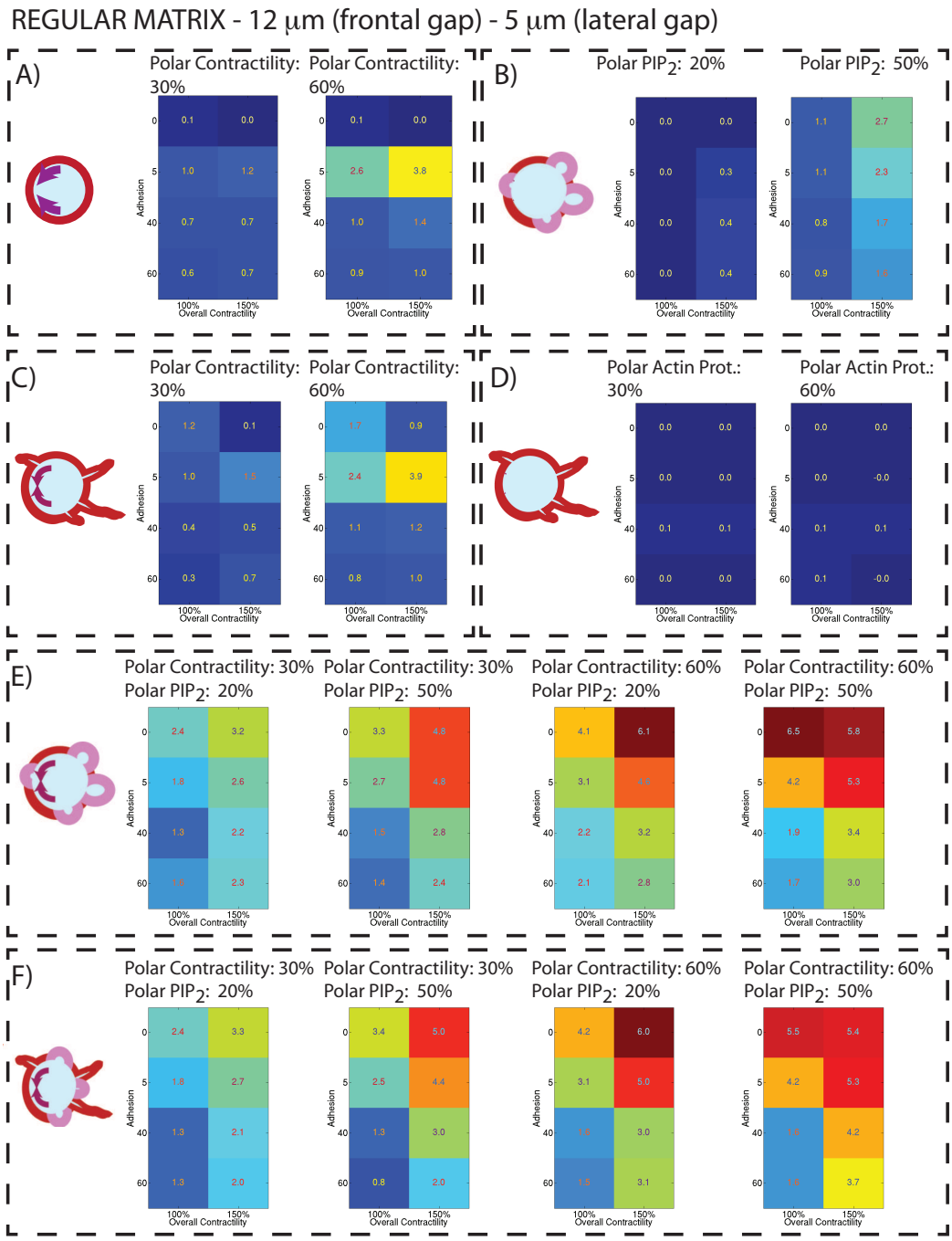

Figure B.5: Heatmaps for confined discontinuous environments with frontal gap size of 12μm and lateral gap size of 5μm, reported for higher polarities and additional motility modes. Legend continued on next page.

Figure B.5: Heatmaps for confined discontinuous environments with frontal gap size of $12\mu m$ and lateral gap size of $5\mu m$, reported for higher polarities and additional motility modes. Schematic in each sub-figure represents the motility mode. All figures throughout this appendix are colour coded in the same scale. All velocity values are the average of at least 10 simulations of $15min$ each. A) Simulations for a cell with polarised contractility at the cell rear, and without the ability to form any protrusions. Magnitude of polarised contractility is as indicated in titles. B) Cell without polarised contractilty, with reduced PIP_2 at the cell front, and the ability to form plasma membrane blebs, but not actin polymerisation based protrusions. Magnitude of PIP_2 polarity is as indicated in titles. C) Cell with polarised contractilty at the cell rear, and ability to form actin polymerisation based protrusions, but not plasma membrane blebs. Polarity in contractility is as indicated in titles, protrusion initiation probability is linked to polarised contractility (Figure 3.12). D) Cell without polarised contractility, and the ability to form actin polymerisation based protrusions, but not plasma membrane blebs. The probability of protrusion initiation is reduced at cell rear. The scale of reduction is equivalent to the the level which would be enforced by the contractility increase at the cell rear indicates in the titles (A 30 % polarisation means the protrusion initiation is reduced to a level that would be induced by 30 % contractility increase at the cell rear). E) Cell with increased contractility at the cell rear, with reduced PIP_2 at the cell front, and the ability to form plasma membrane blebs, but not actin polymerisation based protrusions. Magnitude of polarities are as indicated in titles. F) Cell with increased contractility at the cell rear, with reduced PIP_2 at the cell front, and the ability to form plasma membrane blebs and actin polymerisation based protrusions. Magnitude of polarities are as indicated in titles.

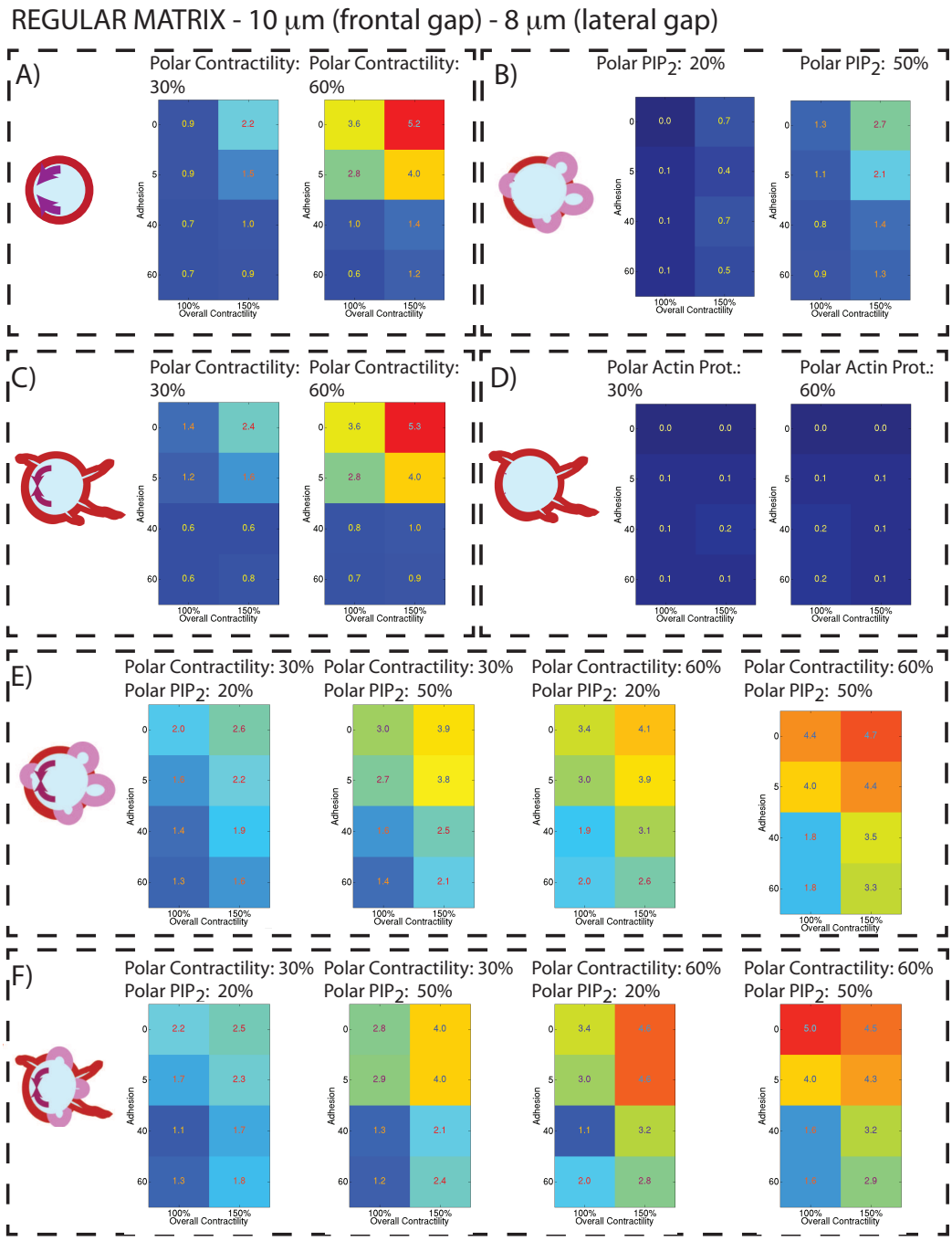

Figure B.6: Heatmaps for confined discontinuous environments with frontal gap size of 10μm and lateral gap size of 8μm, reported for higher polarities and additional motility modes. Legend continued on next page.

Figure B.6: Heatmaps for confined discontinuous environments with frontal gap size of $10\mu m$ and lateral gap size of $8\mu m$, reported for higher polarities and additional motility modes. Schematic in each sub-figure represents the motility mode. All figures throughout this appendix are colour coded in the same scale. All velocity values are the average of at least 10 simulations of $15min$ each. A) Simulations for a cell with polarised contractility at the cell rear, and without the ability to form any protrusions. Magnitude of polarised contractility is as indicated in titles. B) Cell without polarised contractilty, with reduced PIP_2 at the cell front, and the ability to form plasma membrane blebs, but not actin polymerisation based protrusions. Magnitude of PIP_2 polarity is as indicated in titles. C) Cell with polarised contractilty at the cell rear, and ability to form actin polymerisation based protrusions, but not plasma membrane blebs. Polarity in contractility is as indicated in titles, protrusion initiation probability is linked to polarised contractility (Figure 3.12). D) Cell without polarised contractility, and the ability to form actin polymerisation based protrusions, but not plasma membrane blebs. The probability of protrusion initiation is reduced at cell rear. The scale of reduction is equivalent to the the level which would be enforced by the contractility increase at the cell rear indicates in the titles (A 30 % polarisation means the protrusion initiation is reduced to a level that would be induced by 30 % contractility increase at the cell rear). E) Cell with increased contractility at the cell rear, with reduced PIP_2 at the cell front, and the ability to form plasma membrane blebs, but not actin polymerisation based protrusions. Magnitude of polarities are as indicated in titles. F) Cell with increased contractility at the cell rear, with reduced PIP_2 at the cell front, and the ability to form plasma membrane blebs and actin polymerisation based protrusions. Magnitude of polarities are as indicated in titles.

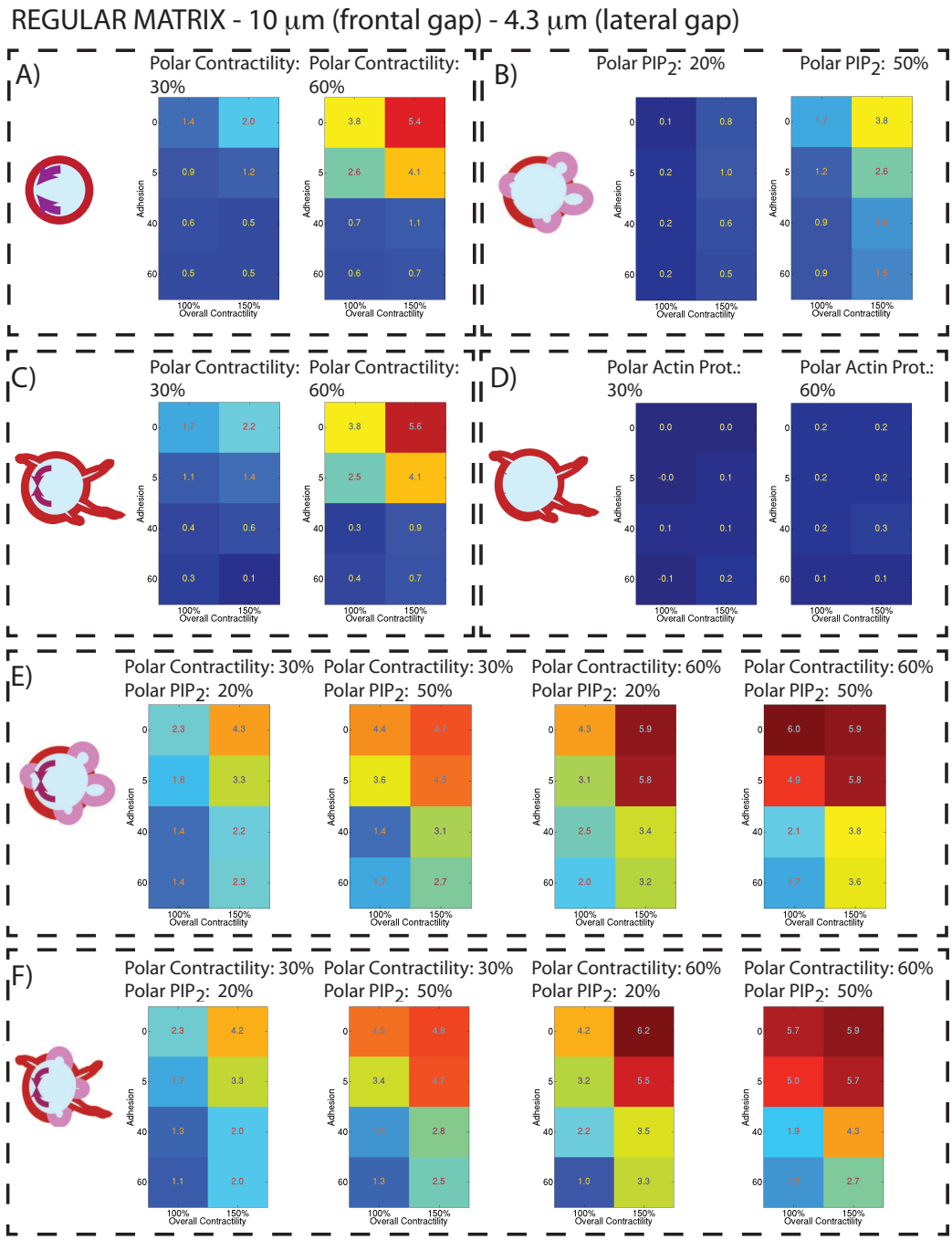

Figure B.7: Heatmaps for confined discontinuous environments with frontal gap size of 10μm and lateral gap size of 4.3μm, reported for higher polarities and additional motility modes.

Figure B.7: Heatmaps for confined discontinuous environments with frontal gap size of $10\mu m$ and lateral gap size of $4.3\mu m$, reported for higher polarities and additional motility modes. Schematic in each sub-figure represents the motility mode. All figures throughout this appendix are colour coded in the same scale. All velocity values are the average of at least 10 simulations of $15min$ each. A) Simulations for a cell with polarised contractility at the cell rear, and without the ability to form any protrusions. Magnitude of polarised contractility is as indicated in titles. B) Cell without polarised contractilty, with reduced PIP_2 at the cell front, and the ability to form plasma membrane blebs, but not actin polymerisation based protrusions. Magnitude of PIP_2 polarity is as indicated in titles. C) Cell with polarised contractilty at the cell rear, and ability to form actin polymerisation based protrusions, but not plasma membrane blebs. Polarity in contractility is as indicated in titles, protrusion initiation probability is linked to polarised contractility (Figure 3.12). D) Cell without polarised contractility, and the ability to form actin polymerisation based protrusions, but not plasma membrane blebs. The probability of protrusion initiation is reduced at cell rear. The scale of reduction is equivalent to the the level which would be enforced by the contractility increase at the cell rear indicates in the titles (A 30 % polarisation means the protrusion initiation is reduced to a level that would be induced by 30 % contractility increase at the cell rear). E) Cell with increased contractility at the cell rear, with reduced PIP_2 at the cell front, and the ability to form plasma membrane blebs, but not actin polymerisation based protrusions. Magnitude of polarities are as indicated in titles. F) Cell with increased contractility at the cell rear, with reduced PIP_2 at the cell front, and the ability to form plasma membrane blebs and actin polymerisation based protrusions. Magnitude of polarities are as indicated in titles.

Appendix C

Velocity Profiles for Drug Treatments in the Abscence of a Cell Nucleus

Throughout the whole time period for the production of this thesis, development of the computational model has been continuous. The model cell has been improved to include higher resolution structures for the already modelled sub-cellular elements, such as the linear bleb necks and flexible bleb necks. Moreover, new features have been implemented as the biological phenomena to be modelled necessitated a more sophisticated cell definition, such as modelling cell motility within *in vivo* mimetic environments and the implementation of the cell nucleus.

The roles of these added structures, and how they affect the predicted velocity magnitudes have been demonstrated in Chapter 5 for the control state of A375M2 cells. This appendix shows the velocity predictions upon biochemical perturbations for model setups on different scales - from the simple cell with linear bleb necks and no nucleus, to the complex cell with flexible bleb necks and a nucleus. Although the predicted velocity magnitudes are different, the predicted relative effect of the biochemical perturbations are almost identical on all three modelling scales (Figure C.1). This data successfully shows that the cell nucleus will become a limiting factor in the velocity of the cell in an environment where the cell needs to squeeze its body through gaps smaller than the nuclear diameter. Meanwhile, the data indicates that the effects of the perturbations are not significantly altered by the resistance of the nucleus, hence these effects are functioning at a level beyond the forces required to change the shape of the nucleus, and directly at the level of traction generation and forward motion of the cell

body. However, to further validate this prediction, a more detailed modelling of the interaction between the cortical myosin levels and the tension exerted on the nuclear lamina should be carried out.

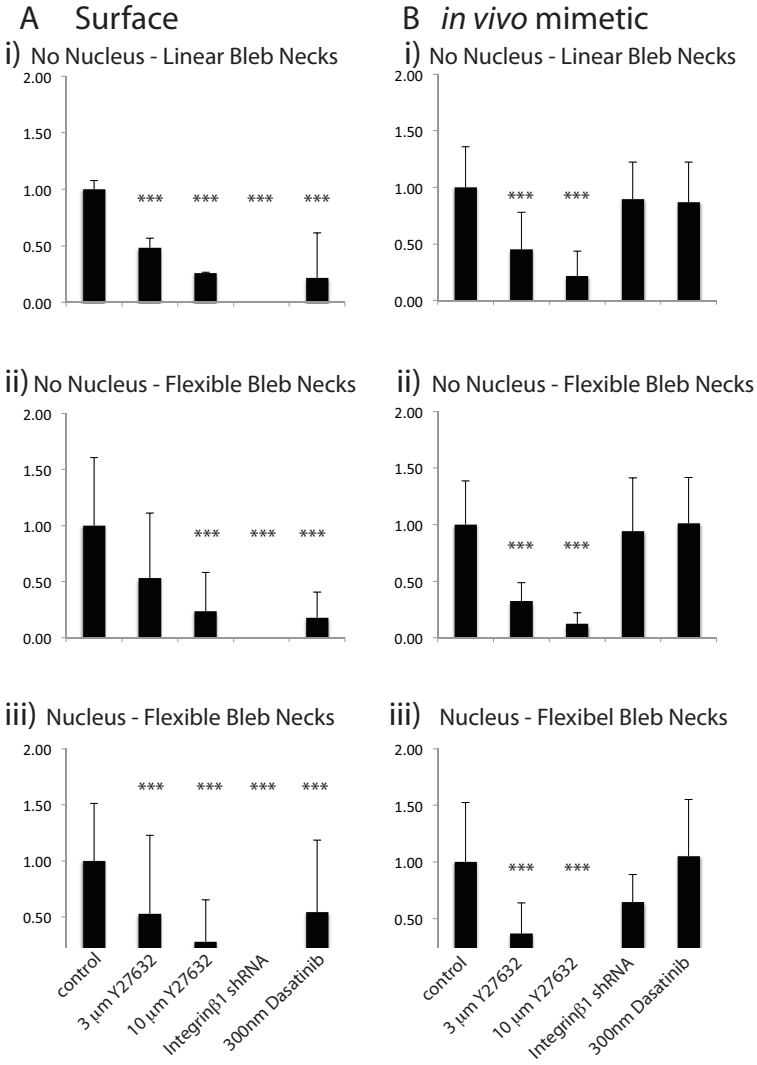

Figure C.1: Model predictions on melanoma velocity upon biochemical perturbations, reported for simpler model setups, A) on unconfined continuous surfaces and B) within *in vivo* mimetic environments. For (A) and (B) top panel (i) reports the predictions for the model setup with no cell nucleus and linear plasma membrane bleb necks, middle panel (ii) reports the predicitions for the model setup with no cell nucleus, but flexible bleb necks, and finally the bottom panel (iii) reports the model predictions for the model setup with the cell nucleus and flexible bleb necks. The data demonstrated at the bottom panels is reported in Figure 5.17, and displayed here for ease of comparison. All the velocities are normalised to the velocity of control under the same conditions. The velocities are the averages of all three polarities tested: 40 %, 50 % and 60 % increased contractility at the cell rear coupled with 30 %, 40 % and 50 % reduced plasma membrane–cortex linker concentration at the cell front, respectively. The error bars report the average standard deviation.(***) indicates significant difference of the velocity from control cells under the same conditions, p-value$>$ 0.001 (two-tail t-test).

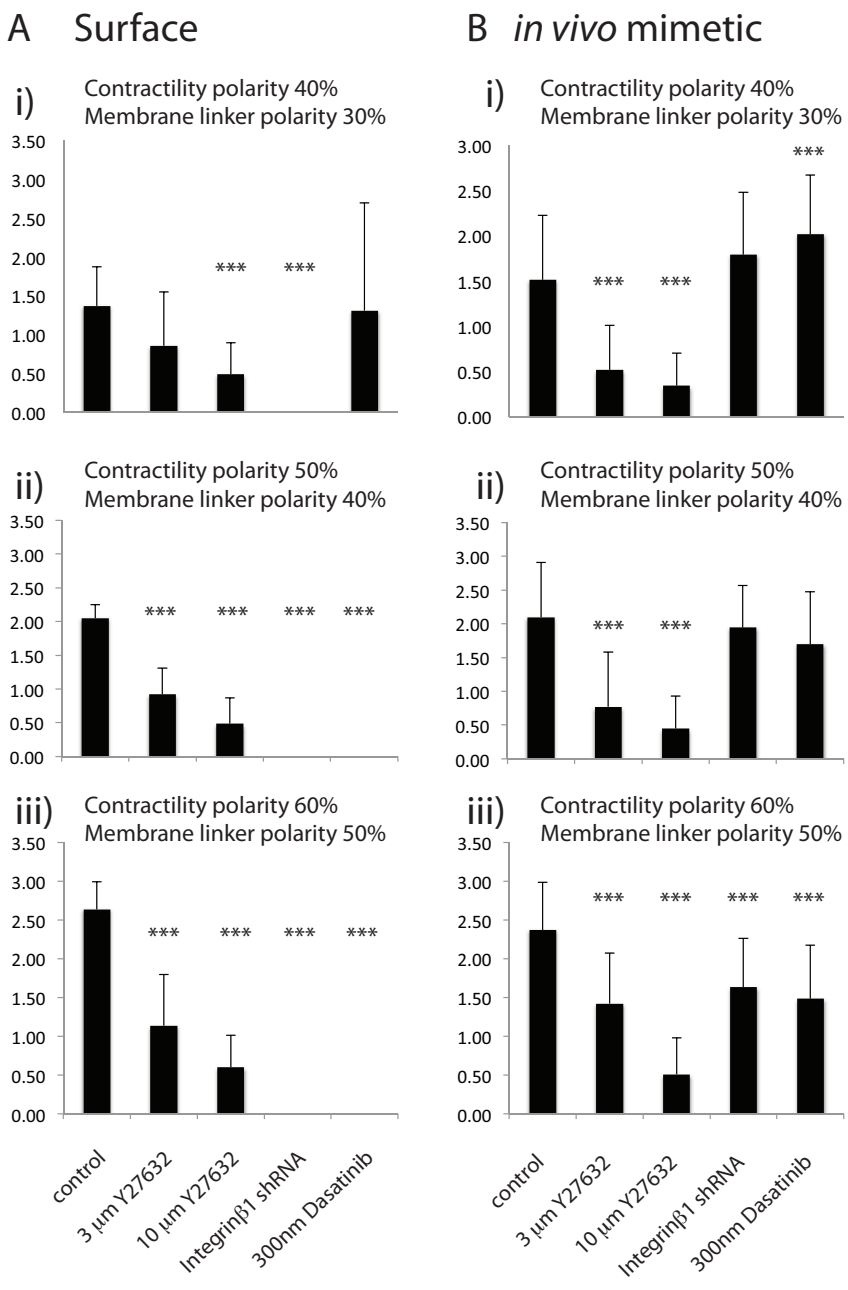

Figure C.2: Model setup with no cell nucleus and linear plasma membrane bleb necks. Model predictions on melanoma velocity upon biochemical perturbation, reported at individual cell polarities. A) On unconfined surface and B) Within *in vivo* mimetic ECM. The cellular asymmetries are indicated on each plot. Error bars mark one standard deviation. (***) indicates significant difference from control cells under the same conditions, p-value$<$ 0.001 (two-tail t-test).

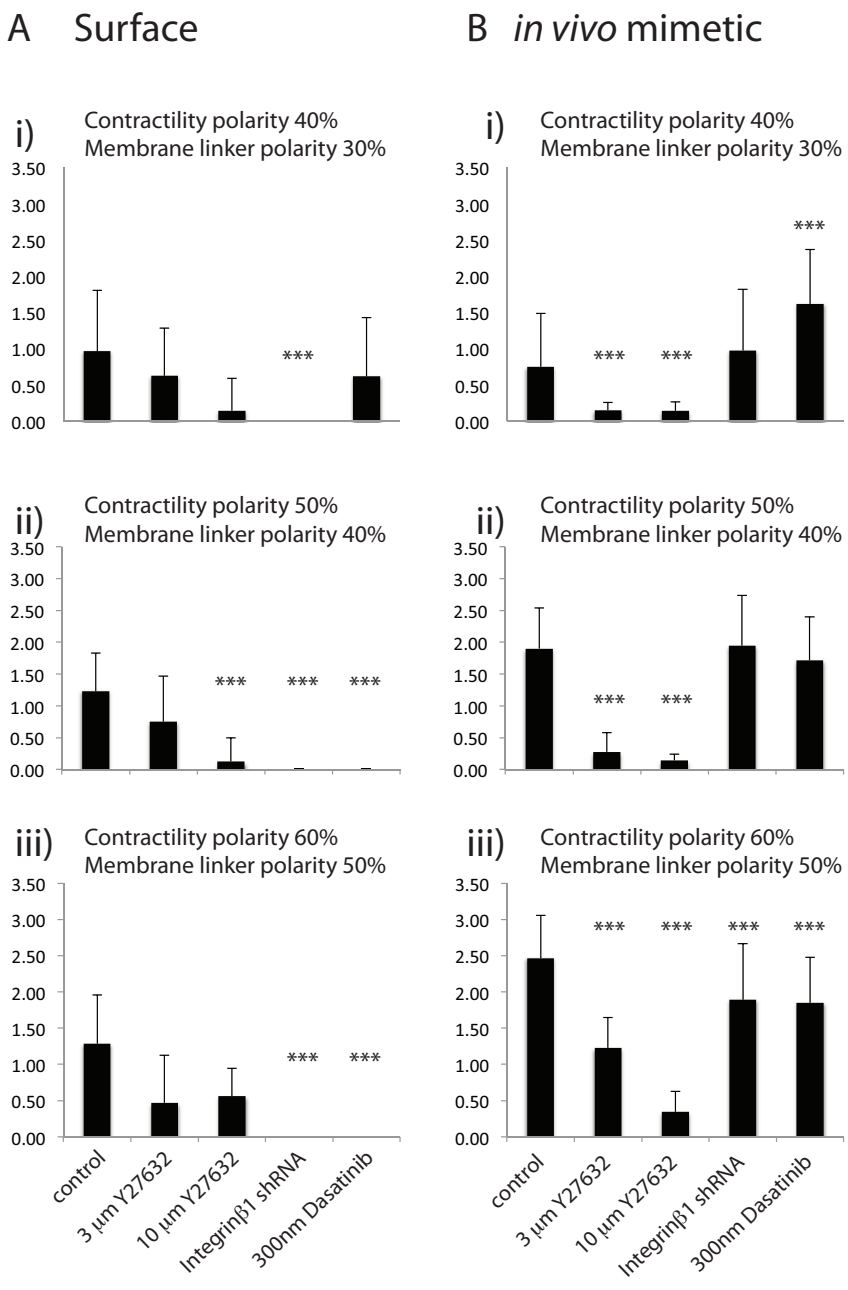

Figure C.3: Model setup with no cell nucleus and flexible plasma membrane bleb necks. Model predictions on melanoma velocity upon biochemical perturbation, reported at individual cell polarities, A) On unconfined surface and B) Within *in vivo* mimetic ECM. The cellular asymmetries are indicated on each plot. Error bars mark one standard deviation. (***) indicates significant difference from control cells under the same conditions, p-value< 0.001 (two-tail t-test).

Bibliography

[1] D. Hanahan and R. A. Weinberg, "The hallmarks of cancer," *Cell*, vol. 100, pp. 57–70, Jan. 2000.

[2] M. B. Sporn, "The war on cancer," *Lancet*, vol. 347, pp. 1377–1381, May 1996.

[3] J. D. Hood and D. A. Cheresh, "Role of integrins in cell invasion and migration," *Nat. Rev. Cancer*, vol. 2, pp. 91–100, Feb. 2002.

[4] C. D. Madsen and E. Sahai, "Cancer dissemination–lessons from leukocytes," *Dev. Cell*, vol. 19, pp. 13–26, July 2010.

[5] J. T. Parsons, A. R. Horwitz, and M. A. Schwartz, "Cell adhesion: integrating cytoskeletal dynamics and cellular tension," *Nature Reviews Molecular Cell Biology*, vol. 11, pp. 633–643, Sept. 2010.

[6] K. Wolf, I. Mazo, H. Leung, K. Engelke, U. H. von Andrian, E. I. Deryugina, A. Y. Strongin, E.-B. B. Bröcker, and P. Friedl, "Compensation mechanism in tumor cell migration: mesenchymal-amoeboid transition after blocking of pericellular proteolysis," *J. Cell Biol.*, vol. 160, pp. 267–277, Jan. 2003.

[7] T. Lämmermann and M. Sixt, "Mechanical modes of 'amoeboid' cell migration," *Curr. Opin. Cell Biol.*, vol. 21, pp. 636–644, Oct. 2009.

[8] A. Lorentzen, J. Bamber, A. Sadok, I. Elson-Schwab, and C. J. Marshall, "An ezrin-rich, rigid uropod-like structure directs movement of amoeboid blebbing cells," *J. Cell Sci.*, vol. 124, pp. 1256–1267, Apr. 2011.

[9] V. Sanz-Moreno, G. Gadea, J. Ahn, H. Paterson, P. Marra, S. Pinner, E. Sahai, and C. J. Marshall, "Rac activation and inactivation control plasticity of tumor cell movement," *Cell*, vol. 135, pp. 510–523, Oct. 2008.

[10] A. Otto, H. Collins-Hooper, A. Patel, P. R. Dash, and K. Patel, "Adult skeletal muscle stem cell migration is mediated by a blebbing/amoeboid mechanism," *Rejuvenation research*, vol. 14, pp. 249–260, June 2011.

[11] D. C. Weiser, R. H. Row, and D. Kimelman, "Rho-regulated myosin phosphatase establishes the level of protrusive activity required for cell movements during zebrafish gastrulation," *Development (Cambridge, England)*, vol. 136, pp. 2375–2384, July 2009.

[12] E. Sahai and C. J. Marshall, "Differing modes of tumour cell invasion have distinct requirements for rho/rock signalling and extracellular proteolysis," *Nat. Cell Biol.*, vol. 5, pp. 711–719, Aug. 2003.

[13] D. Bottino, A. Mogilner, T. Roberts, M. Stewart, and G. Oster, "How nematode sperm crawl," *J. Cell Sci.*, vol. 115, pp. 367–384, Jan. 2002.

[14] D. C. Bottino and L. J. Fauci, "A computational model of ameboid deformation and locomotion," *Eur. Biophys. J.*, vol. 27, no. 5, pp. 532–539, 1998.

[15] M. Herant and M. Dembo, "Cytopede: a three-dimensional tool for modeling cell motility on a flat surface," *J. Comput. Biol.*, vol. 17, pp. 1639–1677, Dec. 2010.

[16] B. Alberts, A. Johnson, J. Lewis, M. Raff, K. Roberts, and P. Walter, *Molecular Biology Cell*. Garland Science, Mar. 2002.

[17] M. A. Dichtl and E. Sackmann, "Microrheometry of semiflexible actin networks through enforced single-filament reptation: Frictional coupling and heterogeneities in entangled networks," *Proc. Natl. Acad. Sci. USA.*, vol. 99, pp. 6533–6538, May 2002.

[18] M. Keller, R. Tharmann, M. A. Dichtl, A. R. Bausch, and E. Sackmann, "Slow filament dynamics and viscoelasticity in entangled and active actin networks," *Philosophical Transactions of the Royal Society of London. Series A: Mathematical, Physical and Engineering Sciences*, vol. 361, pp. 699–712, Apr. 2003.

[19] P. Pullarkat, P. Fernandez, and A. Ott, "Rheological properties of the eukaryotic cell cytoskeleton," *Phys. Rep.*, vol. 449, pp. 29–53, Sept. 2007.

[20] J. Xu, D. Wirtz, and T. D. Pollard, "Dynamic cross-linking by a-actinin determines the mechanical properties of actin filament networks," *J. Biol. Chem.*, vol. 273, pp. 9570–9576, Apr. 1998.

[21] J. Stricker, T. Falzone, and M. L. Gardel, "Mechanics of the f-actin cytoskeleton," *Journal of biomechanics*, vol. 43, pp. 9–14, Jan. 2010.

[22] D. Boal, *Mechanics of the Cell*. Cambridge University Press, 1 ed., Dec. 2001.

[23] S. Yumura, "myosin II dynamics and cortical flow during contractile ring formation in dictyostelium cells," *J. Cell Biol.*, vol. 154, no. 1, pp. 137–145, 2001.

[24] S. Coscoy, F. Waharte, A. Gautreau, M. Martin, D. Louvard, P. Mangeat, M. Arpin, and F. Amblard, "Molecular analysis of microscopic ezrin dynamics by two-photon frap," *Proc. Natl. Acad. Sci. USA.*, vol. 99, pp. 12813–12818, Oct. 2002.

[25] G. T. Charras, T. J. Mitchison, and L. Mahadevan, "Animal cell hydraulics," *J. Cell Sci.*, vol. 122, pp. 3233–3241, Sept. 2009.

[26] D. Zicha, I. M. Dobbie, M. R. Holt, J. Monypenny, D. Y. H. Soong, C. Gray, and G. A. Dunn, "Rapid actin transport during cell protrusion," *Science*, vol. 300, pp. 142–145, Apr. 2003.

[27] J.-Y. Tinevez, U. Schulze, G. Salbreux, J. Roensch, J.-F. Joanny, and E. Paluch, "Role of cortical tension in bleb growth," *Proc. Natl. Acad. Sci. USA.*, vol. 106, pp. 18581–18586, Nov. 2009.

[28] F. C. Mackintosh, "Theoretical models of viscoelasticity of actin solutions and the actin cortex," *The Biological Bulletin*, vol. 194, pp. 351–353, June 1998.

[29] T. D. Pollard and J. A. Cooper, "Actin, a central player in cell shape and movement," *Science*, vol. 326, pp. 1208–1212, Nov. 2009.

[30] D. Sept and J. A. McCammon, "Thermodynamics and kinetics of actin filament nucleation," *Biophys. J.*, vol. 81, pp. 667–674, Aug. 2001.

[31] G. T. Charras, C.-K. Hu, M. Coughlin, and T. J. Mitchison, "Reassembly of contractile actin cortex in cell blebs," *J. Cell Biol.*, vol. 175, no. 3, pp. 477–490, 2006.

[32] S. Diez, G. Gerisch, K. Anderson, A. Müller-Taubenberger, and T. Bretschneider, "Subsecond reorganization of the actin network in cell motility and chemotaxis," *Proc. Natl. Acad. Sci. USA.*, vol. 102, pp. 7601–7606, May 2005.

[33] M. P. Stewart, J. Helenius, Y. Toyoda, S. P. Ramanathan, D. J. Muller, and A. A. Hyman, "Hydrostatic pressure and the actomyosin cortex drive mitotic cell rounding," *Nature*, vol. 469, pp. 226–230, Jan. 2011.

[34] G. T. Charras, J. C. Yarrow, M. A. Horton, L. Mahadevan, and T. J. Mitchison, "Non-equilibration of hydrostatic pressure in blebbing cells," *Nature*, vol. 435, pp. 365–369, May 2005.

[35] G. T. Charras, M. Coughlin, T. J. Mitchinson, and L. Mahadevan, "Life and times of a cellular bleb," *Biophys. J.*, vol. 94, no. 5, pp. 1836–1853, 2008.

[36] J. Dai, H. Ping Ting-Beall, R. M. Hochmuth, M. P. Sheetz, and M. A. Titus, "myosin I contributes to the generation of resting cortical tension," *Biophys. J.*, vol. 77, pp. 1168–1176, Aug. 1999.

[37] J. Lam, M. Herant, M. Dembo, and V. Heinrich, "Baseline mechanical characterization of j774 macrophages," *Biophys. J.*, vol. 96, pp. 248–254, Jan. 2009.

[38] J. B. Wyckoff, S. E. Pinner, S. Gschmeissner, J. S. Condeelis, and E. Sahai, "Rock- and myosin-dependent matrix deformation enables protease-independent tumor-cell invasion *in vivo*," *Curr. Biol.*, vol. 16, pp. 1515–1523, Aug. 2006.

[39] R. Poincloux, O. Collin, F. Lizárraga, M. Romao, M. Debray, M. Piel, and P. Chavrier, "Contractility of the cell rear drives invasion of breast tumor cells in 3d matrigel," *Proc. Natl. Acad. Sci. USA.*, 2011.

[40] G. Kirfel, "Cell migration: mechanisms of rear detachment and the formation of migration tracks," *Eur. J. Cell Biol.*, vol. 83, pp. 717–724, Dec. 2004.

[41] T. Lammermann, B. L. Bader, S. J. Monkley, T. Worbs, R. Wedlich-Soldner, K. Hirsch, M. Keller, R. Forster, D. R. Critchley, R. Fassler, and M. Sixt, "Rapid leukocyte migration by integrin-independent flowing and squeezing," *Nature*, vol. 453, pp. 51–55, May 2008.

[42] D. Raucher, "Characteristics of a membrane reservoir buffering membrane tension," *Biophys. J.*, vol. 77, pp. 1992–2002, Oct. 1999.

[43] K. Wolf and P. Friedl, "Mapping proteolytic cancer cell-extracellular matrix interfaces," *Clinical & experimental metastasis*, vol. 26, pp. 289–298, Apr. 2009.

[44] K. N. Dahl, S. M. Kahn, K. L. Wilson, and D. E. Discher, "The nuclear envelope lamina network has elasticity and a compressibility limit suggestive of a molecular shock absorber," *J. Cell Sci.*, vol. 117, pp. 4779–4786, Sept. 2004.

[45] F. Guilak, J. R. Tedrow, and R. Burgkart, "Viscoelastic properties of the cell nucleus," *Biochemical and Biophysical Research Communications*, vol. 269, pp. 781–786, Mar. 2000.

[46] N. Caille, O. Thoumine, Y. Tardy, and J.-J. J. Meister, "Contribution of the nucleus to the mechanical properties of endothelial cells," *Journal of biomechanics*, vol. 35, pp. 177–187, Feb. 2002.

[47] S. B. Khatau, C. M. Hale, P. J. Stewart-Hutchinson, M. S. Patel, C. L. Stewart, P. C. Searson, D. Hodzic, and D. Wirtz, "A perinuclear actin cap regulates nuclear shape," *Proc. Natl. Acad. Sci. USA.*, Oct. 2009.

[48] J. R. Sims, S. Karp, and D. E. Ingber, "Altering the cellular mechanical force balance results in integrated changes in cell, cytoskeletal and nuclear shape," *J. Cell Sci.*, vol. 103, pp. 1215–1222, Dec. 1992.

[49] K. Yamauchi, M. Yang, P. Jiang, N. Yamamoto, M. Xu, Y. Amoh, K. Tsuji, M. Bouvet, H. Tsuchiya, K. Tomita, A. R. Moossa, and R. M. Hoffman, "Real-time *in vivo* dual-color imaging of intracapillary cancer cell and nucleus deformation and migration," *Cancer Res.*, vol. 65, pp. 4246–4252, May 2005.

[50] M. Nakayama, M. Amano, A. Katsumi, T. Kaneko, S. Kawabata, M. Takefuji, and K. Kaibuchi, "Rho-kinase and myosin II activities are required for cell type and environment specific migration," *Genes to Cells*, vol. 10, pp. 107–117, Feb. 2005.

[51] A. Bellion, J.-P. Baudoin, C. Alvarez, M. Bornens, and C. Métin, "Nucleokinesis in tangentially migrating neurons comprises two alternating phases: Forward migration of the golgi/centrosome associated with centrosome splitting and myosin contraction at the rear," *J. Neurosci.*, vol. 25, pp. 5691–5699, June 2005.

[52] J.-W. W. Tsai, K. H. Bremner, and R. B. Vallee, "Dual subcellular roles for lis1 and dynein in radial neuronal migration in live brain tissue," *Nat. Neurosci.*, vol. 10, pp. 970–979, Aug. 2007.

[53] C. Beadle, M. C. Assanah, P. Monzo, R. Vallee, S. S. Rosenfeld, and P. Canoll, "The role of myosin II in glioma invasion of the brain," *Mol. Biol. Cell*, vol. 19, pp. 3357–3368, Aug. 2008.

[54] I. Dupin and S. Etienne-Manneville, "Nuclear positioning: Mechanisms and functions," *Int. J Biochem. & Cell Biol.*, vol. 43, pp. 1698–1707, Dec. 2011.

[55] A. Mazumdar and M. Mazumdar, "How one becomes many: blastoderm cellularization in drosophila melanogaster," *BioEssays : news and reviews in molecular, cellular and developmental biology*, vol. 24, pp. 1012–1022, Nov. 2002.

[56] F. Del Bene, A. M. Wehman, B. A. Link, and H. Baier, "Regulation of neurogenesis by interkinetic nuclear migration through an apical-basal notch gradient," *Cell*, vol. 134, pp. 1055–1065, Sept. 2008.

[57] E. J. Meyer, A. Ikmi, and M. C. Gibson, "Interkinetic nuclear migration is a broadly conserved feature of cell division in pseudostratified epithelia," *Curr. Biol.*, vol. 21, pp. 485–491, Mar. 2011.

[58] H. Mellor, "Cell motility: Golgi signalling shapes up to ship out," *Curr. Biol.*, vol. 14, June 2004.

[59] D. Wessels, E. Voss, N. Von Bergen, R. Burns, J. Stites, and D. R. Soll, "A computer-assisted system for reconstructing and interpreting the dynamic

three-dimensional relationships of the outer surface, nucleus and pseudopods of crawling cells," *Cell Motil. Cytoskeleton*, vol. 41, no. 3, pp. 225–246, 1998.

[60] K. Schütze, A. Maniotis, and M. Schliwa, "The position of the microtubule-organizing center in directionally migrating fibroblasts depends on the nature of the substratum," *Proc. Natl. Acad. Sci. USA.*, vol. 88, pp. 8367–8371, Oct. 1991.

[61] J. R. Levy and E. L. F. Holzbaur, "Dynein drives nuclear rotation during forward progression of motile fibroblasts," *J. Cell Sci.*, vol. 121, pp. 3187–3195, Oct. 2008.

[62] P. K. Mattila and P. Lappalainen, "Filopodia: molecular architecture and cellular functions," *Nat. Rev. Mol. Cell Biol.*, vol. 9, pp. 446–454, June 2008.

[63] A. Mogilner and B. Rubinstein, "The physics of filopodial protrusion," *Biophys. J.*, vol. 89, pp. 782–795, Aug. 2005.

[64] P. J. Heid, J. Geiger, D. Wessels, E. Voss, and D. R. Soll, "Computer-assisted analysis of filopod formation and the role of myosin II heavy chain phosphorylation in dictyostelium," *J. Cell Sci.*, vol. 118, pp. 2225–2237, May 2005.

[65] T. D. Pollard and G. G. Borisy, "Cellular motility driven by assembly and disassembly of actin filaments," *Cell*, vol. 112, no. 4, pp. 453–465, 2003.

[66] T. M. Svitkina, E. A. Bulanova, O. Y. Chaga, D. M. Vignjevic, S.-i. Kojima, J. M. Vasiliev, and G. G. Borisy, "Mechanism of filopodia initiation by reorganization of a dendritic network," *J. Cell Biol.*, vol. 160, pp. 409–421, Feb. 2003.

[67] M. Cohen, M. Georgiou, N. L. Stevenson, M. Miodownik, and B. Baum, "Dynamic filopodia transmit intermittent delta-notch signaling to drive pattern refinement during lateral inhibition," *Dev. Cell*, vol. 19, pp. 78–89, July 2010.

[68] H. Guillou, A. Depraz-Depland, E. Planus, B. Vianay, J. Chaussy, A. Grichine, C. Albigès-Rizo, and M. R. Block, "Lamellipodia nucleation

by filopodia depends on integrin occupancy and downstream rac1 signaling," *Exp. Cell Res.*, vol. 314, pp. 478–488, Feb. 2008.

[69] J. Renkawitz, K. Schumann, M. Weber, T. Lämmermann, H. Pflicke, M. Piel, J. Polleux, J. P. Spatz, and M. Sixt, "Adaptive force transmission in amoeboid cell migration," *Nat. Cell Biol.*, vol. 11, pp. 1438–1443, Dec. 2009.

[70] N. C. Gauthier, M. A. Fardin, P. Roca-Cusachs, and M. P. Sheetz, "Temporary increase in plasma membrane tension coordinates the activation of exocytosis and contraction during cell spreading," *Proc. Natl. Acad. Sci. USA.*, vol. 108, pp. 14467–14472, Aug. 2011.

[71] H. Kress, E. H. K. Stelzer, D. Holzer, F. Buss, G. Griffiths, and A. Rohrbach, "Filopodia act as phagocytic tentacles and pull with discrete steps and a load-dependent velocity," *Proc. Natl. Acad. Sci. USA.*, vol. 104, pp. 11633–11638, July 2007.

[72] D. R. Kovar and T. D. Pollard, "Insertional assembly of actin filament barbed ends in association with formins produces piconewton forces," *Proc. Natl. Acad. Sci. USA.*, vol. 101, pp. 14725–14730, Oct. 2004.

[73] D. Cojoc, F. Difato, E. Ferrari, R. B. Shahapure, J. Laishram, M. Righi, E. M. Di Fabrizio, and V. Torre, "Properties of the force exerted by filopodia and lamellipodia and the involvement of cytoskeletal components," *PloS one*, vol. 2, no. 10, 2007.

[74] A. Mogilner and G. Oster, "Cell motility driven by actin polymerization," *Biophys. J.*, vol. 71, pp. 3030–3045, Dec. 1996.

[75] T. M. Svitkina, A. B. Verkhovsky, K. M. McQuade, and G. G. Borisy, "Analysis of the actin-myosin II system in fish epidermal keratocytes: Mechanism of cell body translocation," *J. Cell Biol.*, vol. 139, pp. 397–415, Oct. 1997.

[76] A. J. Ridley, "Rho GTPases and cell migration," *J. Cell Sci.*, vol. 114, pp. 2713–2722, Aug. 2001.

[77] M. Amano, K. Chihara, K. Kimura, Y. Fukata, N. Nakamura, Y. Matsuura, and K. Kaibuchi, "Formation of actin stress fibers and focal adhesions enhanced by rho-kinase," *Science*, vol. 275, pp. 1308–1311, Feb. 1997.

[78] K. Kimura, M. Ito, M. Amano, K. Chihara, Y. Fukata, M. Nakafuku, B. Yamamori, J. Feng, T. Nakano, K. Okawa, A. Iwamatsu, and K. Kaibuchi, "Regulation of myosin phosphatase by rho and rho-associated kinase (rho-kinase)," *Science*, vol. 273, pp. 245–248, July 1996.

[79] V. Sanz-Moreno and C. J. Marshall, "The plasticity of cytoskeletal dynamics underlying neoplastic cell migration," *Curr. Opin. Cell Biol.*, vol. 22, pp. 690–696, Oct. 2010.

[80] M. P. Sheetz, J. E. Sable, and H.-G. G. Döbereiner, "Continuous membrane-cytoskeleton adhesion requires continuous accommodation to lipid and cytoskeleton dynamics," *Annual review of biophysics and biomolecular structure*, vol. 35, no. 1, pp. 417–434, 2006.

[81] A. I. McClatchey and R. G. Fehon, "Merlin and the ERM proteins–regulators of receptor distribution and signaling at the cell cortex," *Trends Cell. Biol.*, vol. 19, pp. 198–206, May 2009.

[82] J. Gilden and M. F. Krummel, "Control of cortical rigidity by the cytoskeleton: emerging roles for septins," *Cytoskeleton (Hoboken, N.J.)*, vol. 67, pp. 477–486, Aug. 2010.

[83] A. Ivetic and A. J. Ridley, "Ezrin/radixin/moesin proteins and rho GTPase signalling in leucocytes," *Immunology*, vol. 112, pp. 165–176, June 2004.

[84] B. T. Fievet, A. Gautreau, C. Roy, L. Del Maestro, P. Mangeat, D. Louvard, and M. Arpin, "Phosphoinositide binding and phosphorylation act sequentially in the activation mechanism of ezrin," *J. Cell Biol.*, vol. 164, pp. 653–659, Mar. 2004.

[85] D. Raucher, T. Stauffer, W. Chen, K. Shen, S. Guo, J. D. York, M. P. Sheetz, and T. Meyer, "Phosphatidylinositol 4,5-bisphosphate functions as a second messenger that regulates cytoskeleton-plasma membrane adhesion," *Cell*, vol. 100, pp. 221–228, Jan. 2000.

[86] B. Treanor, D. Depoil, A. Gonzalez-Granja, P. Barral, M. Weber, O. Dushek, A. Bruckbauer, and F. D. Batista, "The membrane skeleton controls diffusion dynamics and signaling through the b cell receptor," *Immunity*, vol. 32, pp. 187–199, Feb. 2010.

[87] A. Byron, "Analyzing the anatomy of integrin adhesions," *Sci. Signal.*, vol. 4, p. jc3, Apr. 2011.

[88] S. Hooper, C. Gaggioli, and E. Sahai, "A chemical biology screen reveals a role for rab21-mediated control of actomyosin contractility in fibroblast-driven cancer invasion," *British Journal of Cancer*, vol. 102, pp. 392–402, Jan. 2010.

[89] J. D. Humphries, A. Byron, and M. J. Humphries, "Integrin ligands at a glance," *J. Cell Sci.*, vol. 119, pp. 3901–3903, Oct. 2006.

[90] J. Friedrichs, A. Manninen, D. J. Muller, and J. Helenius, "Galectin-3 regulates integrin $\alpha 2\beta 1$-mediated adhesion to collagen-i and -iv," *J. Biol. Chem.*, vol. 283, pp. 32264–32272, Nov. 2008.

[91] N. Q. Balaban, U. S. Schwarz, D. Riveline, P. Goichberg, G. Tzur, I. Sabanay, D. Mahalu, S. Safran, A. Bershadsky, L. Addadi, and B. Geiger, "Force and focal adhesion assembly: a close relationship studied using elastic micropatterned substrates," *Nat. Cell Biol.*, vol. 3, pp. 466–472, Apr. 2001.

[92] C. G. Galbraith and M. P. Sheetz, "A micromachined device provides a new bend on fibroblast traction forces," *Proc. Natl. Acad. Sci. USA.*, vol. 94, pp. 9114–9118, Aug. 1997.

[93] C. G. Galbraith, K. M. Yamada, and M. P. Sheetz, "The relationship between force and focal complex development," *J. Cell Biol.*, vol. 159, pp. 695–705, Nov. 2002.

[94] T. S. P. Strangeways, "Observations on the changes seen in living cells during growth and division," *Proceedings of the Royal Society of London. Series B, Containing Papers of a Biological Character*, vol. 94, pp. 137–141, Nov. 1922.

[95] R. Fink, "Fundulus deep cells: Directional migration in response to epithelial wounding," *Dev. Biol.*, vol. 129, pp. 179–190, Sept. 1988.

[96] A. Diz-Muñoz, M. Krieg, M. Bergert, I. Ibarlucea-Benitez, D. J. Muller, E. Paluch, and C.-P. P. Heisenberg, "Control of directed cell migration in vivo by membrane-to-cortex attachment," *PLoS Biol.*, vol. 8, pp. e1000544+, Nov. 2010.

[97] E. Paluch, M. Piel, J. Prost, M. Bornens, and C. Sykes, "Cortical actomyosin breakage triggers shape oscillations in cells and cell fragments," *Biophys. J.*, vol. 89, pp. 724–733, July 2005.

[98] H. Keller, "Differences in cortical actin structure and dynamics document that different types of blebs are formed by distinct mechanisms," *Exp. Cell Res.*, vol. 277, pp. 161–172, July 2002.

[99] J. van der Gucht and C. Sykes, "Physical model of cellular symmetry breaking," *Cold Spring Harbor perspectives in biology*, vol. 1, July 2009.

[100] B. Maugis, J. Brugues, P. Nassoy, N. Guillen, P. Sens, and F. Amblard, "Dynamic instability of the intracellular pressure drives bleb-based motility," *J. Cell Sci.*, vol. 123, pp. 3884–3892, Nov. 2010.

[101] E. Kardash, M. Reichman-Fried, J.-L. Maitre, B. Boldajipour, E. Papusheva, E.-M. Messerschmidt, C.-P. Heisenberg, and E. Raz, "A role for rho GTPases and cell-cell adhesion in single-cell motility *in vivo*," *Nat. Cell Biol.*, vol. 12, pp. 47–53, Dec. 2009.

[102] J. Brugués, B. Maugis, J. Casademunt, P. Nassoy, F. Amblard, and P. Sens, "Dynamical organization of the cytoskeletal cortex probed by micropipette aspiration," *Proc. Natl. Acad. Sci. USA.*, vol. 107, pp. 15415–15420, Aug. 2010.

[103] T. J. Mitchison, G. T. Charras, and L. Mahadevan, "Implications of a poroelastic cytoplasm for the dynamics of animal cell shape," *Seminars in cell & Dev. Biol.*, vol. 19, pp. 215–223, June 2008.

[104] C. C. Cunningham, "Actin polymerization and intracellular solvent flow in cell surface blebbing," *J. Cell Biol.*, vol. 129, pp. 1589–1599, June 1995.

[105] O. T. Fackler and R. Grosse, "Cell motility through plasma membrane blebbing," *J. Cell Biol.*, vol. 181, pp. 879–884, June 2008.

[106] H. Blaser, M. Reichman-Fried, I. Castanon, K. Dumstrei, F. L. Marlow, K. Kawakami, L. Solnica-Krezel, C.-P. P. Heisenberg, and E. Raz, "Migration of zebrafish primordial germ cells: a role for myosin contraction and cytoplasmic flow," *Dev. Cell*, vol. 11, pp. 613–627, Nov. 2006.

[107] P. D. Langridge and R. R. Kay, "Blebbing of dictyostelium cells in response to chemoattractant," *Exp. Cell Res.*, vol. 312, pp. 2009–2017, July 2006.

[108] G. Charras and E. Paluch, "Blebs lead the way: how to migrate without lamellipodia," *Nature Reviews Molecular Cell Biology*, vol. 9, pp. 730–736, July 2008.

[109] S. Tournaviti, S. Hannemann, S. Terjung, T. M. Kitzing, C. Stegmayer, J. Ritzerfeld, P. Walther, R. Grosse, W. Nickel, and O. T. Fackler, "Sh4-domain-induced plasma membrane dynamization promotes bleb-associated cell motility," *J. Cell Sci.*, vol. 120, pp. 3820–3829, Nov. 2007.

[110] M. L. Coleman, E. A. Sahai, M. Yeo, M. Bosch, A. Dewar, and M. F. Olson, "Membrane blebbing during apoptosis results from caspase-mediated activation of rock i," *Nat Cell Biol*, vol. 3, pp. 339–345, Apr. 2001.

[111] M. Sebbagh, C. Renvoize, J. Hamelin, N. Riche, J. Bertoglio, and J. Breard, "Caspase-3-mediated cleavage of ROCK I induces MLC phosphorylation and apoptotic membrane blebbing," *Nat Cell Biol*, vol. 3, pp. 346–352, Apr. 2001.

[112] C. A. Erickson and J. P. Trinkaus, "Microvilli and blebs as sources of reserve surface membrane during cell spreading," *Exp. Cell Res.*, vol. 99, pp. 375–384, May 1976.

[113] J. Bereiter-Hahn, M. Lück, T. Miebach, H. K. Stelzer, and M. Vöth, "Spreading of trypsinized cells: cytoskeletal dynamics and energy requirements," *J. Cell Sci.*, vol. 96 (Pt 1), pp. 171–188, May 1990.

[114] L. L. Norman, J. Brugés, K. Sengupta, P. Sens, and H. Aranda-Espinoza, "Cell blebbing and membrane area homeostasis in spreading and retracting cells," *Biophys. J.*, vol. 99, pp. 1726–1733, Sept. 2010.

[115] L. Norman, K. Sengupta, and H. Aranda-Espinoza, "Blebbing dynamics during endothelial cell spreading," *Eur. J. Cell Biol.*, vol. 90, pp. 37–48, Jan. 2011.

[116] J. Sedzinski, M. Biro, A. Oswald, J.-Y. Y. Tinevez, G. Salbreux, and E. Paluch, "Polar actomyosin contractility destabilizes the position of the cytokinetic furrow," *Nature*, vol. 476, pp. 462–466, Aug. 2011.

[117] K. Yoshida and T. Soldati, "Dissection of amoeboid movement into two mechanically distinct modes," *J. Cell Sci.*, vol. 119, pp. 3833–3844, Sept. 2006.

[118] P. Friedl and K. Wolf, "Tumour-cell invasion and migration: diversity and escape mechanisms," *Nat. Rev. Cancer*, vol. 3, pp. 362–374, May 2003.

[119] P. Friedl and E. B. Bröcker, "The biology of cell locomotion within three-dimensional extracellular matrix," *CMLS*, vol. 57, pp. 41–64, Jan. 2000.

[120] J. Renkawitz and M. Sixt, "Mechanisms of force generation and force transmission during interstitial leukocyte migration," *EMBO reports*, vol. 11, pp. 744–750, Sept. 2010.

[121] A. B. Verkhovsky, T. M. Svitkina, and G. G. Borisy, "Self-polarization and directional motility of cytoplasm," *Curr. Biol.*, vol. 9, pp. 11–20, Jan. 1999.

[122] J. Jacobelli, F. C. Bennett, P. Pandurangi, A. J. Tooley, and M. F. Krummel, "Myosin-iia and ICAM-1 regulate the interchange between two distinct modes of t cell migration," *J. Immunol.*, vol. 182, pp. 2041–2050, Feb. 2009.

[123] R. J. Hawkins, M. Piel, G. F. Andre, A. M. L. Dumenil, J. F. Joanny, J. Prost, and R. Voituriez, "Pushing off the walls: A mechanism of cell motility in confinement," *Phys. Rev. Lett.*, vol. 102, p. 058103, Feb. 2009.

[124] K. Tarbashevich, A. Dzementsei, and T. Pieler, "A novel function for kif13b in germ cell migration," *Dev. Biol.*, vol. 349, pp. 169–178, Jan. 2011.

[125] H. Keller, A. D. D. Zadeh, and P. Eggli, "Localised depletion of polymerised actin at the front of walker carcinosarcoma cells increases the speed of locomotion," *Cell motility and the cytoskeleton*, vol. 53, pp. 189–202, Nov. 2002.

[126] A. Estecha, L. Sánchez-Martín, A. Puig-Kröger, R. A. Bartolomé, J. Teixidó, R. Samaniego, and P. Sánchez-Mateos, "Moesin orchestrates cortical polarity of melanoma tumour cells to initiate 3d invasion," *J. Cell Sci.*, vol. 122, pp. 3492–3501, Oct. 2009.

[127] K. E. Johnson, "Circus movements and blebbing locomotion in dissociated embryonic cells of an amphibian, xenopus laevis," *J. Cell Sci.*, vol. 22, pp. 575–583, Dec. 1976.

[128] M. M. Hanczyc, "Metabolism and motility in prebiotic structures," *Philosophical Transactions of the Royal Society B: Biological Sciences*, vol. 366, pp. 2885–2893, Oct. 2011.

[129] Y. Sumino, H. Kitahata, H. Seto, and K. Yoshikawa, "Blebbing dynamics in an oil-water-surfactant system through the generation and destruction of a gel-like structure," *Phys. Rev. E*, vol. 76, pp. 055202+, Nov. 2007.

[130] Y. Sumino, H. Kitahata, H. Seto, S. Nakata, and K. Yoshikawa, "Spontaneous deformation of an oil droplet induced by the cooperative transport of cationic and anionic surfactants through the interface," *J. Phys. Chem. B*, vol. 113, pp. 15709–15714, Dec. 2009.

[131] Y. Sumino, H. Kitahata, H. Seto, and K. Yoshikawa, "Dynamical blebbing at a droplet interface driven by instability in elastic stress: a novel self-motile system," *Soft Matter*, vol. 7, no. 7, pp. 3204–3212, 2011.

[132] J. M. Osborne, A. Walter, S. K. Kershaw, G. R. Mirams, A. G. Fletcher, P. Pathmanathan, D. Gavaghan, O. E. Jensen, P. K. Maini, and H. M. Byrne, "A hybrid approach to multi-scale modelling of cancer," *Philosophical Transactions of the Royal Society A: Mathematical, Physical and Engineering Sciences*, vol. 368, pp. 5013–5028, Nov. 2010.

[133] R. A. Gatenby and E. T. Gawlinski, "A reaction-diffusion model of cancer invasion," *Cancer Res.*, vol. 56, pp. 5745–5753, Dec. 1996.

[134] A. J. Perumpanani, J. A. Sherratt, J. Norbury, and H. M. Byrne, "Biological inferences from a mathematical model for malignant invasion," *Invasion & metastasis*, vol. 16, no. 4-5, pp. 209–221, 1996.

[135] G. Schaller and M. M. Hermann, "Multicellular tumor spheroid in an off-lattice Voronoi-Delaunay cell model," *Phys. Rev. E*, vol. 71, no. 5, 2005.

[136] A. R. A. Anderson, M. A. J. Chaplain, and K. Rejniak, *Single-Cell-Based Models in Biology and Medicine (Mathematics and Biosciences in Interaction)*. Birkhauser Basel, 1 ed., Aug. 2007.

[137] M. H. Zaman, R. D. Kamm, P. Matsudaira, and D. A. Lauffenburger, "Computational model for cell migration in three-dimensional matrices," *Biophys. J.*, vol. 89, pp. 1389–1397, Aug. 2005.

[138] D. Harjanto and M. H. Zaman, "Computational study of proteolysis-driven single cell migration in a three-dimensional matrix," *Annals of biomedical engineering*, vol. 38, pp. 1815–1825, May 2010.

[139] E. Palsson and H. G. Othmer, "A model for individual and collective cell movement in dictyostelium discoideum," *Proc. Natl. Acad. Sci. USA.*, vol. 97, pp. 10448–10453, Sept. 2000.

[140] M. Buenemann, H. Levine, W.-J. J. Rappel, and L. M. Sander, "The role of cell contraction and adhesion in dictyostelium motility," *Biophys. J.*, vol. 99, pp. 50–58, July 2010.

[141] A. F. Marée, A. Jilkine, A. Dawes, V. A. Grieneisen, and L. Edelstein-Keshet, "Polarization and movement of keratocytes: a multiscale modelling approach," *Bulletin of mathematical biology*, vol. 68, pp. 1169–1211, July 2006.

[142] J. B. Beltman, A. F. M. Marée, J. N. Lynch, M. J. Miller, and R. J. de Boer, "Lymph node topology dictates t cell migration behavior," *The Journal of Experimental Medicine*, vol. 204, pp. 771–780, Apr. 2007.

[143] S. A. Sandersius, C. J. Weijer, and T. J. Newman, "Emergent cell and tissue dynamics from subcellular modeling of active biomechanical processes," *Physical biology*, vol. 8, pp. 045007+, Aug. 2011.

[144] C. R. Sweet, S. Chatterjee, Z. Xu, K. Bisordi, E. D. Rosen, and M. Alber, "Modelling platelet–blood flow interaction using the subcellular element langevin method," *Journal of The Royal Society Interface*, May 2011.

[145] S. A. Sandersius and T. J. Newman, "Modeling cell rheology with the subcellular element model," *Physical Biology*, vol. 5, pp. 015002+, Apr. 2008.

[146] N. Watari and R. G. Larson, "The hydrodynamics of a run-and-tumble bacterium propelled by polymorphic helical flagella," *Biophys. J.*, vol. 98, pp. 12–17, Jan. 2010.

[147] Y. Mao, A. L. Tournier, P. A. Bates, J. E. Gale, N. Tapon, and B. J. Thompson, "Planar polarization of the atypical myosin dachs orients cell divisions in drosophila," *Genes & Development*, vol. 25, pp. 131–136, Jan. 2011.

[148] K. A. Rejniak, "An immersed boundary framework for modelling the growth of individual cells: An application to the early tumour development," *J. Theor. Biol.*, vol. 247, pp. 186–204, July 2007.

[149] V. Pappu and P. Bagchi, "3D computational modeling and simulation of leukocyte rolling adhesion and deformation," *Computers in Biology and Medicine*, vol. 38, pp. 738–753, June 2008.

[150] V. Pappu, S. K. Doddi, and P. Bagchi, "A computational study of leukocyte adhesion and its effect on flow pattern in microvessels," *J. Theor. Biol.*, vol. 254, pp. 483–498, Sept. 2008.

[151] D. Ly and C. Lumsden, "3d amoeboid migration of a eukaryotic cell in a fiber matrix," *Artificial Life and Robotics*, vol. 14, pp. 1–6, Sept. 2009.

[152] K. Bentley, G. Mariggi, H. Gerhardt, and P. A. Bates, "Tipping the balance: Robustness of tip cell selection, migration and fusion in angiogenesis," *PLoS Comput. Biol.*, vol. 5, pp. e1000549+, Oct. 2009.

[153] M. Herant, W. A. Marganski, and M. Dembo, "The mechanics of neutrophils: synthetic modeling of three experiments," *Biophys. J.*, vol. 84, pp. 3389–3413, May 2003.

[154] C. H. Schreiber, M. Stewart, and T. Duke, "Simulation of cell motility that reproduces the force-velocity relationship," *Proc. Natl. Acad. Sci. USA.*, vol. 107, pp. 9141–9146, May 2010.

[155] J. Young and S. Mitran, "A numerical model of cellular blebbing: a volume-conserving, fluid-structure interaction model of the entire cell," *Journal of biomechanics*, vol. 43, pp. 210–220, Jan. 2010.

[156] E. J. Spangler, C. W. Harvey, J. D. Revalee, S. B. Kumar, and M. Laradji, "Computer simulation of cytoskeleton-induced blebbing in lipid membranes," *Physical review. E, Statistical, nonlinear, and soft matter physics*, vol. 84, Nov. 2011.

[157] Y. Lan and G. A. Papoian, "The stochastic dynamics of filopodial growth," *Biophys. J.*, vol. 94, pp. 3839–3852, May 2008.

[158] T. E. Schaus and G. G. Borisy, "Performance of a population of independent filaments in lamellipodial protrusion," *Biophys. J.*, vol. 95, pp. 1393–1411, Aug. 2008.

[159] C. E. Chan and D. J. Odde, "Traction dynamics of filopodia on compliant substrates," *Science*, vol. 322, pp. 1687–1691, Dec. 2008.

[160] B. Chen and H. Gao, "Mechanical principle of enhancing cell-substrate adhesion via pre-tension in the cytoskeleton," *Biophys. J.*, vol. 98, pp. 2154–2162, May 2010.

[161] A. D. Drozdov, *Viscoelastic Structures: Mechanics of Growth and Aging*. Academic Press, Dec. 1997.

[162] P. D. Group, "Mathematical tools or statistics, monte carlo, group theory," *Phys. Lett. B*, vol. 667, pp. 316–339, Sept. 2008.

[163] G. I. Bell, "Models for the specific adhesion of cells to cells," *Science*, vol. 200, pp. 618–627, May 1978.

[164] D. F. J. Tees, K.-C. Chang, S. D. Rodgers, and D. A. Hammer, "Simulation of cell adhesion to bioreactive surfaces in shear: The effect of cell size," *Industrial & Engineering Chemistry Research*, vol. 41, pp. 486–493, Feb. 2002.

[165] D. A. Hammer and S. M. Apte, "Simulation of cell rolling and adhesion on surfaces in shear flow: general results and analysis of selectin-mediated neutrophil adhesion," *Biophys. J.*, vol. 63, pp. 35–57, July 1992.

[166] W. H. Press, B. P. Flannery, S. A. Teukolsky, and W. T. Vetterling, *Numerical Recipes in C: The Art of Scientific Computing, Second Edition*. Cambridge University Press, 2 ed., Oct. 1992.

[167] M. Galassi, J. Davies, J. Theiler, B. Gough, G. Jungman, P. Alken, M. Booth, and F. Rossi, *GNU Scientific Library Reference Manual - Third Edition*. Network Theory Ltd., 3rd revised edition ed., Jan. 2009.

[168] H. Coskun, Y. Li, and M. A. Mackey, "Ameboid cell motility: A model and inverse problem, with an application to live cell imaging data," *J. Theor. Biol.*, vol. 244, no. 2, pp. 169–179, 2007.

[169] R. Tran-Son-Tay, D. Needham, A. Yeung, and R. M. Hochmuth, "Time-dependent recovery of passive neutrophils after large deformation," *Biophys. J.*, vol. 60, pp. 856–866, Oct. 1991.

[170] R. M. Hochmuth, H. P. Ting-Beall, B. B. Beaty, D. Needham, and R. Tran-Son-Tay, "Viscosity of passive human neutrophils undergoing small deformations," *Biophys. J.*, vol. 64, pp. 1596–1601, May 1993.

[171] I. Miller and M. Miller, *John E. Freund's Mathematical Statistics with Applications (7th Edition)*. Prentice Hall, 7 ed., Oct. 2003.

[172] D. Choquet, D. P. Felsenfeld, and M. P. Sheetz, "Extracellular matrix rigidity causes strengthening of integrin-cytoskeleton linkages," *Cell*, vol. 88, pp. 39–48, Jan. 1997.

[173] S. W. Moore, P. Roca-Cusachs, and M. P. Sheetz, "Stretchy proteins on stretchy substrates: The important elements of integrin-mediated rigidity sensing," *Dev. Cell*, vol. 19, pp. 194–206, Aug. 2010.

[174] M. J. Paszek, N. Zahir, K. R. Johnson, J. N. Lakins, G. I. Rozenberg, A. Gefen, C. A. Reinhart-King, S. S. Margulies, M. Dembo, D. Boettiger, D. A. Hammer, and V. M. Weaver, "Tensional homeostasis and the malignant phenotype," *Cancer Cell*, vol. 8, pp. 241–254, Sept. 2005.

[175] K. R. Levental, H. Yu, L. Kass, J. N. Lakins, M. Egeblad, J. T. Erler, S. F. Fong, K. Csiszar, A. Giaccia, W. Weninger, M. Yamauchi, D. L. Gasser, and V. M. Weaver, "Matrix crosslinking forces tumor progression by enhancing integrin signaling," *Cell*, vol. 139, pp. 891–906, Nov. 2009.

[176] M. P. Neilson, D. M. Veltman, P. J. M. van Haastert, S. D. Webb, J. A. Mackenzie, and R. H. Insall, "Chemotaxis: A feedback-based computational model robustly predicts multiple aspects of real cell behaviour," *PLoS Biol.*, vol. 9, pp. e1000618+, May 2011.

[177] P. Rørth, "Whence directionality: Guidance mechanisms in solitary and collective cell migration," *Dev. Cell*, vol. 20, pp. 9–18, Jan. 2011.

[178] E. A. Clark, T. R. Golub, E. S. Lander, and R. O. Hynes, "Genomic analysis of metastasis reveals an essential role for rhoc," *Nature*, vol. 406, pp. 532–535, Aug. 2000.

[179] Y. Hegerfeldt, M. Tusch, E.-B. B. Bröcker, and P. Friedl, "Collective cell movement in primary melanoma explants: plasticity of cell-cell interaction, β1-integrin function, and migration strategies.," *Cancer Research*, vol. 62, pp. 2125–2130, Apr. 2002.

[180] E. Tzima, M. A. del Pozo, S. J. Shattil, S. Chien, and M. A. Schwartz, "Activation of integrins in endothelial cells by fluid shear stress mediates rho-dependent cytoskeletal alignment," *The EMBO Journal*, vol. 20, pp. 4639–4647, Sept. 2001.

[181] C. Hidalgo-Carcedo, S. Hooper, S. I. Chaudhry, P. Williamson, K. Harrington, B. Leitinger, and E. Sahai, "Collective cell migration requires suppression of actomyosin at cell-cell contacts mediated by ddr1 and the cell polarity regulators par3 and par6," *Nat. Cell Biol.*, vol. 13, pp. 49–58, Jan. 2011.

[182] P. Friedl and K. Wolf, "Tube travel: The role of proteases in individual and collective cancer cell invasion," *Cancer Res.*, vol. 68, pp. 7247–7249, Sept. 2008.

[183] C. Gaggioli, S. Hooper, C. Hidalgo-Carcedo, R. Grosse, J. F. Marshall, K. Harrington, and E. Sahai, "Fibroblast-led collective invasion of carcinoma cells with differing roles for rhoGTPases in leading and following cells," *Nat. Cell Biol.*, vol. 9, pp. 1392–1400, Dec. 2007.

[184] P. Kunda, A. E. Pelling, T. Liu, and B. Baum, "Moesin controls cortical rigidity, cell rounding, and spindle morphogenesis during mitosis," *Curr. Biol.*, vol. 18, pp. 91–101, Jan. 2008.

[185] M. Rauzi, P. Verant, T. Lecuit, and P.-F. Lenne, "Nature and anisotropy of cortical forces orienting drosophila tissue morphogenesis," *Nat Cell Biol*, vol. 10, pp. 1401–1410, Dec. 2008.

[186] E. C. Brockbank, J. Bridges, C. J. Marshall, and E. Sahai, "Integrin β1 is required for the invasive behaviour but not proliferation of squamous cell carcinoma cells *in vivo*," *British Journal of Cancer*, vol. 92, pp. 102–112, Jan. 2005.